

Dottorato di Ricerca in Ingegneria Civile
Graduate School in Civil Engineering

Sede: Facoltà di Ingegneria - Università di Pavia - via Ferrata 1 – 27100 Pavia – Italy

Dottorato di Ricerca in Ingegneria Civile VII Nuova serie (XXI Ciclo)

**Wind Effects on Bridges:
Response, Stability and Control**

Ph.D. Thesis
Filippo Ubertini

Advisors:

Prof. F. Bontempi
Prof. L. Faravelli

Revisor:

Prof. F. Casciati

Pavia, October 2008

To my family

Acknowledgements

The author would like to gratefully thank his mentors: Professor Franco Bontempi from University of Rome “La Sapienza” and Professor Lucia Faravelli from University of Pavia, for constantly providing their enthusiastic support, their scientific knowledge and their human experience during the preparation of this thesis.

A special thank goes to Professor Fabio Casciati, coordinator of the PhD School in Civil Engineering at University of Pavia, for encouraging this research and for his useful suggestions.

The author would like to sincerely thank Professor Raimondo Betti from Columbia University for the contribution given to this research and for his precious advices.

The suggestions by Professor Vincenzo Gattulli from University of L’Aquila, by Professor Ni from Hong Kong University and by Mr. Dyab A. Kazhem from Parsons Transportation Group are gratefully acknowledged by the author.

The fruitful collaborations with Dr Ahlum Hong from Columbia University, with Mr. Clemente Fuggini from University of Pavia and with Dr. Fabio Giuliano from University of Rome “La Sapienza” have certainly contributed to improve this work and are totally acknowledged by the author.

Description of the Ph.D. Course

Settore :	Ingegneria
Field :	Engineering
Sede amministrativa non consortile:	Università degli Studi di Pavia
Administrative location:	University of Pavia
Durata del Dottorato:	3 anni
Duration:	3 years
Periodo formativo estero:	Come previsto dal regolamento del Dottorato di Ricerca
Period in external organization:	As required by the School by-law
Numero minimo di corsi:	6
Minimum number of courses:	6

Il dottorato di ricerca in Ingegneria Civile dell'Università degli Studi di Pavia è stato istituito nell'anno accademico 1994/95 (X ciclo). Il corso consente al dottorando di scegliere tra quattro curricula: Idraulico, Sanitario, Sismico e Strutturale. Egli svolge la propria attività di ricerca presso il Dipartimento di Ingegneria Idraulica e Ambientale per i primi due curricula, quello di Meccanica Strutturale per i rimanenti. Durante i primi due anni sono previsti almeno sei corsi. Il Collegio dei Docenti, composto da professori dei due Dipartimenti (e da esterni cooptati in mancanza di competenze interne), organizza i corsi con lo scopo di fornire allo studente di dottorato opportunità di approfondimento su alcune delle discipline di base. Corsi e seminari vengono tenuti da docenti di Università nazionali ed estere. Il Collegio dei Docenti, cui spetta la pianificazione della didattica, si è orientato ad attivare ad anni alterni corsi comuni sui seguenti temi:

- Meccanica dei solidi e dei fluidi.
- Metodi numerici per la meccanica dei solidi e dei fluidi.
- Rischio strutturale e ambientale.
- Metodi sperimentali per la meccanica dei solidi e dei fluidi.
- Intelligenza artificiale.

più corsi specifici di indirizzo. Al termine dei corsi del primo anno il Collegio dei Docenti assegna al dottorando un tema di ricerca da sviluppare sotto forma di tesina entro la fine del secondo anno; il tema, non necessariamente legato all'argomento della tesi finale, è di norma coerente con il curriculum, scelto dal dottorando. All'inizio del secondo anno il dottorando discute con il Coordinatore l'argomento della tesi di dottorato, la cui assegnazione definitiva viene deliberata dal Collegio dei Docenti. Alla fine di ogni anno i dottorandi devono presentare una relazione particolareggiata sull'attività svolta. Sulla base di tale relazione il Collegio dei Docenti, "previa valutazione della assiduità e

dell'operosità dimostrata dall'iscritto", ne propone al Rettore l'esclusione dal corso o il passaggio all'anno successivo. Il dottorando può svolgere attività di ricerca sia di tipo teorico che sperimentale, grazie ai laboratori di cui entrambi i Dipartimenti dispongono, nonché al Laboratorio Numerico di Ingegneria delle Infrastrutture. Il "Laboratorio didattico sperimentale" del Dipartimento di Meccanica Strutturale offre:

- una tavola vibrante che consente di effettuare prove dinamiche su prototipi strutturali;
- opportuni sensori e un sistema di acquisizione dati per la misura della risposta strutturale;
- strumentazione per la progettazione di sistemi di controllo attivo e loro verifica sperimentale;
- strumentazione per la caratterizzazione dei materiali, attraverso prove statiche e dinamiche.

Il laboratorio del Dipartimento di Ingegneria Idraulica e Ambientale dispone di:

- un circuito in pressione per effettuare simulazioni di moto vario;
- un tunnel idrodinamico per lo studio di problemi di cavitazione;
- canalette per lo studio delle correnti a pelo libero.

The Graduate School of Civil Engineering at the University of Pavia was established in the Academic Year of 1994/95 (X cycle). The School allows the student to select one of the four offered curricula: Hydraulics, Environment, Seismic engineering and Structural Mechanics. Each student develops his

research activity either at the Department of Hydraulics and Environmental Engineering or at the Department of Structural Mechanics. During the first two years, a minimum of six courses must be selected and their examinations successfully passed. The Faculty, made by Professors of the two Departments or by internationally recognized scientists, organizes courses and provides the student with opportunities to enlarge his basic knowledge. Courses and seminars are held by University Professors from all over the country and abroad. The Faculty starts up in alternate years common courses, on the following subjects:

- solid and fluid mechanics,
- numerical methods for solid and fluid mechanics,
- structural and environmental risk,
- experimental methods for solid and fluid mechanics,
- artificial intelligence.

More specific courses are devoted to students of the single curricula. At the end of each course, for the first year the Faculty assigns the student a research argument to develop, in the form of report, by the end of the second year; the topic, not necessarily part of the final doctorate thesis, should be consistent with the curriculum selected by the student. At the beginning of the second year the student discusses with his Coordinator the subject of the thesis and, eventually, the Faculty assigns it to the student. At the end of every year, the student has to present a complete report on his research activity, on the basis of which the Faculty proposes to the Rector his admission to the next academic year or to the final examination. The student is supposed to develop either theoretical or experimental research activities, and therefore has access to the Department Experimental Laboratories, even to the Numerical Laboratory of Infrastructure

Engineering. The Experimental Teaching Laboratory of the Department of Structural Mechanics offers:

- a shaking table which permits one to conduct dynamic tests on structural prototypes;
- sensors and acquisition data system for the structural response measurements;
- instrumentation for the design of active control system and their experimental checks;
- an universal testing machine for material characterization through static and dynamic tests.

The Department of Hydraulics and Environmental Engineering offers:

- a pressure circuit simulating various movements;
- a hydrodynamic tunnel studying cavitation problems;
- micro-channels studying free currents.

Recapiti - Addresses

Dipartimento di Meccanica Strutturale
Via Ferrata, 1 27100 – Pavia – Italy
Tel. +39.0382.985450 – Fax +39.0382.528422

Dipartimento di Ingegneria Idraulica ed Ambientale
Via Ferrata, 1 27100 – Pavia – Italy
Tel. +39.0382.985300 – Fax +39.0382.985589

Coordinatore - Coordinator

CASCIATI Fabio – Professore Ordinario – ICAR/08
Dipartimento di Meccanica Strutturale
Via Ferrata, 1 27100 – Pavia – Italy
Tel. +39.0382.985458 – Fax +39.0382.528422
e-mail fabio@dipmec.unipv.it

Collegio dei Docenti – Teaching Staff

CAPODAGLIO Andrea Giuseppe Professore Associato - ICAR/03
CASCIATI Fabio Professore Ordinario - ICAR/08 - (Coordinatore)
CAUVIN Aldo Professore Ordinario - ICAR/09 §
CIAPONI Carlo Professore Straordinario - ICAR/01
FARAVELLI Lucia Professore Ordinario - ICAR/08
FUGAZZA Mario Professore Associato - ICAR/02
GOBETTI Armando Professore Associato - ICAR/08
MOISELLO Ugo Professore Ordinario - ICAR/02
PAPIRI Sergio Professore Associato - ICAR/02
SALA Roberto Professore Associato - ING - IND/08
MARCELLINI Alberto Dirigente di Ricerca, CNR - Milano.

§ Deceduto il 30 gennaio 2007

Previous Ph.D. Theses

Battaini Marco (X Ciclo)	Sistemi strutturali controllati: progettazione ed affidabilità
Mariani Claudia (X Ciclo)	Problemi di ottimizzazione per strutture bidimensionali anisotrope
Negri Antonella (X Ciclo)	Stima delle perdite idrologiche nei bacini di drenaggio urbani
Pisano Aurora Angela (XI Ciclo)	Structural System Identification: Advanced Approaches and Applications
Saltalippi Carla (XI Ciclo)	Preannuncio delle piene in tempo reale nei corsi d'acqua naturali
Barbieri Eugenio (XI Ciclo)	Thermofluid Dynamics and Topology: Optimization of an Active Thermal Insulation Structure
Barbolini Massimiliano (XII Ciclo)	Dense Snow Avalanches: Computational Models, Hazard Mapping and Related Uncertainties
Espa Paolo (XII Ciclo)	Moti atmosferici generati da forze di galleggiamento: simulazioni numeriche e studio su modello fisico
Petrini Lorenza (XII Ciclo)	Shape Memory Alloys: Modelling the Martensitic Phase Behaviour for Structural Engineering Exploitation
Podestà Stefano (XIII Ciclo)	Risposta sismica di antichi edifici religiosi: una nuova proposta per un modello di vulnerabilità
Sturla Daniele (XIII Ciclo)	Simulazioni lagrangiane di flussi rapidamente variati nell'approssimazione di acque poco profonde
Marazzi Francesco (XV Ciclo)	Semi--active Control of Civil Structures: Implementation Aspects
Nascimbene Roberto (XV Ciclo)	Sail Modelling for Maximal Speed Optimum Design

Giudici Massimo (XVI Ciclo)	Progettazione in regime non lineare di strutture in CAP a cavi aderenti e non aderenti
Mutti Matteo (XVI Ciclo)	Stability Analysis of Stratified Three--phase Flows in Pipes
Petaccia Gabriella (XVI Ciclo)	Propagazione di onde a fronte ripido per rottura di sbarramenti in alvei naturali
Casciati Sara (XVII Ciclo)	Damage Detection and Localization in the Space of the Observed Variables
D'Amico Tiziana (XVI Ciclo)	Ricerca e sviluppo di metodologie diagnostiche per il recupero di edifici monumentali: prove vibroacustiche sul tufo
Barco Olga Janet (XVII Ciclo)	Modeling the Quantity and Quality of Storm Water Runoff Using SWMM
Boguniewicz Joanna (XVIII Ciclo)	Integration of Monitoring and Modelling in the Surface Water State Evaluation Process of a Sub--Alpine Lake Watershed
Bornatici Laura (XVIII Ciclo)	L'impiego degli algoritmi generici per la risoluzione dei problemi di progetto di reti di distribuzione idrica
Collivignarelli Maria Cristina (XVIII) Ciclo	Trattamento di rifiuti liquidi mediante processi biologici aerobici termofili e mesofili e processi avanzati di ossidazione chimica in diversa
Domaneschi Marco (XVIII Ciclo)	Structural Control of Cable-stayed and Suspended Bridges
Ráduly Botond (XVIII Ciclo)	Artificial Neural Network applications in Urban Water Quality Modeling
Antoci Carla (XVIII Ciclo)	Simulazione numerica dell'interazione fluido-struttura con la tecnica SPH
Cappabianca Federica (XVIII Ciclo)	La valutazione del rischio valanghivo attraverso la modellazione dinamica
Callegari Arianna (XVIII Ciclo)	Applicazione di tecnologie di monitoraggio on-line per la gestione dei processi di trattamento reflui

Gazzola Elisa (XVIII Ciclo)	Applicazione di processi biologici anaerobici al trattamento di acque reflue e fanghi di depurazione: aspetti tecnici ed energetici\\
Giuliano Fabio (XIX Ciclo)	Performance Based Design and Structural Control for Cable Suspension Bridges
Maranca Federica (XVIII ciclo)	Valutazione del ciclo di vita (LCA): confronto tra sistemi di trasporto gas via gasdotto
Falappi Stefano (XIX Ciclo)	Simulazioni numeriche di flussi di fluidi viscosi e materiali granulari con la tecnica SPH
Zanaboni Sabrina (XIX Ciclo)	Pre-trattamento di rifiuti liquidi industriali mediante ossidazione ad umido
Matteo Bruggi (XX Ciclo)	Topology optimization using mixed finite elements
Gian Paolo Cimellaro (XX Ciclo)	Passive Control of Industrial Structures for Natural Hazard Mitigation: Analytical Studies and Applications

Index

Introduction and main motivation	pag. 1
<i>Abstract</i>	pag. 4
Outline of the thesis	pag. 5

PART 1: BASIC ASPECTS OF CABLE-SUPPORTED BRIDGES

Chapter 0

Basic aspects of cable-supported bridges

Abstract	pag. 7
0.1. Critical aspects in bridge dynamics	pag. 7
0.2. Wind effects on bridges	pag. 9
0.3. Mathematical models of cable-supported bridges	pag. 11
0.4. Concluding remarks	pag. 12

Chapter 1

Hierarchical macro-level models of suspension bridges

Abstract	pag. 13
1.1. Introduction	pag. 13
1.2. Large dimensional models of suspension bridges	pag. 14

1.3. Models validation	pag. 18
1.4. Reduced dimensional models of suspension bridges	pag. 23
1.5. Concluding remarks	pag. 28

Chapter 2

Efficient digital simulation of wind velocity field

Abstract	pag. 29
2.1. Introduction	pag. 30
2.2. Stochastic wind model	pag. 31
2.3. Digital simulation techniques	pag. 35
2.4. Comparison of different methods for digital wind simulation	pag. 45
2.5. Concluding remarks	pag. 63

PART 2: FUNDAMENTAL ASPECTS OF THE DYNAMICS OF CABLE-SUPPORTED BRIDGES

Chapter 3

Modeling unsteady aerodynamics in buffeting analysis of long-span bridges

Abstract	pag. 65
3.1. Introduction	pag. 65
3.2. Wind loading on bridge decks: frequency domain approaches	pag. 66
3.3. Wind loading on bridge deck: time domain approaches	pag. 69
3.4. Buffeting response using different formulations	pag. 74
3.5. Concluding remarks	pag. 80

Chapter 4

Buffeting analysis of bridges based on field measurements

Abstract	pag. 81
4.1. Introduction	pag. 81
4.2. Governing relations	pag. 82
4.3. Wind measurement data	pag. 84
4.4. FE structural modeling and updating	pag. 87
4.5. Wind-excited response: measured vs. simulated	pag. 94
4.6. Concluding remarks	pag.102

Chapter 5

Time domain aeroelastic stability analysis of bridges

Abstract	pag.105
5.1. Introduction	pag.105
5.2. Governing relations	pag.106
5.3. Time domain aeroelastic stability analysis via direct eigenvalue problem	pag.113
5.4. Time domain vs. frequency domain aeroelastic stability analysis of bridge decks: a case study	pag.115
5.5. Prediction of bridge flutter using FE models	pag.122
5.6. Concluding remarks	pag.125

Chapter 6

Including structural nonlinearities, atmospheric turbulence and experimental uncertainties in bridge aeroelasticity

Abstract	pag.127
6.1. Introduction	pag.127

6.2. Flutter in presence of structural nonlinearities	pag.128
6.3. Turbulence effects on aeroelastic stability	pag.137
6.4. Uncertain flutter analysis	pag.141
6.5. Concluding remarks	pag.145

PART 3: ADVANCED ASPECTS OF THE DYNAMICS OF CABLE-SUPPORTED BRIDGES

Chapter 7

Suppression of aeroelastic instabilities in cables and bridges

Abstract	pag.147
7.1. Introduction	pag.147
7.2. Cable galloping	pag.148
7.3. Suppression of cable galloping using TMDs	pag.149
7.4. Robust passive control of flutter via MTMDs	pag.152
7.5. Concluding remarks	pag.163

Chapter 8

Control solutions for cable vibration mitigation

Abstract	pag.165
8.1. Introduction	pag.165
8.2. Active state control	pag.166
8.3. Active control effectiveness	pag.170
8.4. Adaptive solution for intelligent cable vibration mitigation	pag.181
8.5. Analytical prediction and numerical validation	pag.184
8.6. Experimental results	pag.187
8.7. Concluding remarks	pag.193

Chapter 9

Nonlinear state observation for cable dynamics

Abstract	pag.195
9.1. Introduction	pag.195
9.2. Governing relations	pag.196
9.3. State observation for cable dynamics	pag.200
9.4. Numerical evaluation of the observer performances	pag.206
9.5. Application of the observer to active control	pag.215
9.6. Concluding remarks	pag.217

Concluding remarks	pag.219
---------------------------	---------

Bibliography	pag.225
---------------------	---------

Appendix A

Description of the case study bridges	pag.237
--	---------

Appendix B

Static and modal analysis using reduced dimensional models of suspension bridges	pag.245
---	---------

Appendix C

Modeling and identification strategies for cable dynamics	pag.251
--	---------

INTRODUCTION AND MAIN MOTIVATION

Wind effects on cable-supported bridges are studied, with a particular attention to response, stability and control problems.

The steadily growing demand for lighter and longer bridge designs is presently catching the attention of the scientific community. To this regards, realistically predicting the wind-excited response of cable-supported bridges, with a particular attention to stability problems, is mandatory for developing new challenging designs. In the meanwhile, there often exists the need of suppressing undesired levels of wind-excited vibrations which may affect either the deck or the cables (especially in stayed configurations) of these structures.

The work is organized into three parts: basic aspects of cable-supported bridges (part 1), fundamental aspects (part 2) and advanced aspects (part 3) of the dynamic behavior of cable-supported bridges when subjected to wind excitation. Two case studies are mainly considered within the thesis: the Tsing Ma Bridge and the New Carquinez Bridge, which are described in Appendix A. A brief outline of the thesis is given below.

Part 1: Basic aspects of cable-supported bridges

Chapter 0 introduces the basic aspects of cable-supported bridges using a multilayered approach which relies on the decomposition of the structural system at different scales. A particular attention is devoted to wind excitation.

Chapter 1 deals with numerical modeling of bridges, at the macro-level scale, in the framework of the finite element method. Particularly, three hierarchical macro-level models of the Tsing Ma Bridge, Hong Kong, are developed with the purpose of finding a sort of “minimal” model which is capable to catch the main dynamic features of the system (linear normal modes and stress-stiffening effects) with a reasonable computational expense.

Chapter 2 is devoted to the efficient simulation of the multivariate stochastic wind field, which is essential for nonlinear wind-excited response analysis. Indeed, dealing with a complex structure makes it mandatory to reduce

the computational expense required by wind simulations. To this end a comparative study between three relevant methods available in the literature is proposed.

Part 2: Fundamental aspects of the dynamics of cable-supported bridges

The models developed in Chapters 1 and 2 are utilized in **Chapter 3** to investigate the buffeting response of the Tsing Ma Bridge. The problem is attacked, in the time domain, by means of two classic formulations. The results emphasize that the predicted wind-excited response of the bridge could strongly differ depending on the way in which unsteady phenomena are modeled.

One of the main questions arising when reading Chapter 3 concerns the level of accuracy that can be achieved when numerically predicting the buffeting response of a long-span bridge. The purpose of **Chapter 4** is to give an answer to such a question. Referring to the New Carquinez Bridge, California, structural identification and FE model updating via a suitable optimization technique are addressed at first. Afterwards, the buffeting response of the bridge is simulated in the time domain. The comparison with the field measurements validates the adopted numerical procedure.

Chapter 5 deals with time domain aeroelastic stability analysis of bridges. Although most of the approaches currently available for predicting the onset of the flutter instability of bridges have been known since the 1940s (most of them have been borrowed from aerospace engineering), a well-established unified theoretical framework to treat this problem is yet to come. Within this field, the representation of self-excited loads via indicial functions has numerous advantages if compared to frequency domain approaches. To this regards, two main contributions are given. The former concerns the identification of the indicial functions from flutter derivatives via evolutionary algorithms. The latter consists of a manipulation of the governing equations which allows to eliminate integral terms thus trivializing the time domain aeroelastic stability analysis.

Chapter 6 analyzes the effects of nonlinearities, atmospheric turbulence and experimental uncertainties in bridge aeroelasticity. Within this field, geometric

nonlinearities and wind velocity fluctuations are seen to have nontrivial effects on the critic and postcritic behavior of the system. Moreover, the data scattering which is encountered in wind tunnel tests often leads to large uncertainties on the outcomes. This entails that the predictions of the onset of the aeroelastic instability must be treated from a probabilistic point of view, as one discusses through MonteCarlo simulations.

Part 3: Advanced aspects of the dynamics of cable-supported bridges

The suppression of structural aeroelastic instabilities via the use of single (TMD) and multiple tuned mass dampers (MTMD) is addressed in **Chapter 7**. The case of cable galloping is preliminary stressed. Afterwards, the flutter instability of a bridge deck is considered as a more complex and demanding case, in which mistuning effects may become unsustainable and make the single TMD solution completely unfeasible. A MTMD is conceived to enlarge the robustness against detuning effects and its effectiveness is analytically studied.

Chapter 8 focuses on the problem of reducing undesired levels of vibrations in stay cables via structural control policies. Substructure analytical models of the cables are adopted in the analysis. At a first stage of investigation, the effectiveness of an active state controller is studied in the nonlinear regime via analytical/numerical analysis. The main limitation of the active strategy is represented by the need of tracking the state of the system which, in the nonlinear regime, could entail serious difficulties. In order to circumvent this drawback, an innovative hybrid strategy combining a distributed passive solution and an open-loop semi-active actuation is proposed and its effectiveness is investigated via experimental tests and numerical simulations.

Chapter 9 is devoted to the relevant problem of state reconstruction in the nonlinear dynamics of cables. The problem is theoretically solved by introducing a suitable state observer, capable to handle a large class of nonlinearities. After discussing the observability conditions of the system, the feasibility of the adopted observer is investigated and its application to the active control strategy proposed in Chapter 8 is finally discussed.

Abstract

Challenging bridge designs are opening today numerous tasks, which mainly stand in the fields of bridge aeroelasticity and structural control. The thesis focuses on the wind-excited response of cable-supported bridges, with a particular attention to stability problems, and addresses two control priorities arising within this context: flutter suppression and cable vibration mitigation.

The numerical modeling of bridges at the macro-level scale and the efficient simulation of the multivariate stochastic wind field are examined in detail in the first three chapters.

Afterwards, the roles of different formulations to predict the buffeting response of cable-supported bridges are discussed. A particular care is devoted to structural model updating and to the agreement between measured and simulated buffeting responses. Frequency domain and time domain formulations for predicting the onset of the flutter instability of cable-supported bridges are then treated in detail. Structural nonlinearities and atmospheric turbulence are taken into account in the analysis as they are seen to have nontrivial effects on the critic and postcritic behaviors of the system. An effort is finally made to quantify the uncertainty of the predicted flutter velocity when accounting for the large experimental data scattering usually existing in wind tunnel tests.

The final part of the thesis is entirely devoted to flutter suppression in bridge decks and vibration mitigation in cable stays. Namely, controlling cable galloping and bridge flutter via the use of single and multiple tuned mass dampers is the first topic under investigation. Afterwards, the problem of cable vibration control is studied. To this end, two different policies are proposed and investigated both theoretically and experimentally. The problem of state reconstruction in the nonlinear regime, arising when designing an active state controller for cable dynamics, is finally studied.

OUTLINE OF THE THESIS

Chapter 1: From complex to simplified numeric models of suspension bridges in view of nonlinear wind response analysis	Models
Chapter 2: Compare efficiency and accuracy of Gaussian wind simulation methods in the case of large dimensional domains	

Part I: introduce the main numeric tools for bridge modeling and wind simulation

Chapter 3: Use the models developed in Chapters 1-2 to analyze the relevance of unsteady aerodynamics in the buffeting response of cable-supported bridges	Response
Chapter 4: Establish and validate a framework for predicting the buffeting response of cable-supported bridges with the aid of output only system identification and model updating	
Chapter 5: Formulate the flutter problem of bridge decks in the form of the trivial stability analysis of analytic autonomous systems using indicial functions	Stability
Chapter 6: Analyze the effects of structural nonlinearities, atmospheric turbulence and experimental uncertainties on the aeroelastic stability of bridge decks	

Part II: study the wind-excited response of bridges and its stability

Chapter 7: Study the use of multiple tuned mass dampers to suppress the flutter instability of bridge decks	Control
Chapter 8: Study an active state control strategy to suppress nonlinear vibrations in cable stays. Propose and analyze experimentally an alternative hybrid strategy combining an open loop actuation and the use of smart materials.	
Chapter 9: State the observability conditions for cable dynamics and solve the relevant problem of state reconstruction in the nonlinear regime .	

Part III: address control priorities: flutter suppression and cable vibration mitigation

Appendix A: Present the two case study bridges: the Tsing Ma Bridge and the New Carquinez Bridge	Appendices
Appendix B: Report static and modal results using the simplified models of suspension bridges presented in Chapter 1	
Appendix C: Introduce the basic notions for modeling the nonlinear dynamics of cables. Present and identify the experimental model of suspended cable adopted in Chapter 8 to analyze the proposed control strategy	

Complementary Part

Bridge dynamics		Cable dynamics	
<u>Chapter 1</u>		<u>Chapter 7</u>	
<u>Chapter 3</u>		<u>Chapter 8</u>	
<u>Chapter 4</u>		<u>Chapter 9</u>	
<u>Chapter 5</u>		<u>Appendix C</u>	
<u>Chapter 6</u>		Wind simulation	
<u>Chapter 7</u>			
<u>Appendix B</u>		<u>Chapter 2</u>	
Modeling issues	Response problems	Stability problems	Control problems
<u>Chapter 1</u>	<u>Chapter 3</u>	<u>Chapter 5</u>	<u>Chapter 7</u>
<u>Chapter 2</u>	<u>Chapter 4</u>	<u>Chapter 6</u>	<u>Chapter 8</u>
<u>Appendix B</u>		<u>Chapter 7</u>	<u>Chapter 9</u>
<u>Appendix C</u>			

Chapter 0

BASIC ASPECTS OF CABLE-SUPPORTED BRIDGES

Abstract

The basic notions of bridge dynamics are briefly presented, with a specific attention to wind-excitation and to the problems analyzed in the present thesis.

0.1 Critical aspects in bridge dynamics

The main external actions that excite long-span cable-supported bridges at the macro scale (see Appendix A for definitions) can be roughly classified into: wind loads, traffic loads (either produced by highways and railways) and seismic loads. Meso-level structural components are affected by each of these excitations at different levels of intensity as it is represented in Figure 0.1.

Generally speaking, wind excitation represents a severe action for towers at the free standing configuration (during the construction of the bridge), for the decking system and for long cable stays. On the contrary, the most severe action that affects the foundation system is certainly represented by seismic excitation. Traffic loads may be causes of fatigue ruptures in either main cables and hangers of suspension bridges (Petrini and Bontempi, 2008), as well as in the

decking system. Thus, a strong severity of this excitation in the above mentioned components should be accounted for (see Figure 0.1).

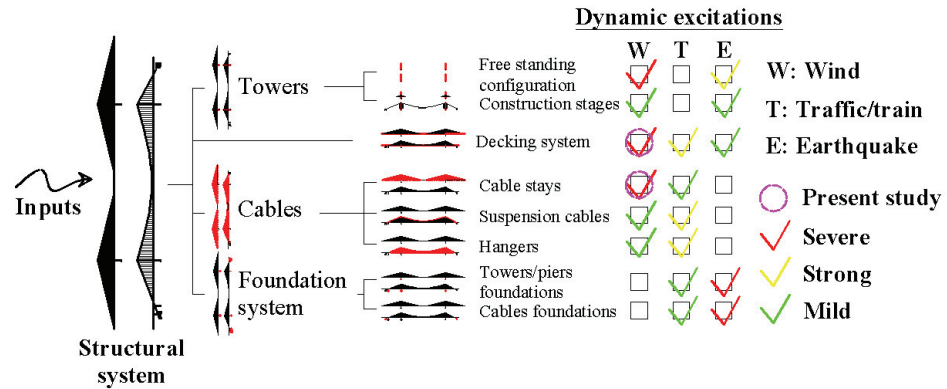


Figure 0.1. Severity of different environmental actions on meso-level components of cable-supported bridges

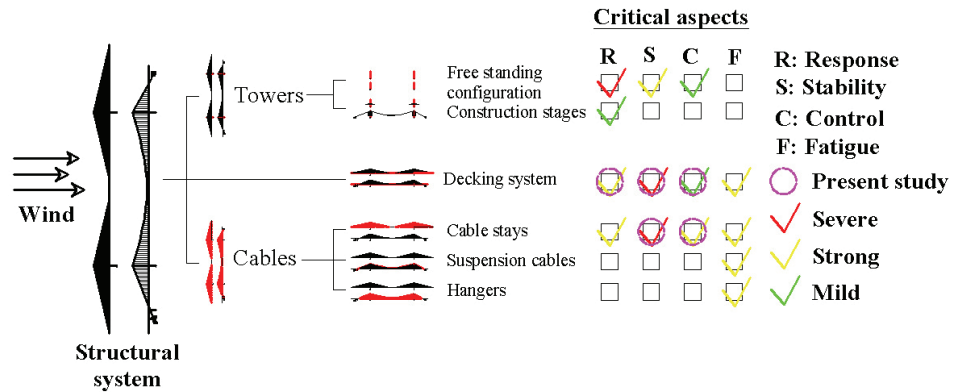


Figure 0.2. Severity of wind effects on meso-level components of cable-supported bridges

As it is also emphasized in Figure 0.1, the present thesis mainly focuses on wind effects on the decking system and on cable stays. Taking a closer look to these two problems, the scenario that is depicted in Figure 0.2 is encountered. Namely, wind effects can be roughly classified into: response, stability, control

and fatigue-related problems. As an example, wind loads on cable-supported bridges may produce runability problems, i.e. large responses of the deck which may prevent running trains to cross the bridge at certain levels of external excitation. This can be seen as a strong response demand to the decking system. However, as the most severe case, wind loads may also produce aeroelastic stability problems (either affecting the deck or the cable stays) eventually leading to structural failures (severe demand). Wind response may also represent a severe demand for the towers at the free standing configurations, while it usually becomes a mild excitation for the towers during successive construction stages due to a change in the natural periods of these structural elements (Giuliano, 2007). Structural control may become a strong requirement for vibration suppression in long cable stays which may exhibit dynamic instabilities such as those ensuing from the contemporary action of wind and rain.

The critical aspects which are primarily considered in the present thesis are: response, stability and control of deck vibrations and stability and control of cable vibrations (see Figure 0.2).

0.2 Wind effects on bridges

The effects of wind on the global dynamic response of cable-supported bridges can be subdivided into response and stability problems (see Figure 0.3). In response problems, there is a dynamic equilibrium between the body and the wind forces, while, in stability problems, interchanging energy between the body motion and the aeroelastic forces leads to a loss of equilibrium stability.

The typical response problem in bridges is represented by the dynamic response to fluctuating wind velocities (buffeting response). Among the several types of possible aeroelastic instabilities occurring in long-span cable-supported bridges a special attention must be paid to torsional divergence (static instability) and to flutter (dynamic instability). The former arises when the system (first order systems of equations of motion) exhibits a double-zero eigenvalue at a certain value of the control parameter (wind velocity). This usually leads to an unbounded torsional response produced by the fact that the

aeroelastic moment overcomes the elastic resistant moment of the structure. Flutter is on the contrary characterized by a pair of complex conjugate eigenvalues with zero real parts. Usually, this leads to a coupled bending-torsional harmonic motion characterized by a nil damping. However, a single degree of freedom flutter may also be encountered in some cases.

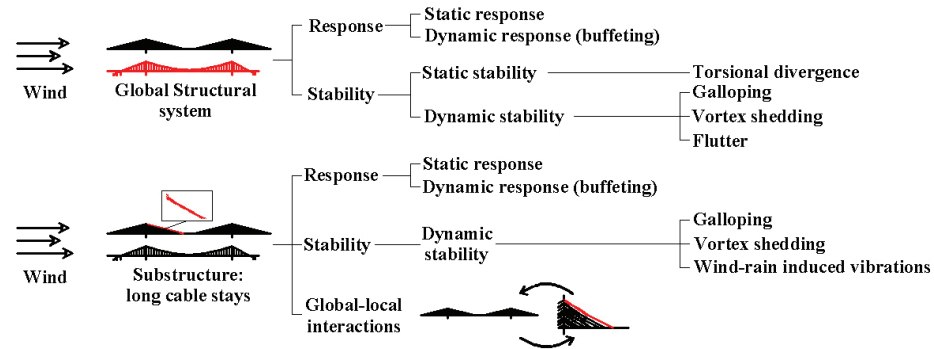


Figure 0.3. Wind effects on bridges and on cable stays

Galloping and vortex shedding are a little less relevant phenomena for bridge decks. The former is produced by an asymmetry in the flow which produces vertical oscillations of the deck. If the aerodynamic damping is greater than the structural damping, this vertical oscillations may become unbounded as a consequence of the fact that, for some body shapes, lift forces and structural damping forces have opposite sign. Finally, vortex shedding is a sort of resonant problem in which the frequency of a structural mode and the one of the alternating vortices arising in the wake of the body are very close to each other and eventually get closer (lock-in phenomenon).

A special attention in the interaction between wind and cable-supported bridges should be paid to the dynamics of long cable stays. These lasts may exhibit large oscillations as a consequence of both response and stability problems (see Figure 0.3). As an example, the problem of wind-rain induced vibrations in cable stays was observed in many cable stayed bridges around the world. Unfortunately, this problem has not been solved yet and a well-established understanding of this phenomenon is yet to come. A particular care

should also be paid to the vertical motion of the deck which represents an external excitation for the cable assuming the well-known parametric nature. This circumstance could lead to large cable vibrations when a global-local interaction exists between the whole structure and the cable itself (see Figure 0.3).

0.3 Mathematical models of cable-supported bridges

It is of particular interest to have an idea of the type of mathematical models of long-span cable-supported bridges usually adopted in the technical literature for wind response and stability analysis.

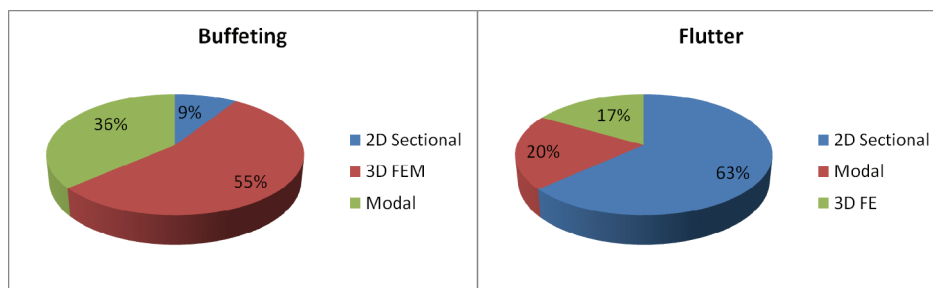


Figure 0.4 Statistics of bridge models available in the technical literature for wind-bridge interaction problems

By randomly selecting 41 technical papers recently published in international journals and specific conferences on these topics, 30 were referring to aeroelastic stability problems and 11 to buffeting problems. Among those, one can roughly define three main categories of models: bidimensional deck models, modal representations and tridimensional finite element (FE) models. Bidimensional deck models are those in which the dynamics (usually linear) of a bridge deck is condensed to the dynamics of an equivalent elastic system usually having a vertical and a torsional degree of freedom. Modal representations usually consider a larger number of degrees of freedom (linear normal modes) of the deck, but still rely on the hypothesis of a linear structural behavior. Finally, tridimensional FE models usually incorporate geometric

nonlinearities in the time domain and are often of the spine-type, i.e. the deck is modeled as a single equivalent frame.

The statistics of the models are represented in Figure 0.4. The results emphasize that the use of tridimensional FE models is dominating in buffeting analysis, although modal representations of the system dynamics are also adopted in some cases. On the contrary, stability analysis are usually performed utilizing bidimensional deck models. This is somehow surprising since geometric nonlinearities, correctly modeled by means of tridimensional FE models, are more likely dominating in stability problems, involving larger external excitations, rather than in response ones. Indeed, though it is true that structural nonlinearities do not affect the critic condition which can be effectively predicted through a linearized dynamics, they anyway govern the postcritical behavior which is fundamental for structural safety evaluations.

0.4 Concluding remarks

The critical aspects of the dynamics of cable-supported bridges, with a particular attention to wind excitation, have been introduced using a multilayered approach which relies on the decomposition of the structural system at different scales.

Chapter 1

HIERARCHICAL MACRO-LEVEL MODELS OF SUSPENSION BRIDGES

Abstract

The numerical modeling of long-span suspension bridges, at the macro-level scale, in view of nonlinear wind response analysis, is the topic of the present chapter. The aim is to compare the accuracy of simplified models with respect to more detailed ones, in predicting the modal parameters of an existing suspension bridge. The capability of simplified models in reproducing the geometric nonlinear behavior of the deck is also accounted for.

1.1 Introduction

Two case study bridges are considered within this thesis: the Tsing Ma Bridge, located in Hong Kong, China and the New Carquinez Bridge located in San Francisco, California. The main structural features of these bridges are presented in Appendix A. In this chapter the Tsing Ma Bridge is assumed as a benchmark to identify a sort of minimal model in view of nonlinear wind response analysis. To this end, three finite element (FE) macro-level models of the Tsing Ma Bridge, developed in the commercial Ansys CivilFEM

environment (Ansys Inc., 2005), are presented in order of decreasing complexity. The first model, called Tsing Ma Complete (TMC), is an accurate numeric replication of the real structure. The necessary information to build such a detailed model was kindly provided by Prof. Ni from Hong Kong University, whose advices are fully acknowledged by the author. In the second model, called Tsing Ma Reduced (TMR), a simplified equivalent deck is considered, while in the third model, called Tsing Ma Spine (TMS), the deck is drastically simplified to a single longitudinal frame, with cross rigid frames (outriggers) in correspondence of the hangers.

1.2 Large dimensional models of suspension bridges

Reduced dimensional numeric models of suspension bridges can be derived by properly simplifying large dimensional ones. An example of large dimensional model of the Tsing Ma Bridge (see Appendix A) is presented in this section. The model, called The Tsing Ma Complete (TMC), is validated by comparison with static and modal experimental results available in the literature.

1.2.1 General FE formulation

The TMC model is coded in the Ansys CivilFEM environment, in the framework of large/small-strains and large displacements. Large strain elements are adopted to model cables, suspenders and deck shells. In all other elements, strains are assumed to be infinitesimal and the large-displacements-small-strains formulation (large-rotations) is applied. The behavior of the materials is presumed to be linear elastic, with the only exception of the lateral bearings of the deck, which have a nonlinear constitutive behavior. The number and type of adopted finite elements are summarized in Table 1.1. The material properties adopted in the model are summarized in Table 1.2.

Two-nodes tridimensional beams are adopted to reproduce the behavior of mono-dimensional elements (including hangers and main cables). In particular, Ansys BEAM4 elements (large deflections, small strains) are adopted to model deck, piers and tower frames, while BEAM188 (large deflections, large strains)

are utilized in the cases of cables and hangers. Both BEAM4 and BEAM188 elements are based on Timoshenko's beam theory, which allows transverse shear deformations and may be used to reproduce the behavior of both thick and slender beams. The lumped mass matrix is considered instead of the consistent mass formulation. BEAM4 elements are also adopted to model rigid bodies, by means of a fictitious rigid material, with no mass density. Four-nodes quadrilateral large-strain membrane elements (Ansys SHELL43) are adopted to model the behavior of the steel plates and the steel cladding of the deck. The lateral bearings of the deck are reproduced through tridimensional nonlinear links (COMBIN39) and tridimensional linear trusses with large displacements capability (LINK8). Additional masses (MASS21) are also adopted in special cases, such as to reproduce the masses and weights of the saddles on the top of the tower legs. Some graphical representations of the TMC model are presented in Figure 1.1.

Group	Element Type	No. of Elements
1	BEAM 4	13534
2	BEAM 188	592
3	SHELL 43	4589
4	COMBIN 39	66
5	LINK 8	34
6	MASS 21	24
Total No. of Elements		18839

Table 1.1. Main features of the TMC model

Material	Density (kg/m ³)	E (N/m ²)	ν
Reinforced Concrete	2400	$3 \cdot 10^{10}$	0.2
Decking Steel	7800	$20 \cdot 10^{10}$	0.3
Cables Steel	7935	$19.6 \cdot 10^{10}$	0.3
Hangers Steel	7800	$13.4 \cdot 10^{10}$	0.3
Plate Steel	16950	$23 \cdot 10^{10}$	0.3
Cladding Steel	7800	$20 \cdot 10^{10}$	0.3

Table 1.2. Material properties assumed in the TMC model

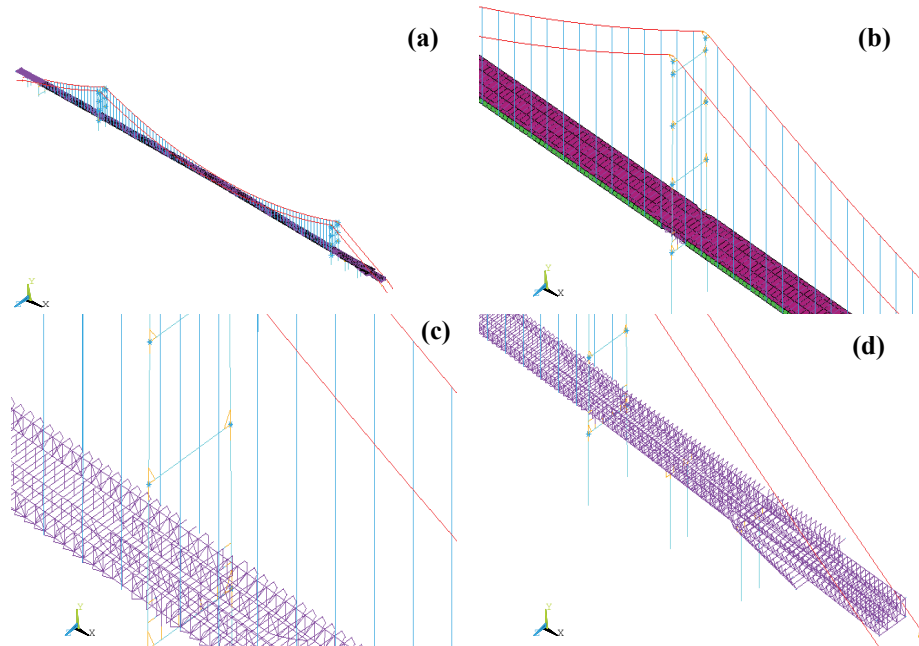


Figure 1.1. TMC FE model: global overview (a); deck and Ma Wan tower (b); additional longitudinal trusses near the Ma Wan tower (c); Tsing Yi span (d)

In large strain elements, strains are assumed to be finite and are evaluated in logarithmic (true) form. The shape of the elements changes and deflections and rotations may be indefinitely large. In small strain elements, strains are assumed to be infinitesimal and engineering strain measures are adopted. Shape structural modifications are neglected except for rigid body motions. Nevertheless, stress-stiffening behavior is considered by assuming the large rotation hypothesis (i.e. large deflections with small strains). The stress stiffness matrix is formally calculated as in large strain elements, but the logarithmic strain measure is replaced by the nonlinear strain-displacements relation, truncated at the second order terms.

1.2.2 Modeling Towers and Piers

The towers are modeled as three-dimensional multilevel portal frames with fixed boundary conditions at the base. Soil-structure interaction is neglected in

consideration of the relative rigidity of the underlying bedrock. The shear deformation of the members is also accounted for by assuming unit shear constants and by using tridimensional Timoshenko beam elements. In order to take into account of the considerable size of the cross sections in the calculation of the flexural rigidities, the nodes of the portal frames are modeled by means of rigid connections. The variation of the section properties along the height is reproduced by using 17 different cross sections to model the frames of each leg from the base to the top.

Each of the tower legs is composed by 25 beam elements. The cross frame supporting the bridge deck is subdivided into 8 elements, while the remaining 3 cross frames are modeled using 2 beam elements for each one. The masses and rotary inertias of the structural joints and of the cable are reproduced by means of three-dimensional point masses elements. Piers M1, M2, T2 and T3 are modeled using three-dimensional beam elements with flexural, shear and torsional rigidities. Pier T1 is on the contrary reproduced by means of fixed displacements boundary conditions. All the piers are considered as fixed at the base.

1.2.3 Modeling Cables and Suspenders

The main cables and the suspenders are modeled using three-dimensional beam elements accounting for reduced flexural rigidities provided by the friction between wires. The main anchorages are reproduced by means of fixed boundary conditions. No rotation releases are introduced in the connections. The cable between two suspender units is modeled by a single beam element, leading to 74 elements per cable in the main span and 21 elements in the Ma Wan span. Each of the main cables in the Tsing Yi span is modeled using 18 beam elements. Each suspender unit is modeled by one single element representing the four strands.

1.2.4 Modeling the Bridge Deck

As already outlined, the bridge deck is modeled in such a way to carefully reproduce the decking system. The hybrid truss and box form of the deck is

reproduced by means of three-dimensional Timoshenko beam elements (for the frames) and four-nodes quadrilateral shell elements (for the steel plates and steel cladding). The curvature of the deck along the longitudinal axis is considered. Initial axial stresses are assigned to the main cables and to the suspenders in order to approximately preserve the same configuration after the application of the dead loads (see Section 1.3). All the changes encountered in the deck sections are accounted for, leading to 6 different sections along the bridge. These “typical” sections include additional longitudinal trusses near the towers (see Figure 1.1 c), approaching streets in the Tsing Yi side (see Figure 1.1 d), Vierendeel cross frames and steel cladding modifications, etc. The connection between the deck and the towers is modeled by means of 4 vertical steel trusses supported by rigid links and 4 horizontal nonlinear links. The same approach is also adopted to model the connection between deck and piers.

1.3 Models validation

FE models of suspension bridges must be validated on the basis of the available information on the real structure, such as static reactions, natural frequencies, mode shapes and so on. This issue is discussed with reference to the TMC model presented in Section 1.2.

A nonlinear static analysis under dead loads and a modal analysis on the linearized system are carried out. Axial pretensions are assigned to main cables and hangers in the nonlinear static analysis. The initial cables stresses are identified through manual tuning, by satisfying the following conditions:

- a maximum vertical deviation from the initial deck configuration of 0.025% with respect to the length of the main span (34 cm);
- a maximum percentage difference of 5% between the computed horizontal tension of the main cables in the Tsing Yi side and the value reported in the paper by Ni et al. (2004).
- a maximum mean percentage difference of 4% between the first 17 computed natural frequencies and those measured and summarized in the paper by Xu and Ko (1997);

1.3.1 Static analysis

As summarized in Table 1.3, the vertical reactions calculated by means of substructure models (from towers alone to the complete one), well reproduce the approximated weights of the components of the Tsing Ma Bridge (see Table A.1).

Model	Vert. Reaction (t)	Approx. Weight (t)
TY tower alone	52401.6	52000
MW tower alone	52962.3	51000
TY-MW Towers-Cables	133741.1	129700
TY-MW Towers-Cables-Hangers	135209.0	131200
No Deck model	168420.0	164200
Complete Model	228878.7	213200

Table 1.3. Computed (using TMC model) vertical reactions vs. expected weights

The vertical displacements of the bridge under dead loads are represented in Figure 1.2. A maximum vertical displacement of 0.314 m is obtained from the analysis, which corresponds to the 0.023 % of the bridge span. The computed horizontal tension of the main cables in the Tsing Yi side is $H_x=388863$ kN, which, compared to value of 405838 kN reported in the paper by Ni et al. (2004), gives a percentage difference of 4.2 %. Thus, the first two conditions stated in the introduction of this section are satisfied.

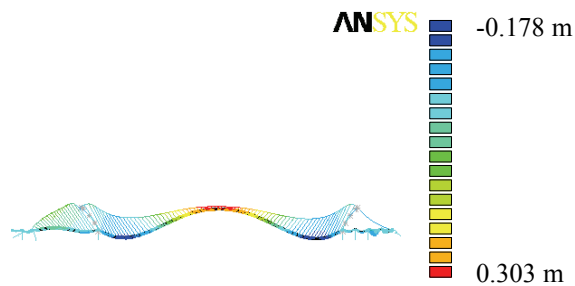


Figure 1.2. Computed (using TMC model) vertical displacements under dead loads with pre-tensioned cables

1.3.2 Linear normal modes

The first 200 natural frequencies and mode shapes (linear normal modes) of the Tsing Ma Bridge are calculated in the neighborhood of the pre-stressed configuration under dead loads using the TMC model. The first 6 mode shapes are represented in Figure 1.3, while Figure 1.4 shows the histogram of the first 200 natural periods. The first 17 natural frequencies of the bridge were experimentally measured and their values were reported in the paper by Xu and Ko (1997). A comparison between computed and measured natural frequencies is reported in Table 1.4, where the percentage differences Δ are also calculated. A mean percentage difference of 3.60% is obtained from the analysis, being therefore satisfied also the third condition stated above.

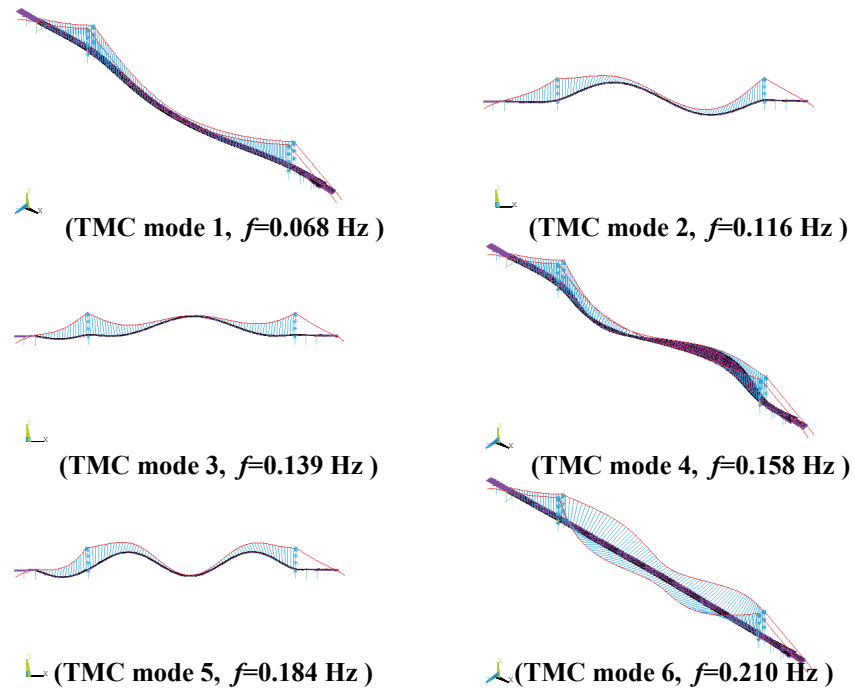


Figure 1.3. First 6 computed (TMC) mode shapes of the bridge

The largest observed differences concern the first two torsional modes (8th and 12th modes) represented in Figure 1.4. However, it must be noted that the

frequency of the 8th mode is in good accordance with the one obtained, numerically, in the paper by Wong (2004), as outlined in Table 1.5.

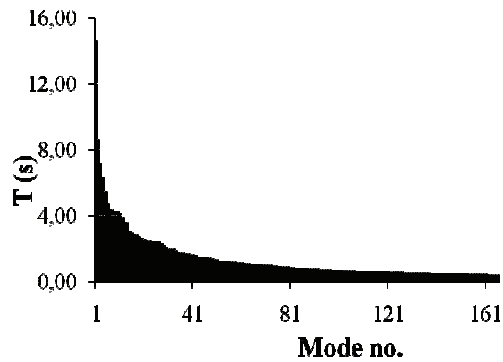


Figure 1.5. Histogram of the first 200 computed (TMC) natural periods

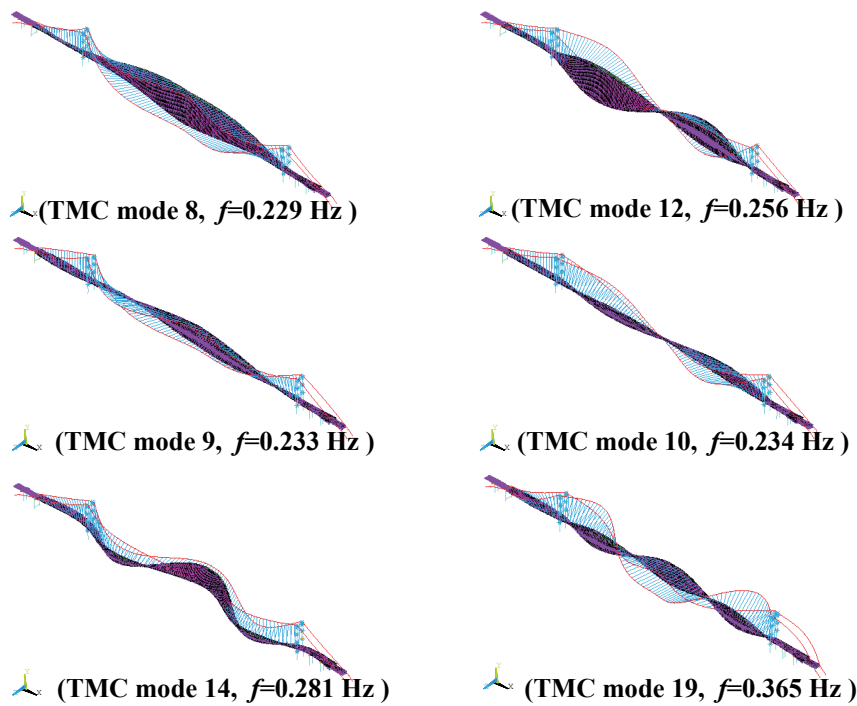


Figure 1.6. Hybrid torsion/bending modes calculated by means of the TMC model

Vertical Modes			
Bridge Mode	TMC	Xu & Ko, 1997	Δ (%)
2	0.116	0.113	2.6
3	0.139	0.130	6.5
5	0.184	0.184	0.0
11	0.242	0.241	0.4
13	0.276	0.284	2.8
15	0.328	0.327	0.3
Transverse Modes			
Bridge Mode	TMC	Xu & Ko, 1997	Δ (%)
1	0.068	0.069	1.4
4	0.158	0.164	3.7
6	0.210	0.214	1.9
7	0.228	0.226	0.9
9	0.233	0.236	1.3
10	0.234	0.240	2.5
16	0.341	0.336	1.5
17	0.351	0.352	0.3
20	0.383	0.381	0.5
Torsional Modes			
Bridge Mode	TMC	Xu & Ko, 1997	Δ (%)
8	0.229	0.267	14.2
12	0.256	0.320	20.0
MEAN DIFFERENCE Δ_{mean} (%)			3.6

Table 1.4 Computed vs. measured natural frequencies

Bridge Mode	COMPUTED	Wong 2004	Δ (%)
1	0.068	0.069	1.4
2	0.116	0.117	0.8
8	0.229	0.238	3.8

Table 1.5 Comparison between computed (TMC) natural frequencies and those obtained (numerically) by Wong (2004)

The model also evidences the participation of both torsion and out-of-plane bending, in the 8th and 12th modes. The same circumstance is also observed in

the 9th and 10th bridge modes, whose calculated frequencies are 0.233 Hz and 0.234 Hz, respectively (see Figure 1.6). Higher order hybrid torsion/bending modes are also detected in the analysis, such as the 14th and 19th ones, which are shown in Figure 1.6. These last two modes assume frequency values of 0.281 Hz and 0.365 Hz respectively, which are not far from the first two torsional frequencies found by Xu and Ko (1997). These circumstances lead to presume that the interaction between torsion and bending produces slight frequency shifts in the bridge modes. Thus, in the numerical model, the torsional mass of the deck participates to several hybrid modes and a pure torsional mode with a frequency value of 0.269 Hz is hard to capture. The accordance with the numerical results presented in the paper by Wong (2004) confirms, to some extent, this hypothesis.

1.4 Reduced dimensional models of suspension bridges

This Section focuses on the derivation of reduced dimensional models of suspension bridges by simplifying large dimensional ones. This approach is applied to the case of the Tsing Ma Bridge for which two simplified models are presented in order of decreasing complexity starting from the TMC model.

A first-step reduction of the TMC model is performed leading to a model called Tsing Ma reduced (TMR). An equivalent deck is adopted in the TMR model, utilizing a significantly smaller number of finite elements with respect to the TMC one. For computational convenience, large displacement trusses (LINK8) are adopted to reproduce the hangers, instead of large strain beams (BEAM188), as done in the TMC model. All other elements (towers frames, cables and piers) are identical in the two models.

In the simplified deck of the TMR model all the major elements existing in the bridge are retained: the two longitudinal trusses and the stiffening plates. A single level deck is adopted, utilizing both BEAM4 and SHELL43 elements. The two longitudinal trusses are modeled by means of mono-dimensional frames, while the stiffening plates are modeled by means of shell elements. Mono-dimensional elements are also adopted to model the outriggers of the

deck. In the TMR model the number of elements is reduced of 73% with respect to the TMC one. This leads to a considerable reduction of the computational effort, which can be roughly quantified to 75%. Some views of the TMR model around the Ma Wan and Tsing Yi towers are presented in Figure 1.7.

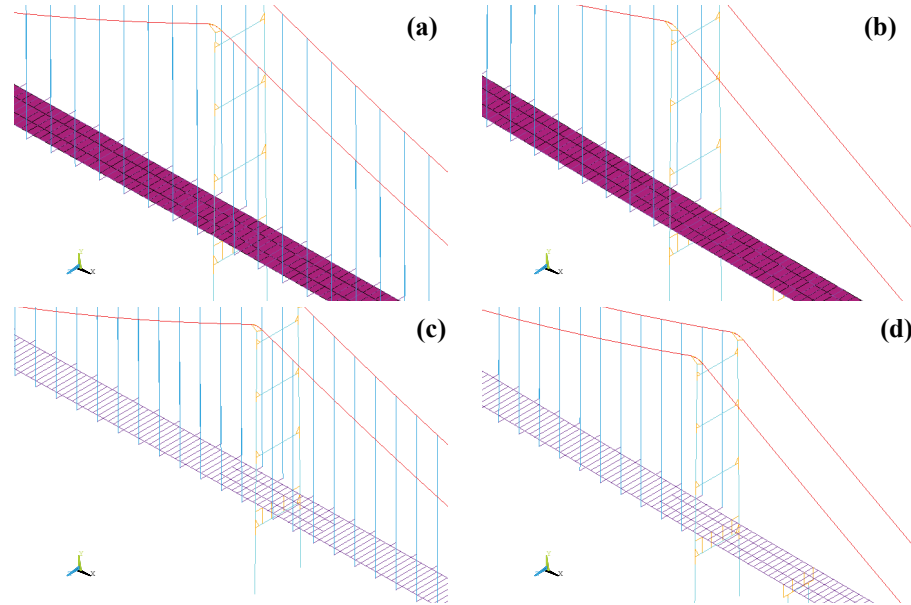


Figure 1.7. TMR FE model: deck and Ma Wan tower (a); deck and Tsing Yi tower (b); Ma Wan span (c); Tsing Yi span (d)

The same axial pretensions assumed in the TMC model are assigned also to the main cables and hangers of the TMR model. As already done in Section 1.3, both static and modal results are considered for model validation purposes.

The results of the validation process, reported in Appendix B for the seek of brevity, outline that the TMR model gives almost similar results to the TMC one and well matches the global bridge vibration features experimentally evaluated by Xu and Ko (1997). In particular, static and modal results are practically identical between the two models. Moreover, first two torsional modes are captured with a much better approximation by the TMR model rather than by the TMC one. This circumstance is due to the fact that, in the TMR

model, the torsional rigidities of the deck have been regulated via manual tuning in order to match the torsional frequencies experimentally obtained in (Xu and Ko, 1997).

The first torsional mode predicted using the TMR model is a hybrid torsional/bending one. This circumstance has been evidenced also by the TMC model. The 13th mode calculated by means of the TMR model is also a hybrid torsional/bending mode, which is quite similar and close to the 14th mode calculated with the TMC model (see Appendix B). These results evidence the good agreement between the modal parameters predicted by the TMC and the TMR model, even for hybrid modes.

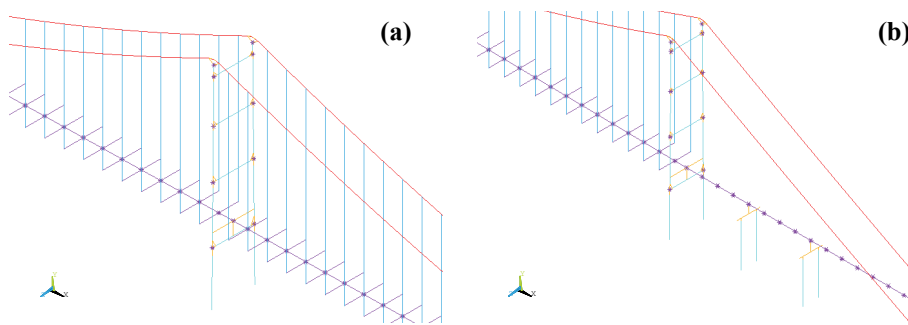


Figure 1.8. TMS FE model: detailed view of the deck and the Ma Wan tower (a); detailed view of the deck and the Tsing Yi tower (b)

The TMR model represents a good compromise between numerical accuracy and computational efficiency. However, a further simplified model with a considerably lower computational effort is required for long time dynamical simulations. To this end, a very light model of the bridge, called Tsing Ma spine model (TMS), is developed. In particular, starting from the TMR model, the deck is simplified to an equivalent longitudinal frame, with transverse rigid frames in correspondence of the hangers (see Figure 1.8).

In the TMS model, the frames of the deck are reproduced by means of BEAM4 elements, with null mass density and mass weight. Concentrated equivalent masses, with rotary inertia in the longitudinal bridge direction, are placed along the deck, at a mutual distance of 18 m. Bending and torsional

rigidities are assigned in such a way to have the best matching as possible between numerical and experimental natural frequencies. In order to correctly evaluate the normal stresses, the thicknesses of the cross section are 7.2 m in the vertical direction and 36 m in the out-of-plane direction. A unit shear constant is assumed to account for shear deformation. Table 1.6 summarizes the total number of elements and nodes adopted in the three FE model of the bridge, thus emphasizing the significant dimension reduction achieved with the TMS model, with respect to the TMR and TMC ones.

Group	Element Type	No. of Elem. (TMC)	No. of Elem. (TMR)	No. of Elem. (TMS)
1	BEAM 4	13534	2986	823
2	BEAM 188	592	588	588
3	SHELL 43	4589	1440	0
4	COMBIN 39	66	0	0
5	LINK 8	34	190	0
6	MASS 21	24	24	123
Total No. of Nodes		7325	3352	1966
Total No. of Elements		18839	5038	1534

Table 1.6. Main features of the TMC, TMR and TMS models

Again for the TMS model, validation with respect to the TMC one and to the experimental results available in the literature is preliminary carried out. The results of this validation process are reported in Appendix B. As in the previous case (TMR model), the TMS model is able to carefully reproduce expected static and modal results, with the same accuracy of the TMC model. Moreover, as for the TMR case, the TMS model carefully predicts also the expected torsional frequencies, which on the contrary are not well predicted by the TMC model. It is worth noting that the TMS model is also able to capture hybrid bending/torsional modes (see Appendix B).

A very relevant point, when simplifying a numeric model, is to correctly reproduce the nonlinear stress-stiffening behavior of its components. Thus, attention is paid to the stress stiffening behavior of the deck predicted by either TMR and TMS models.

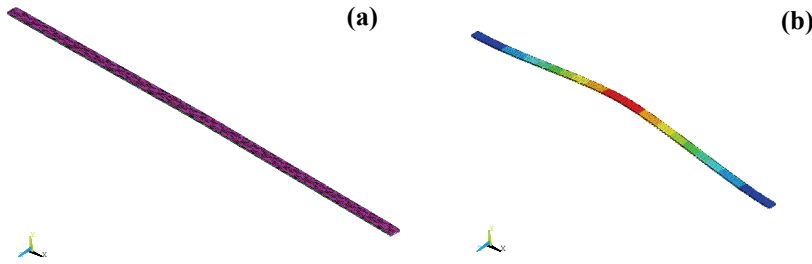


Figure 1.9. TMC deck: undeformed configuration (a); deformed configuration under central vertical load (clamped boundary conditions) (b)

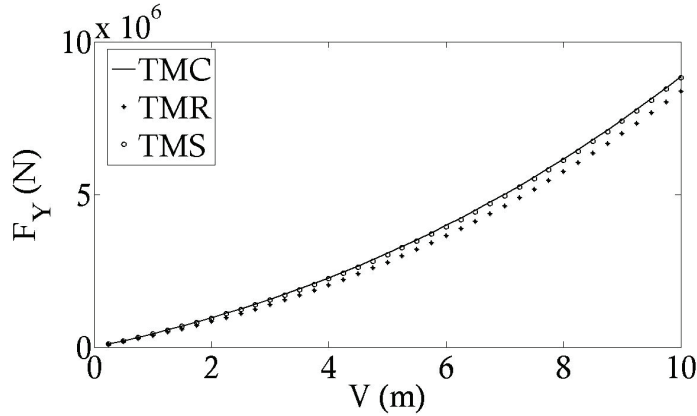


Figure 1.10. Nonlinear force-displacement curve of clamped-clamped deck (V denotes the vertical mid-span displacement, F_Y is the vertical reaction at the boundaries)

The deck of the TMC model is assumed to well reproduce the behavior of the real bridge deck in terms of geometric nonlinearities. In order to obtain a similar behavior, the axial rigidities of the longitudinal elements in the TMR and TMS models are regulated by manual tuning. To do so, the deck of the TMC model clamped at the towers is considered (see Figure 1.9 (a)). A nonlinear static analysis is performed by linearly increasing the mid-span vertical displacement V of the deck (see Figure 1.9 (b)). The corresponding force-displacement curve is obtained by calculating, at each step, the total vertical reaction F_Y at the boundaries. The same procedure is also applied to the reduced models, by varying the axial rigidities of the deck elements until the

obtained force-displacement curves are in good agreement with the one obtained with the TMC model. The results are presented in Figure 1.10 and emphasize the capability of the reduced models to catch the nonlinear stress-stiffening behavior of the deck with a good approximation.

1.5 Concluding remarks

Three hierarchical numerical macro-level models of the Tsing Ma Bridge are developed and presented. The first model is a very detailed one which is adopted as a reference to validate the remaining two simplified numeric schemes.

Although the reduction of the model complexity precludes the analysis of local phenomena, it is shown how the experimental modal parameters (linear normal modes) and the stiffening behavior of the deck are correctly reproduced by simplified models, with a dramatic reduction of the computational effort. This is essential to perform nonlinear transient dynamic analysis with a reasonable computational expense.

Chapter 2

EFFICIENT DIGITAL SIMULATION OF WIND VELOCITY FIELD

Abstract

The digital simulation of the wind velocity field, modeled as a n -variate stationary Gaussian process, is a widely adopted tool to generate the external input for response analysis of wind-sensitive nonlinear structures. The problem does not entail any theoretical difficulty, existing already a large number of well-established techniques (Schuëller (ed.), 1997), such as the robust and accurate weighted amplitude wave superposition (WAWS) method, early proposed by Shinozuka and Jan (1972). However, reducing the computational effort required by the WAWS method is often mandatory when dealing with complex structures and large simulation domains. To this end, less expensive techniques were proposed in the literature, such as autoregressive moving average methods (ARMA) and approximate formulas exploiting the proper orthogonal decomposition (POD) of the spectral matrix. In this Chapter, a comparative study between WAWS, POD-based and ARMA techniques, is proposed, accounting for algorithm structure and computational effort. Two numerical examples, with increasing complexity, are considered, in order to

give some guidelines about which method should be preferred in consideration of the problem under study.

2.1 Introduction

Representing and simulating the wind velocity field has been one of the main topics of wind engineering for the last decades. In this framework, wind velocity is usually idealized as the sum of a mean part, assumed as constant within a conventional time interval, and a fluctuating part representing the atmospheric turbulence. The intensity and direction of the mean wind velocity in different positions within the atmospheric boundary layer are statistical variables that depend upon the ground roughness, the terrain topography, the atmospheric stratification and the geographic latitude. These parameters also influence the statistical properties of the atmospheric turbulence, which is usually modeled as a stationary zero-mean Gaussian random process (Deodatis, 1996; Shinozuka and Deodatis, 1997).

Several techniques were proposed in the literature in order to simulate Gaussian wind velocity fields to be employed in structural analysis (Simiu and Scanlan, 1996; Kareem and Kijewski, 2002). Among those, the classic WAWS method, based on the spectral representation proposed in (Shinozuka and Jan, 1972), has proved to guarantee the best quality of the obtained results (Rossi et al., 2003). Nevertheless, such a procedure requires the Cholesky factorization of the spectral matrix, which unfortunately leads to high computational expenses, especially when dealing with complex structures and large simulation domains. These difficulties are mainly related to memory allocation and time consuming operations, thus requiring, on one hand, the reduction of the problem size. On the other hand, an accurate wind simulation is essential for predicting the wind-induced response of flexible structures, such as transmission power lines, tall buildings, suspension and cable-stayed bridges, etc. Less demanding procedures may be obtained by exploiting the properties of the POD decomposition of the spectral matrix, proposed in the papers by Li and Kareem (1995), Di Paola (1998) and Solari and Carassale (2000). A POD-based technique, in particular, was recently applied to simulate the wind velocity field on a domain

representing a long-span suspension bridge (Carassale and Solari, 2006) with significantly low computational efforts. A third well-established class of simulation methods, is represented by autoregressive (AR) and autoregressive moving average (ARMA) models, early introduced in the paper by Samaras et al. (1985) and more recently analyzed by Di Paola and Gullo in conjunction with the POD decomposition of the spectral matrix (Di Paola and Gullo, 2001). Finally, it must be mentioned that non-Gaussian techniques were also applied in the literature with the aim of directly simulating wind pressure fields on structures. As examples, this problem was analyzed by Gioffrè et al. (2000) and by Borri and Facchini (2000), among others.

Given the above presented scenario, the principal aspects of wind simulation are, at first, reviewed, devoting a special care to algorithm efficiency. Afterwards a comparative study between WAWS, POD-based and ARMA techniques is performed, by considering two numerical examples. The former, represented by the tower of a suspension bridge, is considered to compare the quality of the results obtained using ARMA and POD-based methods, with respect to those obtained using the WAWS method. The latter, represented by an entire suspension bridge, is a more demanding case in which the use of the WAWS method becomes prohibitive. Nevertheless, ARMA and POD-based techniques seem to guarantee efficient and accurate simulations also for this last case.

2.2 Stochastic wind model

Let $Ox_1x_2x_3$ be the global Cartesian reference system, identified by the unit vectors \mathbf{e}_1 , \mathbf{e}_2 and \mathbf{e}_3 and with the origin lying on the ground. In the following developments, without loss of generality, it is assumed that \mathbf{e}_3 is directed in the gravity direction while \mathbf{e}_1 is the direction of the mean wind velocity $\mathbf{U}(\mathbf{x})$, which is therefore assumed to be parallel to the horizontal plane. Considering different directions of the mean wind velocity, in different positions, requires the definition of a local reference system (depending on the position in the space), without any theoretical difficulty (Carassale and Solari, 2006).

However, for the seek of simplicity, the only case with $\mathbf{U}(\mathbf{x})$ parallel to \mathbf{e}_1 is considered herein. Following those definitions, the wind velocity field $\mathbf{V}(\mathbf{x}, t)$ is usually idealized as the sum of a mean value $\mathbf{U}(\mathbf{x}) = (U, 0, 0)$, function of the absolute position $\mathbf{x} = (x_1, x_2, x_3)$, and a stationary zero-mean fluctuation $\mathbf{u}(\mathbf{x}, t) = (u_1, u_2, u_3)$, that depends on the position and varies in time:

$$\mathbf{V}(\mathbf{x}, t) = \mathbf{U}(\mathbf{x}) + \mathbf{u}(\mathbf{x}, t) \quad (2.2.1)$$

The three components u_1, u_2, u_3 of the vector $\mathbf{u}(\mathbf{x}, t)$ represent therefore the longitudinal, lateral and vertical components of turbulence respectively (see Figure 2.1).

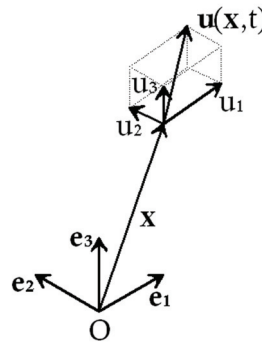


Figure 2.1. Global reference system and turbulent wind velocity field

It is well-known that the mean component $\mathbf{U}(\mathbf{x})$ varies with the elevation from the ground, following a profile that depends on the roughness of the terrain, the geographic latitude and the thermal stratification of the atmosphere. For flat terrains, within the inner boundary layer, this profile is usually approximated by the following logarithmic law:

$$\mathbf{U}(\mathbf{x}) = \frac{1}{k^*} u_* \ln \left(\frac{x_3}{z_0} \right) \mathbf{e}_1 \quad (2.2.2)$$

in which $k^* = 0.4$ is the Von Karman constant, u_* is the shear velocity and z_0 is the roughness length.

The atmospheric turbulence \mathbf{u} is usually modeled as a zero-mean, Gaussian, stationary random field that depends on time. If P and P' denote two points, with absolute positions \mathbf{x} and \mathbf{x}' , then, from a probabilistic point of view, the complete characterization of this field is ensured by the knowledge of the correlation function for every pair of turbulence components, that is defined as:

$$\mathcal{R}_{u_i u_j}(\mathbf{x}, \mathbf{x}', t, t') = E[u_i(\mathbf{x}, t), u_j(\mathbf{x}', t')] \quad (2.2.3)$$

where $E[\cdot]$ is the statistic average operator. As it is well-known, assuming that \mathbf{u} is ergodic, $\mathcal{R}_{u_i u_j}(\mathbf{x}, \mathbf{x}', t, t')$ is given by the Fourier transform of the cross power spectral density function (CPSD) between u_i and u_j , namely:

$$\mathcal{R}_{u_i u_j}(\mathbf{x}, \mathbf{x}', t, t') = \int_{-\infty}^{+\infty} S_{u_i u_j}(\mathbf{x}, \mathbf{x}', \omega) e^{i\omega(t-t')} d\omega \quad (2.2.4)$$

where ω is the circular frequency and i is the imaginary unit. Most of the theoretical models adopted in wind engineering express the CPSD in terms of auto-spectra and coherence function $Co_{u_i u_j}(\mathbf{x}, \mathbf{x}', n)$, namely:

$$S_{u_i u_j}(\mathbf{x}, \mathbf{x}', n) = \sqrt{S_{u_i u_i}(\mathbf{x}, n) S_{u_j u_j}(\mathbf{x}', n)} Co_{u_i u_j}(\mathbf{x}, \mathbf{x}', n) \quad (2.2.5)$$

where $n = \omega/2\pi$ is the frequency. The imaginary part of the CPSD (called quadrature spectrum) introduces a time lag between the simulated velocities, which may become significant for points placed in the along-wind direction x_l . The quadrature spectrum is here neglected, since the considered examples focus on simulation domains located on the $x_2 x_3$ plane. However, neglecting the quadrature spectrum does not limit the generality of the presented results, which apply also to the case in which the CPSD has a nonnegative imaginary part.

The auto-spectrum $S_{u_i u_i}(\mathbf{x}, n)$ of the turbulence component $u_i(\mathbf{x}, n)$, is usually normalized in such a way that:

$$\sigma_{u_i}^2(\mathbf{x}) = \int_0^\infty S_{u_i u_i}(\mathbf{x}, n) dn \quad (2.2.6)$$

where $\sigma_{u_i}^2(\mathbf{x})$ is the variance of $u_i(\mathbf{x}, n)$.

Several models have been developed in the literature to give an analytical representation to $S_{u_j u_j}(\mathbf{x}, n)$, for $j=1,2,3$. Among those, Solari and Piccardo (2001) have developed the following model, which is valid within the inner boundary layer and in neutral regime:

$$\frac{n S_{u_j u_j}(\mathbf{x}, n)}{\sigma_{u_j}^2(\mathbf{x})} = \frac{\lambda_j n (L_{u_j}(\mathbf{x}) / \|\mathbf{U}(\mathbf{x})\|)}{(1 + 1.5 \lambda_j n (L_{u_j}(\mathbf{x}) / \|\mathbf{U}(\mathbf{x})\|))^{5/3}} \quad (2.2.7)$$

where $L_{u_j}(\mathbf{x})$ is the integral length scale of the turbulence component u_j , $\lambda_1 = 6.868$, $\lambda_2 = 9.434$ and $\lambda_3 = 6.103$.

Turbulence components that are orthogonal to each other are usually assumed to be statistically uncorrelated. On the contrary, the coherence between pairs of parallel turbulence components in two distinct points, tends to decrease with increasing distance and frequency difference. This dependency is traditionally modeled with simple exponential laws, assuming the following general form:

$$\begin{aligned} Coh_{u_j(\mathbf{x})u_j(\mathbf{x}')}(n) = \\ \exp \left[- \frac{n \sqrt{[2C_{j1}(x_1 - x'_1)]^2 + [2C_{j2}(x_2 - x'_2)]^2 + [2C_{j3}(x_3 - x'_3)]^2}}{\|\mathbf{U}(\mathbf{x})\| + \|\mathbf{U}(\mathbf{x}')\|} \right], \quad (2.2.8) \\ j = 1, 2, 3 \end{aligned}$$

where C_{js} is the exponential decay coefficient of u_j , versus a displacement in the longitudinal ($s=1$), lateral ($s=2$) and vertical ($s=3$) direction.

By looking at equation (2.2.4) and at the previous definitions, it is clear that the correlation function $\mathcal{R}_{u_i u_j}(\mathbf{x}, \mathbf{x}', t, t')$ depends on $t - t'$ (stationary in time) and on the positions \mathbf{x} and \mathbf{x}' . Nevertheless it is not simply a function of the

absolute value of the distance $\mathbf{x} - \mathbf{x}'$, with the consequence that the random field is not isotropic. Besides, it is neither homogeneous because $\mathcal{R}_{u,u_j}(\mathbf{x}, \mathbf{x}', t, t')$ depends separately from the heights from the ground x_3 and x'_3 . The hypothesis of isotropic random field can be admitted for an horizontal string-like exposed structure, along which the mean wind direction and velocity do not change (Di Paola, 1998).

2.3 Digital simulation techniques

For simulation purposes, the spatial domain is discretized into N points which usually represent significant nodes of the case study structure. The position of the k -th node of the simulation domain is identified by the vector $\mathbf{x}^{(k)} = (x_1^{(k)}, x_2^{(k)}, x_3^{(k)})$, with $k=1, 2, \dots, N$. Thus the discrete wind field is represented by the mean velocity vectors $\mathbf{U}^{(k)}(\mathbf{x}^{(k)})$ and by the turbulence vectors $\mathbf{u}^{(k)}(\mathbf{x}^{(k)}, t)$:

$$\mathbf{V}^{(k)}(\mathbf{x}^{(k)}, t) = \mathbf{U}^{(k)}(\mathbf{x}^{(k)}) + \mathbf{u}^{(k)}(\mathbf{x}^{(k)}, t), \quad k = 1, 2, \dots, N \quad (2.3.1)$$

The projections of the turbulence vector $\mathbf{u}^{(k)}$ in the global reference system are, respectively, the longitudinal $u_1^{(k)}$, transversal $u_2^{(k)}$ and vertical $u_3^{(k)}$ components of turbulence in the k -th node of the simulation domain.

Following the discrete approach, the time-dependent random field $\mathbf{u}(\mathbf{x}, t)$, representing the atmospheric turbulence, is transformed into a $3N$ -variate stationary random process $\underline{\mathbf{u}}(t)$, where $\underline{\mathbf{u}}(t)$ is a $3N$ -order vector containing the components $u_j^{(k)}$, for $j=1, 2, 3$, of the turbulence vectors $\mathbf{u}^{(k)}(t)$. Its complete characterization can be obtained through the power spectral density matrix:

$$\mathbf{S}_{\underline{\mathbf{u}}\underline{\mathbf{u}}}(n) = \begin{bmatrix} \mathbf{S}_{\mathbf{u}^{(1)}\mathbf{u}^{(1)}}(n) & \cdots & \mathbf{S}_{\mathbf{u}^{(1)}\mathbf{u}^{(N)}}(n) \\ \vdots & \ddots & \vdots \\ \mathbf{S}_{\mathbf{u}^{(N)}\mathbf{u}^{(1)}}(n) & \cdots & \mathbf{S}_{\mathbf{u}^{(N)}\mathbf{u}^{(N)}}(n) \end{bmatrix} \quad (2.3.2)$$

in which $\mathbf{S}_{\mathbf{u}^{(h)}\mathbf{u}^{(k)}}(n)$ are matrices of order 3×3 , defined as:

$$\mathbf{S}_{\mathbf{u}^{(h)}\mathbf{u}^{(k)}}(n) = \begin{bmatrix} S_{u_1^{(h)}u_1^{(k)}}(n) & S_{u_1^{(h)}u_2^{(k)}}(n) & S_{u_1^{(h)}u_3^{(k)}}(n) \\ S_{u_2^{(h)}u_1^{(k)}}(n) & S_{u_2^{(h)}u_2^{(k)}}(n) & S_{u_2^{(h)}u_3^{(k)}}(n) \\ S_{u_3^{(h)}u_1^{(k)}}(n) & S_{u_3^{(h)}u_2^{(k)}}(n) & S_{u_3^{(h)}u_3^{(k)}}(n) \end{bmatrix} \quad (2.3.3)$$

The power spectral density matrix defined by Equation (2.3.2) is real (since the quadrature spectrum has been neglected), symmetric and positive definite at each frequency value n (Di Paola and Gullo, 2001). In the following developments the two-side power spectral density matrix $\mathbf{G}_{\mathbf{uu}}(\omega)$ will also be utilized:

$$\mathbf{G}_{\mathbf{uu}}(\omega) = \begin{cases} \frac{1}{2\pi} \mathbf{S}_{\mathbf{uu}}\left(\frac{\omega}{2\pi}\right) & \text{for } \omega \geq 0 \\ \frac{1}{2\pi} \mathbf{S}_{\mathbf{uu}}\left(-\frac{\omega}{2\pi}\right)^* & \text{for } \omega < 0 \end{cases} \quad (2.3.5)$$

where the superscript $*$ denotes the complex conjugate.

2.3.1 WAWS Method

Since $\mathbf{u}(t)$ is a $3N$ -variate stationary, Gaussian, random process, its realizations can be generated by the Priestley spectral representation:

$$\mathbf{u}(t) = \int_{-\infty}^{+\infty} e^{i\omega t} d\mathbf{Z}(\omega) \quad (2.3.6)$$

where $\mathbf{Z}(\omega)$ is a zero-mean normal complex random process having orthogonal increments $d\mathbf{Z}(\omega) = \mathbf{Z}(\omega + d\omega) - \mathbf{Z}(\omega)$ that satisfy the following relations:

$$\begin{aligned} E[d\mathbf{Z}(\omega)] &= \mathbf{0} \quad \forall \omega \\ E[d\mathbf{Z}(\omega)d\mathbf{Z}^*{}^T(\omega')] &= \begin{cases} \mathbf{G}_{\mathbf{uu}}(\omega)d\omega & \text{if } \omega = \omega' \\ \mathbf{0} & \text{otherwise} \end{cases} \end{aligned} \quad (2.3.7)$$

Since $\mathbf{u}(t)$ is a real-valued random process, the increments $d\mathbf{Z}(\omega)$ also satisfy the Hermitian symmetry:

$$d\mathbf{Z}(\omega) = d\mathbf{Z}^*(-\omega) \quad (2.3.8)$$

A convenient representation of $d\mathbf{Z}(\omega)$, satisfying equation (2.3.7), can be expressed in the form:

$$d\mathbf{Z}(\omega) = \mathbf{T}(\omega)\mathbf{w}(\omega)\sqrt{d\omega} \quad (2.3.9)$$

where $\mathbf{w}(\omega)$ is a vector that contains $3N$ complex-valued uncorrelated white noises, with unit variance and Hermitian symmetry, while $\mathbf{T}(\omega)$ is a deterministic matrix obtained through a frequency-dependent decomposition of $\mathbf{G}_{\mathbf{uu}}(\omega)$, namely:

$$\mathbf{G}_{\mathbf{uu}}(\omega) = \mathbf{T}(\omega) \cdot \mathbf{T}^*(\omega)^T \quad (2.3.10)$$

It is worth noting that the decomposition (2.3.10) is not unique. A quite common strategy is based on the Cholesky factorization method, which provides $\mathbf{T}(\omega)$ in lower triangular form:

$$\mathbf{T}(\omega) = \begin{bmatrix} T_{11}(\omega) & 0 & \dots & 0 \\ T_{21}(\omega) & T_{22}(\omega) & \dots & 0 \\ \vdots & \vdots & \ddots & \vdots \\ T_{3N1}(\omega) & T_{3N2}(\omega) & \dots & T_{3N3N}(\omega) \end{bmatrix} \quad (2.3.11)$$

Following the previous definitions, equation (2.3.6) can be rewritten in the form:

$$\mathbf{u}(t) = \int_{-\infty}^{+\infty} e^{i\omega t} \mathbf{T}(\omega) \mathbf{w}(\omega) \sqrt{d\omega} \quad (2.3.12)$$

The discretized version of equation (2.3.12) can be obtained by considering a sequence of uniformly spaced circular frequencies ω_k , with step $\Delta\omega$:

$$\omega_k = \begin{cases} (k-1)\Delta\omega & \text{for } k = 1, \dots, \frac{N_\omega}{2} + 1 \\ -\omega_{N_\omega+2-k} & \text{for } k = \frac{N_\omega}{2} + 2, \dots, N_\omega \end{cases} \quad (2.3.13)$$

where a cut-off circular frequency $\omega_c = N_\omega / 2\Delta\omega$ has been assumed. This leads to the following discrete expression:

$$\underline{\mathbf{u}}(t) \cong \sum_{k=1}^{+\infty} e^{i\omega_k t} \sqrt{\Delta\omega} \mathbf{T}(\omega_k) \mathbf{w}(\omega_k) \quad (2.3.14)$$

When matrix $\mathbf{T}(\omega)$ is selected in the lower triangular form (2.3.11), equation (2.3.14) can be rewritten as:

$$\underline{u}_j(t) \cong \sum_{r=1}^j \sum_{k=1}^{+\infty} e^{i\omega_k t} \sqrt{\Delta\omega} T_{jr}(\omega_k) w_r(\omega_k), \quad j = 1, \dots, 3N \quad (2.3.15)$$

which can be used for simulation purposes by truncating the summation to the finite number N_ω of harmonics. The realizations of the process $\underline{\mathbf{u}}(t)$ are then generated along a sequence of N_t uniformly spaced time instants, given by:

$$t_j = (j-1)\Delta t \quad \text{for } j = 1, \dots, N_t \quad (2.3.16)$$

An alternative version of equation (2.3.15) was early proposed by Shinozuka and Jan (1971) in the following form:

$$\underline{u}_j(t) \cong \sum_{r=1}^j \sum_{k=1}^{N_\omega} T_{jr}(\omega_k) \cos(\omega'_k t + \phi_{rk}) \sqrt{\Delta\omega}, \quad j = 1, \dots, 3N \quad (2.3.17)$$

where ϕ_{rk} are independent random phases uniformly distributed in the interval $[0, 2\pi]$ and $\omega'_k = \omega_k + \delta\omega_k$, $\delta\omega_k$ being a small random frequency introduced to avoid the periodicity of the signal. As observed by Di Paola (Di Paola, 1998), the central limit theorem ensures that the process simulated by means of equation (2.3.17) is asymptotically Gaussian as N_ω becomes large. Equation (2.3.17) is sometimes called “weighted amplitude waves superposition method” (WAWS) and represents the well-known generation formula using harmonics superposition. Equation (2.3.17) will be regarded below as the most accurate method, to which two alternative strategies, requiring lower computational efforts, are compared from the viewpoint of the quality of the obtained results.

Both equations (2.3.15) and (2.3.17) have some computational disadvantages since they require to keep in memory N_w matrices of order $3N$, which often represents a technical limit to the size of the simulation domain. Equation (2.3.15) may be interpreted as a multidimensional Fourier series in which the

fundamental circular frequency is $\Delta\omega$ and the corresponding period is $T_p = 2\pi / \Delta\omega$. The simulation is thus based on the assumption that a process of duration T_p may be interpreted as periodic with period T_p . Therefore, when a sample of such a process is simulated using equation (2.3.15), its total duration $N_t\Delta t$ must be smaller than the period T_p . Besides, an adequate sampling of a sinusoidal function requires, at least, 8 points. This entails that the sinusoid with higher circular frequency ω_c , in equation (2.3.15), must have its period $2\pi / \omega_c$ greater than $\Delta t / 8$, being Δt the smallest period considered in the simulation. Looking at the previous considerations, the simulation parameters must be chosen by satisfying the following conditions (Muscolino, 2001):

$$\Delta\omega \leq \frac{2\pi}{N_t\Delta t}; \quad \Delta t \leq \frac{\pi}{4\omega_c} \quad (2.3.18)$$

2.3.2 POD-based method

An alternative to the WAWS method is represented by the POD-based technique proposed by Carassale and Solari (2006). With such an approach the matrices $\mathbf{T}(\omega_k)$, in Equation (2.3.10), are calculated as:

$$\mathbf{T}(\omega_k) = \sum_{r=1}^{3N} \boldsymbol{\theta}_r^{(k)} \sqrt{\gamma_r^{(k)}} \quad (2.3.19)$$

where $\gamma_r^{(k)}$ are the eigenvalues of the two-side power spectral density matrix $\mathbf{G}_{\underline{u}\underline{u}}(\omega_k)$ and $\boldsymbol{\theta}_r^{(k)}$ are the correspondent eigenvectors. Those last are normalized in such a way that $\|\boldsymbol{\theta}_r^{(k)}\| = 1$ and assume the physical meaning of wind modes (Di Paola, 1998). By substituting equation (2.3.19) into equation (2.3.14), the simulation formula becomes:

$$\underline{\mathbf{u}}(t) \cong \sum_{r=1}^{3N} \sum_{k=1}^{N_\omega} e^{i\omega_k t} \sqrt{\Delta\omega \gamma_r^{(k)}} \boldsymbol{\theta}_r^{(k)} p_r^{(k)} \quad (2.3.20)$$

where $p_r^{(k)}$ are complex-valued, Gaussian random numbers with unit variance:

$$\begin{aligned} E[p_r^{(k)}] &= 0 \\ E[p_r^{(k)} p_s^{(h)*}] &= \delta_{kh} \delta_{rs} \end{aligned} \quad \begin{pmatrix} r, s = 1, \dots, 3N \\ k, h = 1, \dots, N_\omega \end{pmatrix} \quad (2.3.21)$$

where δ denotes the Kronecker operator. The complex numbers $p_r^{(k)}$ are generated as:

$$p_r^{(k)} = R_r^{(k)} + iI_r^{(k)} \quad (2.3.22)$$

where $R_r^{(k)}$ and $I_r^{(k)}$ are zero mean normal random numbers that satisfy the following equations:

$$\begin{aligned} E[R_r^{(k)} R_s^{(h)}] &= \frac{1}{2} \delta_{ij} \delta_{kh} \\ E[I_r^{(k)} I_s^{(h)}] &= \frac{1}{2} \delta_{ij} \delta_{kh} \\ E[R_r^{(k)} I_s^{(h)}] &= 0 \end{aligned} \quad \begin{pmatrix} r, s = 1, \dots, 3N \\ k, h = 1, \dots, N_\omega \end{pmatrix} \quad (2.3.23)$$

The process $\underline{\mathbf{u}}(t)$, in Equation (2.3.20), can be rewritten as the inverse “fast Fourier transform” (FFT) of a $3N$ -order vector $\underline{\mathbf{U}}(\omega)$ thus improving the computational efficiency (Carassale and Solari, 2006). In this case, letting $\Delta\omega = 2\pi / N_t \Delta t$ and $N_\omega = N_t$, it holds:

$$\underline{\mathbf{U}}(\omega_k) = \sum_{r=1}^{3N} \sqrt{\frac{2\pi N_t}{\Delta t}} \gamma_r^{(k)} \boldsymbol{\theta}_r^{(k)} p_r^{(k)} \quad (2.3.24a)$$

$$\begin{aligned} \underline{\mathbf{u}}(t) &= \mathfrak{F}^{-1}[\underline{\mathbf{U}}(\omega)] \cong \\ &\sum_{r=1}^{3N} \left(\frac{1}{N_t} \sum_{k=1}^{N_t} e^{2\pi i (j-1)(k-1) / N_t} \sqrt{\frac{2\pi N_t}{\Delta t}} \gamma_r^{(k)} \boldsymbol{\theta}_r^{(k)} p_r^{(k)} \right) \end{aligned} \quad (2.3.24b)$$

where $\mathfrak{F}^{-1}[\cdot]$ denotes the inverse FFT operator. In Equation (2.3.24b) only the real part is retained since, in engineering applications, the process $\underline{\mathbf{u}}(t)$ is a real-valued one.

Equations (2.3.20) and (2.3.24) represent the process $\underline{\mathbf{u}}(t)$ as the superposition of $3N$ independent fully coherent stochastic processes, which

represent the contribution of the different wind modes. This approach offers two ways for preserving both computer time and allocated memory. Indeed, eigenvectors and eigenvalues of $\mathbf{G}_{uu}(\omega)$ could be calculated only for a small number $\hat{N}_\omega \ll N_\omega$ of circular frequencies and then be interpolated elsewhere. A suitable sequence of those circular frequency values can be calculated as (Carassale and Solari, 2006):

$$\hat{\omega}_h = \frac{2\pi}{N_t \Delta t} \left(\frac{N_t}{2} \right)^{h-1/\hat{N}_\omega-1}, \quad (h=1, \dots, \hat{N}_\omega) \quad (2.3.25)$$

The interpolation of eigenvalues and eigenvectors of matrix $\mathbf{G}_{uu}(\omega)$ along the sequence defined by equation (2.3.25) can be performed as described in (Carassale and Solari, 2006).

The second way of reducing the computational expense required by Equations (2.3.20) and (2.3.24b) is to retain, in the simulation, only the wind modes, say $N_r \ll 3N$, which likely produce considerable effects on the structural response. This can be achieved by noting that the contribution of the r -th wind mode has a frequency dependent spatial distribution $\boldsymbol{\theta}_r^{(k)}$ and a frequency dependent power spectral density corresponding to the eigenvalue $\gamma_r^{(k)}$. The problem was treated in details by Carassale and Solari (2006) and is not reported here for the seek of brevity.

Using equation (2.3.24b) for simulation purposes ($N_\omega = N_t$) requires the following conditions for the simulation parameters:

$$\Delta\omega = \frac{2\omega_c}{N_\omega} = \frac{2\pi}{N_t \Delta t}; \quad \omega_c = \frac{N_\omega}{2} \Delta\omega = \frac{\pi}{\Delta t} \quad (2.3.26)$$

2.3.3 AR and ARMA methods

Auto regressive moving average methods generate the wind velocity field by filtering a $3N$ -order vector $\mathbf{a}(t)$ of uncorrelated band-limited Gaussian white noises $a_j(t)$, for $j=1, 2, \dots, 3N$, with unit variance. The turbulent velocity vector,

at time t_j , is thus expressed through a linear combination of the previous events, in the following form:

$$\underline{\mathbf{u}}(t_j) = \sum_{i=1}^p \Phi_i \underline{\mathbf{u}}(t_j - i\Delta t) + \sum_{i=0}^q \mathbf{B}_i \underline{\mathbf{a}}(t_j - i\Delta t) \quad (2.3.27)$$

where Φ_i and \mathbf{B}_i are convenient $3N \times 3N$ matrices, which will be better specified in the following developments. Equation (2.3.27) represents a general ARMA method, in which p denotes the order of auto regression and q is the order of the moving average component. It is well known (Rossi et al., 2003) that an ARMA(p,q) can be approximated by an AR(p_1) method, with $p_1 \gg p$, where the AR(p_1) method can be obtained by assuming $q=0$ in equation (2.3.27):

$$\underline{\mathbf{u}}(t_j) = \sum_{i=1}^p \Phi_i \underline{\mathbf{u}}(t_j - i\Delta t) + \mathbf{B}_0 \underline{\mathbf{a}}(t_j) \quad (2.3.28)$$

Equations (2.3.27) and (2.3.28) are very popular because of their computational efficiency. The determination of the coefficient matrices Φ_i and \mathbf{B}_i is, in fact, the only delicate point, after which the simulation of the process is extremely fast. Nevertheless, ARMA processes may become unstable as the time step is reduced and the required orders to provide a good approximation may increase considerably as the auto and cross correlations are reduced.

The coefficient matrices Φ_i and \mathbf{B}_0 of an AR(p) model can be calculated in consideration of the covariance structure of the process. In particular, the $3N \times 3N$ correlation matrix $\mathcal{R}_{\underline{\mathbf{u}}\underline{\mathbf{u}}}(\tau)$ must be defined as:

$$\mathcal{R}_{\underline{\mathbf{u}}\underline{\mathbf{u}}}(\tau) = E[\underline{\mathbf{u}}(t) \underline{\mathbf{u}}^T(t + \tau)] \quad (2.3.29)$$

As already described by Equation (2.2.4), under the hypothesis of ergodicity, the components of $\mathcal{R}_{\underline{\mathbf{u}}\underline{\mathbf{u}}}(\tau)$ form a Fourier pair with the corresponding PSD, namely:

$$\mathcal{R}_{\underline{u}\underline{u}}(\tau) = \int_{-\infty}^{+\infty} \mathbf{S}_{ij}(\omega) e^{i\omega\tau} d\omega \quad (2.3.30)$$

Assuming the shorter notation $\mathcal{R}_{\underline{u}\underline{u}}(k\Delta t) = \mathcal{R}_{\underline{u}\underline{u}}(k)$, the following system of algebraic equations can be obtained (Samaras et al., 1985):

$$\begin{bmatrix} \mathcal{R}_{\underline{u}\underline{u}}(0) & \mathcal{R}_{\underline{u}\underline{u}}(1) & \cdots & \mathcal{R}_{\underline{u}\underline{u}}(p-1) \\ \mathcal{R}_{\underline{u}\underline{u}}(-1) & \mathcal{R}_{\underline{u}\underline{u}}(0) & \cdots & \mathcal{R}_{\underline{u}\underline{u}}(p-2) \\ \vdots & \vdots & \ddots & \vdots \\ \mathcal{R}_{\underline{u}\underline{u}}(1-p) & \mathcal{R}_{\underline{u}\underline{u}}(2-p) & \cdots & \mathcal{R}_{\underline{u}\underline{u}}(0) \end{bmatrix} \begin{bmatrix} \Phi_1 \\ \Phi_2 \\ \vdots \\ \Phi_p \end{bmatrix} = \begin{bmatrix} \mathcal{R}_{\underline{u}\underline{u}}(-1) \\ \mathcal{R}_{\underline{u}\underline{u}}(-2) \\ \vdots \\ \mathcal{R}_{\underline{u}\underline{u}}(-p) \end{bmatrix} \quad (2.3.31)$$

Once the correlation matrices are calculated by means of a FFT algorithm using equation (2.3.29), the coefficient matrices Φ_i can be easily determined by solving the system (2.3.31) through Gaussian elimination. Then it is possible to calculate matrix \mathbf{B}_0 , by post-multiplying equation (2.3.28) by $\underline{u}(t_j)^T$ and taking the average, namely:

$$E[\underline{u}(t_j) \underline{u}^T(t_j)] = \sum_{i=1}^p \Phi_i E[\underline{u}(t_j - i\Delta t) \underline{u}^T(t_j)] + \mathbf{B}_0 E[\underline{a}(t_j) \underline{u}^T(t_j)] \quad (2.3.32)$$

By definition of correlation matrix, equation (2.3.32) may be rewritten in the following form:

$$\mathcal{R}_{\underline{u}\underline{u}}(0) = \sum_{i=1}^p \Phi_i \mathcal{R}_{\underline{u}\underline{u}}(i) + \mathbf{B}_0 \mathcal{R}_{\underline{a}\underline{u}}(0) \quad (2.3.33)$$

From equation (2.3.33), it follows that the covariance structure of the process is preserved if the following condition is satisfied:

$$\mathbf{B}_0 \mathcal{R}_{\underline{a}\underline{u}}(0) = \mathcal{R}_{\underline{u}\underline{u}}(0) - \sum_{i=1}^p \Phi_i \mathcal{R}_{\underline{u}\underline{u}}(i) \quad (2.3.34)$$

Thus the choice of matrix \mathbf{B}_0 is not unique and a possible strategy is to assume

$\mathbf{B}_0 = \mathcal{R}_{\underline{a}\underline{u}}(0)^T$ and to obtain it through the Cholesky decomposition.

The weighting coefficients for an ARMA(p,q) technique can be calculated by means of a two-steps approach, as described in (Samaras et al, 1985). In

particular the coefficient matrices Φ_i are calculated, at first, using equation (2.3.31) for an AR(p_1), with $p_1 \gg p$. The coefficient matrices calculated at this stage are then substituted in the following equations, which can be obtained by post-multiplying equation (2.3.28) by $\begin{bmatrix} \underline{\mathbf{a}}(t_j)^T & \underline{\mathbf{a}}(t_j-1)^T & \cdots & \underline{\mathbf{a}}(t_j-q)^T \end{bmatrix}$ and taking the average:

$$\begin{aligned} \mathcal{R}_{\underline{\mathbf{a}}\underline{\mathbf{a}}}^T(0) &= \mathcal{R}_{\underline{\mathbf{u}}\underline{\mathbf{a}}}(0) = \mathbf{B}_0 \\ &\vdots \\ \mathcal{R}_{\underline{\mathbf{u}}\underline{\mathbf{a}}}(-k) &= \sum_{i=1}^k \Phi_i \mathcal{R}_{\underline{\mathbf{u}}\underline{\mathbf{a}}}(i-k) \end{aligned} \quad (2.3.35)$$

Equations (2.3.35) can be solved in chain in order to calculate the correlation matrices $\mathcal{R}_{\underline{\mathbf{u}}\underline{\mathbf{a}}}(-k)$, for $k = 0, 1, \dots, q-1$. The following matrices can then be introduced:

$$\begin{aligned} \mathbf{b} &= \begin{bmatrix} \mathcal{R}_{\underline{\mathbf{u}}\underline{\mathbf{a}}}(0)^T & \cdots & 0 & \cdots & 0 \\ \vdots & \ddots & \vdots & \ddots & \vdots \\ \mathcal{R}_{\underline{\mathbf{u}}\underline{\mathbf{a}}}(1-q)^T & \cdots & \mathcal{R}_{\underline{\mathbf{u}}\underline{\mathbf{a}}}(0)^T & \cdots & 0 \end{bmatrix} \\ \mathbf{c} &= \begin{bmatrix} \mathcal{R}_{\underline{\mathbf{u}}\underline{\mathbf{u}}}(0) & \cdots & \mathcal{R}_{\underline{\mathbf{u}}\underline{\mathbf{u}}}(q-1) & \cdots & \mathcal{R}_{\underline{\mathbf{u}}\underline{\mathbf{u}}}(p-1) \\ \vdots & & \vdots & & \vdots \\ \mathcal{R}_{\underline{\mathbf{u}}\underline{\mathbf{u}}}(1-q) & \cdots & \mathcal{R}_{\underline{\mathbf{u}}\underline{\mathbf{u}}}(0) & \cdots & \mathcal{R}_{\underline{\mathbf{u}}\underline{\mathbf{u}}}(p-q) \\ \vdots & & \vdots & & \vdots \\ \mathcal{R}_{\underline{\mathbf{u}}\underline{\mathbf{u}}}(1-p) & \cdots & \mathcal{R}_{\underline{\mathbf{u}}\underline{\mathbf{u}}}(q-p) & \cdots & \mathcal{R}_{\underline{\mathbf{u}}\underline{\mathbf{u}}}(0) \end{bmatrix} \end{aligned} \quad (2.3.36)$$

The system of algebraic equations for the calculation of the unknown coefficient matrices $\overline{\Phi} = [\Phi_1 \quad \cdots \quad \Phi_p]^T$ and $\overline{\mathbf{B}} = [\mathbf{B}_1 \quad \cdots \quad \mathbf{B}_q]^T$ can thus be written as:

$$\begin{bmatrix} \mathbf{I} & \mathbf{b} \\ \mathbf{b}^T & \mathbf{c} \end{bmatrix} \begin{bmatrix} \overline{\mathbf{B}} \\ \overline{\Phi} \end{bmatrix} = \begin{bmatrix} \mathbf{f} \\ \mathbf{g} \end{bmatrix} \quad (2.3.37)$$

where \mathbf{I} is the $3N \cdot q \times 3N \cdot q$ identity matrix, $\mathbf{f} = [\mathcal{R}_{\underline{u}\underline{a}}(-1)^T \cdots \mathcal{R}_{\underline{u}\underline{a}}(-q)^T]^T$ and $\mathbf{g} = [\mathcal{R}_{\underline{u}\underline{u}}(-1) \cdots \mathcal{R}_{\underline{u}\underline{u}}(-p)]^T$.

The above described procedure shows that implementing an ARMA(p,q) technique requires the calculation of the AR(p₁) coefficients, under the assumption that AR(p₁) is equivalent to ARMA(p,q). Nevertheless, one could adopt the AR(p₁) scheme directly, also considering that the time needed for the generation of long time histories is of the same order in both methods. It must be noted, however, that the quality of the signal generated by an ARMA(p,q) technique is sometimes better than the quality of the one generated by an AR(p₁) technique (Rossi et al., 2003). About this last point, it must be mentioned that AR(20) and ARMA(5,5), estimated by means of AR(20) to AR(30) techniques, provided good results for turbulent wind simulations in many different environmental conditions (Rossi et al., 2003).

2.4 Comparison of different methods for digital wind simulation

The three simulation methods presented in Section 2.3 have been implemented in the MATLAB (The Mathworks Inc, 2002) environment to simulate along-wind and across-wind turbulence velocities u_1 and u_3 , respectively. Without loss of generality, the turbulent wind field is thus reduced to a $2N$ -variate stationary Gaussian process.

Equation (2.3.17) is implemented as the simulation formula of the WAWS method, while Equation (2.3.24b) is exploited in the POD-based technique. In this last, the inverse FFT algorithm is adopted to convert the vector $\underline{\mathbf{U}}(\omega)$ to the time domain and get the simulated process $\underline{\mathbf{u}}(t)$. An AR(p₁) filter, given by Equation (2.3.28), with a sufficiently large p₁, is considered to represent autoregressive methods. A two-steps approach is adopted in the implemented codes, following the diagram reported in Figure 2.2. As represented in such a diagram, there is an initial phase (indicated as “phase 0”), which must be run only once, after which a general number \underline{n} of simulations can be performed

(“phase 1”). Typically, in the “phase 0”, one calculates and collects all the data which are needed for the successive simulations (e.g. spectral matrix, factorizations, coefficients, etc.). This allows minimizing the number of operations when simulating several wind realizations, which is usually the case for performing Monte Carlo simulations. The results of the “phase 0” are deterministic and can be stored in the computer memory. According to these definitions, the three methods described above can be efficiently implemented as follows (for a $2N$ -variate process):

WAWS METHOD:

- Phase 0: calculate and store N_ω Cholesky matrices $\mathbf{T}(\omega)$ of dimension $2N \times 2N$;
- Phase 1: sum $N(N+1)N_\omega$ vectors $\mathbf{u}(t)$ of length N_t .

POD-BASED METHOD:

- Phase 0: calculate and store \hat{N}_ω matrices (of eigenvectors) $\boldsymbol{\theta}_r^{(k)}$ of dimension $2N \times 2N$ and $2N \cdot \hat{N}_\omega$ eigenvalues $\gamma_r^{(k)}$;
- Phase 1: perform N_ω interpolations of $\gamma_r^{(k)}$ and N_ω interpolations of $\boldsymbol{\theta}_r^{(k)}$, sum $2N$ vectors of length N_ω and perform $2N$ FFTs to convert $\underline{\mathbf{U}}(\omega)$ from the frequency domain to the time domain and get $\underline{\mathbf{u}}(t)$.

AR METHOD:

- Phase 0: calculate and store p_1 matrices $\boldsymbol{\Phi}_i$ of dimension $2N \times 2N$ and one matrix \mathbf{B}_0 of dimension $2N \times 2N$;
- Phase 1: sum N_t vectors of length $2N$ to calculate $\underline{\mathbf{u}}(t)$.

The two main aspects that should be considered when comparing different wind simulation techniques, from a computational point of view, are: the

allocated memory in the “phase 0” and the time needed for each single simulation. The first aspect is crucial since collecting a lot of data in the computer RAM may cause memory overflow and thus may preclude the use of a certain procedure when the simulation domain is too large. The second aspect is even more important since it gives the measure of the computational effort required by the considered method.

When comparing the quality of the results of different simulation techniques, the main points that should be considered are: the preservation of the wind auto-spectra, of the wind cross-spectra and of the corresponding auto-correlation and cross-correlation functions.

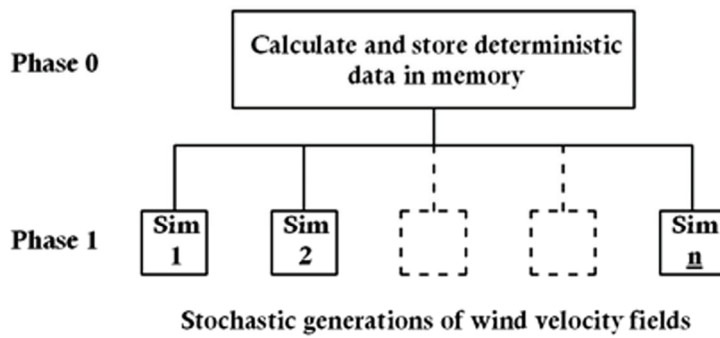


Figure 2.2. Typical computational scheme of a wind simulation technique

The memory that is allocated by the WAWS method, in the “phase 0”, grows with the $(2N)^2 N_\omega$ law. The corresponding memory, in the POD-based method, roughly grows with the $(2N)^2 \hat{N}_\omega$ law, while, in the AR method, it grows with the $(2N)^2 p_1$ law. Thus, the ratio between allocated memory in the POD-based method and in the WAWS method is almost equal to $2\hat{N}_\omega / N_\omega$, while the ratio between allocated memory in the AR method and in the POD-based method is equal to p_1 / \hat{N}_ω . In the next section it will be shown that the POD-based

method gives sufficiently accurate results with $\hat{N}_\omega = 256$, if compared to the corresponding WAWS method with $N_\omega = 16384$. The POD-based method allows therefore reducing the memory required by the WAWS method by more than 90%. This practically eliminates the risk of memory overflows in many technical conditions. Nevertheless, if memory occupation is still representing a problematic issue, an AR(p_1) method can be adopted, since it even guarantees a further memory reduction.

From the point of view of the computational effort it must be noted that, using the WAWS method, the computer time increases with the $N(N+1)N_\omega$ law, since the algorithm sums $N(N+1)N_\omega$ vectors of length N_t . In the case of the POD-based method the wind field is simulated, at first, in the frequency domain, by summing $2N$ vectors of length N_ω . Afterwards, it is converted back to the time domain through the efficient inverse FFT algorithm. By operating in this way, if one neglects the computational expense required by the interpolations of $\gamma_r^{(k)}$ and $\theta_r^{(k)}$ and by the FFT calculations, the computer time roughly increases with the $2N$ law. Finally, the use of the AR method leads to even faster simulations, since it requires a computational effort that increases with the $p_1 + 1$ law.

2.4.1 Numerical example I: the tower of a suspension bridge

The above described wind simulation techniques are commonly employed for the definition of the external inputs for nonlinear analyses of slender, flexible structures, as described in (Augusti et al., 1990; Petrini et al., 2006; Gattulli et al., 2007; Cluni et al. 2007), among others.

A first numerical example is considered to compare the three methods. The simulation domain is composed by 9 significant points disposed along the height of one tower of a suspension bridge (see Figure 2.3). The modulus of the mean wind velocity is assigned by means of the logarithmic profile given by equation (2.2.2). The parameters $k^* = 0.4$ and $u_* = 1.9 \text{ m/s}$ are considered

which produce a value of 48.0m/s at the top of the tower (node 9), as proposed in the paper by Solari and Carassale (2006).

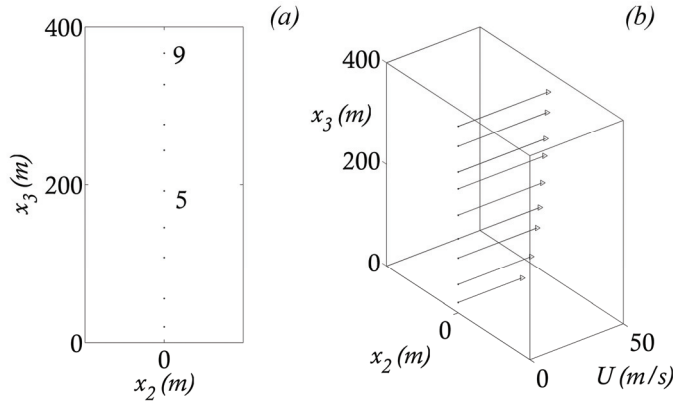


Figure 2.3. Example I: grid for wind simulation (a); mean wind velocity profile (b)

The following matrix contains the exponential decay coefficients C_{js} adopted herein:

$$\mathbf{C} = \begin{bmatrix} 3.0 & 3.0 & 0.5 \\ 10.0 & 6.5 & 6.5 \\ 10.0 & 6.5 & 3.0 \end{bmatrix} \quad (2.4.1)$$

The variance and the integral length scale of the turbulence components are assumed as follows (Solari and Piccardo, 2001):

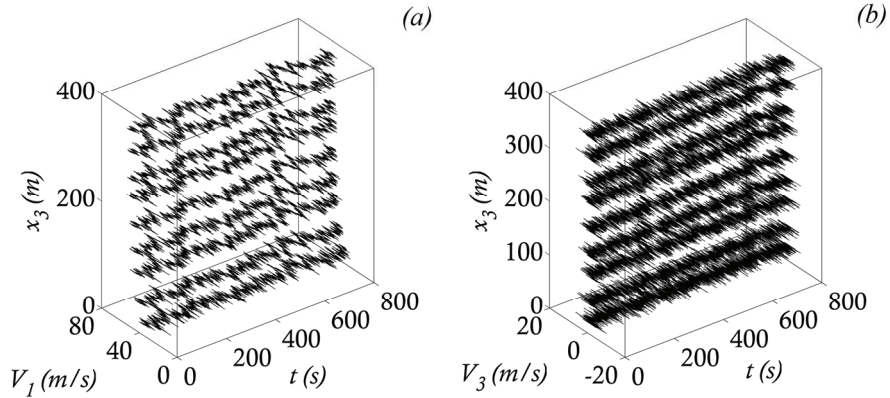
$$\sigma_{uj}^2 = \left[6 - 1.1 \tan^{-1}(\ln z_0 + 1.75) \right] u_*^2 \alpha_j$$

$$L_j = \beta_j 300 \left(\frac{x_3}{200} \right)^{0.67 + 0.05 \ln z_0} \quad (2.4.1)$$

where $\alpha_1 = 1.00$, $\alpha_2 = 0.75$, $\alpha_3 = 0.25$, $\beta_1 = 1.00$, $\beta_2 = 0.25$, $\beta_3 = 0.10$ and the dimensional quantities are expressed in meters and meters per seconds. A nil coherence is assumed between the turbulence components \mathbf{u}_1 and \mathbf{u}_3 .

The following simulation parameters are adopted: sample time $dt=0.05$ s, number of time and frequency steps $N_t=N_\omega=2^{14}$, frequency step amplitude

$\Delta\omega=0.00767$ rad/s, cut-off circular frequency $\omega_c=62.8$ rad/s, reduced number of factorizations (for POD-based method only) $\hat{N}_\omega=256$, order of auto regression (for AR method only) $p_I=20$.



Fig

Figure 2.4. Example I: wind velocity field with WAWS method: along-wind velocities (a); across-wind velocities (b)

Simulating the 18-variate wind field with the aid of a Pentium IV Intel Processor, 2MB DDRAM, in the MATLAB 7.0.1 (The Mathworks Inc, 2002) environment, led to the following computer times T_{sim} :

- WAWS $T_{sim} = 5874.5s$
- AR $T_{sim} = 4.0s$
- POD $T_{sim} = 21.0s$

The results reported above emphasize that, as expected, POD and AR method are more computationally efficient than the WAWS method. It is implicit, however, that those results strongly depend on the environment of simulation. Indeed, the inverse FFT algorithm adopted in Equation (2.3.24b) is directly available in binary language in the internal database library of MATLAB 7.0.1. This circumstance guarantees a high computational efficiency when converting $\underline{\mathbf{U}}(\omega)$ to $\underline{\mathbf{u}}(t)$ and allows to code the POD-based method using one single “do

loop” as in the case of the AR filter. The WAWS method, on the contrary, requires three nested “do loops” which justify the larger computational effort.

The turbulent wind field simulated by means of the WAWS method is represented in Figure 2.4. The quality of the results obtained using the three different methods is analyzed in Figures 2.5-2.10. In particular the turbulence velocities simulated in two points (number 5 and 9 in Figure 2.3) of the simulation domain are considered to compare the results. Figures 2.5 and 2.6 refer to along-wind and across-wind velocities, respectively, simulated by means of the WAWS method. The corresponding results obtained by means of the POD-based and AR methods are reported in figures 2.7-2.10. From the presented results it follows that:

- the WAWS method gives a very accurate representation of the wind velocity field, in which spectra and correlation functions are very well conserved;
- The POD method, with $\hat{N}_\omega \ll N_\omega$, gives an accurate description of the wind field in terms of simulated spectra. In the high frequency range, the agreement between target and simulated spectra seems to be even improved with respect to the WAWS method;
- AR methods seem to produce a small disagreement of the spectra in the very low frequency range (which usually has small effects on the structural response). Spectra are well conserved elsewhere;
- POD and AR methods produce slight errors in the correlation functions. The agreement is improved as the coherence is decreased (as, for instance, in the across-wind components);

Regarding the last point, it must be noted that the errors introduced by the POD method are only due to interpolation of the spectral eigenvectors and eigenvalues along the sequence defined by Equation (2.3.25). If no interpolation

is performed ($\hat{N}_\omega \equiv N_\omega$), POD and WAWS method would give almost similar results since they only derive from different (but equivalent) factorizations of the spectral matrix. Thus, in general, the WAWS and the POD methods share the same potentialities in terms of the quality of the obtained results, which does not rigorously hold for autoregressive methods.

Another advantage of the POD-based method is to furnish a physically relevant representation of the wind field in view of a structural analysis. In the presented case, for instance, the POD decomposition reveals that the first eigenvalue is much larger than the others, in all the considered frequency range. This can be observed in Figure 2.11 where the first ten eigenvalues γ_r ($r=1,2,\dots,10$) are plotted versus the frequency n . Figure 2.12 shows the first six eigenvectors evaluated for a fixed frequency value. From such a figure it immediately turns out that the first, the third and the sixth blowing modes involve the along-wind component, while the others involve the across-wind one. Hybrid modes are not found since a nil coherence was assumed between along-wind and across-wind turbulence components. Figure 2.12 reveals that the first blowing mode has a shape which is similar to the mean wind profile, due to the strong coherence of the along-wind components along the vertical axis. Since the associated eigenvector is the largest one, the first blowing mode indicates the predominant shape of the wind load acting on the structure.

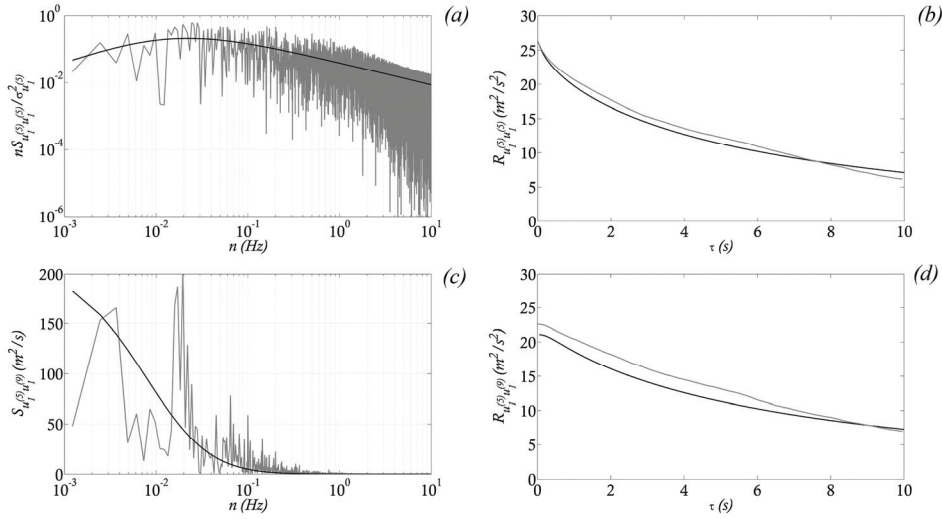


Figure 2.5. Example I using WAWS method (black lines denote theoretical functions, gray lines denote numeric approximations): PSD of along-wind velocity at point 5 (a); corresponding autocorrelation function (b); CPSD between along-wind velocities at points 5 and 9 (c); corresponding cross-correlation function (d)

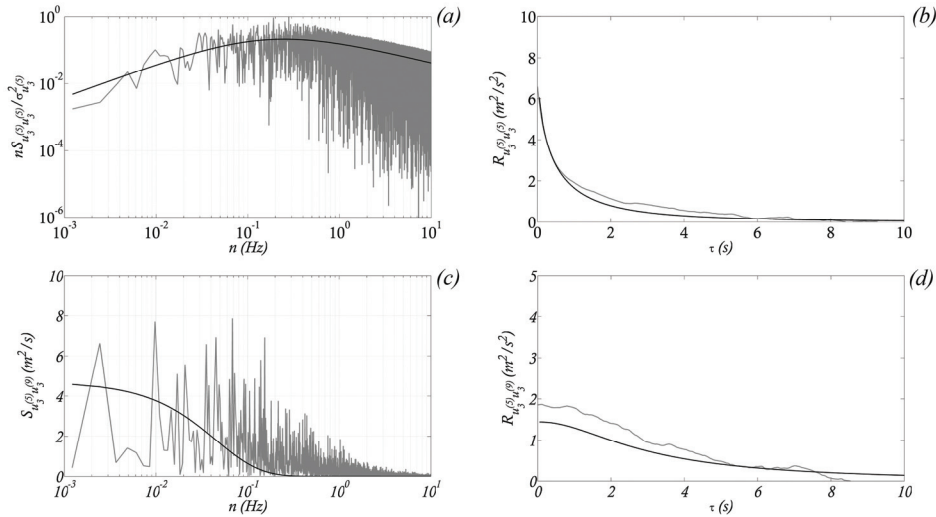


Figure 2.6. Example I using WAWS method (black lines denote theoretical functions, gray lines denote numeric approximations): PSD of across-wind velocity at point 5 (a); corresponding autocorrelation function (b); CPSD between across-wind velocities at points 5 and 9 (c); corresponding cross-correlation function (d)

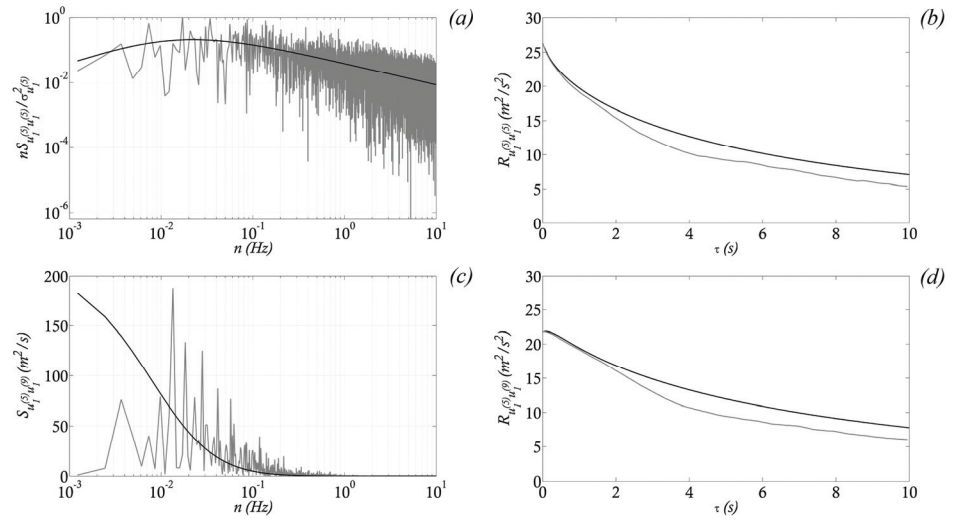


Figure 2.7. Example I using POD method (black lines denote theoretical functions, gray lines denote numeric approximations): PSD of along-wind velocity at point 5 (a); corresponding autocorrelation function (b); CPSD between along-wind velocities at points 5 and 9 (c); corresponding cross-correlation function (d)

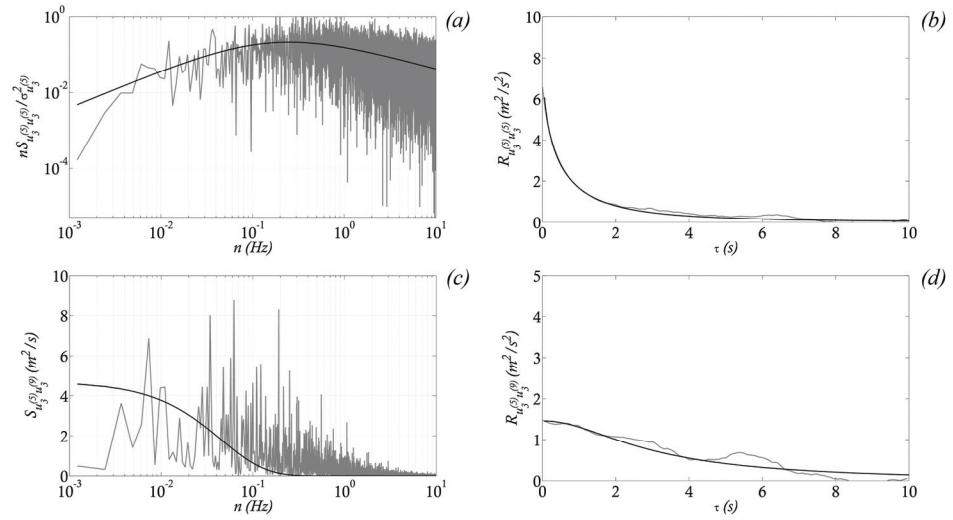


Figure 2.8. Example I using POD method (black lines denote theoretical functions, gray lines denote numeric approximations): PSD of across-wind velocity at point 5 (a); corresponding autocorrelation function (b); CPSD between across-wind velocities at points 5 and 9 (c); corresponding cross-correlation function (d)

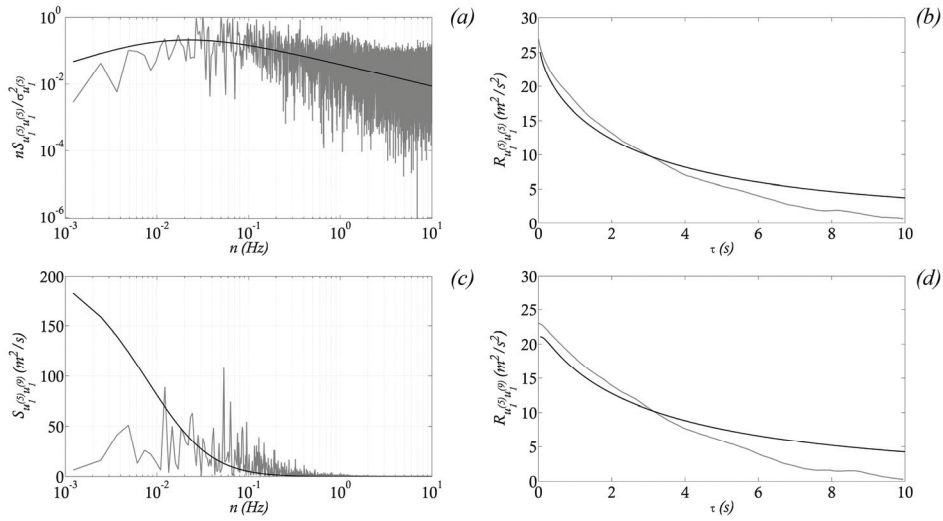


Figure 2.9. Example I using AR method (black lines denote theoretical functions, gray lines denote numeric approximations): PSD of along-wind velocity at point 5 (a); corresponding autocorrelation function (b); CPSD between along-wind velocities at points 5 and 9 (c); corresponding cross-correlation function (d)

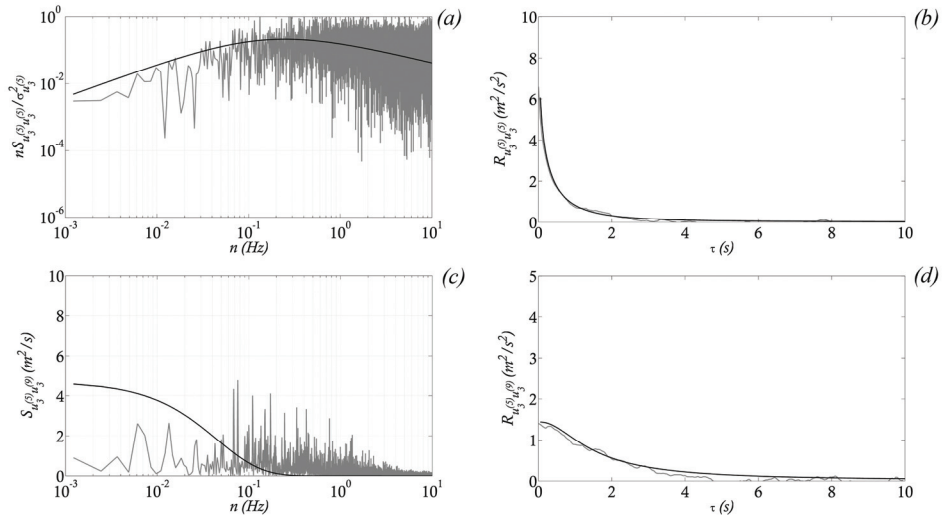


Figure 2.10. Example I using AR method (black lines denote theoretical functions, gray lines denote numeric approximations): PSD of across-wind velocity at point 5 (a); corresponding autocorrelation function (b); CPSD between across-wind velocities at points 5 and 9 (c); corresponding cross-correlation function (d)

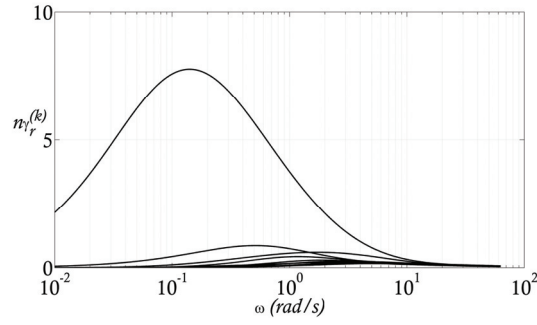


Figure 2.11. Example I: first ten non-dimensional eigenvalues (POD) of atmospheric turbulence as a function of the frequency n

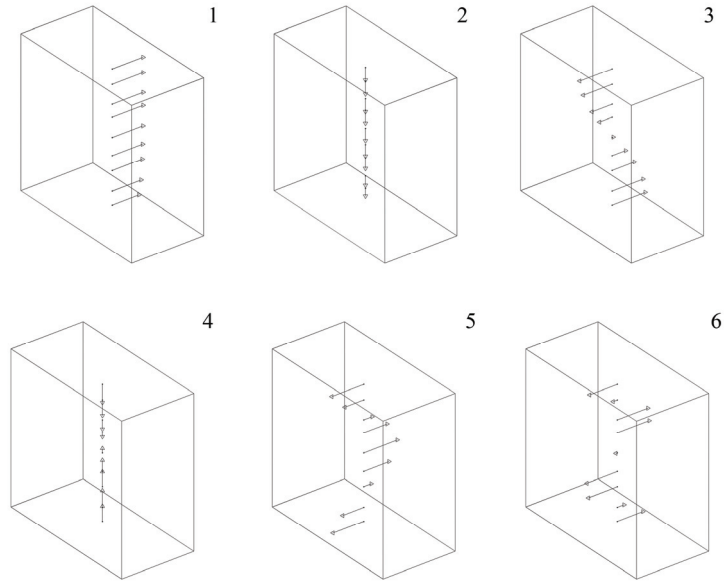


Figure 2.12. Example I: first 6 blowing modes for the frequency value $\omega=0.015\text{rad/s}$

2.4.2 Numerical example II: the Tsing Ma Bridge

A second, more demanding, numerical example is considered to test the wind simulation techniques. In particular, the wind velocity field is simulated

on a grid representing the Tsing Ma suspension bridge, described in Chapter 1. The simulation domain is constituted by 83 nodes located on the mean plan of the bridge (see Figure 2.13 (a)).

The direction of the mean wind velocity is orthogonal to the plane of the simulation domain and its modulus is assigned by means of the logarithmic profile given by equation (2.2.2) (see Figure 2.13 (b)). The parameters $k^* = 0.4$ and $u_* = 1.9 \text{ m/s}$ are considered which produce a value of 40.1 m/s at the mid-span. The variance and the integral length scale of the turbulence components are assumed in accordance to equation (2.4.1). The same simulation parameters adopted for example I and summarized in Table 2.1 are also adopted in example II.

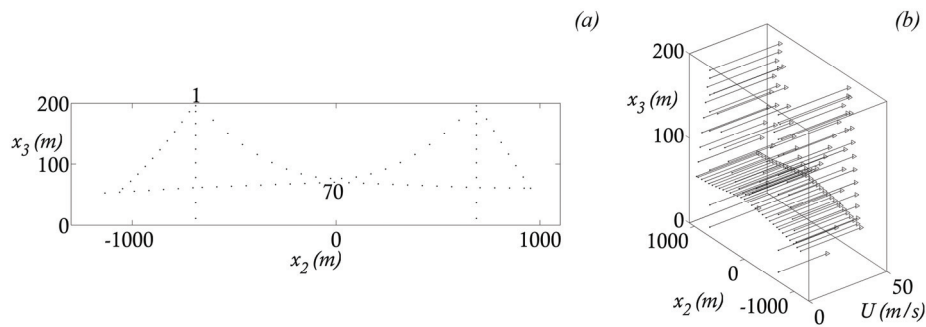


Figure 2.13. Example II : grid for wind simulation (a); mean wind velocity profile (b)

The simulation using the WAWS method led, in example II, to some numerical difficulties to compute the Cholesky decompositions. Since the spectral matrix is positive definite, this circumstance was probably due to the large dimension of the simulation domain. Only the results obtained by means of the POD-based and the AR methods are therefore presented herein.

Simulating the 166-variate wind field using the same machine as in example I led to the following computer times T_{sim} :

- POD $T_{sim} = 90.5s$
- AR $T_{sim} = 141.8s$

The results presented above indicate that, for a large dimensional simulation domain, the POD method is more competitive than the AR method. This circumstance is opposite to what has been observed in the case of the low dimensional simulation domain considered in example I. The POD-based technique also reveals to be more efficient than the AR method when performing the preliminary calculations (“phase 0”). This circumstance could become relevant when computing only a few wind simulations. The following computer times T_0 were needed to run the “phase 0”:

- POD $T_0 = 258.6s$
- AR $T_0 = 3957.0s$

The above presented results emphasize that the POD-based technique can be faster than the AR filter. However, both methods are computationally efficient and practically eliminate any technical difficulty, at least for the kind of problems here considered.

The quality of the simulated results is analyzed in Figures 2.14-2.17, referring to the along-wind and across-wind velocities at the points number 1 (top of one tower) and 70 (bridge mid-span) indicated in Figure 2.13 (a). The presented results are analogous to those obtained for example I, thus indicating that the quality of the simulated field is, as expected, independent on the dimension of the simulation domain. From those results it can be also noted that POD and AR methods give accurate results with comparable quality and computational efficiency. The POD method seems to be a little more accurate in the low frequency range.

The eigenvalue analysis of the spectral matrix again reveals interesting properties of the wind field. As an example, Figure 2.18 (a) shows the first 10 non-dimensional eigenvalues $\gamma_r^{(k)}$ ($r=1, \dots, 10$) plotted versus the circular frequency ω . A detailed view of the different paths of the eigenvalues is also reported in Figure 2.18 (b), showing that different paths do not cross since the spectral matrix must have distinct eigenvalues. As inferable from those figures the first blowing mode has its maximum energetic content close to the circular frequency value of 0.069 rad/s. The eigenvectors corresponding to the first 6

eigenvalues $\gamma_r^{(k)}$ ($r=1, \dots, 6$), calculated for $\omega=0.069$ rad/s, are reported in Figure 2.19. The figure shows that the first blowing mode involves the whole bridge in the out-of-plane (along-wind) direction, with a shape that roughly reproduces the first bridge mode shape. A strong dynamic effect of this mode on the structural response is thus expectable. The fourth blowing mode, for $\omega=0.069$ Hz, is the first one concerning the across-wind velocity and contemporary affects the bridge deck and the main cables.

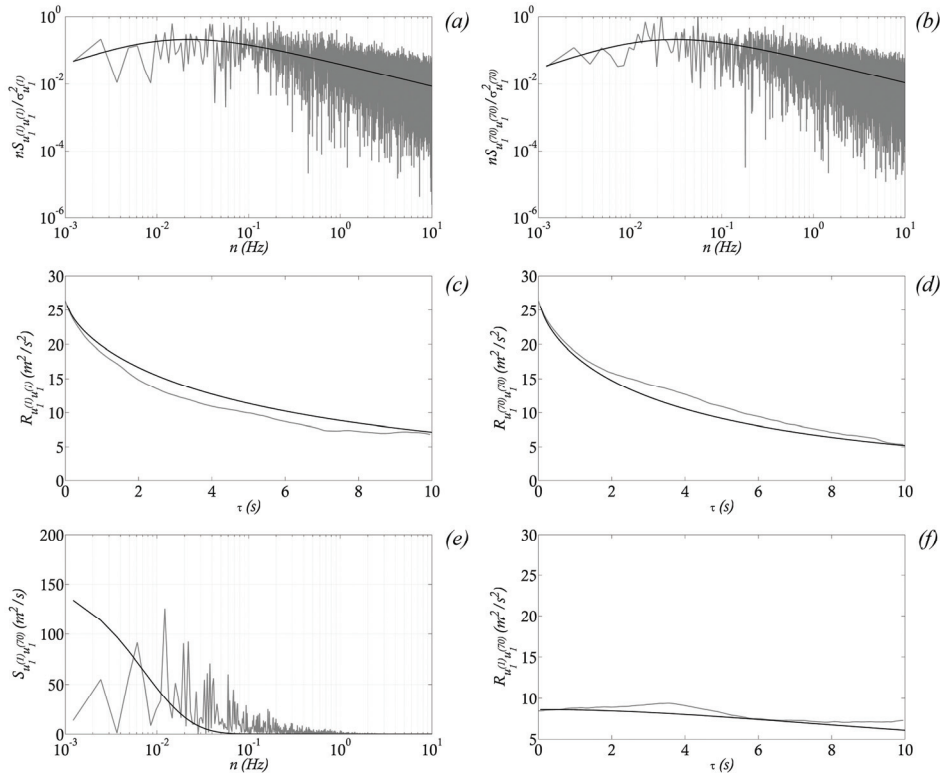


Figure 2.14. Example II using POD method (black lines denote theoretical functions, gray lines denote numeric approximations): PSD of along-wind velocities at points 1 and 70 (a), (b); corresponding autocorrelation functions (c), (d); CPSD of along-wind velocities in points 1 and 70 (e); corresponding cross-correlation function (f)

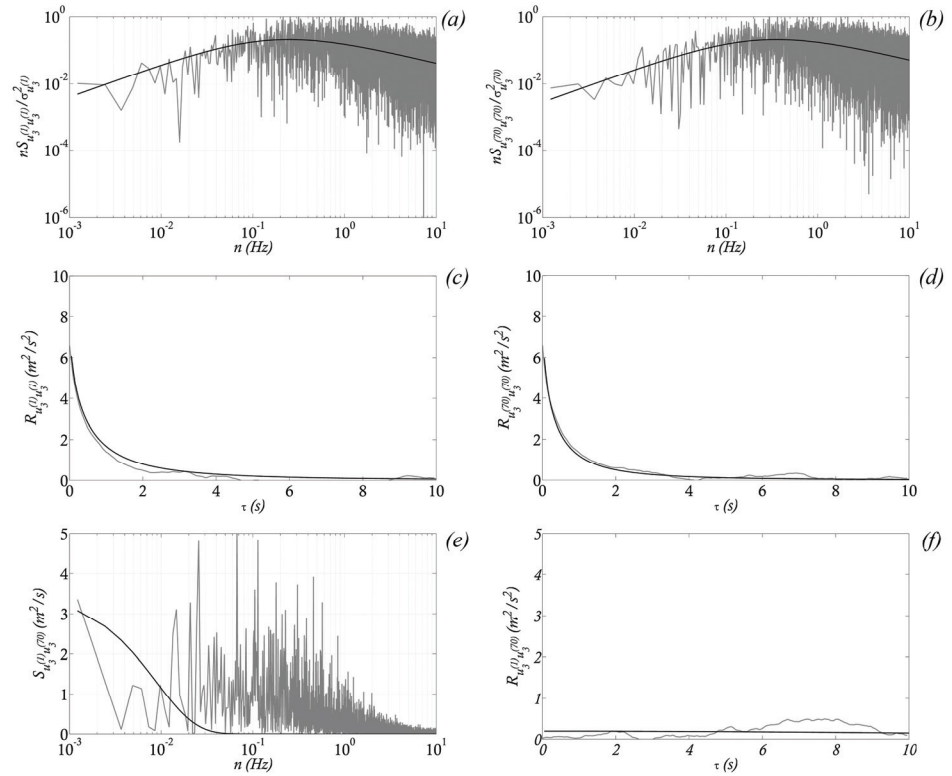


Figure 2.15. Example II using POD method (black lines denote theoretical functions, gray lines denote numeric approximations): PSD of across-wind velocities at points 1 and 70 (a), (b); corresponding autocorrelation functions (c), (d); CPSD between along-wind velocities at points 1 and 70 (e); corresponding cross-correlation function (f)

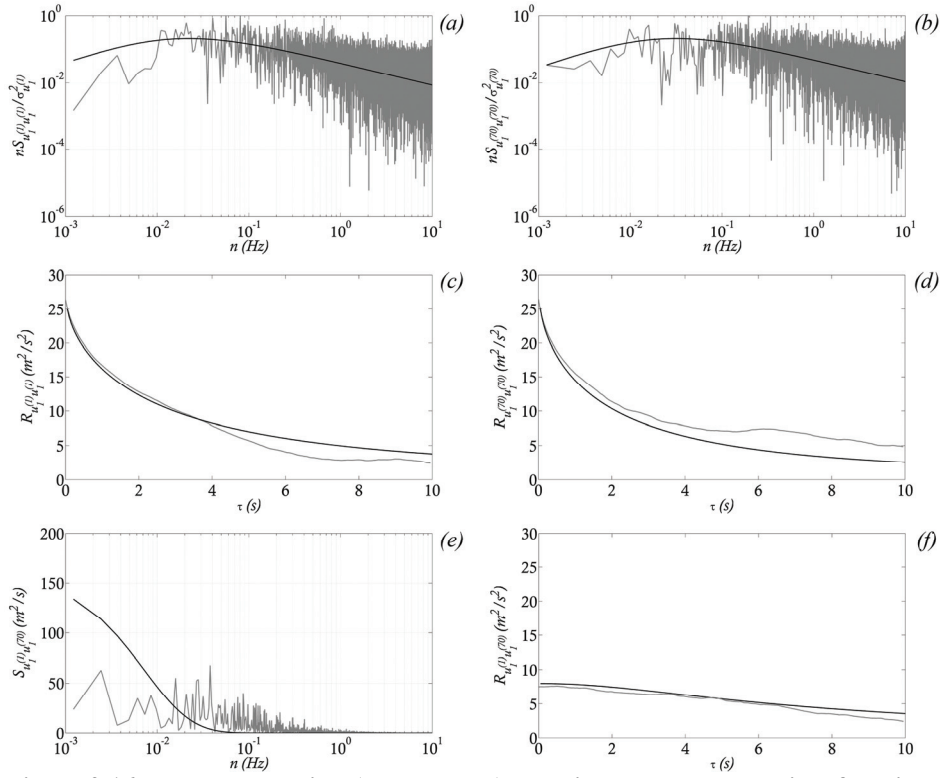


Figure 2.16. Example II using AR method (black lines denote theoretical functions, gray lines denote numeric approximations): PSD of along-wind velocities at points 1 and 70 (a), (b); corresponding autocorrelation functions (c), (d); CPSD between along-wind velocities at points 1 and 70 (e); corresponding cross-correlation function (f)

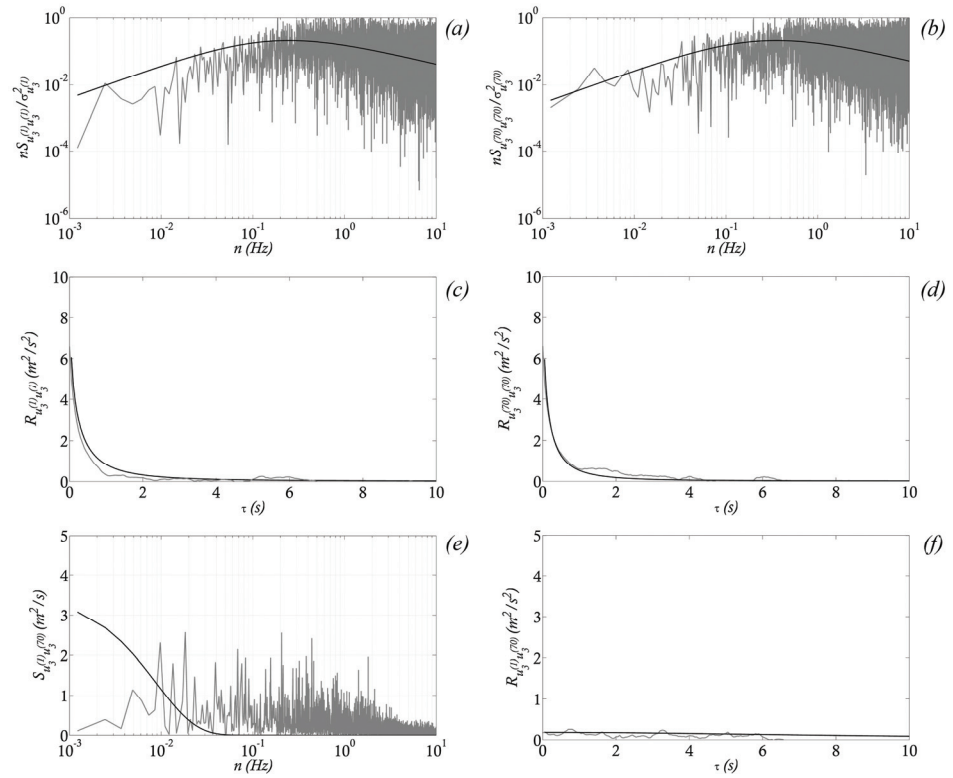


Figure 2.17. Example II using AR method (black lines denote theoretical functions, gray lines denote numeric approximations): PSD of across-wind velocities at points 1 and 70 (a), (b); corresponding autocorrelation functions (c), (d); CPSD between along-wind velocities at points 1 and 70 (e); corresponding cross-correlation function (f)

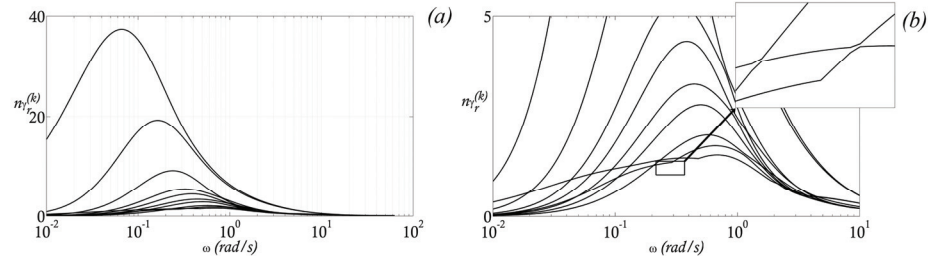


Figure 2.18. Example II: first ten non-dimensional eigenvalues (POD) of atmospheric turbulence as a function of the circular frequency ω (a); interaction of closed eigenvalues (b)

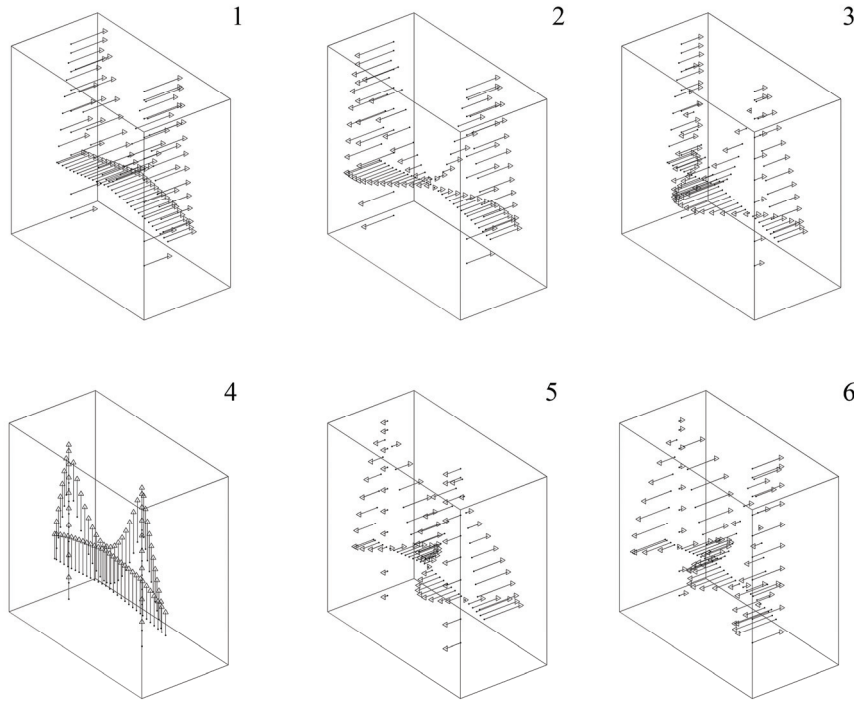


Figure 2.19. Example II: first 6 blowing modes for the frequency value $\omega=0.069$ rad/s

2.5 Concluding remarks

Simulating the wind velocity field in large dimensional domains may become a very demanding computational task due to memory occupation and time consuming simulations. A brief review of the three main classes of simulation methods is proposed, devoting special care to algorithm structure and computational expense. Starting from the well-established WAWS method, based on the historical pioneering work of Shinozuka and Jan (1972), it is discussed how AR and POD-based techniques may be adopted in order to gain a higher computational efficiency.

A first numerical example, represented by a one-dimensional structure, is presented to compare the accuracy of the three methods in terms of preservation of wind spectra and correlation functions. From the computational viewpoint, it is shown that POD-based and AR techniques dramatically reduce both computer time and memory allocation, with respect to the WAWS method. As far as algorithm accuracy, as expected, the WAWS method seems to guarantee the best quality of the obtained results. Nevertheless, either POD-based or AR techniques appear to furnish a comparable accuracy with respect to the WAWS method. Particularly, POD-based and AR methods are seen to produce only slight errors in the correlation functions, when the coherence becomes large, while spectra are essentially well-conserved. A small disagreement of the spectra in the very low frequency range is observed in the case of the AR method, which is not the case for the POD-based technique, and in any case does not bias the overall quality of the obtained results.

For larger domains, such as those of large structures and long-span bridges, the WAWS method seems to be non-competitive or even unfeasible. Conversely, AR and POD-based appear to be the only methods capable to efficiently simulate the wind velocity field on complex domains. However, when performing structural analysis, the POD method seems to be more attractive because the POD decomposition of the spectral matrix provides a significant physical representation of the wind field which gives indications of the potential wind dynamic effects on the structure and of the interaction between the structure of the loads and that of the mechanical system. Finally, the quality of the results obtained by means of the POD method tends asymptotically to that of the WAWS method as the number of calculations of the spectral matrix decompositions grows. The same property is not rigorously shared by autoregressive methods.

Chapter 3

MODELING UNSTEADY AERODYNAMICS IN BUFFETING ANALYSIS OF LONG-SPAN BRIDGES

Abstract

The role of unsteady phenomena in the buffeting response of suspension bridges is analyzed with reference to a case study. To this end, time domain analyses are carried out to incorporate geometric nonlinearities. In particular, a fully aeroelastic formulation and a wide-applied simplified method which neglects frequency dependency and memory terms in the self-excited loads are adopted. The results obtained by means of the two methods are compared and discussed from the viewpoint of modal participations and nonlinear effects.

3.1 Introduction

Suspension bridges are significantly prone to wind action (Simiu and Scanlan, 1996). In particular, buffeting analysis is one of the most important aspects of structural reliability in modern bridge design (Thorbek and Hansen, 1998; Ding and Lee, 2000; Chen and Kareem, 2001; Chen and Kareem, 2002).

Indeed, vibrations originated by turbulent wind occur at both construction and completion stages for the whole life of the bridge (Petrini et al., 2007). These vibrations are sometimes “large” in the sense that they may produce fatigue ruptures, discomfort, runability problems and so on.

Traditional buffeting analysis of bridges relies on linear models in the frequency domain (Xu et al., 2000; Guo et al., 2007). Nevertheless, the hypothesis of linearization may lead to either conservative or unsafe results. In contrast, time domain modeling of aeroelastic loads (Salvatori and Borri, 2007), although much more expensive from a computational viewpoint, does not require the hypothesis of a linear structural behavior and can effectively predict non-Gaussian responses (Gusella and Materazzi, 1998; Gusella and Materazzi, 2000).

The wide-applied method for predicting the buffeting response of bridges in the time domain is represented by the quasi-steady (QS) formulation, which makes use of steady aerodynamic coefficients and dynamic derivatives, accounting for effective wind angle of attack. As it is well-known, this simplified method is not fully capable to catch unsteady phenomena, as it neglects frequency dependency and memory terms. In contrast, fully aeroelastic formulations are: the classic method based on aeroelastic derivatives in the time domain (ADTD) and the formulation using indicial functions (IF).

Comparing the predictions obtained by using QS and ADTD formulations gives indications on the relevance of unsteady phenomena in the buffeting response of suspension bridges. This topic is addressed by considering the case study of the Tsing Ma Bridge, whose aerodynamic characteristics are known from wind tunnel tests (Zhu et al., 2002).

3.2 Wind loading on bridge decks: frequency domain approaches

Before entering into the details of time-domain modeling of aeroelastic forces on bridge decks, a brief introduction to the classic frequency domain approach is given in this section, starting from the classic airfoil theory.

Let us consider a thin airfoil of width $B = 2b$, subjected to an incoming flow of mean velocity U (see Figure 3.1 (a)). The vertical (bending) displacement of the airfoil is denoted by h , while α represents its (twist) rotation (assumed, without loss of generality, around the center of the chord). Assuming a harmonic motion with circular frequency ω , self-excited lift force (L_{se}) and pitching moment (M_{se}) acting on the airfoil may be expressed in the following well-known form (Lazzari, 2005):

$$\begin{aligned}
 L_{se} &= \underbrace{\pi \rho b^2 (U \dot{\alpha} + \ddot{h})}_{\text{non-circulatory}} - \underbrace{2 \pi \rho b U C(k) \left[U \alpha + \dot{h} + \frac{b}{2} \dot{\alpha} \right]}_{\text{non-stationary}} \\
 M_{se} &= \underbrace{-\pi \rho b^2 \left[U \frac{b}{2} \dot{\alpha} + \frac{b^2}{8} \ddot{\alpha} \right]}_{\text{non-circulatory}} + \underbrace{\pi \rho U b^2 C(k) \left[U \alpha + \dot{h} + \frac{b}{2} \dot{\alpha} \right]}_{\text{non-stationary}}
 \end{aligned} \tag{3.2.1}$$

where ρ denotes the air density. Equation (3.2.1) was early obtained by Theodorsen, on the basis of incompressible fluids theory and gives the lift and moment expressions as the sum of a non-circulatory and a non-stationary contribution. Drag force is, as usual, neglected for airfoil motion. The non-circulatory contribution is frequency-independent and it is related to a fluid portion moving rigidly with the body. Non-stationary contribution, on the contrary, arises due to the presence of fluid circulation around the body. This last is a non-conservative load, which depends on the aerodynamic coefficient $C(k)$ that is a function of the reduced frequency $k = b\omega/U$. The expression of $C(k)$ can be given as follows:

$$C(k) = F(k) + iG(k) \tag{3.2.2}$$

where i is the imaginary unit. Equation (3.2.2) is known as “Theodorsen’s circulatory function” and it is widely approximated as follows:

$$\begin{aligned}
 F(k) &= 1 - \frac{0.165k^2}{0.0455^2 + k^2} - \frac{0.335k^2}{0.300^2 + k^2} \\
 G(k) &= -k \left(\frac{0.165 \cdot 0.0455}{0.0455^2 + k^2} + \frac{0.335 \cdot 0.300}{0.300^2 + k^2} \right)
 \end{aligned} \tag{3.2.3}$$

The functions $F(k)$ and $G(k)$ are plotted versus $2\pi/k$ in Figure 3.1 (b).

Bridge deck sections usually have “bluff” shapes, with edges on which the airflow detaches. Closed expressions of aerodynamic coefficients for such kind of shapes cannot be assessed by fluid theory. Experimental results are adopted instead, following the classic theory by Simiu and Scanlan (1996). Following this approach, the aeroelastic forces acting on the deck (including the drag force D) are calculated by means of linear combinations of displacements, rotations and their prime derivatives, with frequency-dependent coefficients $H_i^*(k)$, $P_i^*(k)$, $A_i^*(k)$ for $i = 1, \dots, 6$, called “flutter derivatives” and experimentally measured in wind tunnel tests.

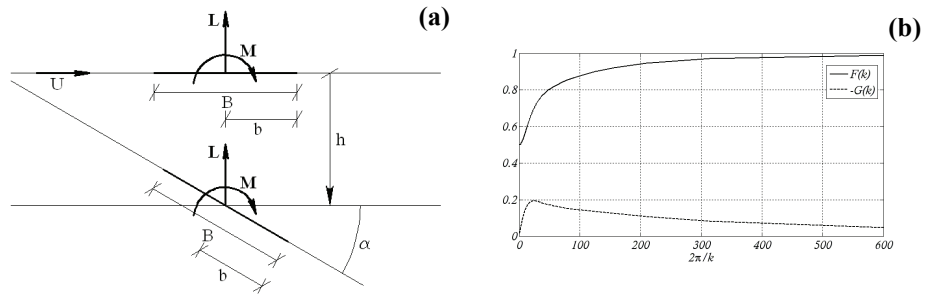


Figure 3.1. Aeroelastic forces on a thin airfoil (a); real and imaginary parts of “Theodoresen circulatory function” (b)

According to the sign conventions reported in Figure. 3.2 (a), in which the horizontal displacement p is introduced, the aeroelastic forces acting on a bluff deck section read as (Simiu and Scanlan, 1996):

$$\begin{aligned}
 L_{se} = \frac{1}{2} \rho U^2 B & \left(KH_1^* \frac{\dot{h}}{U} + KH_2^* \frac{B \dot{\alpha}}{U} + K^2 H_3^* \alpha + \right. \\
 & \left. + K^2 H_4^* \frac{h}{B} + KH_5^* \frac{\dot{p}}{U} + K^2 H_6^* \frac{p}{B} \right)
 \end{aligned} \tag{3.2.4a}$$

$$D_{se} = \frac{1}{2} \rho U^2 B \left(KP_1^* \frac{\dot{h}}{U} + KP_2^* \frac{B\dot{\alpha}}{U} + K^2 P_3^* \alpha + K^2 P_4^* \frac{h}{B} + KP_5^* \frac{\dot{p}}{U} + K^2 P_6^* \frac{p}{B} \right) \quad (3.2.4b)$$

$$M_{se} = \frac{1}{2} \rho U^2 B^2 \left(KA_1^* \frac{\dot{h}}{U} + KA_2^* \frac{B\dot{\alpha}}{U} + K^2 A_3^* \alpha + K^2 A_4^* \frac{h}{B} + KA_5^* \frac{\dot{p}}{U} + K^2 A_6^* \frac{p}{B} \right) \quad (3.2.4c)$$

In Equations (3.2.4) the aeroelastic forces are expressed as functions of the reduced frequency of the motion $K = B\omega/U$.

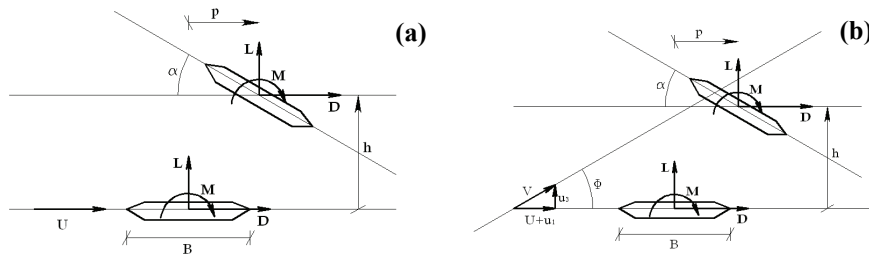


Figure 3.2. Aeroelastic forces on a bluff deck section

3.3 Wind loading on bridge decks: time domain approaches

Frequency domain approaches require the fundamental hypothesis of a structural linear behavior. As it is well known, this hypothesis may become essentially inadequate for flexible structures such as cables, bridges, etc. which have a geometric nonlinear behavior. In all these cases, time domain representations of aeroelastic forces must be preferred. This topic was extensively analyzed in the paper by Lazzari (2005), in which the following two formulations were presented in order of increasing complexity:

- “Quasi-steady formulation” (QS), which neglects frequency dependency and memory terms;
- “Theory of aeroelastic derivatives in the time domain” (ADTD), which accounts for frequency-dependent behavior and memory terms.

3.3.1 Aeroelastic derivatives in the time domain (ADTD)

With reference to a general bluff section of a bridge deck, subjected to an incoming mean flow of intensity U , the drag force $D(t)$, the lift force $L(t)$ and the aerodynamic moment $M(t)$ are defined following the sign conventions reported in Figure 3.2 (b). The total wind velocity has intensity V and inclination Φ with respect to the mean wind direction. Given these definitions, the effective wind angle of attack α_0 attains the value $\alpha + \Phi$. In the most general case, the aerodynamic forces are given by the sum of steady-state (subscript “0”), buffeting (subscript “b”) and self-excited (subscript “se”) loads. The drag, lift and moment aerodynamic coefficients (C_D , C_L and C_M , respectively) can be measured by means of wind tunnel tests. Steady-state loads are related to the mean component of the incoming flow and, as a first approximation, depend upon the aerodynamic coefficients evaluated at the initial configuration ($\alpha_0=0$):

$$\begin{Bmatrix} D_0 \\ L_0 \\ M_0 \end{Bmatrix} = \frac{1}{2} \rho U^2 B \begin{Bmatrix} C_D(0) \\ C_L(0) \\ C_M(0)B \end{Bmatrix} \quad (3.3.1)$$

The presence of the atmospheric wind turbulent components u_1 and u_3 (see Chapter 2) produce buffeting forces per unit length, which can be expressed as:

$$\begin{Bmatrix} D_b \\ L_b \\ M_b \end{Bmatrix} = \frac{1}{2} \rho U^2 B \begin{Bmatrix} 2C_D(\alpha_0) \frac{u_1}{U} + C'_D(\alpha_0) \frac{u_3}{U} \\ 2C_L(\alpha_0) \frac{u_1}{U} + (C'_L(\alpha_0) + C_D(\alpha_0)) \frac{u_3}{U} \\ 2C_M(\alpha_0) \frac{Bu_1}{U} + 2C'_M(\alpha_0) \frac{Bu_3}{U} \end{Bmatrix} \quad (3.3.2)$$

Self-excited loads can be evaluated by expressing Equations (3.2.4) in the time domain, as proposed by Lazzari (2005). Let us consider, for instance, the

expression of the lift force. By considering the Fourier transform $\mathfrak{F}(\lambda)$ of a function of time $\lambda(t)$ and by exploiting the relation $\mathfrak{F}(\dot{\lambda}) = i\omega\mathfrak{F}(\lambda)$ one can obtain an expression of the lift force fully written in the frequency domain:

$$\begin{aligned} \frac{2\mathfrak{F}(L_{se})}{\rho U^2 B} = & \left(\frac{KH_1^*}{U} \mathfrak{F}(\dot{h}) + \frac{KH_2^* B}{U} \mathfrak{F}(\dot{\alpha}) + K^2 H_3^* \mathfrak{F}(\alpha) + \right. \\ & \left. \frac{K^2 H_4^*}{B} \mathfrak{F}(h) + \frac{KH_5^*}{U} \mathfrak{F}(\dot{p}) + \frac{K^2 H_6^*}{B} \mathfrak{F}(p) \right) \end{aligned} \quad (3.3.3)$$

By operating in the same way, the following matrix expression can be given:

$$\begin{aligned} \begin{bmatrix} \mathfrak{F}(L_{se}) \\ \mathfrak{F}(D_{se}) \\ \mathfrak{F}(M_{se}) \end{bmatrix} = \frac{1}{2} \rho U^2 \begin{bmatrix} K^2 (H_4^* + iH_1^*) \\ K^2 (P_4^* + iP_1^*) \\ K^2 (A_4^* + iA_1^*) \end{bmatrix} \begin{bmatrix} \mathfrak{F}(h) \\ \mathfrak{F}(p) \\ \mathfrak{F}(\alpha) \end{bmatrix} \\ + \begin{bmatrix} K^2 (H_6^* + iH_5^*) & K^2 (H_3^* + iH_2^*) \\ K^2 (P_6^* + iP_5^*) & K^2 (P_3^* + iP_2^*) \\ K^2 (A_6^* + iA_5^*) & K^2 (A_3^* + iA_2^*) \end{bmatrix} \begin{bmatrix} \mathfrak{F}(h) \\ \mathfrak{F}(p) \\ \mathfrak{F}(\alpha) \end{bmatrix} \end{aligned} \quad (3.3.4)$$

A very common strategy to write the self-excited forces on a bridge deck, consists of deriving them from a linear superposition of impulses. Although not theoretically rigorous when structural nonlinearities are considered, this approach allows to derive time domain representation of aeroelastic forces. In particular, for the lift force one can write:

$$\begin{aligned} L_{se}(t) = & \frac{1}{2} \rho U^2 \int_{-\infty}^t (I_{L_{seh}}(t-\tau)h(\tau) + \\ & I_{L_{sep}}(t-\tau)p(\tau) + I_{L_{se\alpha}}(t-\tau)\alpha(\tau)) d\tau \end{aligned} \quad (3.3.5)$$

where $I_{L_{seh}}$, $I_{L_{sep}}$, $I_{L_{se\alpha}}$ are the impulsive functions of the self-excited lift force with respect to the generalized displacements h , p and α , respectively. The Fourier transform of Equation (3.3.5) reads as:

$$\frac{2\mathfrak{F}(L_{se})}{\rho U^2 B} = \mathfrak{F}(I_{L_{seh}})\mathfrak{F}(h) + \mathfrak{F}(I_{L_{sep}})\mathfrak{F}(p) + \mathfrak{F}(I_{L_{se\alpha}})\mathfrak{F}(\alpha) \quad (3.3.6)$$

The compact form analogous to Equation (3.3.4) can thus be written as:

$$\begin{bmatrix} \Im(L_{se}) \\ \Im(D_{se}) \\ \Im(M_{se}) \end{bmatrix} = \frac{1}{2} \rho U^2 \begin{bmatrix} \Im(I_{Lseh}) & \Im(I_{Lsep}) & \Im(I_{Lse\alpha}) \\ \Im(I_{Dseh}) & \Im(I_{Dsep}) & \Im(I_{Dse\alpha}) \\ \Im(I_{Mseh}) & \Im(I_{Msep}) & \Im(I_{Mse\alpha}) \end{bmatrix} \begin{bmatrix} \Im(h) \\ \Im(p) \\ \Im(\alpha) \end{bmatrix} \quad (3.3.7)$$

By comparing Equations (3.3.4) and (3.3.7), the following relations can be obtained:

$$\begin{aligned} \Im(I_{Lseh}) &= K^2 (H_4^* + iH_1^*) \\ \Im(I_{Lsep}) &= K^2 (H_6^* + iH_5^*) \\ \Im(I_{Lse\alpha}) &= K^2 (H_3^* + iH_2^*) \end{aligned} \quad (3.3.8)$$

Similar expressions to (3.3.8) can also be derived for drag and moment impulsive functions. Assuming in Equations (3.3.8) the so-called “rational function approximation” of the aeroelastic derivatives and then performing the inverse Fourier transform of Equations (3.3.7), the following expression of the Lift force can be achieved:

$$\begin{aligned} \frac{2L_{seh}(t)}{\rho U^2} &= a_0 h(t) + a_1 \frac{B}{U} \dot{h}(t) + a_2 \left(\frac{B}{U} \right)^2 \ddot{h}(t) + \\ &\sum_{j=3}^{m+2} \int_{-\infty}^t a_j e^{-(d_j U/B)(t-\tau)} \dot{h}(\tau) d\tau \end{aligned} \quad (3.3.9)$$

where the fourth term in the right-end-side represents the so-called “memory term” of the lift force. The coefficients a_0, a_1, \dots, a_{m+2} , which appear in Equation (3.3.9), can be calculated by curve fitting of the aeroelastic derivatives exploiting the following relations:

$$\begin{aligned} K^2 H_4^* &\cong a_0 - \frac{4\pi^2}{U_r^2} a_2 + \sum_{j=3}^{m+2} a_j \frac{4\pi^2}{d_j^2 U_r^2 + 4\pi^2} \\ K^2 H_1^* &\cong a_1 \frac{2\pi}{U_r} + \sum_{j=3}^{m+2} a_j \frac{4\pi d_j U_r}{d_j^2 U_r^2 + 4\pi^2} \end{aligned} \quad (3.3.10)$$

The memory term which appears in Equation (3.3.9) can be efficiently calculated through the following recursive expression:

$$\int_{-\infty}^{t_j} a_g e^{-(d_g U / B)(t_j - \tau)} \dot{h}(\tau) d\tau = \Gamma_{L,gh}(t_j) \cong$$

$$b_g \Gamma_{L,gh}(t_{j-1}) + a_g \sqrt{b_g} \Delta h \left(t_{j-1} + \frac{\Delta t}{2} \right), \quad b_g = e^{-(d_g U / B)(t_j - t_{j-1})} \quad (3.3.11)$$

The above described approach was applied to the case of the Tsing Ma Bridge by Ding and Lee (2000) using wind tunnel experimental results. By assuming that the self-excited drag force is negligible with respect to the other terms involved and that coupled terms between lift and torsion are small, the following expression of the self-excited loads was achieved:

$$\begin{Bmatrix} L_{se} \\ M_{se} \end{Bmatrix} \cong \rho B U^2 \begin{Bmatrix} C_{L1} \frac{h}{B} + C_{L2} \frac{\dot{h}}{U} + \\ C_{L3} \int_{-\infty}^t \exp[-C_{L5} U / B(t - \tau)] \frac{\dot{h}(\tau)}{B} d\tau \\ + C_{L4} \int_{-\infty}^t \exp[-C_{L6} U / B(t - \tau)] \frac{\dot{h}(\tau)}{B} d\tau \\ C_{M1} B \alpha + C_{M2} \frac{B^2}{U} \dot{\alpha} + \\ C_{M3} B \int_{-\infty}^t \exp[-C_{M5} U / B(t - \tau)] \dot{\alpha}(\tau) d\tau \\ + C_{M4} B \int_{-\infty}^t \exp[-C_{M6} U / B(t - \tau)] \dot{\alpha}(\tau) d\tau \end{Bmatrix} \quad (3.3.12)$$

3.3.2 Quasi-steady formulation

In the quasi-steady approach, steady aerodynamic coefficients are adopted by considering the relative motion between the deck and the airflow. The sign conventions and the definition of the aeroelastic forces are represented in Figure 3.2 (b). The relative velocity U_r between the deck and the wind flow assumes the following value:

$$U_r = \sqrt{(U + u_1 - \dot{p})^2 + (u_3 - \dot{h} + m_1 B \dot{\alpha})^2} \quad (3.3.13)$$

where m_1 is the distance between the rotation point and the center of the bridge deck (here neglected without loss of generality). The aeroelastic forces can thus be written as (Lazzari, 2005):

$$\begin{Bmatrix} D \\ L \\ M \end{Bmatrix} = \frac{1}{2} \rho U_r^2 B \begin{Bmatrix} C_D(\gamma) \cos(\phi_r) - C_L(\gamma) \sin(\phi_r) \\ C_L(\gamma) \cos(\phi_r) + C_D(\gamma) \sin(\phi_r) \\ C_M(\phi_r) \end{Bmatrix} \quad (3.3.14)$$

where C_L , C_D , C_M are the aerodynamic coefficients for lift, drag and torsion, respectively. Those coefficients are functions of the actual angle of attack γ , of the relative wind velocity, which is calculated as follows:

$$\gamma = \arctan\left(\frac{u_3 - \dot{h} + m_1 B \dot{\alpha}}{U + u_1 - \dot{p}}\right) \quad (3.3.15)$$

The angle ϕ_r between the relative wind velocity and the horizontal axis x_I is also utilized in Equation (3.3.14) to project the aerodynamic forces on the initial reference system.

3.4 Buffeting response using different formulations

A comparative study between the predicted buffeting responses using QS and ADTD formulations is carried out for the case study of the Tsing Ma Bridge. The TMS model, described in Chapter 1, is adopted in the simulation and the turbulent wind field is generated using the POD-based method described in Chapter 2. The simulations have a total duration of 600 s, using an integration time step $dt=0.05$ s.

The aeroelastic derivatives and the aerodynamic coefficients of the Tsing Ma Bridge deck section were measured by means of wind tunnel tests in reference (Lau and Wong, 1997). Using these results, Ding and Lee (2000) calculated the coefficients C_{L1}, \dots, C_{L6} and C_{M1}, \dots, C_{M6} , that appear in Equation (3.3.12), leading to the values summarized in Table 3.1. The aerodynamic coefficients of the bridge section for a nil angle of attack and their prime derivatives are also

reported in Table 3.1 to be adopted in the QS formulation. A drag coefficient of 1.5 is adopted for the bridge towers, while a drag coefficient of 0.8 is assumed for the main cables (Cluni et al., 2007).

The nonlinear buffeting response of the bridge is calculated at different values of the shear velocity u_* . The correspondence between the adopted values of u_* and the values of the mean wind velocity U_m at mid-span is reported in Table 3.2. The considered excitation levels are such that U_m varies linearly from 20 m/s up to 50 m/s which represents an extreme event for the bridge. Indeed, as reported in the paper by Beard (1995), the one minute mean wind speed with 120 years of return period for the bridge is 58 m/s . It is also worth noting that the mean wind velocity registered during the Typhoon York, occurred in 1997, at the bridge mid-span was only 20 m/s (Guo et al., 2007).

ADTD	C_1	C_2	C_3	C_4	C_5	C_6
M_{se}	0.26412	-0.51993	0.16645	0.29121	13.43210	5.87260
L_{se}	-1.08827	2.79466	0.99064	1.06341	13.09312	229.358
QS	$C_D(0)$	$C_L(0)$	$C_M(0)$	$C_D'(0)$	$C_M'(0)$	$C_L'(0)$
	0.135	0.090	0.063	-0.253	0.278	1.324
Towers: $C_D(0)=1.5$ Cables: $C_D(0)=0.8$						

Table 3.1. Aerodynamic coefficients of Tsing Ma deck section (Ding et al., 1999)

u_* (m/s)	0.950	1.425	1.900	2.375
U_m (m/s)	20.1	30.1	40.1	50.2

Table 3.2. Correspondence between u_* and mid-span mean velocities U_m

Figure 3.3 represents the time histories of the mid-span vertical displacement h_m of the deck. As it can be observed from such a figure, regardless the level of external excitation, the ADTD formulation predicts values of h_m which are approximately 30% smaller than those obtained by means of the QS formulation. This circumstance emphasizes that the QS formulation is not fully capable to reproduce the non-conservative aeroelastic loads caused by the

positive vertical and torsional aerodynamic damping exhibited by the deck of the Tsing Ma Bridge in wind tunnel tests (Xu et al., 2000).

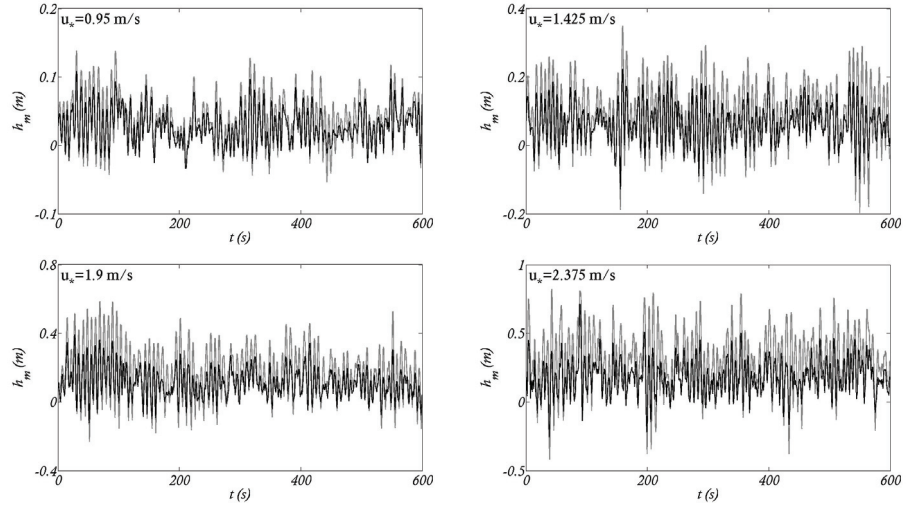


Figure 3.3. Time histories of vertical mid-span displacement h_m computed by means of QS (gray line) and ADTD (black line) formulations

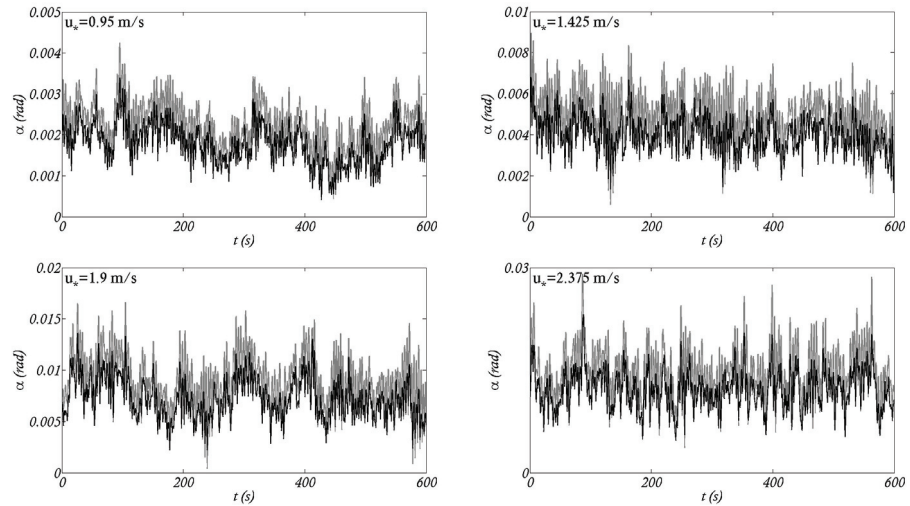


Figure 3.4. Time history of mid-span twist angle α_m computed by means of QS (gray line) and ADTD (black line) formulations

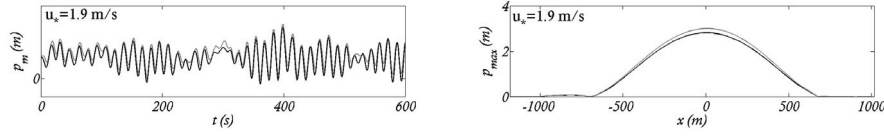


Figure 3.5. Time history of horizontal mid-span displacement p_m computed by means of QS (gray line) and ADTD (black line) formulations

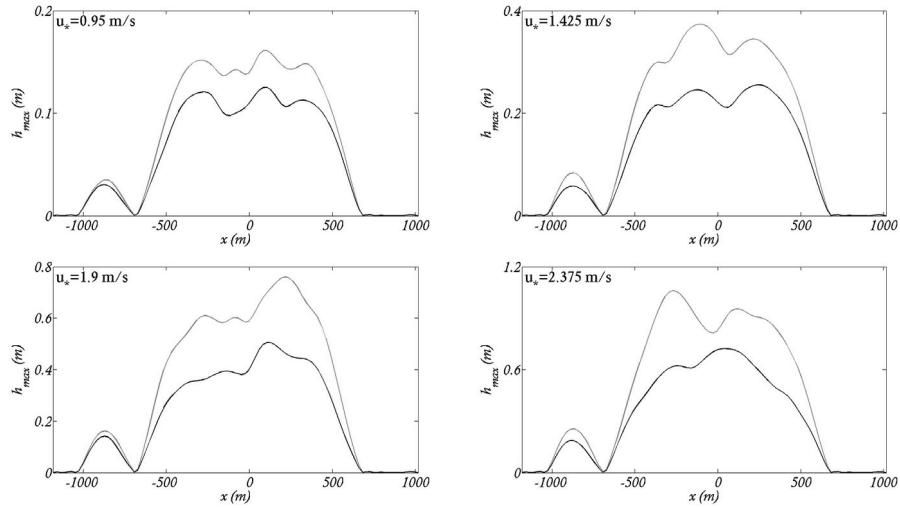


Figure 3.6 Envelopes of maximum deck displacements computed by means of QS (grey lines) and ADTD (black lines) formulations for different values of the shear velocity u_s

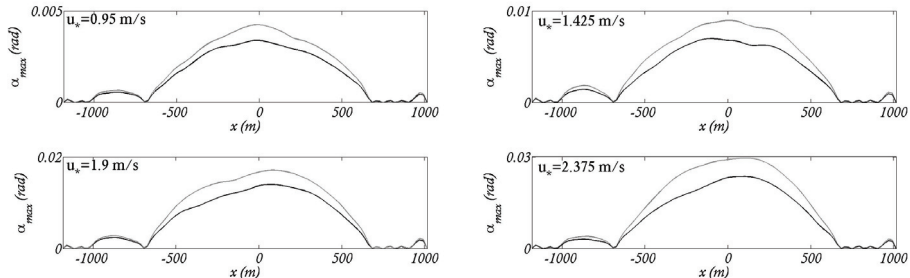


Figure 3.7. Envelopes of maximum deck rotations computed by means of QS (grey lines) and ADTD (black lines) formulations for different values of the shear velocity u_s

The difference between QS and ADTD formulations is not negligible and it seems to be independent on the excitation level. Similar conclusions can be made by looking at Figure 3.4, which shows the time histories of the mid-span twist angle α_m , obtained using the two different approaches. As expected, having neglected self-excited terms in the out-of-plane direction, QS and ADTD formulation produce almost similar results as concerns the out-of-plane mid-span displacement p_m (see Figure 3.5).

The comparison between the envelopes of the maximum deck displacements, obtained by means of the two different formulations, is reported in Figures 3.6 and 3.7. These figures emphasize that the shapes of the said envelopes are mostly equivalent. This circumstance suggests that the two approaches predict similar modal participations. In order to better investigate this last point, the power spectral density functions (PSD) of the mid-span deck displacements are represented in Figure 3.8 for the case $u^*=1.9$ m/s. The results confirm that the spectral compositions of the motions are almost independent on the chosen approach. Specifically, it can be observed that the out-of-plane motion is mainly composed by first symmetric mode (frequency 0.069 Hz). In the in-plane motion, the first symmetric mode is prevailing (frequency 0.141 Hz), although the participations of the first anti-symmetric mode (frequency 0.118 Hz) and the second symmetric mode (frequency 0.191 Hz) are also detected.

The role played by nonlinearities in the buffeting response can be analyzed by considering the high order statistics (skewness and kurtosis) of the results. Namely, assuming a Gaussian wind excitation entails that, in the linear regime, the bridge response would also be Gaussian. This means that the expected values of the skewness and the kurtosis would be 0 and 3, respectively. However, when nonlinearities take place, a non-Gaussian response should be expected. As examples, Figure 3.9 represents the histograms of the vertical mid-span displacement h_m . Looking at this figure, one can hardly judge on the Gaussianity of the response. In order to better investigate this point, the high order statistics of the generalized mid-span displacements are reported in Figure 3.10. The presented results suggest that, mostly, the hypothesis of a Gaussian

bridge response is admissible, though it is sometimes inadequate. This circumstance is usually more evident at large levels of external excitation, although it may be observed even at low values of the shear velocity u_* (see for instance the kurtosis of α_m). It must be also noted that, although lower in terms of absolute values, the response calculated by means of the ADTD formulation is generally a little less Gaussian than the one predicted by using the QS theory.

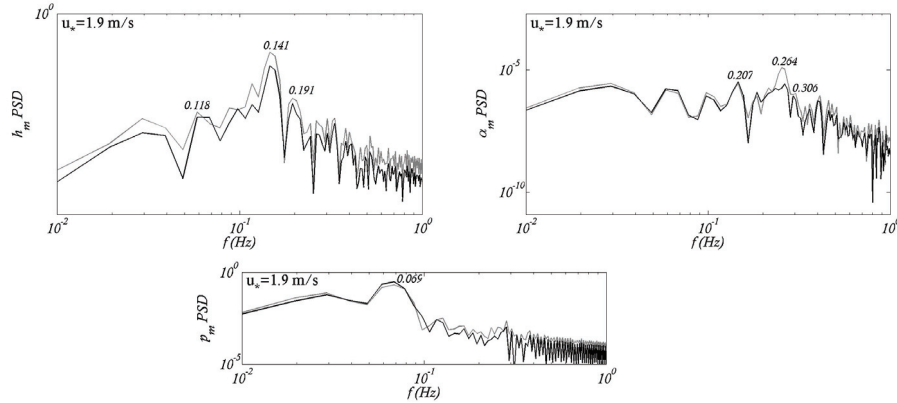


Figure 3.8. PSD functions of mid-span displacements computed by means of QS (grey lines) and ADTD (black lines) formulations ($u_*=1.9$ m/s)

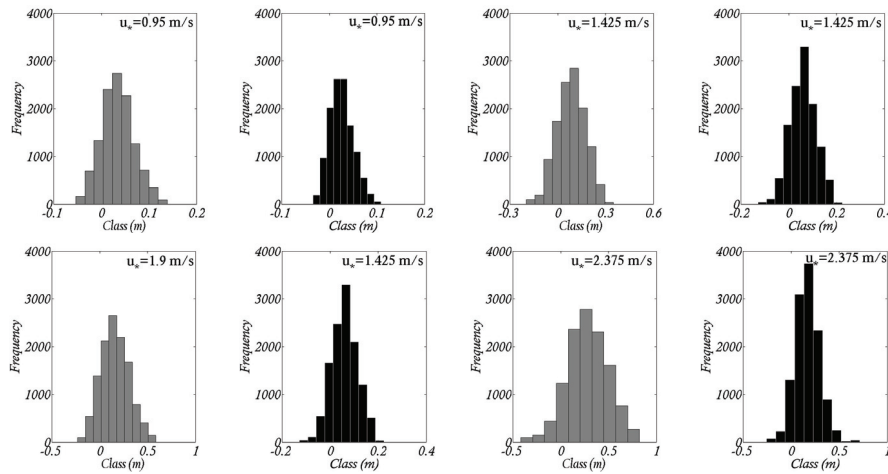


Figure 3.9. Histograms of mid-span vertical displacement computed by means of QS (grey bars) and ADTD (black bars) formulations

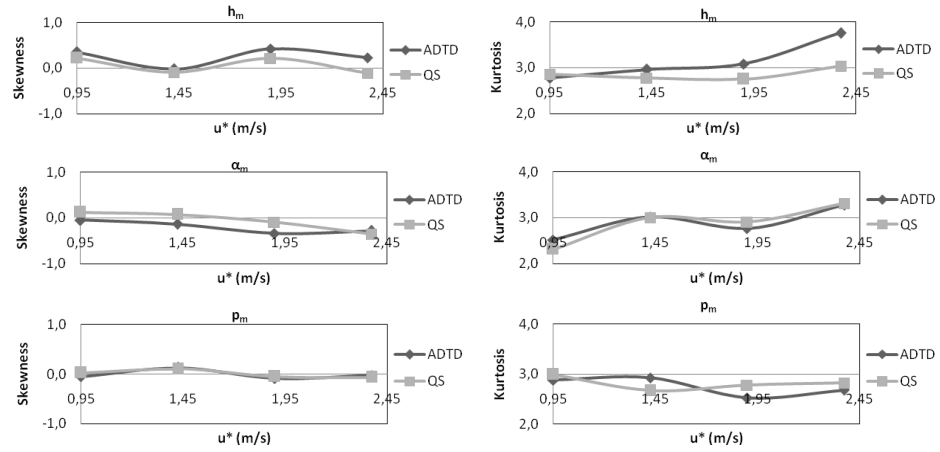


Figure 3.10. High order statistics of generalized mid-span displacements

3.5 Concluding remarks

The role of unsteady aerodynamics in the time domain buffeting response of suspension bridges is discussed with reference to a case study. To this end, both quasi steady theory and the fully aeroelastic formulation based on aeroelastic derivatives in the time domain are adopted. The turbulent wind field is simulated by means of the POD-based technique described in Chapter 2.

The comparison of the predicted responses using QS and ADTD formulations reveals that the former is not fully capable to catch unsteady phenomena even at low excitation levels. Indeed, in the considered case, self-excited loads contain a positive aerodynamic damping which is correctly accounted for only by adopting the ADTD formulation. However, the two approaches are seen to furnish similar results in terms of modal participations.

The stochastic analysis of the results indicates that the wind-excited response of the bridge is influenced by nonlinear phenomena, sometimes even at low vibration amplitudes. This circumstance is more evident when analyzing the results obtained by means of the ADTD formulation rather than those obtained using the QS theory.

Chapter 4

BUFFETING ANALYSIS OF BRIDGES BASED ON FIELD MEASUREMENTS

Abstract

A framework for numerically predicting the buffeting response of long-span bridges is established, which makes use of field measurements. In order to validate the proposed computational scheme, the numerical predictions are compared to the measured responses for the case study of the New Carquinez Bridge. To this end, the results of the system identification performed elsewhere are adopted to update a finite element model of the structure, via an optimization technique. After checking the agreement between theoretical and measured wind spectra, the turbulent wind field is artificially generated via proper orthogonal decomposition of the spectral matrix. The results of the nonlinear response analysis emphasize the good agreement between predicted and measured accelerations of the deck, both in time and frequency domain.

4.1 Introduction

Numerical prediction of the dynamical behavior of long-span bridges under operating conditions is necessary for structural safety analysis, remaining

lifetime evaluation, etc. To this end, structural monitoring and system identification are essential tools to calibrate the numeric models in order to obtain realistic results.

Because of the difficulty to measure excitation to long-span bridges, stochastic system identification techniques have been paid close attention to, with no need of input information (Magalhães et al., 2007; Betti et al., 2008). In addition, when performing numerical simulations, a particular care must be paid on characterizing and simulating the wind field. This problem can be treated as described in Chapter 2. Due to the complexity of the problem under investigation, comparison with field measurements is the only way to validate, to some extent, the numerical frameworks which are established in order to predict the wind-excited response of a bridge (Xu et al, 2007).

This chapter focuses on predicting the wind-excited response of a newly built suspension bridge, making use of field measurements. The considered case study is represented by the New Carquinez Bridge (NCB), San Francisco. The main topic under investigation is the agreement between the field measurements and the numerical predictions obtained by using updated structural as well as wind field models. The results of the data driven stochastic system identification (SSI/data) of the NCB are adopted to update the structural model. Time domain quasi steady representation of aerodynamic loads is adopted since this approach makes use of steady aerodynamic coefficients and does not require to measure the aeroelastic derivatives of the deck, which are usually affected by a large data scattering.

4.2 Governing relations

4.2.1 Model updating technique

Identified modal parameters are employed to update the numerical model of the NCB. To this end, a first order optimization technique is here adopted such that the optimal model, depending on the p design parameters X_1, \dots, X_p , is identified by minimizing the following cost function (Gentile and Gallino 2008):

$$J = \sum_{i=1}^N \frac{w_i \cdot \left| f_i^*(X_1, X_2, \dots, X_p) - f_i^E \right|}{f_i^E} \quad (4.2.1)$$

where f_i^E and f_i^* represent the i -th expected and calculated natural frequencies of the structure and w_i are user-defined weight coefficients. A certain number N of modes is considered in Equation (4.2.1).

The first order optimization technique is an iterative procedure to find a minimum of the cost function. Particularly, the algorithm calculates, at each iteration, the gradients of the cost function with respect to the design parameters and determines a search direction for the next design point. Thus, each iteration is composed by sub-iterations, i.e. by several analysis loops. In the presented case, each single loop consists in a nonlinear static analysis followed by the modal analysis.

The design variables are constrained to vary within a user defined feasible region of the design space. No further limit to the size of the line search step is assumed, which therefore can be as large as the design range. The gradients of the cost function are calculated by adopting a forward difference which is equal to 0.2 % of the design variable range.

Convergence to an optimum is achieved when the change in the cost function from the best design, or from the previous design, to the current one is smaller than a given tolerance, which is assumed to be equal to one percent of the current value. Since the method starts from an existing point in design space and tries to find a path toward the minimum, it should be checked that it does not find a local minimum instead of a global one. Unfortunately, a minimum can hardly be judged to be local or global without the knowledge of the objective function in the whole design space. Nonetheless, some carefulness in the optimization can help to improve the obtained results by limiting the risk that the algorithm is stuck into a local minimum. First of all, the initial design point should be chosen in such a way that it is already close to the optimal design set. This obviously outlines the need of developing an initial model which is an accurate replication of the real structure and contains as much information as possible about the structure itself. By operating in this way, it is

possible to choose a limited number of design variables and to restrict their variability within reasonable limits. Particularly, the design variables will be those for which the largest sensitivities of the cost function are evidenced. Several attempts to find the global minimum should then be performed. Particularly, the initial design point and the region of the design space in which design variables can vary must be manually adjusted until a satisfactory reduction of the cost function is obtained after optimization. Usually, convergence to a minimum should be achieved after about 5-10 iterations. The combination of initial design set and limits of design variables offering the minimum value of the cost function is the feasible global minimum or, at least, a good approximation of it. Although more computationally demanding than other possible optimization strategies, the first order method is found to be effective and feasible for the presented case.

4.2.2 Wind simulation technique

As customary in wind engineering the wind velocity field is idealized as the sum of a mean value, following the well-know logarithmic law, and a multivariate stationary Gaussian zero-mean fluctuation (atmospheric turbulence) that depends on the position and varies in time (see Chapter 2).

For response analysis purposes, it is necessary to simulate tridimensional correlated turbulent wind velocities in a certain number n of points, which usually correspond to relevant nodes of the numerical model of the structure. This reflects on a $3n$ -variate Gaussian stochastic process. The efficient POD-based method described and implemented in Chapter 2 is adopted for wind simulation purposes.

4.3 Wind measurement data

Four records of the horizontal wind velocity and its direction, in correspondence of the bridge mid-span, are available. The measured along-wind velocity records V (i.e. the measured records projected onto the mean wind direction) are shown in Figure 4.1. In table 4.1, the mean along-wind velocity, the mean direction Dir (270° correspond to west-ward direction, i.e. transversal

to the bridge deck), the longitudinal turbulence intensity and the skewness and kurtosis of the along-wind velocity, are reported for each data set. The calculated values of skewness and kurtosis are almost close to 0 and 3, respectively, which correspond to the Gaussian distribution. This circumstance indicates that the hypothesis of a Gaussian stochastic wind field, usually assumed in the technical literature, is an acceptable simplification.

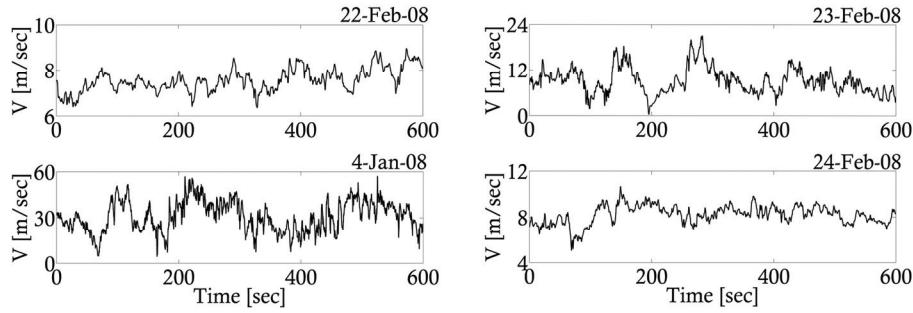


Figure 4.1 Time history records of along-wind velocities

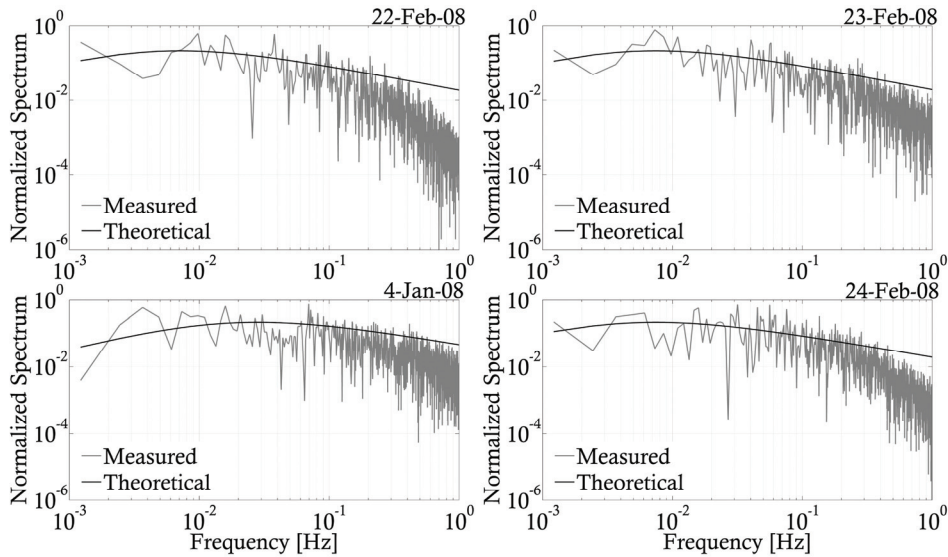


Figure 4.2 Comparison between measured and theoretical auto-spectra of along-wind velocities

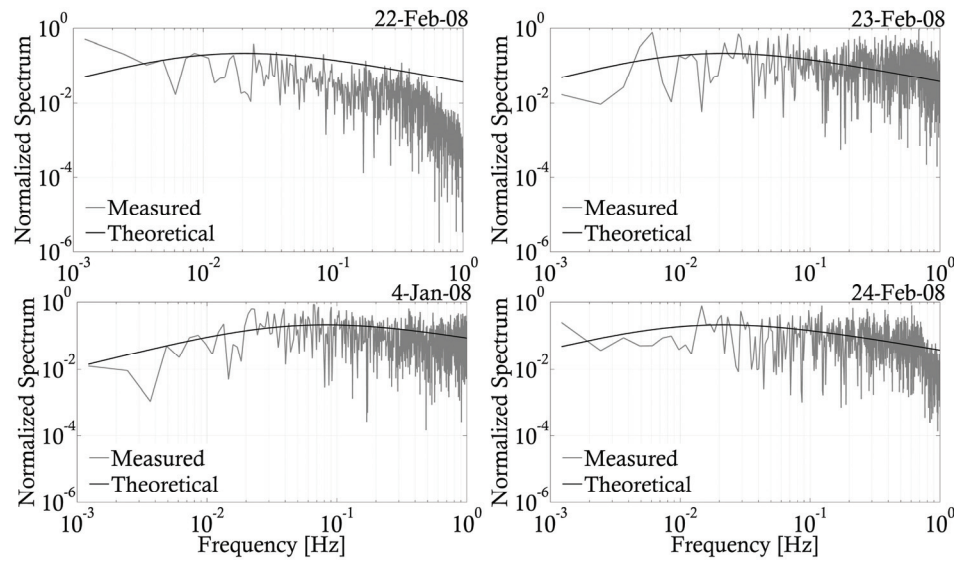


Figure 4.3 Comparison between measured and theoretical auto-spectra of across-wind horizontal velocities

Date	Mean [m/sec]	Dir [°]	Turb. Int. [%]	Skewness	Kurtosis
04-Jan-08	30.9	195.8	31.8	-0.0293	2.4152
22-Feb-08	7.7	283.0	6.82	-0.0349	2.3858
23-Feb-08	8.1	179.5	43.8	0.6872	3.5599
24-Feb-08	8.1	230.5	9.66	-0.2994	3.2861

Table 4.1 Stochastic characteristics of wind velocity measurements

The model by Solari and Piccardo (2001), which requires the knowledge of the roughness length z_0 , is adopted to give an analytical representation to wind spectra (see Chapter 2). The characterization of the wind environment at the site of the NCB was performed at the West Wind Laboratory (Ragget, 1998). From the referenced report it can be seen that the appropriate roughness length z_0 for a “coastal” exposure, such as the one of the NCB, is equal to 0.005 m. By assuming this value, the agreement between theoretical and measured auto-spectra that is shown in Figures 4.2 and 4.3 is obtained.

The results presented in Figures 4.2 and 4.3 emphasize that the model by Solari and Piccardo (2001) well matches the power spectral density functions

(auto-spectra) of the measured along-wind and across-wind velocities. It is worth noting that the spectra that are shown in Figures 4.2 and 4.3 are normalized to the variance of the turbulent velocities and multiplied by the frequency. Based on the presented results it is also assumed that the same model works for vertical turbulent components as well.

4.4 FE structural modeling and updating

A spine-type tridimensional nonlinear FE model of the NCB, which is composed by 947 finite elements and 652 nodes, is developed in the ANSYS environment (Ansys Inc. 2005). A graphical view of the model is presented in Figure 4.4. The orthotropic deck is modeled by an equivalent longitudinal frame completed by outriggers in correspondence of each hanger. The frames of the deck are reproduced by means of BEAM4 elements, i.e. tridimensional elastic beams, capable for large displacements and small strains. A null mass density and mass weight is assigned to these elements, while lumped equivalent masses (MASS 21 elements), with rotary inertia in the longitudinal direction, are placed along the deck, in correspondence of each suspender (i.e. at a mutual distance of 12.5 m). BEAM 4 elements are also adopted to model either horizontal and vertical frames of the towers. BEAM 188 elements, i.e. large displacements and large strains beam elements, are adopted to model the main cables and the suspenders.

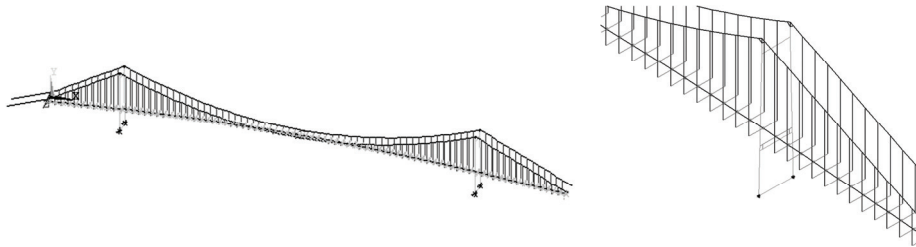


Figure 4.4 FE model representing the New Carquinez Bridge

The deck is rigidly linked to the towers in the lateral direction. In the vertical direction it is supported by rocker links placed on the edges of the outriggers

and connected to the lower horizontal beams of the towers. The rocker links are axially rigid vertical steel beams which can undergo elastic bending deflections. Thus, small relative longitudinal displacements between the deck and the towers are allowed. Similarly, the deck in correspondence of the bridge ends is restrained in the lateral direction and supported by rocker links in the vertical direction. The tower saddles have been reproduced by means of rigid bodies with a rotational hinge in correspondence of the tower vertical frames (the saddles are constrained to rotate in their planes). Equivalent six-degrees of freedom elastic springs have been placed at the bottom of the vertical frames of the towers to reproduce soil-piles deformability. The masses of the pile caps have been lumped at the bottom of each tower leg.

Mode no.	Frequencies (Hz)		Shape	Δ (%)
	Calculated	Expected		
1	0.136	0.136	symmetric transverse	0.0
2	0.144	0.144	anti-symmetric longitudinal/vertical	0.0
3	0.200	0.193	symmetric vertical	3.5
Mean percentage difference Δ_{mean} (%)				1.2

Table 4.2 Calculated vs. expected (PTG model) modal frequencies of the bridge

Section	Axial forces (kN)		Δ (%)
	Calculated	Expected	
South lateral	95557	96521	1.0
South main	88769	88515	0.3
North main	88895	88960	0.1
North lateral	91895	92963	1.2
Mean percentage difference Δ_{mean} (%)			0.6

Table 4.3 Calculated vs. expected (PTG model) axial forces in main cables

The pre-stressed initial configuration is achieved by increasing the initial curvature of the deck such that, after the application of the self weight, it almost assumes the prescribed curved shape. By operating in this way it is not necessary to assign initial stresses to the cables.

	Mode no.	Shape	w_i	Frequencies (Hz)		Δ (%)
				Objective	Calculated	
Transverse modes	1	symmetric	1	0.168	0.165	1.8
	8	anti-symm.	1	0.373	0.390	4.6
	18	symmetric	0	0.538	0.589	9.5
Vertical modes	2	anti-symm.	1	0.184	0.186	1.1
	3	symmetric	1	0.193	0.195	1.0
	5	symmetric	1	0.258	0.253	1.9
	7	anti-symm.	1	0.351	0.319	9.1
	10	north span	1	0.410	0.416	1.5
	15	symmetric	0	0.479	0.476	0.6
	17	symmetric	0	0.554	0.572	3.2
	23	anti-symm.	0	0.642	0.643	0.2
Torsional modes	30	symmetric	0	0.797	0.777	2.5
	14	symmetric	1	0.461	0.472	2.4
	27	anti-symm.	1	0.742	0.729	1.8
Hybrid modes	38	symmetric	1	0.974	0.981	0.7
	12	tors./transv.	0	0.486	0.434	10.7
	13	tors./transv.	0	0.499	0.440	11.8
	29	tors./transv.	0	0.781	0.741	5.1

Table 4.4 Objective vs. calculated natural frequencies after model updating

Mean percentage difference (all frequencies) Δ_{mean} (%)	3.9
Initial value of the cost function J	0.115
Final value of the cost function J	0.026
Number of iterations	7

Table 4.5 Optimization results

The mechanical characteristics of the model were known from the information provided by Parsons Transportation Group (PTG) that carried out the initial design for the NCB. As a first check, it has been verified that the modal parameters (linear normal modes) predicted by the FE model developed in this study were in good agreement with those provided by PTG. Particularly, in Table 4.2, the mode shapes and natural frequencies of the first three modes of the bridge from the current FE model are compared with those provided by PTG, showing a good agreement between the calculated values and those obtained by PTG. As an additional check, a comparison between the calculated axial forces and those provided by PTG at different sections of the main cables

is presented in Table 4.3. Also for the axial forces in the cable, the agreement between the two sets of values is excellent.

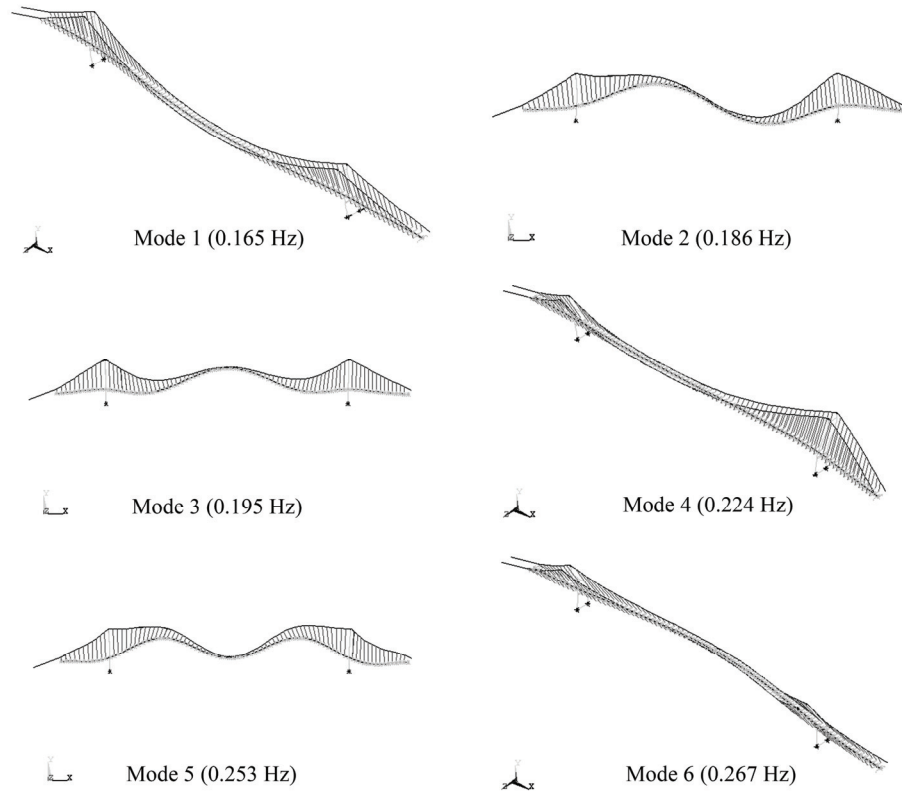


Figure 4.5 First six linear normal modes and corresponding periods T calculated by means of the updated FE model

An updating of the FE model was done using ten natural frequencies and mode shapes experimentally identified via SSI/data. This FE model updating was based on the optimization technique described in Section 4.2.

The updated numerical model shows the same mode shapes experimentally identified via SSI/data, particularly, hybrid modes such as torsion/transverse and vertical/longitudinal ones. In calculating the cost function in the

optimization process, only the first two transverse, the first six vertical and the three torsional identified modes have been considered. The hybrid torsion/transverse modes have not been included in the cost function since they were not easily detectable by the numerical model for each combination of the design variables (i.e. at design set) and were characterized by relatively small participation factors. However, those modes were detected by the updated FE model and thus, for completeness, the agreement of the modal characteristics of the updated FE model with those from the data analysis has been checked in all the eighteen identified modes, as it is discussed below.

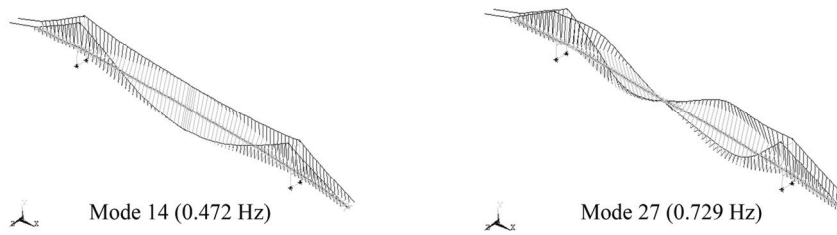


Figure 4.6 First two torsional modes and corresponding periods T calculated by means of the updated FE model

Eight optimization variables have been considered: the values of the translational and torsional lumped masses along the deck, the in-plane and out-of-plane bending rigidities of the deck, the torsional rigidity of the deck, the bending rigidity of the rocker links and the lateral rigidities of the soil springs, assumed to be different for the north and south towers.

The results of the optimization, reported in Tables 4.4 and 4.5, evidence a remarkable reduction of the cost function from the initial model to the final one with a few iterations. To have an idea of the computational expense required by the presented procedure it can be mentioned that the optimization was performed in about 20 minutes using a standard personal computer (Intel Core 2 Duo Processor T7250, 2 GB SDRAM).

The mean percentage difference Δ_{mean} between the ten identified and calculated natural frequencies included in the cost function is equal to 2.6%,

while the percentage difference calculated on all the identified sixteen modes is equal to 3.9 % (see Table 4.5). This confirms, to some extent, the good agreement between the updated FE model and the experimental data.

Looking at the percentage errors between calculated and identified natural frequencies, it can be observed that the largest differences concern the two hybrid torsion/transverse modes (modes 12 and 13) (percentage differences of 10.7% and 11.8%, respectively). Including these two modes in the optimization would reduce these errors at the expense of weakening the accordance on the more relevant torsional and lateral modes thus deteriorating the overall quality of the model. For this reason and because of the difficulty to detect hybrid modes using the numerical model at each design set, modes 12 and 13 have not been included in the cost function during the optimization process. The first six mode shapes and the first two torsional ones, calculated by means of the updated FE model are shown in Figures 4.5 and 4.6.

	Mode no.	Calculated frequencies (Hz)		Δ (%)
		No SSI	SSI	
Transverse modes	1	0.192	0.165	14.1
	8	0.556	0.390	29.8
	18	0.763	0.589	22.8
Vertical modes	2	0.186	0.186	0.0
	3	0.195	0.195	0.0
	5	0.253	0.253	0.0
	7	0.319	0.319	0.0
	10	0.416	0.416	0.0
	15	0.476	0.476	0.0
	17	0.572	0.572	0.0
	23	0.643	0.643	0.0
	30	0.777	0.777	0.0
Torsional modes	14	0.472	0.472	0.0
	27	0.729	0.729	0.0
	38	0.981	0.981	0.0
Hybrid modes	12	0.434	0.434	0.0
	13	0.437	0.440	0.7
	29	0.763	0.781	2.4

Table 4.6 Sensitivity of natural frequencies to soil-structure interaction (SSI)

	Mode no.	Calculated frequencies (Hz)		Δ (%)
		Rigid rocker links	Elastic rocker links	
Transverse modes	1	0.164	0.165	0.6
	8	0.387	0.390	0.8
	18	0.585	0.589	0.7
Vertical modes	2	0.208	0.186	10.6
	3	0.178	0.195	9.5
	5	0.243	0.253	4.1
	7	0.284	0.319	12.3
	10	0.439	0.416	5.2
	15	0.526	0.476	9.5
	17	0.617	0.572	7.3
	23	0.652	0.643	1.4
	30	0.737	0.777	5.4
Torsional modes	14	0.472	0.472	0.0
	27	0.729	0.729	0.0
	38	0.982	0.981	0.1
Hybrid modes	12	0.429	0.434	1.2
	13	0.436	0.440	0.9
	29	0.734	0.781	6.4

Table 4.7 Sensitivity of natural frequencies to the deformability of rocker links

It is important to mention that some structural details have proved to be essential for accurately matching the experimentally identified natural frequencies. First of all, modeling the center tie connecting the deck to the main cables at mid-span had a strong influence on the frequency of the vertical anti-symmetric mode (mode 2 in Figure 4.5). Namely, by removing such a connecting element, the frequency of the first anti-symmetric in-plane mode varied from 0.186 Hz to 0.148 Hz, while the one of the first symmetric in-plane mode (mode 3 in Figure 4.5) varied from 0.195 Hz to 0.196 Hz. Soil-structure interaction (SSI) effects, simply modeled by means of elastic springs at the base of the tower frames, affected the frequencies of the out-of-plane modes, as evidenced in Table 4.6. The natural frequencies of the in-plane modes revealed to be strongly sensitive to the deformability of the rocker links at the boundaries. Indeed, as evidenced in Table 4.7, imposing fixed boundary

conditions to the deck in the longitudinal direction reflected in drastic changes of the frequencies of the in-plane modes.

4.5 Wind-excited response: measured vs. simulated

4.5.1 Digital simulation of wind velocity field

Turbulent wind field realizations, corresponding to wind events similar to those registered and described in Section 4.3, are digitally simulated on a grid composed by 161 nodes deployed along the deck, the towers and the cables of the NCB. In the simulation, attention is paid to reproduce the theoretical spectra described in Section 4.3 and the measured mean directions, mean velocities and turbulence intensities at mid-span. The grid for wind simulation is shown in Figure 4.7 (a).

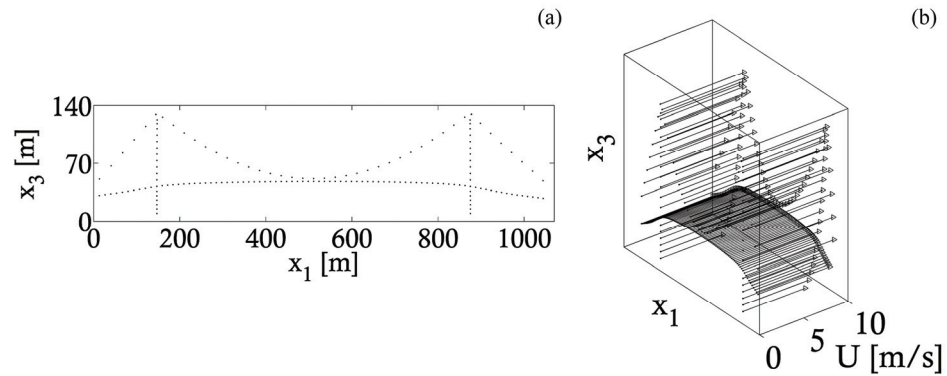


Figure 4.7 Grid for digital wind simulation (a); profile of mean velocity projected onto the transversal direction to the deck (b)

By considering all the three components of the wind velocities at each point, a 483-variate Gaussian stochastic process is obtained. The sample time $dt=0.05$ s is assumed in the wind simulation and a total of 2^{14} time and frequency steps are considered, with a cut-off circular frequency of 62.8 rad/s. For computational convenience, eigenvalues and eigenvectors (wind blowing modes) of the 483×483 spectral matrix are calculated along a sequence of 2^8

points and interpolated elsewhere as discussed in Chapter 2. No blowing modes are neglected in the wind simulation for accuracy.

To have an idea of the computational effort required by the adopted method, it can be mentioned that each digital generation of the wind velocity field, using an Intel Core 2 Duo Processor T7250, 2 GB SDRAM, required around 10 minutes for the calculation of the frequency-dependent eigenvectors and eigenvalues of the spectral matrix and around 50 s for the stochastic simulation of the wind field.

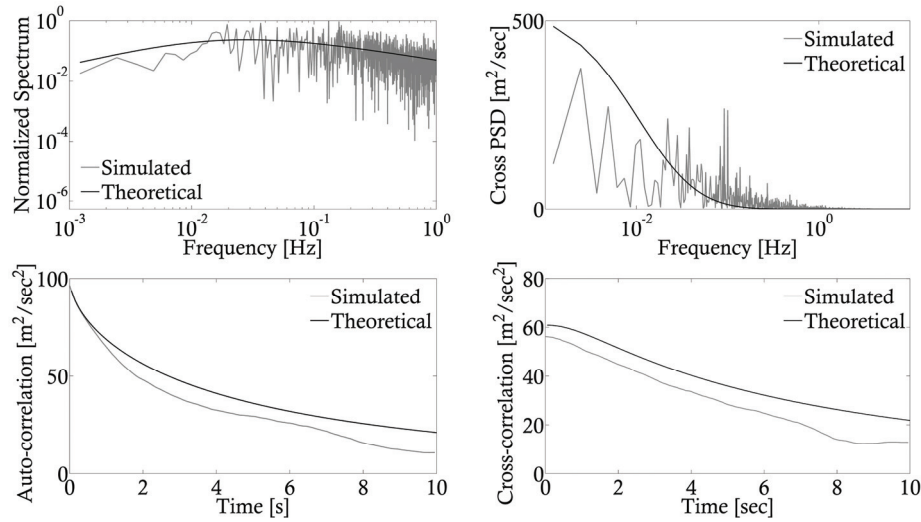


Figure 4.8 Comparison between simulated and theoretical spectra, cross-spectra, auto-correlation and cross-correlation functions

In order to discuss the quality of the performed wind simulations, the case of the wind event registered on January 4th 2008 is here considered. Indeed, among the measured wind events, the one registered on January 4th 2008 is characterized by the largest longitudinal turbulence intensity and mean velocity. Thus, it is the one for which the largest dynamic excitation on the structure is likely to be expected. According to the experimental measurements, the horizontal along-wind direction on January 4th 2008 had an inclination with respect to the transversal direction to the bridge deck of 74.2° . This corresponds

to the profile of the mean velocities projected onto the transversal direction which is reported in Figure 4.7 (b). The auto-spectrum of the along wind velocity at the bridge mid-span, the cross-spectrum between the along-wind velocities in two close nodes at mid-span and the corresponding auto- and cross-correlation functions are reported in Figure 4.8 and compared to the objective functions. The auto-spectrum is normalized by multiplying the power spectral density (PSD) amplitude by the frequency and dividing it by the variance of the turbulent velocity. The presented results emphasize the capability of the method to preserve the frequency content and the level of correlation of the turbulent velocities.

Figure 4.9 shows the frequency variation of the first three along-wind and the first three across-wind vertical eigenvalues (normalized by multiplication by the frequency) and the corresponding eigenvectors calculated for a frequency of 0.1 Hz. The eigenvalues denote the energy that is associated to each blowing mode, while the similarity between the blowing modes and the structural mode shapes govern the energy that is transferred by the wind to the structure.

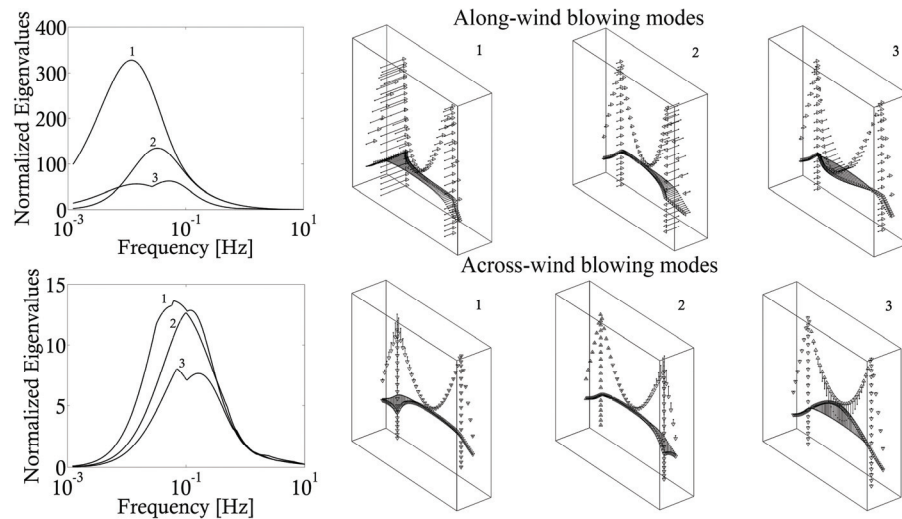


Figure 4.9 First three along-wind and across-wind vertical normalized eigenvalues and corresponding blowing modes

4.5.2 Buffeting response analysis

The nonlinear response of the bridge to turbulent wind excitation is evaluated by using the quasi steady (QS) representation of aerodynamic loads (Ding et al. 2000) which accounts for effective wind angle of attack, relative velocities between the structure and the airflow and makes use of steady aerodynamic coefficients. As it is well-known, the quasi steady theory belongs to the so-called “Aeroelastic Theories” (Petrini et al. 2007). This means that the wind loads depend on the structural response, i.e. the equations of motion contain self-excited terms.

The aerodynamic coefficients of the deck of the New Carquinez Bridge were determined from wind tunnel experimental tests in reference (Ragget 1998). The drag, lift and moment aerodynamic coefficients are represented in Figure 4.10 as functions of the effective wind angle of attack. As emphasized by the results shown in Figure 4.10, lift and moment coefficients are well approximated by straight lines and thus, as customary in buffeting analysis, the variability with the effective wind angle of attack is here taken into account by means of a first order approximation (by using the so called “aerodynamic derivatives” evaluated for a nil angle of attack). On the contrary, assuming a first order regression line for the drag coefficient would lead to quite erroneous results. For this reason, the drag coefficient is approximated through a fourth order regression line evaluated via least square approximation. It is worth mentioning that the calculated regression line and the experimental data have a statistical correlation factor equal to 0.98.

Using the realizations of the digitally simulated stochastic wind field and the updated FE model of the structure, nonlinear transient buffeting analyses are performed to evaluate the wind-excited responses of the bridge. The equations of motion are integrated in time by means of the classic Newmark method performing Newton Raphson iterations at any integration step. A maximum integration time step of 0.05 s is assumed in the simulations for a total duration of 10 min. Buffeting loads are applied to the deck, the towers and the cables. According to (Ragget, 1998) the drag coefficient of the tower frames is assumed to be equal to 1.3 while the one of the main cables is assumed to be equal to 0.8

(Cluni et al. 2007). Each simulation was completed in about six hours using an Intel Core 2 Duo Processor T7250, 2 GB SDRAM.

The case of a turbulent wind field realization similar to the one measured on January 4th 2008 is here analyzed in some detail. Indeed, this wind event corresponds to the largest recorded structural responses. Figures 4.11, 4.12 and 4.13 show the comparison between measured and simulated accelerations and corresponding PSD functions, at mid- and quarter-span of the deck. It is worth noting that in the time history plots the scales of the abscissas vary at time equal to 50 sec and that the PSD amplitudes are normalized to the maximum peak values.

Although only a qualitative comparison can be made since measured and simulated wind velocities correspond to different realizations, the presented results emphasize a good agreement between measured and simulated structural responses. In particular, numeric and measured accelerations have very similar amplitudes which means that the aerodynamic forces of the numerical model are of the same order of magnitude of those existing in the real bridge. Moreover, the PSD functions of the predicted and measured accelerations exhibit peaks in correspondence of the same frequencies. This last circumstance is particularly evident in the cases of vertical and rotational accelerations. Namely, either numeric or measured vertical motions of the deck are mainly composed by the first two symmetric vertical modes, while the rotational accelerations essentially correspond to the excitation of the first and second torsional modes. In the case of the transversal accelerations, the records of the data set registered on January 4th 2008 evidence that the second and the third modes participate to the motion along with the first one. Numeric predictions confirm the presence of the leading component corresponding to the first out-of-plane mode, with a smaller participation of the higher modes. This circumstance could be related to a difference between the simulated wind field and the real one. Indeed, as it is commented below, this difference is almost unnoticeable when considering different wind events.

Table 4.8 summarizes the high order statistics of the mid-span and quarter-span bridge responses for the case of January 4th 2008. The presented results

emphasize that either the numerical or the measured structural responses approximately follow the Gaussian distribution (skewness and kurtosis are close to 0 and 3, respectively). As an example, the histograms of the predicted and measured vertical accelerations at mid- and quarter-span for the case of January 4th 2008 are shown in Figure 4.14.

It is worth noting that the agreement between numerical predictions and field measurements is confirmed also for the other measurement sets. For example, the case of February 23rd 2008 is briefly analyzed in Figure 4.15 where the PSD amplitudes of simulated and measured mid-span responses are compared. Also for this case a good agreement is achieved between the two responses which approximately share the same frequency components. It is also worth noting that, in this case, both measured and simulated transversal accelerations almost exhibit a single component corresponding to the first transversal mode.

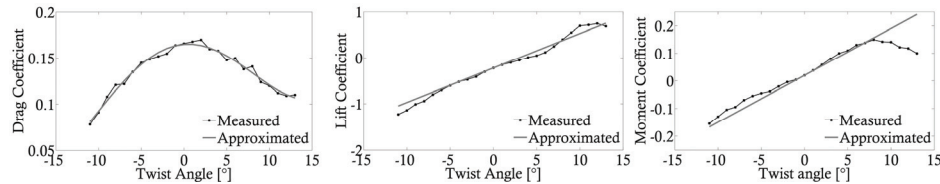


Figure 4.10 Steady aerodynamic coefficients of the deck of the NCB (Scanlan and Jones, 1998; Ragget, 1998)

Item	Mid-span	Vertical	Transverse	Rotation
Kurtosis	Measured response	3.441	3.755	3.394
	Simulated response	3.536	3.017	3.807
Skewness	Measured response	0.035	-0.522	0.003
	Simulated response	-0.052	-0.058	0.080
Item	Quarter-span	Vertical	Transverse	Rotation
Kurtosis	Measured response	2.896	3.385	3.274
	Simulated response	3.148	3.122	3.926
Skewness	Measured response	0.020	-0.142	0.024
	Simulated response	0.000	-0.009	-0.004

Table 4.8. High order statistics of simulated and measured bridge responses

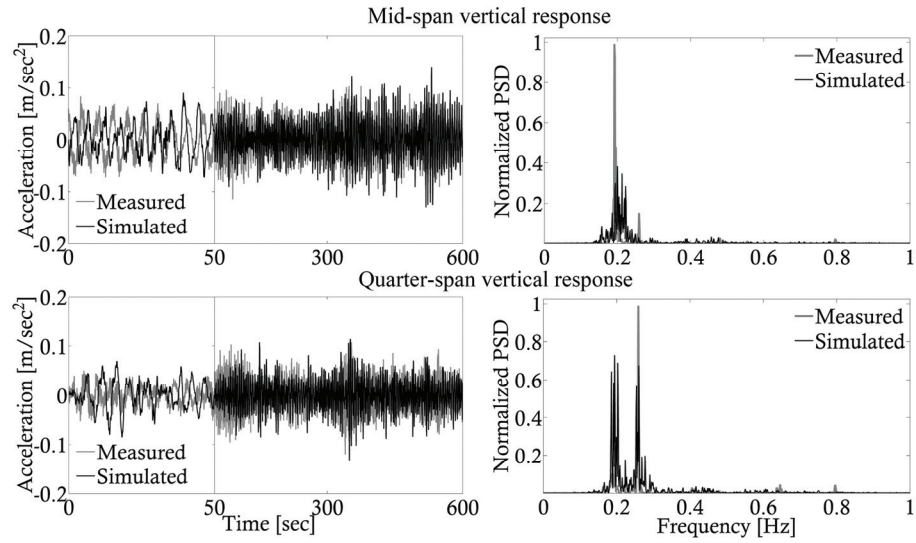


Figure 4.11 Comparison between simulated and measured mid- and quarter-span vertical responses (4th-Jan-2008 case)

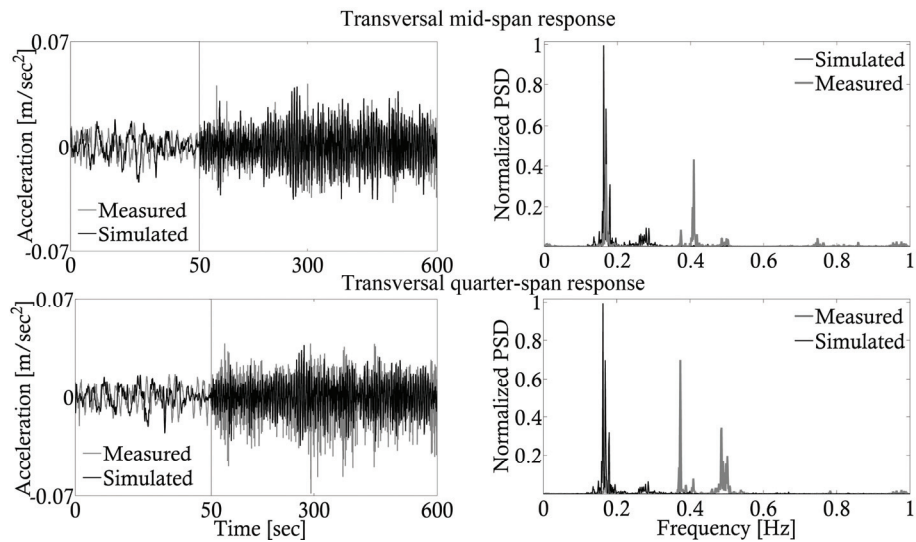


Figure 4.12 Comparison between simulated and measured mid- and quarter-span transversal responses (4th-January-2008 case)

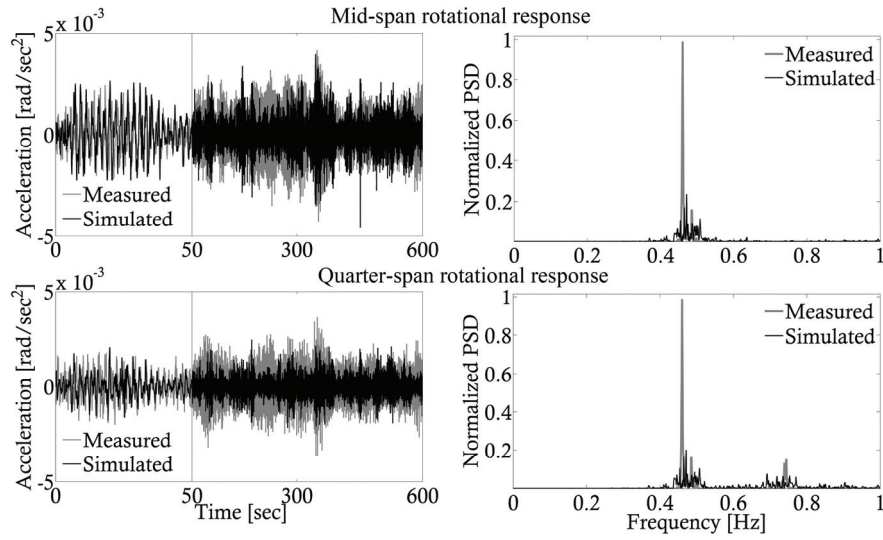


Figure 4.13 Comparison between simulated and measured mid- and quarter-span rotational responses (4th-January-2008 case)

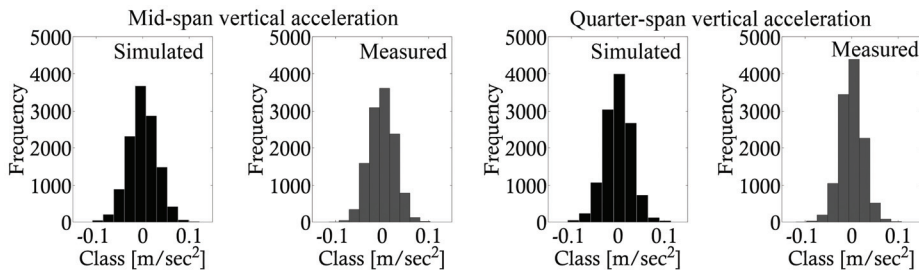


Figure 4.14 Comparison between histograms of simulated and measured vertical accelerations at mid- and quarter-span (4th-January-2008 case)

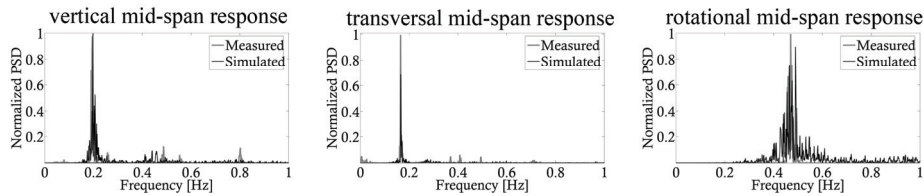


Figure 4.15 Comparison between simulated and measured mid-span responses (23rd-Feb-2008 case)

The presented results outline that the numerical procedure, updated with the aid of the field measurements, furnishes realistic predictions of the dynamic behavior of the bridge under wind action. The validated numerical model can then be employed for evaluating the operability of the bridge under different wind conditions, for safety evaluations and so on.

4.6 Concluding remarks

A numerical procedure for computing the buffeting response of bridges accounting for structural monitoring data, is outlined. A case study, represented by a newly built suspension bridge, is chosen to test the reliability of the adopted computational scheme.

The SSI/data technique was implemented elsewhere and the identified modal parameters of the NCB are adopted to update a numerical FE model of the structure. To this end, a first order optimization technique is utilized to minimize the difference between identified and calculated modal frequencies. The adopted optimization strategy reveals to be simple and effective for the case study, thus guaranteeing a significant reduction of the cost function after a few iterations.

Some natural frequencies calculated by means of the numerical FE model have exhibited a high sensitivity with respect to modeling details. Indeed, soil-piles deformability at the bottom of the tower legs have a strong influence on the frequencies of the out-of-plane modes, while in-plane ones are sensibly affected by the boundary conditions of the deck.

The stochastic characteristics of the available wind velocity measurements confirm that the assumption of a Gaussian wind can be accepted with a good level of approximation. The power spectral density functions of the measurements also emphasize a good agreement with a theoretical representation of wind spectra taken from the literature. These circumstances allow an efficient computational technique, recently proposed in the literature, to be adopted for digital wind generation purposes.

As a final result, validating to some extent the proposed computational framework, simulated and measured buffeting responses of the bridge are

compared. The results emphasize a good agreement in both time and frequency domains between the computed response and the field measurements. Moreover, predicted and measured responses exhibit similar stochastic characteristics, approximately corresponding to the Gaussian distribution.

Acknowledgements

The results presented in this chapter have been obtained during the research period spent by the author at the Department of Civil Engineering and Engineering Mechanics at Columbia University, New York, under the supervision of Prof. Raimondo Betti and in collaboration with Dr. Ahlum Hong.

The author would like to gratefully thank Prof. Raimondo Betti for inviting him as a visitor at Columbia University, for enthusiastically supervising this research and for providing all the essential measurement data which were necessary to complete this study.

The author would also like to acknowledge the fruitful collaboration with Dr. Ahlum Hong for sharing the results concerning the structural identification of the New Carquinez Bridge and for her kind co-operation.

The author wishes to thank Mr. Dyab A. Khazem from Parsons Transportation Group for providing all the structural information, including drawings and reports, about the New Carquinez Bridge.

Chapter 5

TIME DOMAIN AEROELASTIC STABILITY ANALYSIS OF BRIDGES

Abstract

The time domain aeroelastic stability analysis of bridges is studied using both low-dimensional and large dimensional models. Within this framework, it is shown how the time domain formulation using indicial functions allows to transform the aeroelastic stability analysis in the form of a simple direct eigenvalue problem. This approach is tested with reference to a case study by comparison with the classic frequency domain formulation based on aeroelastic derivatives.

5.1 Introduction

The steadily growing demand for lighter and more economical designs of long-span bridges, is enhancing today the risk of fluid structure interactions leading to aeroelastic instabilities (Bontempi and Malerba, 1994; Bontempi et al., 2000). Although technically tightening, a comprehensive understanding of this problem is still lacking and there has not yet been established a unique theoretical nor an experimental framework to predict the critic condition.

Self-excited wind loads on bridge deck sections are commonly predicted by identifying sets of frequency-dependent flutter derivatives, through wind tunnel tests conducted on cross-sectional models of the bridge deck. The major shortcoming of this approach is that a large data scattering is often encountered in wind tunnel experiments, since non-structural details may change significantly the aerodynamics of the deck. Thus, many experiments are required to determine the critical wind speed with a reasonable level of confidence. Computational fluid dynamics (CFD) is an alternative strategy to investigate, numerically, the aeroelastic behavior of bridge deck sections (Cavagna et al., 2005). However, CFD will unlikely replace wind tunnel testing in the next future, although it will surely play a role in modern bridge design.

The critic flutter condition is a Hopf bifurcation that can be predicted analytically or numerically, using either bi-dimensional deck models or more costly tridimensional finite element (FE) numerical schemes. Both frequency domain (Simiu and Scanlan, 1996) and time domain (Caracoglia and Jones, 2003; Lazzari et al., 2004) methods can be adopted for this purpose. In the frequency domain, the most accurate method is the so-called multi-modal approach, where some selected modes of the structure can contribute to the bridge response and to the flutter critical mode. Unfortunately, frequency domain approaches rely on a linear structural behavior and cannot easily handle the presence of non-classical damping devices and atmospheric turbulence. An alternative strategy, which overcomes these drawbacks, is to operate in the time domain. To this end, aeroelastic forces are introduced in the equations of motion, using time-domain formulations which are the counterparts of the flutter derivatives. Within this framework two classic strategies are usually adopted: the theory of aeroelastic derivatives in the time domain and the formulation based on indicial functions. The former has been presented in Chapter 3, while the latter is mainly considered within this chapter.

5.2 Governing relations

The most intuitive and physically relevant model which can be adopted for aerodynamic assessments in bridge design is represented by the so-called “deck

model". This model simply considers the two degrees-of-freedom (dofs) linear dynamics of the bridge cross section. Although very simple, sectional models are those for which wind tunnel experimental results are determined and thus, in principle, the most consistent with the classic quasi-steady and unsteady formulations presented in Chapter 3.

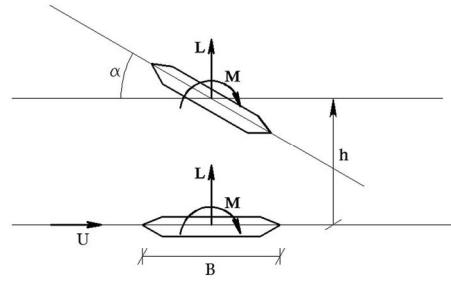


Figure 5.1. Two-dofs aeroelastic deck model

The motion of a rigid unit-length deck portion of the bridge is considered (see Figure 5.1). Consistently with the definitions given in Chapter 3 of the aeroelastic lift L and pitching moment M , h denotes the vertical degree of freedom (heaving) and α denotes the rotation (twist angle). Consequently, if m is the translational mass and I is the mass inertial momentum of the unit-length deck portion, the equations of motion of this simple mechanical system read as:

$$\begin{aligned} m\ddot{h} + c_h\dot{h} + k_h h &= L \\ I\ddot{\alpha} + c_\alpha\dot{\alpha} + k_\alpha \alpha &= M \end{aligned} \quad (5.2.1)$$

where c_h and c_α are viscous damping coefficients, while k_h and k_α are the elastic stiffness coefficients. It is worth noting that, without loss of generality, Equations (5.2.1) are written under the assumption that the center of mass and the elastic center are coincident.

5.2.1 Frequency domain approach using aeroelastic derivatives

A widely adopted method to determine the critical velocity for the onset of the flutter instability of a deck section, is to represent the lift and moment

linearly in the generalized displacements and velocities $h, \dot{h}, \alpha, \dot{\alpha}$. The relevant non-dimensional coefficients appearing in the expressions of the self-excited loads are called “aeroelastic derivatives” (Simiu and Scanlan, 1996). These last are functions of the frequency of the motion (which is presumed to be harmonic) and can be evaluated either analytically, by assuming the flat plate analogy, or experimentally. The self-excited lift and pitching moment can thus be expressed as (Simiu and Scanlan, 1996):

$$\begin{aligned} L &= \frac{1}{2} \rho U^2 B \left(KH_1^* \frac{\dot{h}}{U} + KH_2^* \frac{B \dot{\alpha}}{U} + K^2 H_3^* \alpha + K^2 H_4^* \frac{h}{B} \right) \\ M &= \frac{1}{2} \rho U^2 B^2 \left(KA_1^* \frac{\dot{h}}{U} + KA_2^* \frac{B \dot{\alpha}}{U} + K^2 A_3^* \alpha + K^2 A_4^* \frac{h}{B} \right) \end{aligned} \quad (5.2.2)$$

In order to solve the critic flutter condition (Hopf bifurcation), it is convenient to rewrite the equations of motion (5.2.1) in the following form:

$$\begin{aligned} m(\ddot{h} + 2\xi_h \omega_h \dot{h} + \omega_h^2 h) &= L \\ I(\ddot{\alpha} + 2\xi_\alpha \omega_\alpha \dot{\alpha} + \omega_\alpha^2 \alpha) &= M \end{aligned} \quad (5.2.3)$$

where ξ_h, ξ_α are damping ratios and ω_h, ω_α are the natural circular frequencies of the bending and twist motions, respectively. By substituting Equations (5.2.2) into Equations (5.2.3) one gets the classic Flutter Equations (Simiu and Scanlan, 1996). A harmonic solution to the Flutter problem is sought in the form:

$$\begin{aligned} h(t) &= h_0 e^{i\omega t} = h_0 e^{iKs} \\ \alpha(t) &= \alpha_0 e^{i\omega t} = \alpha_0 e^{iKs} \end{aligned} \quad (5.2.4)$$

where ω is the complex circular frequency of the motion, which, by definition of reduced frequency K , is equal to UK/B and $s=Ut/B$ is a convenient non-dimensional time. By substituting Equations (5.2.4) into the Flutter equations and by imposing that the system admits a nontrivial solution, one gets the following eigenvalue problem:

$$\begin{bmatrix} A(K) & B(K) \\ C(K) & D(K) \end{bmatrix} \begin{bmatrix} h_0/B \\ \alpha_0 \end{bmatrix} = \begin{bmatrix} 0 \\ 0 \end{bmatrix} \quad (5.2.5a)$$

$$\begin{aligned}
A(K) &= -K^2 + 2i\xi_h K_h K + K_h^2 - \frac{\rho B^2}{m} iK^2 H_1^* \\
B(K) &= -\frac{\rho B^2}{m} iK^2 H_2^* - \frac{\rho B^2}{m} K^2 H_3^* \\
C(K) &= -\frac{\rho B^4}{I} iK^2 A_1^* \\
D(K) &= -K^2 + 2i\xi_\alpha K_\alpha K + K_\alpha^2 - \frac{\rho B^4}{I} iK^2 A_2^* - \frac{\rho B^4}{I} iK^2 A_3^*
\end{aligned} \tag{5.2.5b}$$

where $K_h = B\omega_h/U$ and $K_\alpha = B\omega_\alpha/U$. Equations (5.2.5) were found in reference (Simiu and Scanlan, 1996) by neglecting the contributions of H_4^* and A_4^* . Nevertheless, the derivation of analogous expressions in which H_4^* and A_4^* are also retained is straightforward. The problem of finding the critical eigenvalue K_{crit} , stated in Equation (5.2.5), is implicit in the sense that the aeroelastic derivatives depend on the solution K_{crit} . Thus an iterative procedure is necessary to solve equations (5.2.5).

The iterative procedure to find the critic eigenvalue K_{crit} converges when K is equal to one of the calculated four roots of the characteristic equation. The reduced frequency K is taken therefore to be a complex number of the form $K = K_r + iK_i$, whose real part K_r denotes the frequency of the motion while the sign of the imaginary one dictates if the motion is growing ($K_i > 0$) or decaying ($K_i < 0$). The condition $K_i = 0$ identifies a Hopf bifurcation point (two complex conjugate eigenvalues cross the imaginary axis) which represents the critic flutter condition ($K = K_{crit}$) and the velocity U_{crit} , at which this condition is satisfied, is identified as the critic flutter velocity. It is worth noting that when the critic eigenvalue comes into the form (0,0) a steady state bifurcation occurs which usually corresponds to a torsional divergence.

A convenient strategy to find the pair (U_{crit}, K_{crit}) is reported in reference (Simiu and Scanlan, 1996). Following such an approach, the determinant of the matrix operator defined in Equation (5.2.5) is forced to be zero, which results in a complex polynomial characteristic quartic equation. By defining the unknown $X = \omega/\omega_h$ and assuming that X is real at the flutter condition, the following two

equations are obtained (the former for the real part and the latter for the imaginary part):

$$X^4 \left(1 + \frac{\rho B^4}{I} A_3^* - \frac{\rho B^2}{m} \frac{\rho B^4}{I} (A_2^* H_1^* + A_1^* H_2^*) \right) + X^3 \left(2\xi_\alpha \frac{\omega_\alpha}{\omega_h} \frac{\rho B^2}{m} H_1^* + 2\xi_h \frac{\rho B^4}{I} A_2^* \right) + \quad (5.2.6a)$$

$$X^2 \left(-\frac{\omega_\alpha^2}{\omega_h^2} - 4\xi_h \xi_\alpha \frac{\omega_\alpha}{\omega_h} - 1 - \frac{\rho B^4}{I} A_3^* \right) + \frac{\omega_\alpha^2}{\omega_h^2} = 0$$

$$X^3 \left(\frac{\rho B^4}{I} A_2^* + \frac{\rho B^2}{m} H_1^* + \frac{\rho B^2}{m} \frac{\rho B^4}{I} (A_3^* H_1^* - A_1^* H_3^*) \right) + X^2 \left(-2\xi_\alpha \frac{\omega_\alpha}{\omega_h} - 2\xi_h - 2\xi_h \frac{\rho B^4}{I} A_3^* \right) + \quad (5.2.6b)$$

$$X \left(-\frac{\rho B^2}{m} H_1^* \frac{\omega_\alpha^2}{\omega_h^2} - \frac{\rho B^4}{I} A_2^* \right) + \left(2\xi_h \frac{\omega_\alpha^2}{\omega_h^2} + 2\xi_\alpha \frac{\omega_\alpha}{\omega_h} \right) = 0$$

The two real equations (5.2.6a) and (5.2.6b) are solved for different values of K and their roots are plotted vs. K . At the point (X_{crit}, K_{crit}) , where the two plots cross (with $X_{crit} > 0$), the flutter condition is identified.

5.2.2 Time domain approach using indicial functions

Time domain formulations of aeroelastic forces have a wider application with respect to classic frequency domain methods (Caracoglia and Jones, 2003; Lazzari et al., 2004). However, well-established experimental techniques currently exist only for the determination of the aeroelastic derivatives. Thus, time-domain counterparts of aeroelastic derivatives must be found, utilizing optimization schemes that introduce in the system a degree of approximation.

The most effective and up-to-date method to express aeroelastic forces for bridge deck sections in the time domain, is probably represented by the load model for self-excited forces via indicial functions (Salvatori and Borri, 2007). This model seems promising in the sense that it was formulated directly in the

time domain (Bisplinghoff et al. 1955), for the thin airfoil, and it allows direct experimental assessments (Caracoglia and Jones, 2003).

Wagner's function, in thin airfoil Theory, can be considered as the first indicial function (Costa and Borri, 2006). A common approximation of Wagner's function is due to Jones (1940), as the sum of exponential functions, suitable for Fourier-transforming (Costa, 2007). More general functions were proposed by Bisplinghoff et al. (1955), for describing aerodynamic moment and distinguishing the effects of the different components of the motion on self-excited loads. The extension to bluff cross-sections of the formulation developed theoretically for the thin airfoil is due to Scanlan et al. (1974) and it is based on the exponential approximation of Wagner's function.

The indicial functions represent the time evolutions of the wind loads caused by generalized unit displacements. Thus, the self excited loads are calculated through convolution integrals between indicial functions and generalized displacements, namely:

$$L = \frac{1}{2} \rho U^2 B C'_L \left(\Phi_{Lh}(0) \frac{\dot{h}}{U} + \Phi_{L\alpha}(0) \alpha + \int_0^t \dot{\Phi}_{Lh}(t-\tau) \frac{\dot{h}(\tau)}{U} d\tau + \int_0^t \dot{\Phi}_{L\alpha}(t-\tau) \alpha(\tau) d\tau \right) \quad (5.2.7a)$$

$$M = \frac{1}{2} \rho U^2 B^2 C'_M \left(\Phi_{Mh}(0) \frac{\dot{h}}{U} + \Phi_{M\alpha}(0) \alpha + \int_0^t \dot{\Phi}_{Mh}(t-\tau) \frac{\dot{h}(\tau)}{U} d\tau + \int_0^t \dot{\Phi}_{M\alpha}(t-\tau) \alpha(\tau) d\tau \right) \quad (5.2.7b)$$

As customary in aeroelasticity (Salvatori and Borri, 2007) the following approximation of the indicial functions via exponential filters is adopted:

$$\Phi_{hk}(t) = 1 - \sum_{i=1}^{N_{hk}} a_i^{hk} \exp\left(-b_i^{hk} \frac{2U}{B} t\right) \quad (5.2.8)$$

The dimensionless parameters a_i^{hk} and b_i^{hk} ($h=L, M$, $k=h, \alpha$) appearing in Equation (5.2.8) must be identified by matching the measured aeroelastic derivatives in the frequency domain. To this end, an optimization strategy can

be performed, in which the number of exponential groups N_{hk} accounts for the desired level of accuracy. In the optimization phase, the following equivalence between aeroelastic derivatives and coefficients of indicial functions must be exploited (Costa and Borri, 2006):

$$H_1^* = \frac{1}{K} C'_L \left(1 - \sum_{i=1}^{N_{Lh}} a_i^{Lh} \frac{K^2}{b_i^{Lh^2} 4 + K^2} \right) \quad (5.2.9a)$$

$$H_4^* = \frac{2}{K^2} C'_L \left(\sum_{i=1}^{N_{Lh}} a_i^{Lh} b_i^{Lh} \frac{K^2}{b_i^{Lh^2} 4 + K^2} \right)$$

$$H_2^* = -\frac{2}{K^3} C'_L \left(\sum_{i=1}^{N_{Lh}} a_i^{L\alpha} b_i^{L\alpha} \frac{K^2}{b_i^{L\alpha^2} 4 + K^2} \right) \quad (5.2.9b)$$

$$H_3^* = \frac{1}{K^2} C'_L \left(1 - \sum_{i=1}^{N_{L\alpha}} a_i^{L\alpha} \frac{K^2}{b_i^{L\alpha^2} 4 + K^2} \right)$$

$$A_1^* = \frac{1}{K} C'_M \left(1 - \sum_{i=1}^{N_{Lh}} a_i^{Mh} \frac{K^2}{b_i^{Mh^2} 4 + K^2} \right) \quad (5.2.9c)$$

$$A_4^* = \frac{2}{K^2} C'_M \left(\sum_{i=1}^{N_{Lh}} a_i^{Mh} b_i^{Mh} \frac{K^2}{b_i^{Mh^2} 4 + K^2} \right)$$

$$A_2^* = -\frac{2}{K^3} C'_M \left(\sum_{i=1}^{N_{Lh}} a_i^{M\alpha} b_i^{M\alpha} \frac{K^2}{b_i^{M\alpha^2} 4 + K^2} \right) \quad (5.2.9d)$$

$$A_3^* = \frac{1}{K^2} C'_M \left(1 - \sum_{i=1}^{N_{L\alpha}} a_i^{M\alpha} \frac{K^2}{b_i^{M\alpha^2} 4 + K^2} \right)$$

Looking at Equations (5.2.9), the parameters a_i^{hk} and b_i^{hk} ($h=L, M, k=h, \alpha$) must be identified by fitting, at each turn, two aeroelastic derivatives simultaneously. In order to do so, one must minimize a suitable cost function E^{Lh} such as, for instance, the one proposed by Costa and Borri (2007):

$$E^{Lh} = \left\| \tilde{H}_1^* - H_1^* \right\| + \left\| \tilde{H}_4^* - H_4^* \right\| \quad (5.2.10)$$

where \tilde{H}_i^* denote the identified aeroelastic derivatives calculated by means of Equations (5.2.9). Analogous expressions can be derived for the cost functions of the remaining pairs of aeroelastic derivatives.

5.3 Time domain aeroelastic stability analysis via direct eigenvalue problem

The representation of self-excited wind loads through Equations (5.2.7) and (5.2.8) is particularly useful since it allows to express the dynamics of the system without using integral terms which are difficult to handle in practical applications. This results to be trivial for the thin airfoil using Wagner's function (Coller and Chamara, 2004). A similar procedure to the one described in reference (Coller and Chamara, 2004) can be also applied to general bluff deck sections as described below.

Similarly to what was done in reference (Lee et al., 1997), the following additional variables can be introduced:

$$\begin{aligned} w_i^{Lh} &= \int_0^t \frac{b_i^{Lh} a_i^{Lh}}{b} \exp\left(-b_i^{Lh} \frac{U}{b} (t-\tau)\right) \dot{h}(\tau) d\tau \\ w_i^{L\alpha} &= \int_0^t \frac{b_i^{L\alpha} a_i^{L\alpha} U}{b} \exp\left(-b_i^{L\alpha} \frac{U}{b} (t-\tau)\right) \alpha(\tau) d\tau \\ w_i^{Mh} &= \int_0^t \frac{b_i^{Mh} a_i^{Mh}}{b} \exp\left(-b_i^{Mh} \frac{U}{b} (t-\tau)\right) \dot{h}(\tau) d\tau \\ w_i^{M\alpha} &= \int_0^t \frac{b_i^{M\alpha} a_i^{M\alpha} U}{b} \exp\left(-b_i^{M\alpha} \frac{U}{b} (t-\tau)\right) \alpha(\tau) d\tau \end{aligned} \quad (5.3.1)$$

In the case, for instance, in which one single exponential group is considered for each indicial functions, four additional variables are defined as:

$$w_1 = w_1^{Lh} \quad w_2 = w_1^{L\alpha} \quad w_3 = w_1^{Mh} \quad w_4 = w_1^{M\alpha} \quad (5.3.2)$$

By substituting Equations (5.3.2) into Equations (5.3.1) it results:

$$\dot{w}_1 = \frac{b_1^{Lh} a_1^{Lh}}{b} \dot{h}(\tau) - w_1 \quad (5.3.4)$$

With the positions stated above, the equations of motion can be rewritten as:

$$m(\ddot{h} + 2\xi_h \omega_h \dot{h} + \omega_h^2 h) = \frac{1}{2} \rho U^2 B C'_L \left((1 - a_1^{Lh}) \frac{\dot{h}}{U} + (1 - a_1^{L\alpha}) \alpha + w_1 + w_2 \right) \quad (5.3.4a)$$

$$I(\ddot{\alpha} + 2\xi_\alpha \omega_\alpha \dot{\alpha} + \omega_\alpha^2 \alpha) = \frac{1}{2} \rho U^2 B^2 C'_M \left((1 - a_1^{Mh}) \frac{\dot{h}}{U} + (1 - a_1^{M\alpha}) \alpha + w_3 + w_4 \right) \quad (5.3.4b)$$

$$\dot{w}_1 = \frac{b_1^{Lh} a_1^{Lh}}{b} \dot{h}(\tau) - w_1 \quad (5.3.4c)$$

$$\dot{w}_2 = \frac{b_1^{L\alpha} a_1^{L\alpha} U}{b} \alpha(\tau) - w_2$$

$$\dot{w}_3 = \frac{b_1^{Mh} a_1^{Mh}}{b} \dot{h}(\tau) - w_3 \quad (5.3.4d)$$

$$\dot{w}_4 = \frac{b_1^{M\alpha} a_1^{M\alpha} U}{b} \alpha(\tau) - w_4$$

Equations (5.3.4) assume the form of a linear first-order autonomous system of the form:

$$\dot{x} = A(U)x \quad (5.3.5)$$

where A is a real $n \times n$ matrix, U represents the control parameter and the eight-dimensional state vector x is defined as:

$$x = (h, \dot{h}, \alpha, \dot{\alpha}, w_1, w_2, w_3, w_4)^T \quad (5.3.6)$$

Clearly, the above described approach allows also to include nonlinearities in the system. In such a case, discussed in detail in Chapter 6, the equations of motion (5.3.5) are generalized as:

$$\dot{x} = f(x, U) \quad (5.3.7)$$

where f denotes a convenient vector field.

A first glance to equations (5.3.5) and (5.3.7) reveals that considering a general bluff section reflects on a larger dimensional system of ordinary differential equations with respect to the airfoil case. Namely, the dimension of the first order form of the flutter problem grows as the number of exponential filters adopted to approximate the indicial functions. Namely, each exponential filter produces an additional first order equation and the minimal number of state variables to describe the flutter problem is equal to 8.

In order to investigate the linear stability of an equilibrium point, a local linearization of Equation (5.3.7) in the form of Equation (5.3.5) must be sought. This reflects on a non-symmetric real matrix operator A whose eigenvalues judge on the stability of the chosen point. Two different formulations can be stated for the problem of finding eigenvalues of a non-symmetric real matrix: finding vectors x such that $Ax = \lambda x$, and finding vectors y such that $y^H A = \lambda y^H$ (y^H implies a complex conjugate transposition of y). Vector x denotes a right eigenvector, while vector y denotes a left eigenvector. Both x and y correspond to the same eigenvalue λ . Differently from the symmetric problem, the eigenvalues of a non-symmetric matrix do not form an orthogonal system and might also not form a linear-independent vector system (this may happen in case of multiple eigenvalues, where a subspace with size strictly less than k can correspond to the eigenvalue with multiplicity k). Moreover, the eigenvalues and the eigenvectors of a non-symmetric matrix could be complex even though the matrix operator is real. In this case, complex eigenvalues always come in conjugate pairs (Mailybaev et al., 2005).

5.4 Time domain vs. frequency domain aeroelastic stability analysis of bridge decks: a case study

The above described formulations are adopted to evaluate the critic flutter condition for the two-dofs deck model of the Tsing Ma Bridge (see Appendix A). For generality purposes, the flat plate analogy is assumed as a benchmark, which means that the aeroelastic derivatives of the thin airfoil are adopted in the analysis. In thin airfoil theory, the aeroelastic derivatives can be evaluated analytically as functions of the real and imaginary parts of Theodorsen's

function, introduced in Section 3.2. Particularly, the following theoretical relations hold:

$$\begin{aligned}
 H_1^* &= \pi F(k) / 2k \\
 H_2^* &= \pi / 8k \left(1 + F(k) + 2G(k) / k \right) \\
 H_3^* &= \pi / 4k^2 \left(F(k) - kG(k) / 2 \right) \\
 H_4^* &= \pi / 4 \left(1 + 2G(k) / k \right)
 \end{aligned}
 \tag{5.4.1a}$$

$$\begin{aligned}
 A_1^* &= \pi F(k) / 8k \\
 A_2^* &= -\pi / 32k \left(1 - F(k) - 2G(k) / k \right) \\
 A_3^* &= \pi / 16k^2 \left(F(k) - kG(k) / 2 \right) \\
 A_4^* &= -\pi / 8 G(k) / k
 \end{aligned}
 \tag{5.4.1b}$$

where $k=K/2$.

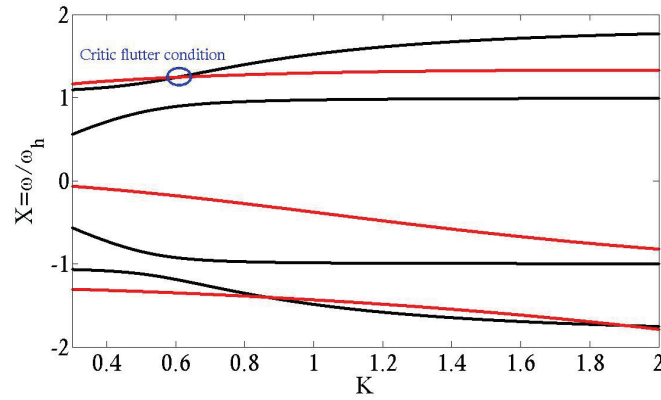


Figure 5.2. Bi-dimensional analysis in the frequency domain: graphic determination of the critic solution (K_{crit} , X_{crit})

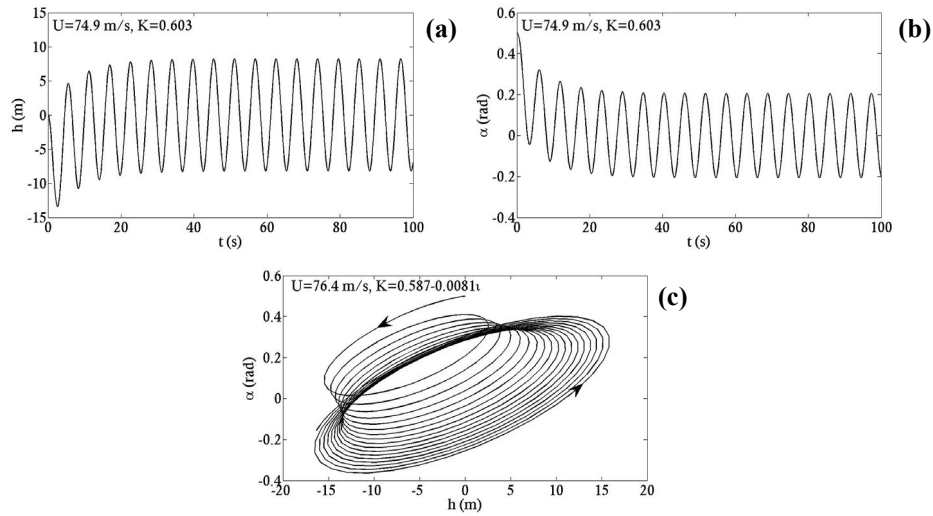


Figure 5.3. Bi-dimensional analysis in the frequency domain: time histories of heave and rotation at criticality (a, b); phase plane projection of unstable harmonic orbit at post-criticality (c)

B (m)	ω_h (rad/s)	ω_α (rad/s)	m (kg)	I ($\text{kg}\cdot\text{m}^2$)	ζ_h	ζ_α
41	0.8859	1.6588	27778	$2.5\cdot 10^6$	0.0222	0.0384

Table 5.1. Unit-length (1 m) deck model of the Tsing Ma bridge

The characteristics of the unit-length deck model of the Tsing Ma Bridge are summarized in Table 5.1. The graphic solution of Equations (5.2.6) is reported in Figure 5.2, where the black lines denote the roots of Equation (5.2.6a), while red lines denote the roots of Equation (5.2.6b). As evidenced in such a figure, the critic flutter condition is identified as the point at which two plots cross, with the physical constraint $X > 0$. The following solution is thus obtained:

Frequency domain approach (H_4^* and A_4^* neglected)

- $K_{crit} = 0.603$
- $X_{crit} = 1.245$
- $\omega_{crit} = X_{crit} \cdot \omega_h = 1.103 \text{ rad/s}$
- $U_{crit} = B \cdot \omega_{crit} / K_{crit} = 74.9 \text{ m/s}$

The above presented results emphasize that the frequency ω_{crit} of the coupled flutter mode, is located, as expected, between the natural values ω_h and ω_a . The time histories of heave and rotation at the critic and postcritic flutter conditions and the phase portrait of the postcritic motion, corresponding to Equation (5.2.4) are reported in Figure 5.3. By assuming a linear structural behavior the postcritic motion is obviously unstable.

The calculation of the critic eigenvalue, by considering also the contribution of the aeroelastic derivatives H_4^* and A_4^* , in Equations (5.2.5), leads to the following solution:

Frequency domain approach (H_4^* and A_4^* considered)

$$\begin{aligned} - K_{crit} &= 0.7349 \\ - X_{crit} &= 1.2898 \\ - \omega_{crit} &= X_{crit} \cdot \omega_h = 1.143 \text{ rad/s} \\ - U_{crit} &= B \cdot \omega_{crit} / K_{crit} = 63.756 \text{ m/s} \end{aligned}$$

Thus, in the presented case, neglecting the contribution of the aeroelastic derivatives H_4^* and A_4^* means overestimating the critic flutter velocity of about 17 %.

The solution of the flutter problem applied to the case study is also sought by means of the direct eigenvalue problem stated in Section 5.3 with the aid of indicial functions. To this end, the cost function E^{Lh} defined in Equation (5.2.10) is minimized using evolutionary algorithms, which are often capable to avoid local minima. Clearly, this procedure finds its justification only when working with measured aeroelastic derivatives (indeed, for the thin airfoil, Wagner's function is already an analytic indicial function with no need of parameter fitting via optimization). However, the considered case is here assumed as a benchmark and the optimization is applied to the aeroelastic derivatives of the thin airfoil as if they were measured aeroelastic derivatives of the deck model.

Figure 5.4 shows the results of the optimization when using one, two or three exponential groups for each indicial function. As it can be noted, one

exponential group already guarantees a satisfactory approximation of the aeroelastic derivatives reported in Equations (5.4.1).

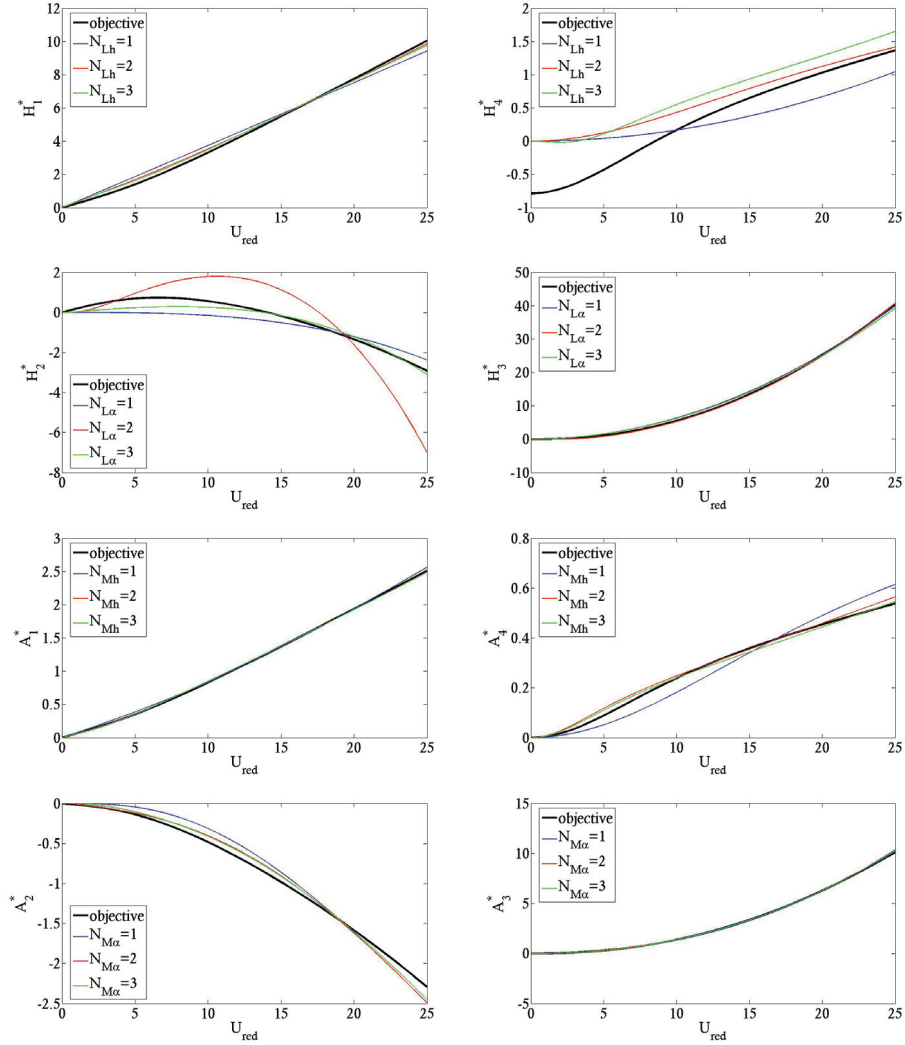


Figure 5.4. Identified aeroelastic derivatives via evolutionary algorithm using 1, 2 and 3 exponential groups

The critic condition is solved for the case study using 1, 2 and 3 exponential groups in the indicial functions. Particularly, at each time, the value U_{crit} at which matrix A (introduced in Equation (5.3.5)) exhibits a pair of complex conjugate eigenvalues with nil real parts is found. The results of the analysis are the following:

Time domain approach using indicial functions

- 1 Exponential group: $U_{crit}=66.837$ m/s $\omega_{crit}=1.373$ rad/s
- 2 Exponential groups: $U_{crit}=64.034$ m/s $\omega_{crit}=1.446$ rad/s
- 3 Exponential groups: $U_{crit}=62.122$ m/s $\omega_{crit}=1.501$ rad/s

The comparison between the results presented above and those calculated in the frequency domain ($U_{crit}=63.756$ m/s and $\omega_{crit}=1.143$ rad/s), reveals that considering more than one exponential group in the indicial functions does not necessarily entail a better approximation of the critic condition. Particularly, the case with two exponential groups results to be the most accurate in predicting the critic velocity, while the one with one single exponential group is the most accurate in predicting the circular frequency of the critic motion. However, one single exponential group is already sufficient to guarantee a very accurate approximation of both critic velocity and critic frequency of the system.

The critic condition evaluated in the time domain with one exponential group is analyzed in Figure 5.5. The figure represents the time histories of heave and rotation and the corresponding PSD functions at criticality and the root locus of the two complex conjugate pairs of eigenvalues of the structural system. The frequency content of the motion reveals that, as expected, a coupled flutter occurs with critic circular frequency ω_{crit} equal to 1.373 rad/s. The postcritic condition is analyzed in Figure 5.6 which is obviously unstable since a linear structural behavior has been presumed.

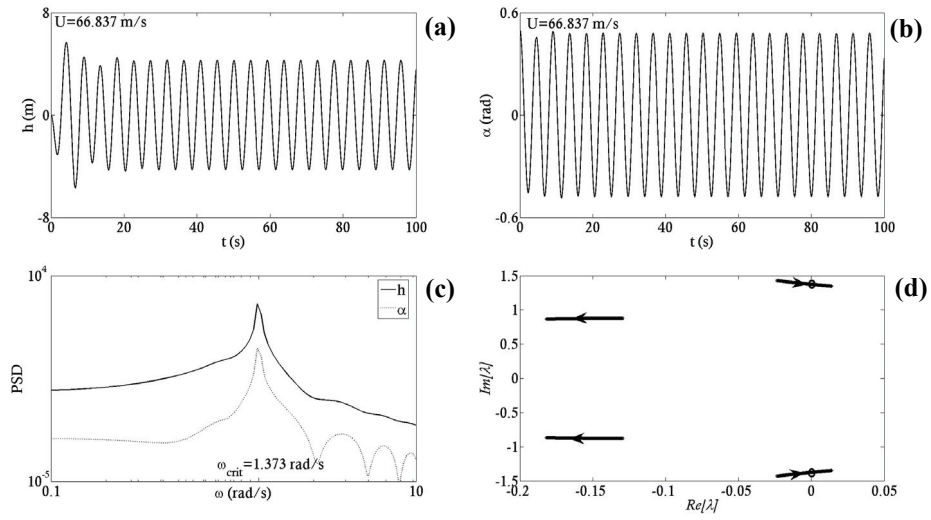


Figure 5.5. Bi-dimensional analysis using indicial functions: time histories of heave and rotation at criticality (a, b); corresponding PSD functions (c); root locus of structural eigenvalues by increasing the wind velocity (the circles indicate the Hopf bifurcation point)

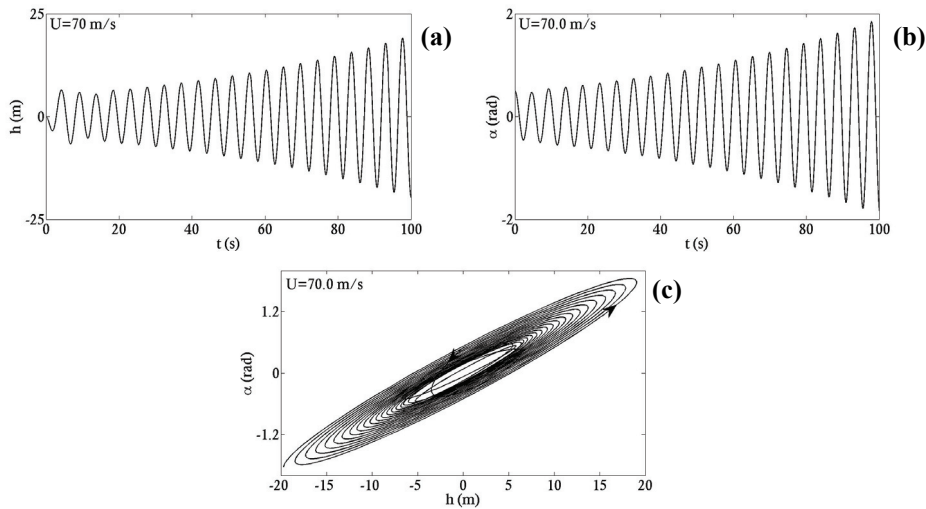


Figure 5.6. Bi-dimensional analysis using indicial functions: time histories of heave and rotation at post-criticality (a, b); phase portrait of the solution (c)

5.5 Prediction of bridge flutter using FE models

Time domain expressions of self-excited loads can also be introduced into a tridimensional FE model of the structure with the aim of analyzing the critic condition in a tridimensional framework.

By adopting the same coefficients obtained in Section 5.4 for the case with 1 exponential group in all aeroelastic derivatives, the following critic condition is detected using the spine-type FE model presented in Chapter 1:

- Time domain FE analysis using indicial functions (1 exponential group, flat plate analogy):
 $U_{crit} = 136.25 \text{ m/s}, \omega_{crit} = 1.17 \text{ rad/s}$

The above presented results cannot be compared to those obtained by means of the planar deck model. Indeed, such a model was only adopted as a benchmark to validate the time domain approach using indicial functions. However, it did not consider relevant effects such as the modal participation of the aeroelastic loads and the masses of the main cables participating to the flutter mode.

The critic solution obtained by means of the tridimensional model is analyzed in Figures 5.7, 5.8 and 5.9. In particular, Figures 5.7 and 5.8 give indications on the shape of the flutter mode, while Figure 5.9 analyzes the motion of the mid-span of the deck at criticality. Figure 5.7 shows instantaneous plots of the deformed structure, during the harmonic motion ensuing from the onset of the flutter instability, while Figure 5.8 shows the envelopes of the maximum generalized displacements at criticality. In Figure 5.7 T_0 represents a general time instant in which the mid-span vertical displacement attains a maximum, while T denotes the period of the harmonic motion. Figures 5.7 and 5.8 emphasize that the critic mode is essentially characterized by a coupling between the first symmetric vertical in-plane mode and the first symmetric torsional mode. However, a participation of the second symmetric in-plane mode is also evidenced by the fourth frame ($T_0 + 0.75T$) reported in Figure 5.7.

The results presented in Figure 5.9 confirm that the critic condition is harmonic with a circular frequency $\omega_{crit}=1.17 \text{ rad/s}$.

The spine-type FE model is finally adopted to evaluate the critic condition of the case study structure, by considering the measured aerodynamic characteristics of the deck. The analysis is conducted by adopting the formulation of aeroelastic derivatives in the time domain (ADTD), using the coefficients reported in (Ding et al., 1999) and calculated to match the aeroelastic derivatives of the Tsing Ma deck section measured in wind tunnel experiments.

The analysis has revealed that a static instability (torsional divergence) takes place before the onset of the oscillatory Hopf bifurcation. This is a consequence of the positive aerodynamic damping exhibited by the deck of the bridge in wind tunnel tests. Particularly, the following critic condition leading to a torsional divergence has been found:

- Time domain FE analysis using aeroelastic derivatives in the time domain (measured aeroelastic derivatives):
 $U_{crit}=149.7 \text{ m/s}$

Since torsional divergence is a static instability (a purely real eigenvalue crosses the imaginary axis) one expects that it can be correctly predicted by adopting the quasi-steady representation of the aerodynamic forces. In this case, the following formula can be given:

$$U_{crit} = \sqrt{\frac{2\omega_{\alpha}^2 I}{\rho B^2 C'_M}} = 155.02 \text{ m/s} \quad (5.5.1)$$

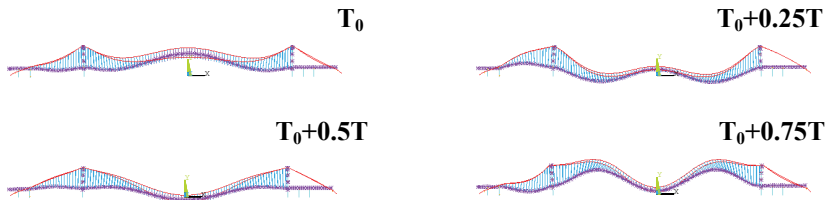


Figure 5.7. Numeric FE analysis using indicial functions: flutter mode

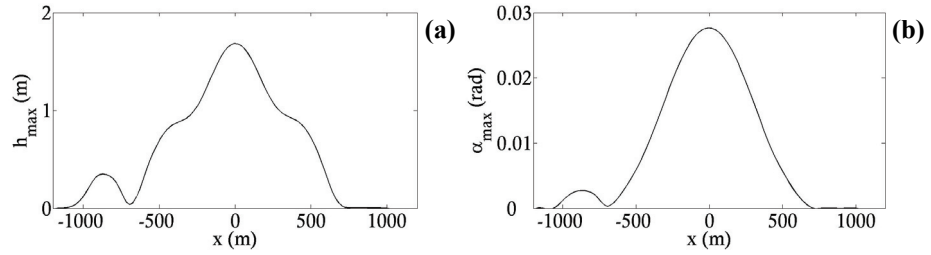


Figure 5.8. Numeric FE analysis using indicial functions: envelopes of maximum generalized displacements at criticality

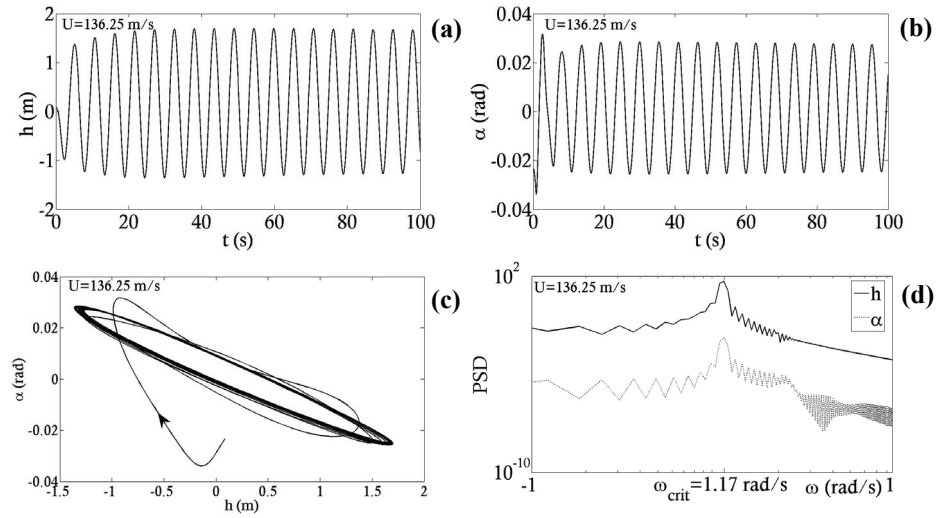


Figure 5.9. Numeric FE analysis using indicial functions: mid-span motion at criticality (a, b, c, d)

The results reported above confirm, as expected, the correspondence between unsteady and steady models in predicting the critic condition leading to a torsional divergence. The post-critic time history of the mid-span deck rotation is represented in Figure 5.15, while the deformed configuration of the structure at a general time instant is represented in Figure 5.16. As shown by these figures, the unstable motion has the shape of the first symmetric torsional mode

with the participation of the vertical displacements due to the geometric nonlinearity.

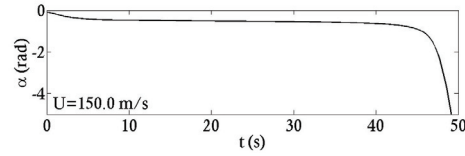


Figure 5.10. Numeric FE analysis using ADTD: unstable postcritical rotation at bridge mid-span ensuing from a torsional divergence bifurcation

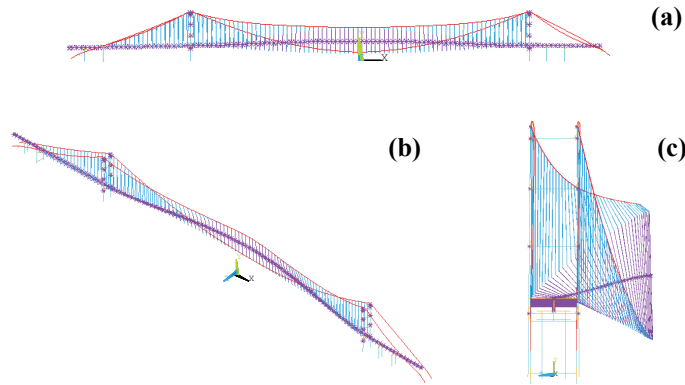


Figure 5.11. Numeric FE analysis using ADTD: critic mode of torsional divergence (U=150 m/s)

5.6 Concluding remarks

The aeroelastic stability of bridges is studied with a particular attention to time domain formulations.

The introduction of convenient additional variables, with the aid of indicial functions, allows to write the equations of motion in the form of an autonomous system without integral terms. This allows to state a simple direct eigenvalue problem to solve the critic condition. This approach, combined with the identification of indicial functions from flutter derivatives via evolutionary algorithms, is seen to be in good agreement with the more involved iterative

search of the Hopf bifurcation point in the frequency domain. Besides its computational convenience, the proposed time domain approach is more general than the frequency domain formulation, since it naturally handles the presence of structural nonlinearities, non-classic damping devices and so on.

With the aim of investigating the critic condition in a tridimensional framework, time domain representations of self-excited loads are introduced into a tridimensional FE model of a case study structure. The analysis of the critic condition reveals that, for the considered case, the flutter mode is characterized by a coupling between the first symmetric vertical in-plane mode and the first symmetric torsional mode, with a small participation of the second symmetric vertical mode. The analysis also reveals that, as expected, the aeroelastic instability can also arise in the form of a static torsional divergence.

Chapter 6

INCLUDING STRUCTURAL NONLINEARITIES, ATMOSPHERIC TURBULENCE AND EXPERIMENTAL UNCERTAINTIES IN BRIDGE AEROELASTICITY

Abstract

The roles played by structural nonlinearities, atmospheric turbulence and experimental uncertainties in bridge aeroelasticity are studied. A FE analysis shows that, in the case of an unstable postcritical behavior, the atmospheric turbulence may destabilize the structural response even below criticality. The presented results are seen to assume a stochastic meaning when accounting for the experimental uncertainties that usually arise in wind tunnel tests.

6.1 Introduction

The theory of bridge aeroelasticity has been well-established since the 1940s (Kehoe, 2005). However, some aspects still deserve higher efforts as they have

not been completely clarified yet. The agreement between different formulations to evaluate the aeroelastic stability of long-span bridges has been discussed in the previous chapters. Here one investigates the roles played by structural nonlinearities, atmospheric turbulence and experimental uncertainties, which were traditionally neglected in bridge aeroelasticity. The problem of incorporating structural nonlinearities into the flutter equations (Lee et al., 1997; Lee et al., 1999) has been analytically treated by Collier and Chamara (2004), with reference to bi-dimensional airfoil theory, while only a few studies, among which the work by Salvatori and Spinelli (2006), considered the effects of the atmospheric turbulence in the aeroelastic stability analysis.

The main theoretical achievements reported in the paper by Collier and Chamara (2004) are recalled and extended to general bluff sections. The effect of the atmospheric turbulence on the critic condition, in the case of an unstable postcritical behavior, is then analyzed via numerical simulations. When accounting for the experimental uncertainties that usually arise in wind tunnel tests, the predicted critic condition assumes a random nature (Jacobsen and Tanaka, 2003). This topic is addressed in some details through a direct Montecarlo approach.

6.2 Flutter in presence of structural nonlinearities

6.2.1 Analytic equations of motion for general bluff sections

Let us extend the two-dofs deck model, already introduced in Chapter 5, to incorporate the presence of quadratic and cubic structural nonlinearities (see Figure 6.1). The equations of motion thus read as:

$$\begin{aligned} m\ddot{h} - mb\chi\ddot{\alpha} + k_{h1}h + k_{h2}h^2 + k_{h3}h^3 &= L \\ -mb\chi\ddot{h} + I_\alpha\ddot{\alpha} + k_{\alpha1}\alpha + k_{\alpha2}\alpha^2 + k_{\alpha3}\alpha^3 &= M \end{aligned} \quad (6.2.1)$$

where I_α is the rotary inertia. In Equation (6.2.1) it is assumed that the elastic center of the deck lies at a distance $b\zeta_{ea}$ from one edge, where b denotes the half chord of the system. The distance along the chord between the elastic

center and the center of rotation is denoted by $b\chi$. Inertial nonlinearities, in Equations (6.2.1), are also neglected according to the hypothesis of small angular rotations.

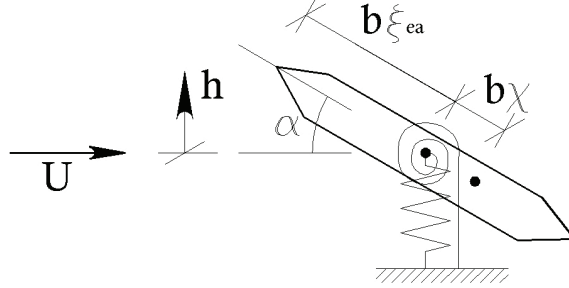


Figure 6.1. Deck section subjected to an incoming wind flow

In the case of an ideal thin airfoil, Equations (6.1) can be reduced to a 6-dimensional first order problem by making use of Wagner's function (Coller and Chamara, 2004). In the case of a bluff section it is convenient to represent the aeroelastic loads via indicial functions approximated by exponential filters, as described in Chapter 5.

Repeating the same steps described in Chapter 5, Equations (6.2.1) can be rewritten in the form of an autonomous system of ordinary differential equations without using integral terms. Particularly, for the case with one single exponential group for each indicial function, the equations of motion become:

$$m\ddot{h} - mb\chi\ddot{\alpha} + k_{h1}h + k_{h2}h^2 + k_{h3}h^3 = \frac{1}{2}\rho U^2 BC'_L \left((1 - a_1^{Lh}) \frac{\dot{h}}{U} + (1 - a_1^{L\alpha}) \alpha + w_1 + w_2 \right) \quad (6.2.2a)$$

$$-mb\chi\ddot{h} + I_\alpha \ddot{\alpha} + k_{\alpha1}\alpha + k_{\alpha2}\alpha^2 + k_{\alpha3}\alpha^3 = \frac{1}{2}\rho U^2 B^2 C'_M \left((1 - a_1^{Mh}) \frac{\dot{h}}{U} + (1 - a_1^{M\alpha}) \alpha + w_3 + w_4 \right) \quad (6.2.2b)$$

$$\dot{w}_1 = \frac{b_1^{Lh} a_1^{Lh}}{b} \dot{h}(\tau) - w_1 \quad (6.2.2c)$$

$$\dot{w}_2 = \frac{b_1^{L\alpha} a_1^{L\alpha} U}{b} \alpha(\tau) - w_2$$

$$\dot{w}_3 = \frac{b_1^{Mh} a_1^{Mh}}{b} \dot{h}(\tau) - w_3 \quad (6.2.2d)$$

$$\dot{w}_4 = \frac{b_1^{M\alpha} a_1^{M\alpha} U}{b} \alpha(\tau) - w_4$$

Equations (6.2.2) can be expressed in the following form:

$$\dot{\underline{x}} = \mathfrak{T}(\underline{x}, U) \quad (6.2.3)$$

where the eight-dimensional state vector \underline{x} is analogous to the state vector already defined in Chapter 5. The vector field \mathfrak{T} , appearing in Equation (6.2.3), can be specialized as follows:

$$\mathfrak{T}_1 = \underline{x}_2 \quad (6.2.4a)$$

$$\mathfrak{T}_2 = \frac{I_\alpha}{I_\alpha - mb^2 \chi^2} (\Gamma + \chi \Theta)$$

$$\mathfrak{T}_3 = \underline{x}_4 \quad (6.2.4b)$$

$$\mathfrak{T}_4 = \frac{I_\alpha}{I_\alpha - mb^2 \chi^2} (\Gamma + \chi \Theta)$$

$$\mathfrak{T}_5 = \frac{b_1^{Lh} a_1^{Lh}}{b} \underline{x}_2 - \underline{x}_5 \quad (6.2.4c)$$

$$\mathfrak{T}_6 = \frac{b_1^{L\alpha} a_1^{L\alpha} U}{b} \underline{x}_3 - \underline{x}_6$$

$$\mathfrak{T}_7 = \frac{b_1^{Mh} a_1^{Mh}}{b} \underline{x}_2 - \underline{x}_7 \quad (6.2.4d)$$

$$\mathfrak{T}_8 = \frac{b_1^{M\alpha} a_1^{M\alpha} U}{b} \underline{x}_2 - \underline{x}_8$$

where the following expressions have been introduced:

$$\begin{aligned}
\Gamma = & -\omega_h^2 \underline{x}_1 - \frac{k_{h2}}{m} \underline{x}_1^2 - \frac{k_{h3}}{m} \underline{x}_1^3 + \\
& \frac{1}{2} \frac{\rho U^2 B C'}{m} \left(\left(1 - a_1^{Lh}\right) \frac{\underline{x}_2}{U} + \left(1 - a_1^{L\alpha}\right) \underline{x}_3 + \underline{x}_5 + \underline{x}_6 \right) \\
\Theta = & -\omega_\alpha^2 \underline{x}_4 - \frac{k_{\alpha 2}}{I_\alpha} \underline{x}_4^2 - \frac{k_{\alpha 3}}{I_\alpha} \underline{x}_4^3 + \\
& \frac{1}{2} \frac{\rho U^2 B^2 C'}{I_\alpha} \left(\left(1 - a_1^{Mh}\right) \frac{\underline{x}_2}{U} + \left(1 - a_1^{M\alpha}\right) \underline{x}_3 + \underline{x}_7 + \underline{x}_8 \right)
\end{aligned} \tag{6.2.5}$$

6.2.2 Problem dimension reduction by Center Manifold Theory

The dimension of the flutter problem at the critical point can be reduced by means of the Center Manifold Theory, as described extensively in reference (Coller and Chamara, 2004). At the onset of instability, the set of differential equations of motions can be decomposed as:

$$\begin{aligned}
\dot{x} &= Ax + f(x, y), \quad x \in \mathfrak{R}^a \\
\dot{y} &= By + g(x, y), \quad y \in \mathfrak{R}^b
\end{aligned} \tag{6.2.6}$$

where all the eigenvalues of the matrices A and B have zero and negative real parts, respectively. By operating in this way the x co-ordinates represent the critical modes while the y variables are locally stable (non-critical co-ordinates).

According to the Center Manifold Theorem (Guckenheimer and Holmes, 1983), there exists a p -dimensional invariant manifold W^c (see Figure 6.2) lying tangent at $x=y=0$ to the linear center eigenspace spanned by the x variables. Since the critical eigenvalues for the flutter problem occur in a complex conjugate pair, the center eigenspace E^c and the center manifold W^c are two dimensional. Invariance implies that solutions starting on W^c remain on the center manifold for all time. Besides, it can be shown that solutions close to the center manifold are attracted to it. Thus, local properties such as system stability are determined by the dynamics restricted to the center manifold.

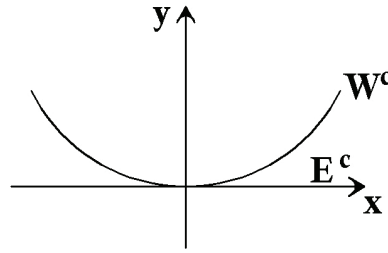


Figure 6.2. Schematic representation of the center manifold in the flutter problem

The center manifold $y=h(x)$ can be explicitly expressed in the form of a power series that, by substitution into the second expression of Equation (6.2.6), gives:

$$\frac{\partial h}{\partial x} \dot{x} = Bh(x) + g(x, h(x)) \quad (6.2.7)$$

Then, by employing the first expression of Equation (6.2.6), invariance is expressed by:

$$\frac{\partial h}{\partial x} Ax + \frac{\partial h}{\partial x} f(x, h(x)) = Bh(x) + g(x, h(x)) \quad (6.2.8)$$

which can be solved for the coefficients that appear in the power series in h . The dynamics on the center manifold, which determine the local qualitative behavior of the system, thus follow:

$$\dot{x} = Ax + f(x, h(x)) \quad (6.2.9)$$

To study system behavior close to, but not at criticality, one may embed system parameters into the center manifold, as:

$$\dot{x} = A_\lambda x + f_\lambda(x, h_\lambda(x)) \quad (6.2.10)$$

where λ corresponds to one or more system parameters (in the case of bridge flutter obviously $\lambda=U$).

The two-dimensional non-trivial dynamics of the center manifold are expressed in the form of a power series whose coefficients depend on system parameters and details of the mathematical model. The tool of normal forms, establishes the existence of a co-ordinate transformation, $x=T_\lambda \xi + P_\lambda(\xi)$ that

simplifies Equation (6.2.10) considerably. T_λ is a matrix conceived to put the linear part of the dynamical system in a canonical form. $P_\lambda(\xi)$ is a vector of polynomials, beginning at quadratic order, whose coefficients are chosen to eliminate certain terms in the ordinary differential equations (ODEs). According to the Normal Form Theorem (Guckenheimer and Holmes, 1983), given a Hopf bifurcation, the equations can be re-arranged into the following simplified form:

$$\begin{aligned}\dot{\xi}_1 &= \xi_1 \left[\sigma_\lambda + c_\lambda (\xi_1^2 + \xi_2^2) \right] - \xi_2 \left[\omega_\lambda + b_\lambda (\xi_1^2 + \xi_2^2) \right] + o(5) \\ \dot{\xi}_2 &= \xi_1 \left[\omega_\lambda + b_\lambda (\xi_1^2 + \xi_2^2) \right] + \xi_2 \left[\sigma_\lambda + c_\lambda (\xi_1^2 + \xi_2^2) \right] + o(5)\end{aligned}\quad (6.2.11)$$

where terms of fifth and higher order have been truncated.

Equations (6.2.11) possess rotational symmetry that can be exploited by switching to polar co-ordinates. Defining $r = \sqrt{\xi_1^2 + \xi_2^2}$ and $\vartheta = \arctan(\xi_2 / \xi_1)$ the equations of the normal form become:

$$\begin{aligned}\dot{r} &= \sigma_\lambda r + c_\lambda r^3 \\ \dot{\vartheta} &= \omega_\lambda + b_\lambda r^2\end{aligned}\quad (6.2.12)$$

The first expression of Equation (6.2.12) is an equation for oscillation amplitude which de-couples from θ . It must be noted that $\dot{r} \equiv 0$ when $r = 0$ and when $r = -\sqrt{\sigma_\lambda / c_\lambda}$. The point $r = 0$ is a zero amplitude equilibrium corresponding to an un-displaced airfoil. Meanwhile, when σ_λ and c_λ are of opposite sign, $r = -\sqrt{\sigma_\lambda / c_\lambda}$ corresponds to a finite amplitude limit cycle. Figure 6.3 depicts the typical behaviors for different values of σ_λ and c_λ .

If one varies a system parameter λ (e.g., the wind velocity), the values of σ_λ and c_λ change. Let λ^* denote the critic value at which instability occurs (i.e., $\sigma_{\lambda^*} = 0$), and assume, without loss of generality, that $\sigma_\lambda < 0$ for $\lambda < \lambda^*$ and $\sigma_\lambda > 0$ for $\lambda > \lambda^*$. Generically it is also expected that $c_{\lambda^*} \neq 0$ and thus, by varying continuously λ in a neighborhood of λ^* a curve in the σ_λ - c_λ plane is traced. If $c_\lambda > 0$ the Hopf bifurcation is said to be subcritical, while for $c_\lambda < 0$

it is supercritical. Qualitative sketches in the amplitude-parameter space depicting the emergence of periodic orbits are also given in Figure 6.3. It is worth noting that at $\lambda=\lambda_*$ the zero amplitude equilibrium changes stability: the solid line (stable) becomes dashed (unstable). Arrows indicate regions in which oscillation amplitudes either grow or decay. In the supercritical case, the instability spawns a stable periodic solution for $\lambda>\lambda_*$ whose amplitude initially grows as $k\sqrt{\lambda-\lambda_*}$. In the subcritical case, the periodic orbit is unstable and lies on the stable side of the bifurcation. This latter case is recognized to be potentially dangerous: because of the unstable limit cycle in the vicinity of the origin, small but finite perturbations may lead to growing oscillations even though the system is linearly stable.

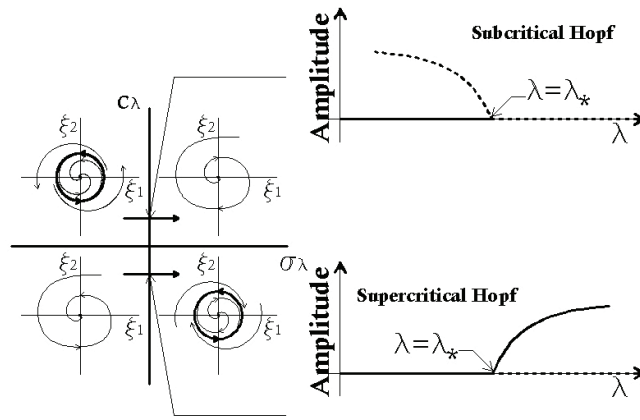


Figure 6.3. Typical phase portraits for different values of σ_λ and c_λ and corresponding two generic Hopf bifurcations (Coller and Chamara, 2004)

To determine whether a flutter instability is subcritical or supercritical, it is simply necessary to check the sign of c_{λ^*} . At $\lambda=\lambda_*$, the first expression of Equations (6.2.10) becomes:

$$\begin{aligned}\dot{x}_1 &= \omega_{\lambda^*} x_2 + f_1(x_1, x_2) \\ \dot{x}_2 &= -\omega_{\lambda^*} x_1 + f_2(x_1, x_2)\end{aligned}\tag{6.2.13}$$

Guckenheimer and Holmes (1983) report that the cubic normal form coefficient can be calculated by:

$$c_{\lambda^*} = \frac{1}{16}(f_{1,111} + f_{1,122} + f_{2,112} + f_{2,222}) + \frac{1}{16\lambda^*} [f_{1,12}(f_{1,11} + f_{1,22}) - f_{2,12}(f_{2,11} + f_{2,22}) - f_{1,11}f_{2,11} + f_{1,22}f_{2,22}] \quad (6.2.14)$$

where the subscripts after the comma denote partial derivatives, i.e.:

$$f_{i,lmn} = \left. \frac{\partial^3 f_i}{\partial x_l \partial x_m \partial x_n} \right|_{x=0} \quad (6.2.15)$$

Thus, to determine the criticality of the Hopf bifurcation, a small algebraic calculation is only necessary rather than the full normal form transformation which usually is a difficult task.

6.2.3 Cubic structural nonlinearities

At a first stage of investigation, the cases for which the only non-linearity of the system appears as cubic restoring forces in the springs is considered: $\delta_{a2} = \delta_{h2} = 0$, $\delta_{a3} \neq 0$ and/or $\delta_{h3} \neq 0$.

With such an assumption, the computation of the cubic order normal form coefficient c_{λ^*} does not require to compute the center manifold. After some calculations, it results (Coller and Chamara, 2004):

$$c_{\lambda^*} = \frac{1}{16} (f_{\lambda^* 1,111}^{(3)} + f_{\lambda^* 1,122}^{(3)} + f_{\lambda^* 2,112}^{(3)} + f_{\lambda^* 2,222}^{(3)}) \quad (6.2.16)$$

where $f^{(3)}$ is the part of f containing only cubic nonlinearities. Therefore, c_{λ^*} is given by a linear combination of third derivatives of $f_{\lambda^*}^{(3)}$, thus assuming the following general form:

$$c_{\lambda^*} = p\delta_{a3} + q\delta_{h3} \quad (6.2.17)$$

where the constants p and q depend on the system parameters.

From Equation (6.2.17) it can be recognized that, in the δ_{a3} - δ_{h3} parameter space, a straight line with inclination θ separates regions of super-criticality

from regions of sub-criticality (see Figure 6.4). When $\theta > 0$ (depending on the system parameters p and q), the so-called flutter criticality hypothesis hold, namely the flutter instability is of the benign supercritical nature if the pitch spring is of the hardening type ($\delta_{\alpha 3} > 0$, with $\delta_{h3} = 0$), while it is of the subcritical type if the pitch spring is softening ($\delta_{\alpha 3} < 0$, with $\delta_{h3} = 0$). Cases in which $\theta < 0$ may represent counterexamples to this hypothesis.

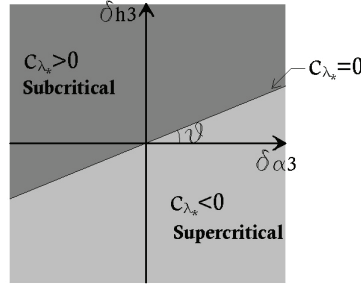


Figure 6.4. Regions of supercritical and subcritical Hopf bifurcation in the parameter space in presence of cubic nonlinearities (Coller and Chamara, 2004)

6.2.4 Quadratic structural nonlinearities

Including quadratic nonlinearities in the restoring forces entails a break of the symmetry $(h, \alpha) \rightarrow (-h, -\alpha)$ of the system. Nonetheless, the system is still invariant with respect to the transformation $(h, \alpha, \delta_{h2}, \delta_{\alpha 2}) \rightarrow (-h, -\alpha, -\delta_{h2}, -\delta_{\alpha 2})$ and thus the cubic normal form coefficient c_{λ^*} must be invariant under $(\delta_{h2}, \delta_{\alpha 2}) \rightarrow (-\delta_{h2}, -\delta_{\alpha 2})$, which means that the qualitative nature of the instability is the same regardless the direction in which the symmetry is broken.

In order to account for quadratic nonlinearities in the calculation of c_{λ^*} one has to incorporate the center manifold in the analysis. Letting $g^{(2)}(x, y)$ denote the quadratic part of $g(x, y)$ in Equation (6.2.6), then the quadratic part

of $g(x, h(x))$ in Equation (6.2.7) is $g^{(2)}(x, 0)$. Thus, at quadratic order, Equation (6.2.7) becomes:

$$\frac{\partial h^{(2)}}{\partial x} Ax = Bh^{(2)}(x) + g^{(2)}(x, 0) \quad (6.2.18)$$

Equation (6.2.18) can be solved for the expansion coefficients in $h^{(2)}$, which will be linear functions of the coefficients $\delta_{\alpha 2}$ and $\delta_{h 2}$. Then in Equation (6.2.9) it can be written:

$$f(x, h(x)) = f^{(2)}(x, 0) + f^{(3)}(x, 0) + f^{(2)}(x, h^{(2)}(x)) + o(4) \quad (6.2.19)$$

In Equation (6.2.19) the expansion coefficients in $f^{(2)}(x, 0)$ are quadratic in $\delta_{\alpha 2}$ and $\delta_{h 2}$ and the expansion coefficients in $f^{(3)}(x, 0)$ are linear in $\delta_{\alpha 3}$ and $\delta_{h 3}$. Finally, since Equation (6.2.14) is linear in the cubic expansion coefficients and quadratic in the quadratic expansion coefficients, the following relation is obtained:

$$c_{\lambda^*} = d_{\alpha\alpha} \delta_{\alpha 2}^2 + d_{\alpha h} \delta_{\alpha 2} \delta_{h 2} + d_{hh} \delta_{h 2}^2 + p \delta_{\alpha 3} + q \delta_{h 3} \quad (6.2.20)$$

Equation (6.2.23) governs the nature of the Hopf bifurcation when quadratic and cubic nonlinearities are introduced in the system.

6.3 Turbulence effects on aeroelastic stability

6.3.1 Numeric prediction of unstable postcritical behavior

The results presented in Section 6.2 allow to discern between supercritical and subcritical flutter instability of a bridge deck. This issue is primarily important when considering the influence of atmospheric turbulence on the system response, as it is discussed here through numerical simulations. In the analysis, the FE spine type model of the Tsing Ma Bridge (TMS) presented in Chapter 1 is adopted along with the time domain model of aeroelastic forces via indicial functions. Flat plate analogy and one exponential group for each indicial functions are also assumed.

First of all, it must be checked whether the postcritical behavior predicted by the TMS model is stable or unstable. In the model (see Chapter 1) the deck is reproduced by large displacements beams, which have a hardening behavior with deflection but are linear with rotation. Thus we are in the case $\delta_{\alpha 2} = \delta_{\alpha 3} = 0$ and $\delta_{h3} \geq 0$, which always yields a subcritical instability since $c_{\lambda*}$, in Equation (6.2.20), is always positive.

It is worth noting that the nature of the postcritical behavior predicted by the numeric model has nothing to do with the postcritical behavior of the real structure. Indeed, this last can be assessed only by accurately modeling the torsional nonlinearities of the deck of the bridge. Looking at this problem goes, however, beyond the purposes of this study which is primarily focused on turbulence effects in the case of unstable postcritical behaviors.

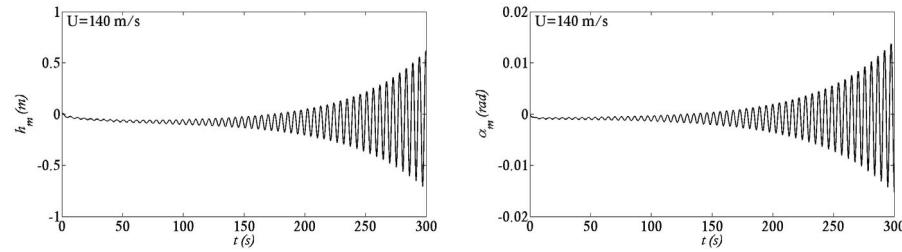


Figure 6.5. Unstable postcritical behavior evaluated via time domain FE analysis using the TMS model

The critic condition, already analyzed in Chapter 5, corresponds to a velocity of 136.25 m/s and a circular frequency of 1.17 rad/s. If the postcritical behavior is unstable, steady state oscillations do never take place when the wind velocity is larger than the critic value and a divergent solution is encountered. This more dangerous case, as theoretically expected, characterizes the numeric model. As an example showing this conclusion, the dynamic response of the structure to an external wind velocity of 140 m/s is shown in Figure 6.5. The results evidence that a divergent unstable solution is encountered at the

considered velocity. Clearly, it has also been checked that analogous results can be found at velocities that are closer (but higher) to the critic one and that the response does not eventually become steady on a limit cycle after a longer time.

6.3.2 Turbulence effects in the case of an unstable postcritic behavior

The problem of including turbulent components in the aeroelastic stability assessment of a bridge has not been yet clarified in the literature although it has been already analyzed in reference (Simiu and Scanlan, 1996). Salvatori and Spinelli (2006) have shown that, although turbulence has no effects on the onset of the aeroelastic instability in the linear regime, it may strongly affect the amplitudes of vibration in the nonlinear postcritic regime. Particularly, it results that a partial correlation between turbulent velocities may lead to quite larger displacements than the less realistic full correlation case. Nevertheless it must be mentioned that the results presented in reference (Salvatori and Spinelli, 2006) apply only to the cases in which the postcritic behavior is stable. On the contrary when the structure exhibits a postcritic unstable flutter behavior, small but finite perturbations may lead to growing oscillations even though the system is linearly stable (Coller and Chamara, 2004). This entails that turbulent components might play a significant role and destabilize the structural motion even below criticality.

With the aim of investigating this point in deeper details, numerical simulations are here performed. Namely, both along-wind and across-wind turbulent components are introduced in the tridimensional TMS model of the bridge. Steady state loads are neglected according to the basic assumption of flat plate analogy. Buffeting and self-excited loads are introduced instead, as described in Chapters 3 and 5. The turbulent wind field is artificially simulated by adopting the POD-based technique described in Chapter 2, accounting for a partial correlation between turbulent velocities.

The effects of an increasing level of turbulence intensity are accounted for by generating the stochastic turbulent wind field for two values of the shear velocity, namely $u_* = 0.95$ m/s (low turbulence intensity) and $u_* = 1.9$ m/s (high

turbulence intensity). Clearly, the assumed values of the shear velocity do not correspond to a mean velocity at mid-span equal to the critic flutter velocity. Indeed, as commented in Chapter 5, the critic velocity (assuming flat plate analogy) without turbulence, is equal to $U_{crit}=136.25$ m/s. This value would correspond to a shear velocity $u_{*crit}=6.45$ m/s which would produce quite large (even unphysical) turbulent components. On the contrary the assumed values of the shear velocity are seen to lead to reasonable and realistic wind simulations.

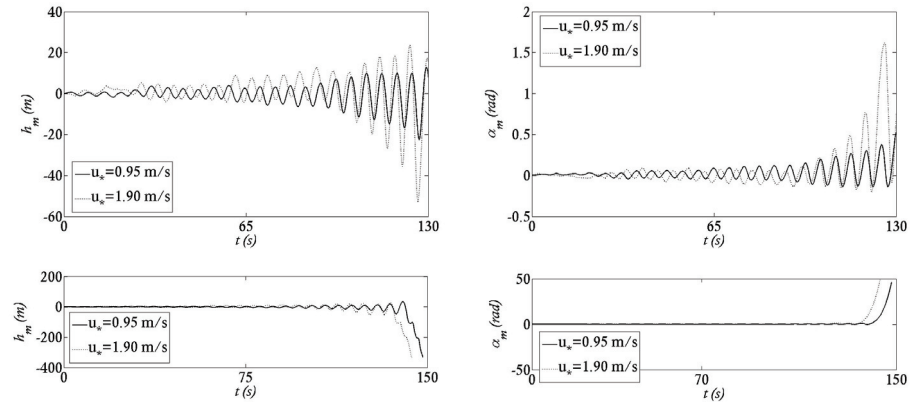


Figure 6.6. Unstable driven motion at criticality ($U=U_{crit}=136.2$ m/s) due to the presence of the atmospheric turbulence

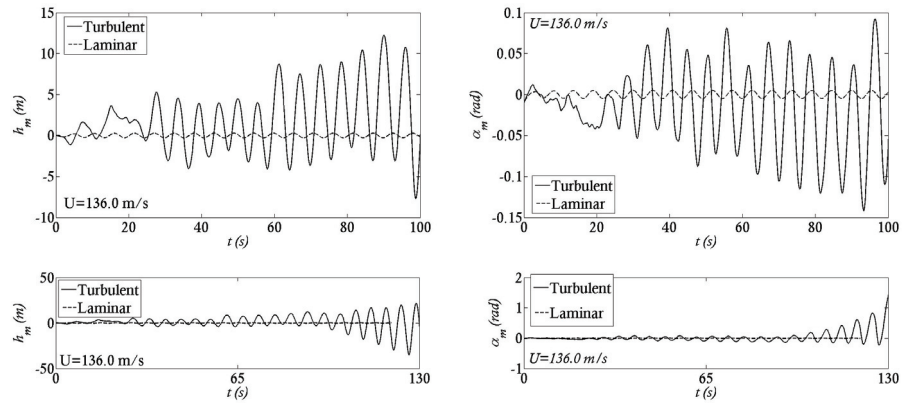


Figure 6.7. Stable case in laminar flow driven to instability by the presence of the atmospheric turbulence ($u_*=1.90$ m/s)

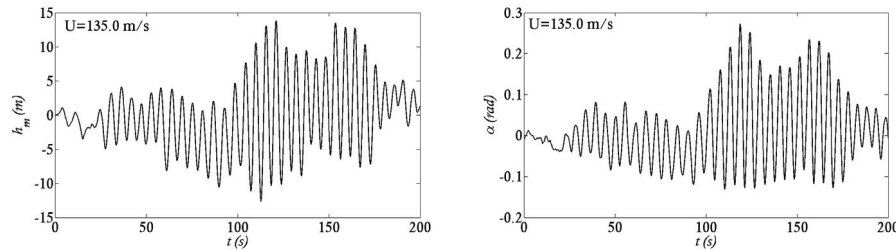


Figure 6.8. Stable response with turbulent wind flow ($u^*=1.90$ m/s)

The results of the analysis have confirmed that the presence of a low level of turbulence can destabilize the motion even at smaller velocities than the critical one. Figure 6.6 shows the time history of the mid-span vertical displacement and rotation for $U=136.2$ m/s and for the two different values of the shear velocity: $u^*=0.95$ m/s and $u^*=1.9$ m/s. As evidenced by the presented results, the motion close to criticality becomes unstable due to the presence of the buffeting loads regardless the level of turbulence intensity.

In the case $u^*=1.90$ m/s the lower velocity at which an unstable motion is encountered is found to be equal to $U_{crit}^*=135.2$ m/s, which is a little smaller value than U_{crit} . Moreover, as it is also evidenced in Figure 6.6, the effect of an increasing level of atmospheric turbulence is to increase the amplitude of the oscillations in the postcritical regime, thus accelerating the onset of the non-oscillatory divergent motion. These circumstances indicate the major role played by turbulence in the case of an unstable post-critical regime and that neglecting turbulence effects in flutter analysis could lead to serious inaccuracies and even non-conservative results. An example of dynamic behavior which is stable without turbulence and it is driven into instability by the buffeting loads is reported in figure 6.7 for the case $U=136.0$ m/s $< U_{crit}$, while Figure 6.8 represents a stable motion close to criticality ($U=135.0$ m/s) under turbulent wind flow.

6.4 Uncertain flutter analysis

Differently from aerospace engineering, flutter analysis in civil structural engineering is related to numerous uncertainties. Thus, the main questions

arising concerns the actual reliability of the predicted critic condition (model reliability) and the level of structural safety with respect to onset of the flutter instability (structural reliability). In order to discuss the former point, the planar deck model presented in Chapter 5 is here adopted and the aeroelastic stability analysis is treated from a probabilistic viewpoint. Since geometric nonlinearities are neglected, the classic frequency domain approach is utilized as it does not introduce any further approximation into the problem.

Uncertainties in the mass, stiffness and damping properties of the mechanical system should be certainly incorporated in the aeroelastic stability analysis (Pourzeynali and Datta, 2002). However, the variability of the mechanical properties of the bridge, leading to variations of mass and stiffness properties, is complex and difficult to model. A possible solution is to multiply the deterministic structural matrices by a sequence of log-normally distributed random variable factors. If standard deviation and mean values are known, a set of mass and stiffness matrices can be artificially generated and, for each combination, the corresponding critical flutter speed can be determined (Pourzeynali and Datta, 2002).

At a first stage of investigation, variability of the flutter derivatives is only considered here, since the main sources of uncertainty usually come from wind tunnel tests results. Particularly, the i -th flutter derivatives are calculated as:

$$\tilde{H}_i^*, \tilde{A}_i^* = H_i^*, A_i^* \cdot (1 + \varepsilon \cdot C_v) \quad (6.4.1)$$

where H_i^*, A_i^* are the (deterministic) flutter derivatives of the thin airfoil, C_v is a user defined coefficient of variation and ε is a normally distributed random number.

According to literature results (see, for instance, Simiu and Scanlan (1996)), disparity between the results of flutter derivatives obtained under turbulent and laminar conditions is of the order of 15%. In addition, experimental errors and curve-fitting techniques introduce extra uncertainties into the analysis. Thus, values of C_v around 15-20% are likely expectable in technical applications.

According to Equation (6.4.1), all the flutter derivatives are presumed to share the same frequency independent Gaussian variability. Clearly, considering frequency dependent variability indices and defining different levels of

confidence for different aeroelastic derivatives would not entail any difficulty in the analysis. However, Equation (6.4.1) allows to describe the level of uncertainty on the flutter derivatives by the single parameter C_v , thus guaranteeing a significant simplification in presenting the results, without anyway reducing the generality of the proposed approach.

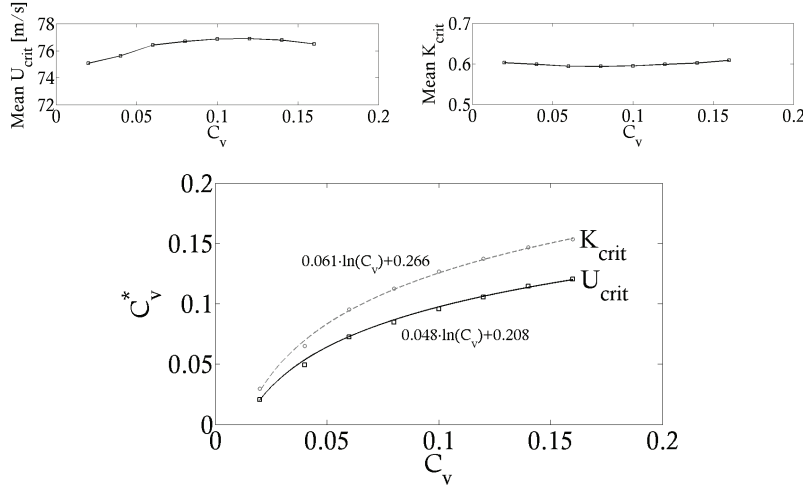


Figure 6.9. Results of the Montecarlo simulation: mean values and coefficients of variation of predicted critic velocity U_{crit} and critic frequency K_{crit} , by varying the coefficient of variation C_v of the aeroelastic derivatives

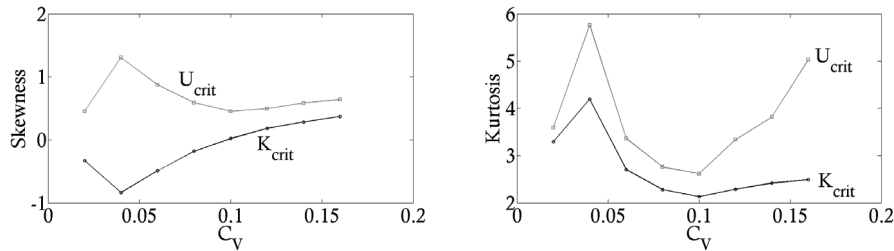


Figure 6.10. Results of the Montecarlo simulation: skewness and kurtosis of predicted critic velocity U_{crit} and critic frequency K_{crit} , by varying the coefficient of variation C_v of the aeroelastic derivatives

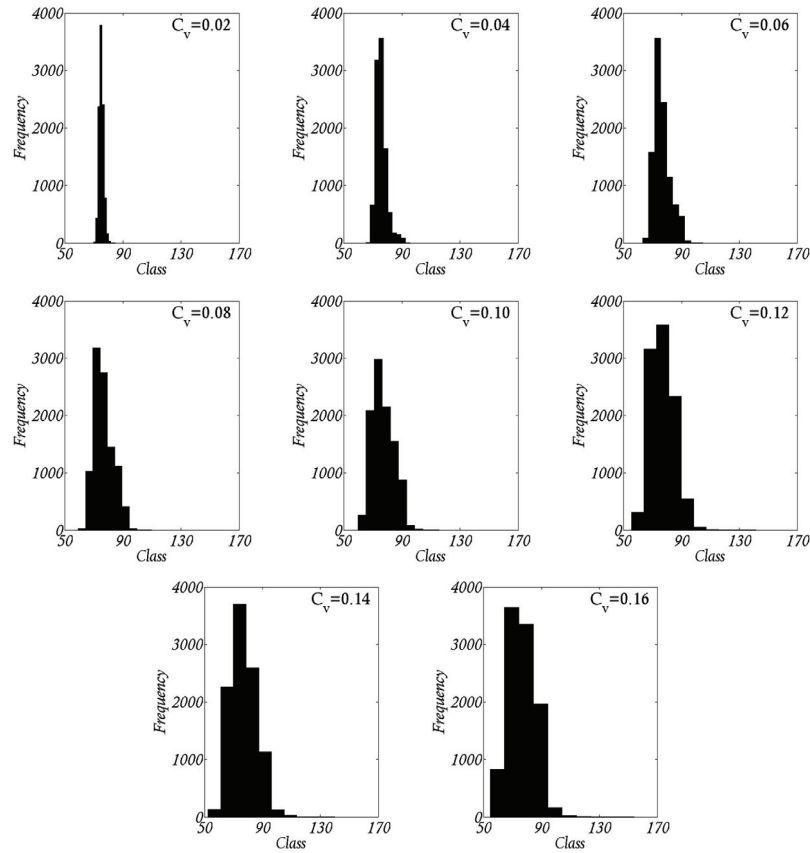


Figure 6.11. Results of the Monte Carlo simulation: histograms of predicted critic velocity U_{crit} (values in m/s), by varying the coefficient of variation C_v of the aeroelastic derivatives

Different values of the coefficient of variation C_v are considered in the analysis and, for each of these values, 10^4 sets of flutter derivatives are artificially simulated using Equation (6.4.1). It must be mentioned that the number of 10^4 samples is chosen since it was seen to be sufficiently large to give a significant statistic characterization of the results. For each set of flutter derivatives, the Hopf bifurcation point is calculated using the iterative procedure described in (Simiu and Scanlan, 1996). This approach is chosen for its computational efficiency. As mentioned in Chapter 5, the fourth aeroelastic

derivatives H_4^* and A_4^* are neglected by the said method. This leads to the following deterministic critic condition ($C_v=0$):

$$U_{crit}=74.90 \text{ m/s}, K_{crit}=0.603 \quad (6.4.2)$$

The adopted probabilistic approach relies on a straightforward Montecarlo simulation which gives an accurate estimate of the probability density functions (pdf) of the results, mainly consisting of critic velocities and critic circular frequencies. The main topics under investigation are: the differences between expected and mean values, the variability of the obtained results versus the input variability coefficient C_v , the Gaussianity of the results.

Figure 6.9 summarizes the main results of the Montecarlo simulation. As already mentioned, each point in this figure corresponds to 10^4 iterative calculations of the critic eigenvalue. The results show that the mean values of both U_{crit} and K_{crit} exhibit, as expected, a small sensitivity on C_v . On the contrary the coefficients of variation C_v^* of U_{crit} and K_{crit} grow with C_v following the logarithmic lines reported in Figure 6.9.

Figure 6.10 analyzes the Gaussianity of the pdfs of U_{crit} and K_{crit} by varying the coefficient of variation C_v of the aeroelastic derivatives. The presented results emphasize a strong non-Gaussianity of both U_{crit} and K_{crit} . This circumstance is also evidenced by the histograms of U_{crit} which are shown in Figure 6.11.

The results presented in Figure 6.11 also emphasize that U_{crit} likely follows right skew distributions even at small values of C_v . This last circumstance entails that common levels of experimental uncertainties may lead to unsafe predictions of the critic velocity.

6.5 Concluding remarks

The role of structural nonlinearities and atmospheric turbulence on the aeroelastic behavior of bridges and the effects of experimental uncertainties on the predicted critic condition have been analyzed.

Structural nonlinearities judge on the nature of the postcritic behavior. Within this framework, a FE analysis has shown that, in the case of an unstable postcritic behavior, small but finite perturbations may destabilize the motion

even below the critic velocity. In particular, in the presented case, the motion at criticality is seen to become unstable due to the presence of the atmospheric turbulence which can even destabilize the motion slightly below the critic velocity. Besides, the effect of an increasing level of atmospheric turbulence is to increase the amplitude of the oscillations in the postcritic regime and thus to shorten the route towards a structural failure.

When accounting for the data scattering usually arising in wind tunnel experiments, the results of the aeroelastic stability analysis assume a probabilistic meaning. A Montecarlo study has shown that, in the case of a Gaussian variability of the flutter derivatives, the predicted critic velocity follows a non-Gaussian right skew distribution. This entails that common levels of experimental uncertainties could lead to unsafe predictions of the critic flutter velocity.

Chapter 7

SUPPRESSION OF AEROELASTIC INSTABILITIES IN CABLES AND BRIDGES

Abstract

Long-span bridges and cables are lightly damped structures for which wind loads may produce large amplitude oscillations or even catastrophic instabilities. The use of single and multiple tuned mass dampers as control solutions against cable galloping and bridge flutter are analyzed, by paying a special attention to mistuning effects.

7.1 Introduction

Increasing the safety against aeroelastic instabilities is sometimes mandatory in Civil engineering structures. This is mostly the case of cable galloping and bridge flutter. To this regards, passive control strategies are probably the most economical and robust control solutions among those currently available in the literature.

The occurrence of catastrophic dynamic instabilities (such as for instance rain-wind induced vibrations or galloping oscillations), in cables, is essentially influenced by the damping of the system (Faravelli and Ubertini, 2008). Cable

galloping is a well-known catastrophic event which was studied by Luongo & Piccardo (2005). The application of tuned mass dampers (TMDs) as control devices against cable galloping was investigated in reference (Gattulli et al. 2003).

The flutter instability of a bridge deck section ensues from a Hopf bifurcation which is analogous to the one leading to cable galloping. Recently, a great attention was devoted in the technical literature to conceiving control strategies against deck flutter (Preidikman and Mook, 1997; Kwon and Chang, 2000). The idea of using TMDs for this purpose was proposed in (Gu et al., 1998) and in (Lin and Cheng, 2000), while multiple tuned mass dampers were proposed, for instance, in (Lin et al., 1999; Chen and Kareem, 2003; Kwon and Chang, 2004).

In this chapter the effectiveness of a single TMD as a control device against cable galloping is studied. Since a strong sensitivity to mistuning effects is evidenced in this case, which may become unsustainable when dealing with bridge flutter, a multiple tuned mass damper (MTMD) is proposed for this more demanding case. Indeed, multiple tuned mass dampers proved to be capable to increase the robustness against mistuning effects when dealing with buffeting vibrations mitigation of flexible structures (Giuliano, 2007).

7.2 Cable galloping

The classic 2-degrees-of-freedom (DOFs) cable galloping is considered. As it is well-known, the critic condition is represented by a Hopf bifurcation, which is the case in which two complex conjugate eigenvalues cross the imaginary axis. In the case of cables, this may happen when icing conditions modify the aerodynamics of the system, originating lift forces. A simple linear two-DOFs cable sectional model, subjected to an incoming wind flow of velocity U , can be written as (Luongo & Piccardo 2005):

$$\begin{aligned} \ddot{q}_1 + (2\omega\xi_s + 2\mu C_D)\dot{q}_1 + \\ \mu(C'_D - C_L)\dot{q}_2 + \omega^2 q_1 &= 0 \\ \ddot{q}_2 + 2\mu C_L\dot{q}_1 + (2\xi_s + \mu(C_D + C'_L))\dot{q}_2 + q_2 &= 0 \end{aligned} \quad (7.2.1)$$

In which q_1 represents the out-of-plane displacement and q_2 denotes the in-plane one. In Equation (7.2.1) C_D and C_L represent the drag and lift coefficients of the cable, while C_D' and C_L' denote their derivatives with respect to the effective wind angle of attack, calculated for a nil value of this angle. The same structural damping ξ_s is assumed in the two directions, while $\omega=\omega_1/\omega_2$ denotes the ratio between the first out-of-plane and the first in-plane circular frequencies. It is worth noting that, in Equation (7.2.1), the time variable has been normalized by multiplication to ω_1 . The non-dimensional wind velocity μ has also been defined as $\mu=0.5\rho bU/(m\omega^2)$, where ρ is the air density, b is a reference dimension of the cylinder cross-section and m is the cylinder mass per unit length.

The following eigenvalue problem can be written from Equations (7.2.1), to analyze the incipient instability of the trivial solution ($q_1=0, q_2=0$):

$$\det[\lambda^2 \mathbf{M} + \lambda \mathbf{D} + \mathbf{K}] = 0 \quad (7.2.2)$$

where \mathbf{M} is the mass matrix, \mathbf{D} is the aerodynamic damping matrix and \mathbf{K} is the stiffness matrix which can be immediately derived from Equations (7.2.1).

In the non-resonant case ($|\omega-1|>\varepsilon$, ε being a small perturbation parameter), a first order approximation of the system eigenvalues can be achieved by means of the multiple scale method (Luongo & Piccardo 2005), leading to the approximate critic wind velocity $\mu_{crit}^0 = -2\xi_s/(C_D+C_L')$, which is positive for $C_D+C_L'<0$. When the system is under internal resonance conditions ($|\omega-1|=0$), the linear stability diagram can be drawn in the $\det\mathbf{D}$ - $\text{tr}\mathbf{D}$ plane, where \det and tr denote the determinant and the trace operators, respectively, and an approximate expression of the critic velocity can be derived in which the linear proportionality between μ_{crit}^0 and ξ_s still holds (Luongo & Piccardo 2005).

7.3 Suppression of cable galloping using TMDs

The critic wind velocity of the uncontrolled system grows linearly with the structural damping, in both resonant and non-resonant cases. A way to increase the critic velocity is therefore to increase the damping of the system as, for instance, by adopting a small TMD.

The relevant mass, damping and stiffness matrices then become:

$$\mathbf{M} = \begin{bmatrix} 1 & 0 & 0 \\ 0 & 1 & 0 \\ 0 & 0 & 1 \end{bmatrix} \quad (7.3.1a)$$

$$\mathbf{D} = \begin{bmatrix} 2\omega\xi_s + 2\mu C_D & \mu(C'_D - C_L) & 0 \\ 2\mu C_L & 2\xi_s + \mu(C_D + C'_L) + 2\psi\xi_t\omega_t & -2\psi\xi_t\omega_t \\ 0 & -2\xi_t\omega_t & 2\xi_t\omega_t \end{bmatrix} \quad (7.3.1b)$$

$$\mathbf{K} = \begin{bmatrix} \omega^2 & 0 & 0 \\ 0 & 1 + \psi\omega_t^2 & -\psi\omega_t^2 \\ 0 & -\omega_t^2 & \omega_t^2 \end{bmatrix} \quad (7.3.1c)$$

where ψ is the ratio between the mass of the TMD and the mass of the cable, while ω_t is the ratio between the circular frequency of the TMD and the in-plane cable circular frequency ω_l . The third rows of the matrices reported in Equations (7.3.1) correspond to the degree of freedom q_t of the TMD.

A linear eigenvalue problem, analogous to Equation (7.2.2), can be written from Equations (7.3.1) to evaluate the incipient instability of the controlled trivial solution ($q_1=0$, $q_2=0$, $q_t=0$). Figure 7.1 shows the root locus of the eigenvalues of the cable-TMD system, obtained by solving numerically the eigenvalue problem for increasing values of the control variable μ . In the calculations, the mass, damping and stiffness parameters of the cable model identified in Appendix C have been assumed. Moreover the TMD has been presumed to be perfectly tuned to the vertical mode of the cable ($\omega_t=1$) and the optimal Dan Hartog's damping parameter $\xi_{t,opt}=[3/8\psi/(1+\psi)]^{0.5}$ has been chosen for the TMD. The mass ratio $\psi=0.01$ has been assumed, as usual in technical applications, while the aerodynamic coefficients are: $C_D=0.8$, $C'_D=1.5$, $C_L=0.1$ and $C'_L=1.3$. It must be noted that, even by choosing $\omega_t=1$, the perfect tuning of the system is never achieved as a consequence of *veering* interactions between closed eigenvalues. This is the reason why, in Figure 7.1, all the three pairs of complex conjugate eigenvalues are distinct for the value $\mu=0$.

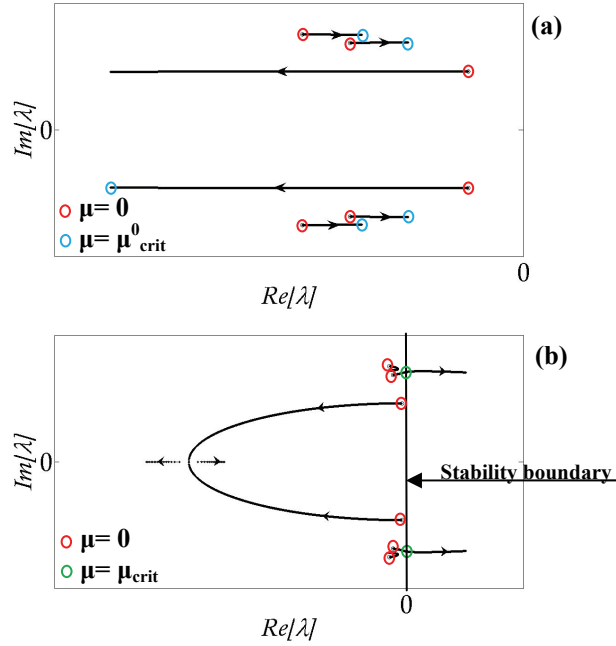


Figure 7.1. Root locus of the eigenvalues of the cable-TMD system by increasing the control variable μ below (a) and above (b) the critic value

The results presented in Figure 7.1 (a) emphasize that, in correspondence of the critic velocity of the uncontrolled system ($\mu = \mu^0_{crit}$), the cable-TMD system is still in the stability region, which is encountered at the value $\mu = \mu_{crit} > \mu^0_{crit}$.

Figure 7.2 investigates the effect of the tuning of the TMD on the critic velocity. As it was expectable, the increment of the critic velocity is very sensitive to variations of the frequency tuning ω_t and attains a maximum close to the perfectly tuned condition ($\omega_t = 1$). It must be mentioned however, that the maximum increment of the critic velocity which can be achieved by using the TMD is remarkable (larger than 100%). This is a consequence of the fact that, in cable galloping, the critic velocity is proportional to the damping of the system. Thus, for instance, doubling the mechanical damping of the cable means doubling its critic velocity. On the contrary, this is not the case of the coupled flutter instability of bridge decks, as it is discussed below.

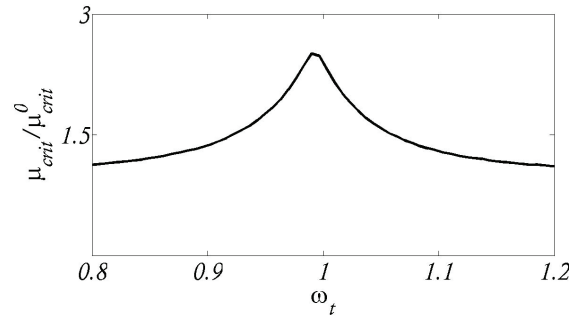


Figure 7.2. Critic velocity as a function of the frequency ratio of the TMD

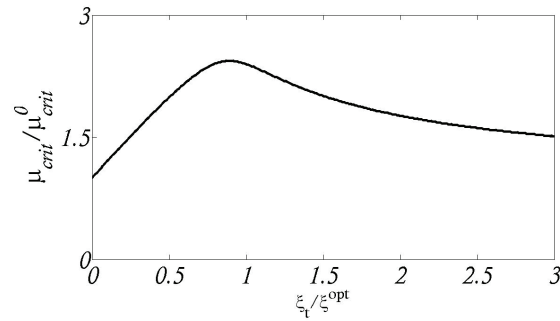


Figure 7.3. Critic velocity as a function of the damping ratio of the TMD

The effect of the damping ratio of the TMD on the critic velocity is analyzed in Figure 7.3. The results show that the optimal damping value of the TMD, against structural galloping, is smaller than the classic Den Hartog's optimum ξ_t^{opt} . It must be also noted that the critic wind velocity rapidly grows below the optimum value, while it slowly decreases above it. This circumstance suggests that, in practical applications, overestimating the optimum damping of the TMD is more conservative than underestimating it.

7.4 Robust passive control of flutter via MTMDs

7.4.1 Multiple tuned mass damper system

The use of multiple tuned mass dampers (MTMDs) to increase the critic velocity leading to a coupled flexural-torsional flutter in bridge decks is studied.

The proposed MTMD is derived as an extension of the single tuned mass damper (TMD) presented in reference (Lin et al., 2000), which has two degrees of freedom corresponding to vertical motion and rotation.

By adopting the deck model presented in Chapter 5, the equations of motion of the system equipped with the TMD read as:

$$m\ddot{h} + c_h\dot{h} + k_h h = L + c_T(\dot{h}_T - \dot{h}) + k_T(h_T - h) \quad (7.4.1a)$$

$$I\ddot{\alpha} + c_\alpha\dot{\alpha} + k_\alpha \alpha = M + c_T(\dot{\alpha}_T - \dot{\alpha})l^2 + k_T(\alpha_T - \alpha)l^2$$

$$m_T\ddot{h}_T + c_T(\dot{h}_T - \dot{h}) + k_T(h_T - h) = 0 \quad (7.4.1b)$$

$$I_T\ddot{\alpha}_T + c_T(\dot{\alpha}_T - \dot{\alpha})l^2 + k_T(\alpha_T - \alpha)l^2 = 0$$

h , α being the DOFs of the deck model and h_T , α_T the DOFs of the TMD. In Equations (7.4.1) m , I , k and c denote the total mass, the total inertia, the total stiffness and the total damping coefficients of the TMD, respectively.

It is convenient to rewrite equations (7.4.1) in the following form:

$$\begin{aligned} &\ddot{h} + (2\xi_h\omega_h + 2\psi\xi_T\omega_T)\dot{h} + (\omega_h^2 + \psi\omega_T^2)h \\ &- 2\psi\xi_T\omega_T\dot{h}_T - \psi\omega_T^2 h_T = L/m \\ &\ddot{\alpha} + (2\xi_\alpha\omega_\alpha + 2\psi_\alpha\xi_{T\alpha}\omega_{T\alpha})\dot{\alpha} + (\omega_\alpha^2 + \psi_\alpha\omega_{T\alpha}^2)\alpha \\ &- 2\psi_\alpha\xi_{T\alpha}\omega_{T\alpha}\dot{\alpha}_T - \psi_\alpha\omega_{T\alpha}^2\alpha_T = M/I \\ &\ddot{h}_T + 2\xi_T\omega_T(\dot{h}_T - \dot{h}) + \omega_T^2(h_T - h) = 0 \\ &\ddot{\alpha}_T + 2\xi_{T\alpha}\omega_{T\alpha}(\dot{\alpha}_T - \dot{\alpha}) + \omega_{T\alpha}^2(\alpha_T - \alpha) = 0 \end{aligned} \quad (7.4.2)$$

where $\psi = m_T/m$ and $\psi_\alpha = I_T/I$ are the mass and inertial ratios of the TMD-deck system. The following relations are adopted in Equation (7.4.2):

$$\begin{aligned} \omega_{T\alpha}^2 &= \omega_T^2 \cdot m_T l^2 / I_T \\ \xi_{T\alpha} &= \xi_T \omega_{T\alpha} / \omega_T \end{aligned} \quad (7.4.3)$$

Looking at Equations (7.4.3), the TMD can be designed to have two distinct natural frequencies. In the paper by Lin et al. (2000), these last were tuned to the frequencies of the first flexural and torsional structural modes to suppress

the resonant effects thus reducing the buffeting response of the deck. When dealing with the classic flutter instability, it is more convenient to tune the two frequencies of the TMD to the same value, nearly corresponding to the critic flutter circular frequency of the system (optimal tuning of the TMD). This can be achieved by simply concentrating two equal masses at the positions of the elastic and viscous forces ($I_T = m_T l^2$).

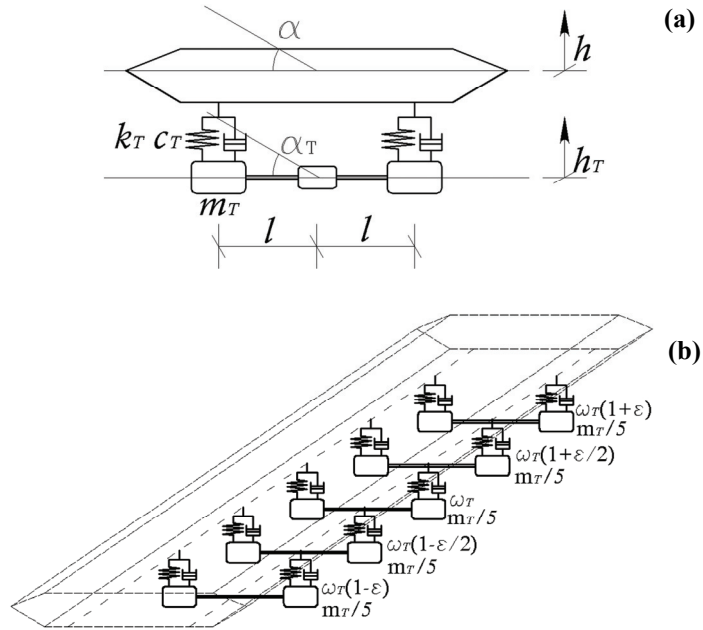


Figure 7.4. TMD system for bridge decks (Lin et al., 2000): (a); proposed MTMD system with $n=5$: (b)

The proposed MTMD system is obtained by splitting the equivalent single TMD into a certain odd number n of TMDs having the same total masses (equal to l/n of the total mass m_t of the single TMD) and damping ratios equal to the one of the equivalent single TMD. The detuning parameter $\varepsilon = 0 \div 1$ is defined such that the circular frequencies (ω_{Ti} , $i=1, \dots, n$) of the TMDs composing the MTMD are calculated as:

$$\begin{aligned}
\omega_{T1} &= \omega_T \\
\omega_{T2} &= \omega_T (1 - \varepsilon) \\
\omega_{T3} &= \omega_T (1 + \varepsilon) \\
&\dots \\
\omega_{T_{n-1}} &= \omega_T \left(1 - \varepsilon / (n-1) / 2 \right) \\
\omega_{Tn} &= \omega_T \left(1 + \varepsilon / (n-1) / 2 \right)
\end{aligned} \tag{7.4.4}$$

As an example, a MTMD system with $n=5$ is sketched in Figure 7.5.

From equations (7.4.4) it can be recognized that the TMD proposed by Lin et al. (2000) can be interpreted as the MTMD with $\varepsilon=0$. The equations of motion of the deck equipped with the MTMD system can simply be obtained by extending equations (7.4.2) and (7.4.3) to the presence of n TMDs.

7.4.2 Aeroelastic stability analysis

As commented in Chapter 5, a convenient time domain representation of self excited lift L and pitching moment M can be obtained by using aerodynamic indicial functions approximated by exponential filters. The main advantage of this approach is that the introduction of an additional variable w_i for each exponential group allows to eliminate integral terms from the equations of motion thus making the aeroelastic stability analysis a straightforward task.

As an example, let us rewrite Equations (7.4.2) by adopting one single exponential group for each indicial function (see Chapter 5). After some calculations one gets:

$$\begin{aligned}
\ddot{h} + 2(\xi_h \omega_h + \psi \xi_T \omega_T) \dot{h} + (\omega_h^2 + \psi \omega_T^2) h &= 2\psi \xi_T \omega_T \dot{h}_T + \psi \omega_T^2 h_T + \\
\frac{1}{2} \frac{\rho U^2 B C'_L}{m} \left((1 - a_1^{Lh}) \frac{\dot{h}}{U} + (1 - a_1^{L\alpha}) \alpha + w_1 + w_2 \right) &+ \\
\ddot{\alpha} + 2(\xi_\alpha \omega_\alpha + \psi_\alpha \xi_{T\alpha} \omega_{T\alpha}) \dot{\alpha} + (\omega_\alpha^2 + \psi_\alpha \omega_{T\alpha}^2) \alpha &= 2\psi_\alpha \xi_{T\alpha} \omega_{T\alpha} \dot{\alpha}_T +
\end{aligned} \tag{7.4.5a}$$

$$\begin{aligned} & \psi_\alpha \omega_{T\alpha}^2 \alpha_T + \frac{1}{2} \frac{\rho U^2 B^2 C'_M}{I} \left((1 - a_1^{Mh}) \frac{\dot{h}}{U} + (1 - a_1^{M\alpha}) \alpha + w_3 + w_4 \right) \\ & \ddot{h}_T + 2\xi_T \omega_T (\dot{h}_T - \dot{h}) + \omega_T^2 (h_T - h) = 0 \end{aligned} \quad (7.4.5b)$$

$$\begin{aligned} & \ddot{\alpha}_T + 2\xi_{T\alpha} \omega_{T\alpha} (\dot{\alpha}_T - \dot{\alpha}) + \omega_{T\alpha}^2 (\alpha_T - \alpha) = 0 \\ & \dot{w}_1 = \frac{b_1^{Lh} a_1^{Lh}}{b} \dot{h}(\tau) - w_1 \\ & \dot{w}_2 = \frac{b_1^{L\alpha} a_1^{L\alpha} U}{b} \alpha(\tau) - w_2 \\ & \dot{w}_3 = \frac{b_1^{Mh} a_1^{Mh}}{b} \dot{h}(\tau) - w_3 \\ & \dot{w}_4 = \frac{b_1^{M\alpha} a_1^{M\alpha} U}{b} \alpha(\tau) - w_4 \end{aligned} \quad (7.4.5c)$$

Equations (7.4.5) can be rewritten in first order form as:

$$\dot{x} = A(U)x \quad (7.4.6)$$

where A is a real 12×12 matrix depending on the wind velocity U . The state vector x , in Equation (7.4.6), is defined as:

$$x = (h, \dot{h}, \alpha, \dot{\alpha}, h_T, \dot{h}_T, \alpha_T, \dot{\alpha}_T, w_1, \dots, w_4)^T \quad (7.4.7)$$

The extension of the above described procedure to consider a MTMD system composed by n TMDs and to use an arbitrary number k of exponential groups is straightforward. Eventually, a system of ordinary differential equations (ODEs) of the form (7.4.6) is obtained, in which the state vector is defined as:

$$x = (h, \dot{h}, \alpha, \dot{\alpha}, h_{T1}, \dot{h}_{T1}, \alpha_{T1}, \dot{\alpha}_{T1}, \dots, h_{Tn}, \dot{h}_{Tn}, \alpha_{Tn}, \dot{\alpha}_{Tn}, w_1, \dots, w_k)^T \quad (7.4.8)$$

and A reflects in a $\underline{n} \times \underline{n}$ matrix, being $\underline{n} = 4(n+1) + k$.

After deriving equation (7.4.6), the aeroelastic stability analysis of the deck-MTMD system can simply be performed by calculating the eigenvalues of matrix A . The flutter instability is encountered when a pair of complex conjugate eigenvalues have zero real parts (Hopf bifurcation point). The minimal velocity U_{crit} at which this condition is satisfied is the critic velocity of

the system, while the imaginary part ω_{crit} of the critic eigenvalue represents the circular frequency of the motion at criticality.

7.4.3 Analysis of control effectiveness

The opportunity of using a MTMD rather than a single TMD to suppress bridge flutter is discussed with reference to a case study. Without loss of generality, the considered MTMD is composed by $n=5$ TMDs.

The mechanical and geometric characteristics of the considered deck model are summarized in Table 7.1. As discussed in Section 7.4.1, the MTMD is designed to have $\omega_T = \omega_{T\alpha}$ and $\zeta_T = \zeta_{T\alpha}$. The mass ratio ψ is assumed to be equal to 0.01, as usual in technical applications, which corresponds to the generalized mass ratio $\psi_\alpha = 0.047$ of the rotational DOF ($l=20.5$ m).

B (m)	ω_h (rad/s)	ω_α (rad/s)	m (kg)	I (kg*m ²)	ζ_h	ζ_α
41	0.8859	1.6588	27778	$2.5 \cdot 10^6$	0.0222	0.0384

Table 7.1. Characteristics of the deck model assumed as case study

In order to generalize the obtained results as much as possible, the aeroelastic derivatives of the thin airfoil are assumed in the calculations. Thus, as shown in Chapter 5, one single exponential group for each indicial function is adopted as it is already sufficient to obtain accurate results in the aeroelastic stability analysis.

The parameter η is introduced as the evaluation criterion of control effectiveness:

$$\eta(\%) = \frac{U_{crit} - U_{crit}^0}{U_{crit}^0} \quad (7.4.9)$$

where U_{crit}^0 denotes the critic velocity of the uncontrolled system.

In order to investigate the effect of the frequency tuning of the MTMD, the critic conditions are solved as described in Section 7.4.2 for different values of ω_T and for the following values of the detuning parameter: $\varepsilon=0$ (single TMD case), $\varepsilon=0.10$, $\varepsilon=0.15$ and $\varepsilon=0.20$. The case in which $\zeta_T = \zeta_{T\alpha} = \zeta^{opt}$, being ζ^{opt} the

optimum Dan Hartog's criterion calculated with respect to the bending mode is considered at this stage.

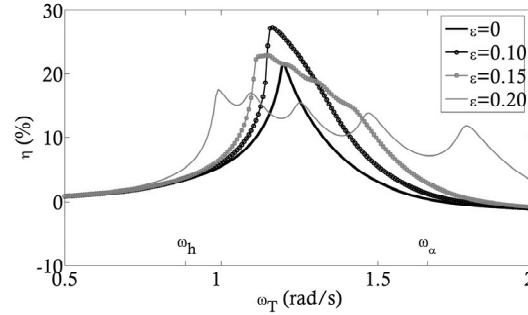


Figure 7.5. Control effectiveness of MTMDs by varying the frequency tuning ω_T and the detuning parameter ε

The results of the analysis, presented in Figure 7.5, emphasize that the maximum achievable increment of the critic velocity is around 20% and that the performance of the single TMD is very sensitive to mistuning effects. This means that a small mistuning of the TMD could lead to poor control performances. In addition, it must be mentioned that mistuning effects can hardly be eliminated in coupled flutter of bridge decks since the critic frequency of the motion (perfect tuning of the TMD) is usually unknown. Indeed, this last is a result of the analysis and its calculation is usually related to large uncertainties descending from wind tunnel experimental data scattering and uncertainties of the mechanical system. Thus, enlarging the frequency band of control effectiveness is always mandatory in these applications in order to meet the fundamental requirement of a large control robustness. As it is discussed below, this can be achieved by increasing the detuning parameter ε of the MTMD system.

The case $\varepsilon=0.10$, in Figure 7.5, guarantees a better performance at the perfectly tuned condition ($\eta>25\%$) with respect to the single TMD solution. However, the curve of control effectiveness is still evidencing some sensitivity to mistuning effects. On the contrary, as ε assumes the values 0.15 and 0.20, the

frequency band of control effectiveness is enlarged at the expense of slightly reducing the peak of effectiveness at the perfectly tuned condition. It is also worth noting that, as the detuning parameter is increased, the η vs. ω_T curves assume a “softening” aspect. This circumstance entails that frequencies lower than the optimum tuning of the single TMD may produce a better performance with respect to slightly higher ones. The increment of the detuning parameter may also produce the appearance of n local maxima in the η vs. ω_T curves.

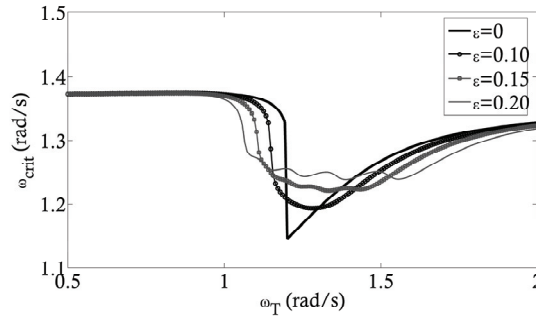


Figure 7.6. Critic flutter circular frequency as a function of the frequency tuning ω_T of the MTMD and of the detuning parameter ε

Figure 7.6 presents the critic circular frequency ω_{crit} of the system vs. the frequency tuning ω_T , for the solutions analyzed in Figure 7.5. In the single TMD case, the optimal tuning corresponds to a global minimum of ω_{crit} and to a cusp of the ω_{crit} vs. ω_T line. The effect of an increasing detuning parameter ε , within the considered values, is to smoothen this cusp and to produce local minima of ω_{crit} .

The results presented in Figures 7.5 and 7.6 also reveal that large values of ω_T could reflect on critic velocities which are 1-2% lower than the critic velocity of the uncontrolled system. This circumstance certainly represents a critical point although it does not impair the overall effectiveness of the proposed control solution.

An example of critical flutter motion of the deck-MTMD system is reported in Figure 7.6 by considering the values $\varepsilon=0.1$ and $\omega_T=1.16$ rad/s, corresponding

to the optimal tuning of the MTMD with $\varepsilon=0.1$. As evidenced by the presented results, the critic condition is characterized by a coupled harmonic motion. The root locus of the eigenvalues of the system, by increasing the wind velocity up to criticality, is shown in Figure 7.8. Particularly, 24 pairs of complex conjugate eigenvalues descend from the structural system, while 4 real eigenvalues descend from the additional variables w_i introduced to represent aeroelastic loads via indicial functions. As the wind velocity is increased, the eigenvalue corresponding to the bending mode is driven towards the stability region, while the eigenvalue of the twist mode is initially pushed towards the stability boundary. Eventually, instability is reached by the eigenvalue corresponding to the twist motion of deck. Wind coupling makes the bending mode participate to the critic motion as shown in Figure 7.7. The DOFs of the MTMD also participate to the motion as a consequence of mechanical couplings between the twist mode and the twist DOFs of the MTMD and between the bending mode and the vertical DOFs of the MTMD. Thus the critic condition is characterized by a 12 DOFs coupled harmonic motion.

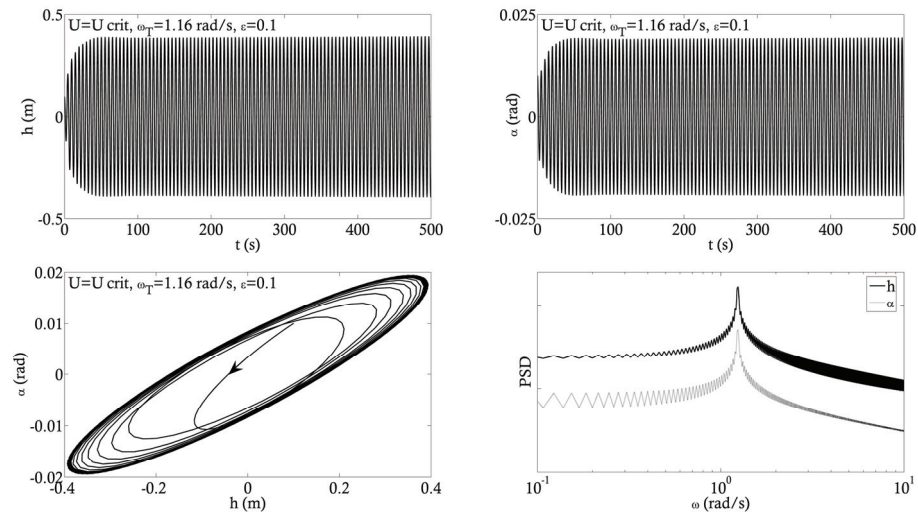


Figure 7.7. Critic flutter condition for $\omega_T=1.16$ rad/s and $\varepsilon=0.1$

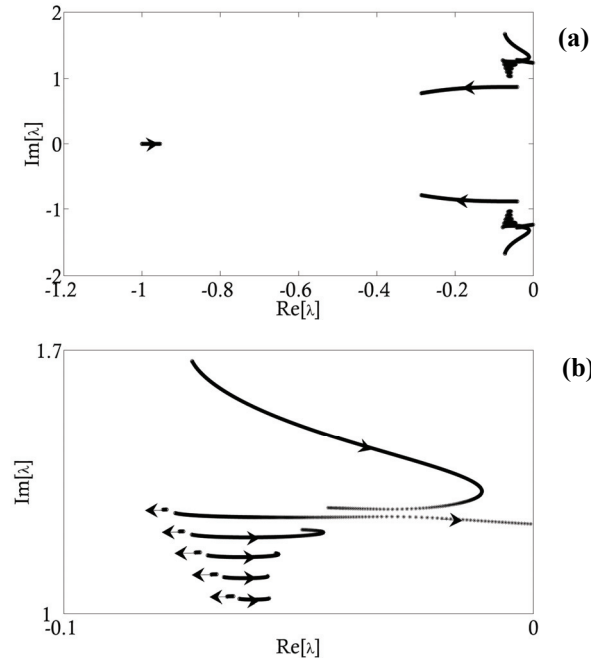


Figure 7.8. Root locus of the eigenvalues of the deck-MTMD system ($\omega_T=1.16$, $\varepsilon=0.1$) by increasing the wind velocity U up to criticality: (a); detailed view of critic eigenvalue: (b)

In the results presented above, the damping ratio of the MTMD has been fixed to the optimum Dan Hartog's value for the bending mode ($\zeta_T = \zeta^{\text{opt}}$). However, it must be mentioned that ζ^{opt} is not optimal for the twist mode. Thus, analyzing the influence of different values of ζ_T on the control effectiveness is a worth effort. To this end the critic conditions are solved by varying the ratio $\zeta_T/\zeta^{\text{opt}}$ for $\omega_T=1.16$ rad/s.

The results are presented in Figure 7.9 and emphasize that the optimal damping ratio of the MTMD depends on the detuning parameter ε . As an example, for the single TMD case, the optimal value of ζ_T is roughly equal to $1.4 \cdot \zeta^{\text{opt}}$, while in the case $\varepsilon=0.1$ it is close to $0.9 \cdot \zeta^{\text{opt}}$. In Figure 7.9, both the lines η vs. $\zeta_T/\zeta^{\text{opt}}$ and ω_{crit} vs. $\zeta_T/\zeta^{\text{opt}}$ evidence cusps and jumps at certain values of $\zeta_T/\zeta^{\text{opt}}$. The effect of an increasing detuning parameter ε , within the considered values, is to smoothen these cusps.

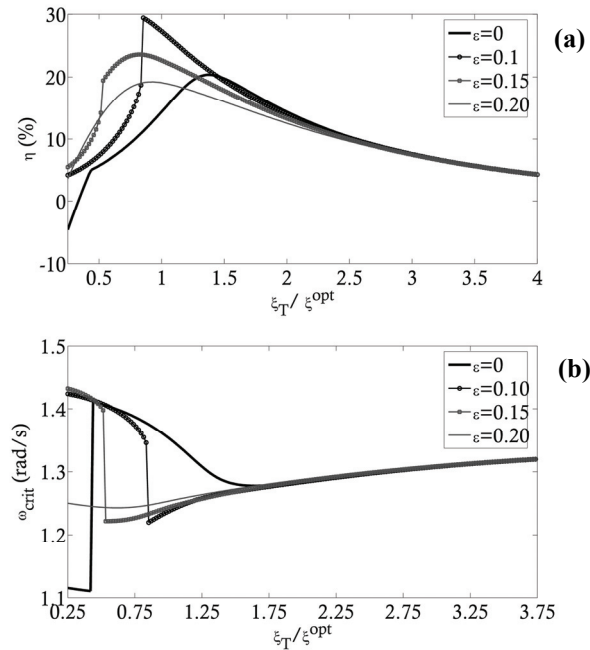


Figure 7.9. Control effectiveness of MTMDs by varying the damping ratio and the detuning parameter ε (ξ^{opt} denotes the optimum Dan Hartog's value for the vertical bending mode): (a); variation of the flutter circular frequency: (b)

A final remark concerns the maximum increment of the critic flutter velocity which can be achieved utilizing MTMDs. The analysis of the considered case study has revealed that a mass ratio of 0.01 leads to increments of the critic velocity which are hardly larger than 25%. Though, this conclusion is limited to the considered example and cannot be generalized, it is worth noting that the obtained control performances are sensibly smaller those obtained, for a similar mass ratio, in the case of cable galloping using a single TMD (see Section 7.3). One main explanation of this result is given below by investigating the variability of the uncontrolled critic velocity of the considered case study with respect to variations of the mechanical damping parameters. Particularly, the critic conditions are solved by separately multiplying the mechanical damping ratios of the system ζ_h and ζ_a by the coefficients β_{ζ_h} and β_{ζ_a} , respectively. The

case in which ζ_h and ζ_α are contemporary multiplied by the same coefficient β_ζ is also considered.

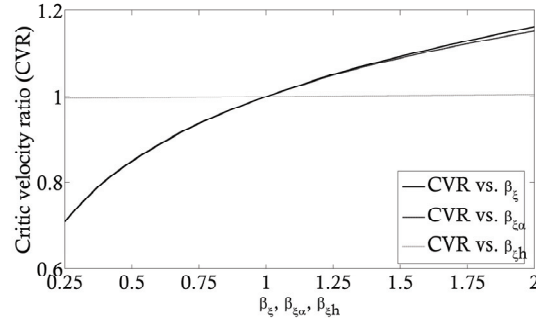


Figure 7.10. Variability of critic flutter velocity (uncontrolled system) with mechanical damping

The ratio between the critic velocity of the system and the critic velocity for $\beta_{\zeta h}=\beta_{\zeta\alpha}=\beta_\zeta=1$ is plotted versus $\beta_{\zeta h}$, $\beta_{\zeta\alpha}$ and β_ζ in Figure 7.10. The presented results emphasize that the critic velocity is rather insensitive to the mechanical damping of the bending mode, while it increases nonlinearly as ζ_α increases. This increment is slow if compared to the case of cable galloping in which there is a linear proportionality between CVR and the mechanical damping. Thus, it is likely expectable that added damping via the use of TMDs produces larger increments of the critic velocity in the case of cable galloping rather than in the case of deck flutter. It must be noted, however, that an increment of about 25% of the critic flutter velocity, which is easily achievable utilizing the proposed MTMD, is usually sufficient to strongly increase the safety of a structure against aeroelastic instability.

7.5 Concluding remarks

When utilizing tuned mass dampers as passive control devices against structural aeroelastic instabilities, a large sensitivity to mistuning effects is usually evidenced as it is discussed for the case of cable galloping. In the case of the classic coupled flutter instability of a bridge deck, the sensitivity to

mistuning effects makes the single tuned mass damper solution practically unfeasible, as the calculation of the optimal tuning of the device is related to numerous uncertainties. To overcome this drawback, a multiple tuned mass damper system for suppressing bridge flutter is conceived.

The aeroelastic stability analysis of the system incorporating the proposed control device is performed by representing the aeroelastic loads in the time domain via indicial functions and by rewriting the equations of motion in the form of a first order system without integral terms. The opportunity of utilizing multiple tuned mass dampers instead of the single device is discussed with reference to a case study. The results show that a correct design of the multiple tuned mass damper may enhance the performance at the perfectly tuned condition and enlarge the frequency band of effectiveness with respect to the single tuned mass damper system. Additional reductions of the sensitivity to mistuning effects can be obtained at the expense of slightly reducing the peak of effectiveness at the perfectly tuned condition.

As a final remark, it must be mentioned that the use of tuned mass dampers in cables guarantees increments of the critic velocity which are sensibly larger than those achievable in the case of bridge flutter. An explanation of this result is given, based on the observation that in bridge flutter there is not a linear proportionality between mechanical damping and critic velocity, which on the contrary holds in cable galloping.

Chapter 8

CONTROL SOLUTIONS FOR CABLE VIBRATION MITIGATION

Abstract

Two control strategies for cable vibration mitigation are conceived. The former, based on the application of an active state controller, is theoretically and numerically investigated, while the latter, consisting of an adaptive strategy combining a distributed passive solution with a semi-active actuation, is investigated via experimental tests.

8.1 Introduction

Cables represent core structural elements of either suspension or cable-stayed bridges. Especially in cable stayed bridges (Caetano et al., 2008) these elements may be prone to large amplitude oscillations which often require control solutions as in the cases of guyed masts and tall buildings (Gioffré et al. 2004; Breccolotti et al., 2007; Venanzi and Materazzi, 2007).

As discussed in Appendix C, a rich technical literature on cable dynamics was established (Cluni et al., 2007; Luongo et al., 1984; Benedettini et al., 1995; Nayfeh et al., 2002; Rega, 2004) and several effective control strategies for

cable vibration mitigation were recently proposed. Passive solutions, based on the use of classic tuned mass dampers (TMDs) were analyzed in the two papers by Cai et al. (2006), while a semi-active version (Casciati et al., 2006) of the TMD device, employing variable out-of-plane inclination, was proposed in (Casciati and Ubertini, 2008). An active control solution based on longitudinal actuation was analyzed in references (Susumpow and Fujino, 1995; Gattulli et al., 1997; Pasca et al., 1998; Gattulli and Vestroni, 2000; Gattulli et al., 2008). Transverse control is probably the most applied solution for mitigating the vibration of cables. Within this field, semi-active dampers were mainly investigated in both theoretical and numeric frameworks (Ubertini, 2008; Faravelli et al., 2008).

Currently, the growing demand for robust structural control solutions and reduced energy consumption makes passive or hybrid (passive-semi-active) control strategies more attractive and feasible (Casciati et al., 2006). Within this context, a convenient passive strategy is to adopt “intelligent” materials as for instance by adding a pre-stressed shape memory alloy wire to a steel taut cable thus providing a control solution which is distributed along the cable and hence it is not affected by the device localization (Casciati et al., 2008).

Two control strategies for cable vibration mitigation are conceived. The former is based on an active state controller (Ubertini, 2008) while the latter consists of a hybrid solution (Faravelli et al., 2008) combining the distributed passive solution utilizing wrapped SMA wires and an open loop control strategy which is based on nonlinear energy transfer between modes. Generally speaking, this solution can be included in the framework of those control strategies that exploit the strongly nonlinear behavior of the dynamical system for control purposes (Rega and Lenci, 2008; Lenci and Rega, 2004).

8.2 Active state control

8.2.1 Linear case

Let us consider the tridimensional motion of a heavy suspended cable, hanging in the vertical plane Oxy (see Figure 8.1). The cable is assumed to

behave as an ideal cord with no bending, torsion or shear rigidities. Two point forces $F_{cv}(t)$ and $F_{cw}(t)$, parallel to the y and z directions respectively, are also applied in the vicinity of one of the cable ends ($l_c \ll l$), z being the out-of-plane direction. In the successive developments, these two forces represent two control inputs, calculated according to a non-collocated active feedback algorithm.

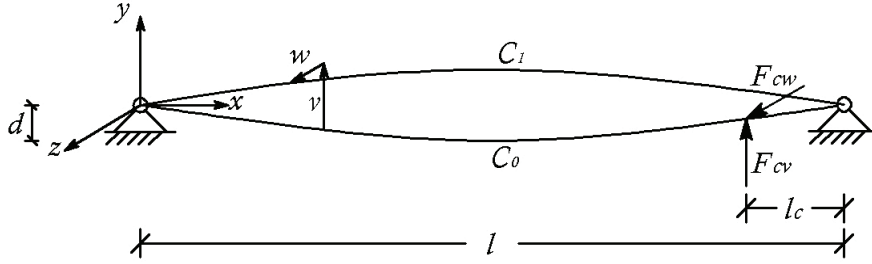


Figure 8.1. Cable static and dynamic varied configurations

Under the hypothesis of small displacements, the motion of the cable can be analyzed in the framework of the linear models. In this case, a convenient representation of the system is sought by expanding the vector of nodal displacements \underline{Q} in the space of modal coordinates $q = \Phi \underline{Q}$, where Φ is the $n \times n$ matrix of linear cable eigenvectors, calculated by Irvine's Theory (Irvine and Caughey 1974). The vector of modal amplitudes is composed as $q = [q_1^z, q_1^y, q_2^z, q_2^y, \dots, q_n^z, q_n^y]$, where q_i^z indicates the i -th out-of-plane coordinate and q_i^y is the i -th in-plane one. By omitting the superscript y , the equation of motion of the i -th in-plane mode can be written as:

$$\ddot{q}_i(t) + 2\xi_i \omega_i \dot{q}_i(t) + \omega_i^2 q_i(t) = f_i(t) + \phi_i^0 F_{cv}(t) \quad (8.2.1)$$

where ϕ_i^0 is the component of the i -th in-plane eigenvector at the position of the control force and f_i is the i -th modal-component of the external excitation. In Equation (8.2.1), ω_i represents the natural circular frequency of the i -th in-plane mode and ξ_i is the modal damping. Similarly, by omitting the superscript z , the

equation of motion of the i -th out-of-plane mode reads as Equation (8.2.1), in which F_{cv} is substituted by F_{cw} .

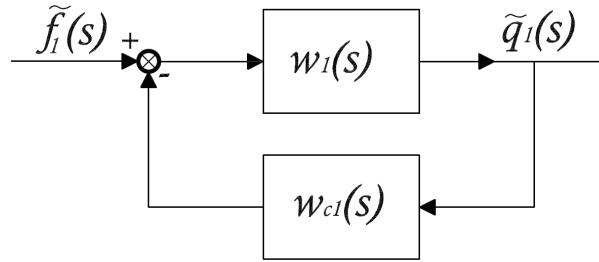


Figure 8.2. Closed loop system illustrating Equation (8.2.4)

In the presented results, the control devices are placed at a distance $l_c=0.05 \cdot l$. Such a distance is sufficiently small to attach the control devices to the deck or to the vertical support of the cable, in a typical structural context. In order to introduce an additional damping in the first in-plane and out-of-plane modes, a modal derivative (MD) controller is designed as:

$$\begin{aligned} F_{cv}(t) &= -g_{d1}^y \cdot \dot{q}_1^y(t) \\ F_{cw}(t) &= -g_{d1}^z \cdot \dot{q}_1^z(t) \end{aligned} \quad (8.2.2)$$

where g_{d1}^y and g_{d1}^z are user-defined control gains. The motion of the first in-plane and out-of-plane modes, with the MD controller, can be obtained by substituting Equations (8.2.2) into Equation (8.2.1):

$$\ddot{q}_1(t) + (2\xi_1\omega_1 + \phi_1^0 g_{d1}^0) \dot{q}_1(t) + \omega_1^2 q_1(t) = f_1(t) \quad (8.2.3)$$

Equation (8.2.3) shows that the control action enters the first in-plane and out-of-plane modes as an additional damping. Nevertheless, in the higher modes, it enters as an external disturbance. Therefore, a compromise has to be searched in order to find an optimum set of control parameters. For the higher modes an equation of the following type holds true:

$$\ddot{q}_j(t) + 2\xi_j\omega_j\dot{q}_j(t) + \omega_j^2 q_j(t) = f_j(t) - \phi_j^0 g_{d1} \dot{q}_1 \quad (8.2.4)$$

where $1 < j \leq n$.

Equation (8.2.3) can be written in the frequency domain as:

$$\tilde{q}_1(s) = \frac{w_1(s)}{1 + w_1(s)w_{c1}(s)} \tilde{f}_1(s) = W_1^c(s) \tilde{f}_1(s) \quad (8.2.5)$$

where the tilde indicates the Laplace transform and s is the Laplace variable. The term $w_1(s)$, in Equation (8.2.5), is the transfer function of the uncontrolled system between the first modal amplitude and the correspondent modal load component. It can be expressed by the following equation:

$$w_1(s) = \frac{1}{s^2 + 2\xi_1\omega_1 s + \omega_1^2} \quad (8.2.6)$$

The feedback transfer function $w_{c1}(s)$ is also introduced in Equation (8.2.5). It is defined as the ratio between the control action and the modal amplitude, in the frequency domain, and it is given by:

$$w_{c1}(s) = \phi_1^0 g_{d1} s \quad (8.2.7)$$

The term $W_1^c(s)$, in Equation (8.2.5), is the closed-loop transfer function of the system composed by the cable mode and the modal control action, as illustrated in Figure 8.2. The equations of motion of the higher modes ($1 < j \leq n$), in the frequency domain, can now be written as:

$$\tilde{q}_j(s) = w_j(s) \tilde{f}_j(s) - w_{cj}(s) \tilde{q}_1(s) \quad (8.2.8)$$

where it holds:

$$w_{cj}(s) = \phi_j^0 g_{d1} s \quad (8.2.9)$$

The first mode with MD controller is asymptotically stable as long as the poles of the closed loop transfer function $W_1^c(s)$ have strictly negative real parts. By looking at Equation (8.2.3), one can easily recognize that $W_1^c(s)$ is simply the transfer function of a second-order system with circular frequency ω_1 and damping $2\xi_1\omega_1 + \phi_1^0 g_{d1}$. Thus, the stability condition of the system reads as:

$$\phi_1^0 g_{d1} > -2\xi_1\omega_1 \quad (8.2.10)$$

8.2.2 Nonlinear case

A more general modal-proportional-derivative (MPD) control law is adopted in the nonlinear case. Four in-plane and four out-of-plane modes are considered in the MPD controller, including proportional terms. The control forces are then calculated as:

$$\begin{aligned} F_{cv}(t) &= -\sum_{i=1}^4 \left(g_{pi}^y \cdot \hat{q}_i^y(t) + g_{di}^y \cdot \dot{\hat{q}}_i^y(t) \right) \\ F_{cw}(t) &= -\sum_{i=1}^4 \left(g_{pi}^z \cdot \hat{q}_i^z(t) + g_{di}^z \cdot \dot{\hat{q}}_i^z(t) \right) \end{aligned} \quad (8.2.11)$$

where the over-hat indicates an estimate based on the observed variables. Without adopting a nonlinear state observer, a simple estimate of the vector of nodal positions is obtained through a "not a knot" cubic spline, that interpolates the nodal observations. The estimate of the vector of nodal velocities is instead obtained by linear interpolation. Five monitored points are considered and placed at equidistant points along the cable.

The control gains in Equation (8.2.11) are calculated by means of an optimal linear quadratic regulator (LQR) calculated by using the matrices of the linearized system. More details on the application of the LQR controller to the presented case can be found in (Ubertini, 2008). As it is well-known from linear control theory, LQR control guarantees asymptotic stability for the linear system, if the controllability condition holds and the weight matrix that appears in the Riccati equation is properly chosen. Nevertheless, it must be mentioned that, even if designed for linear systems, the LQR regulator is often stabilizing also for nonlinear ones. However, no proof of this result exists, even if the gain matrix is assumed to be state-dependent and it is calculated in real time in the neighborhood of the actual state. Thus, a constant gain matrix is here assumed, in order to minimize the computational expense.

8.3 Active control effectiveness

The two cables C^1 and C^2 , reported in reference (Ubertini, 2008), are here considered to test the effectiveness of the proposed control strategy. Cable C^1 is

characterized by the stiffness non-dimensional Irvine parameter $\lambda^2=2.91\pi^2$. Cable C^2 represents the physical model described and identified in Appendix C.

8.3.1 Linear free vibrations

The spatial linear free vibrations of cable C^I with MD control are studied analytically in closed form. From a mathematical point of view this corresponds to the application of Dirac-delta nodal forces (in both y and z directions) with the value $A_\Delta\delta(t)$, where A_Δ is the amplitude of the single impulses.

The i -th modal equation of motion in the frequency domain, can be obtained from Equations (8.2.5), (8.2.6) and (8.2.7) by adopting $g_{dl}=0$ and by considering that the Laplace transform of the Dirac-delta function is the constant unit function:

$$\tilde{q}_i(s) = \frac{\tilde{A}_{\Delta i}}{s^2 + 2\xi_i\omega_i s + \omega_i^2} \quad (8.3.1)$$

where $\tilde{A}_{\Delta i} = A_\Delta \sum_{j=1}^n \Phi_{ij}$. Equation (8.3.1) can be decomposed as follows:

$$\tilde{q}_i(s) = \left[\frac{A_i}{(s-a_i)} - \frac{A_i}{(s-b_i)} \right] \tilde{A}_{\Delta i} \quad (8.3.2)$$

where $a_i = -\xi_i\omega_i + \omega_i\sqrt{\xi_i^2 - 1}$ is a complex number, b_i is its conjugate and $A_i = 1/(a_i - b_i)$. Equation (8.3.2) can be easily converted to the time domain by considering the properties of the Laplace transform. The following explicit formula can be derived to evaluate the uncontrolled solution in the time domain:

$$q_i(t) = [A_i \exp(a_i t) - A_i \exp(b_i t)] \tilde{A}_{\Delta i} \quad (8.3.3)$$

The overall cable response can be then calculated by modes superposition.

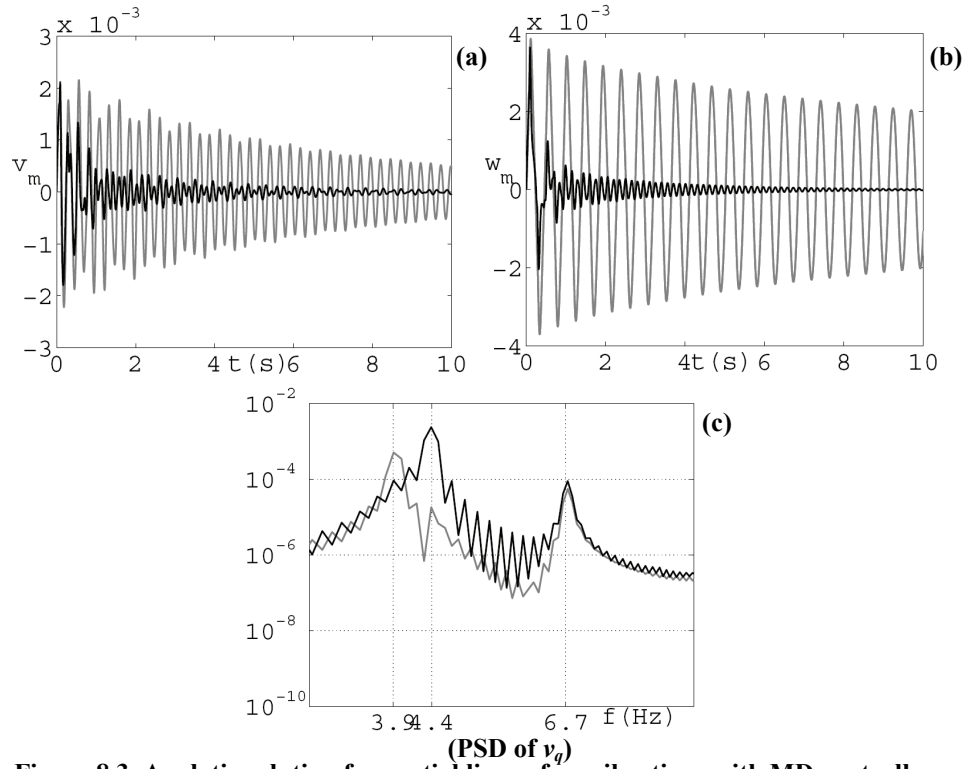


Figure 8.3. Analytic solution for spatial linear free vibrations with MD controller (uncontrolled solution in gray, controlled solution in black)

The motion of the first in-plane or out-of-plane mode, with MD control, is described by Equation (8.2.1). The modal amplitudes, in the time domain, can thus be calculated as described by Equation (8.3.3). By indicating with the apices c the controlled solutions, it holds in particular:

$$q_1^c(t) = [A_1^c \exp(a_1^c t) - A_1^c \exp(b_1^c t)] \tilde{A}_{\Delta 1} \quad (8.3.4)$$

where $a_1^c = -\xi_1 \omega_1 - \phi_1^0 g_{d1} / 2 + \omega_1 \sqrt{(\xi_1 + \phi_1^0 g_{d1} / 2 \omega_1)^2 - 1}$ is a complex number, b_1^c is its conjugate and $A_1^c = 1 / (a_1^c - b_1^c)$. The motion of the higher order modes ($j > 1$) is described by Equation (8.2.3) which, in the frequency domain, becomes:

$$\begin{aligned} \tilde{q}_j^c(s) = \tilde{q}_j(s) - \phi_j^0 g_{d1} \tilde{A}_{\Delta 1} \left[\frac{A_j}{(s-a_j)} - \frac{A_j}{(s-b_j)} \right] \cdot \\ \left[\frac{A_1^c}{(s-a_1^c)} - \frac{A_1^c}{(s-b_1^c)} \right] s \end{aligned} \quad (8.3.5)$$

where $\tilde{q}_j^c(s)$ is the controlled solution and $\tilde{q}_j(s)$ is the uncontrolled one calculated with Equation (8.3.2). The expressions of A_j , a_j and b_j in Equation (8.3.5) are the same as in Equation (8.3.3). Equation (8.3.5) can be converted back to the time domain as follows:

$$\begin{aligned} \tilde{q}_j^c(t) = q_j(t) - \phi_j^0 g_{d1} \tilde{A}_{\Delta 1} A_1^c A_j \left[\frac{1}{a_j - a_1^c} (\exp(a_j t) - \exp(a_1^c t)) \right. \\ \left. + \frac{1}{b_j - b_1^c} (\exp(b_j t) - \exp(b_1^c t)) - \frac{1}{a_j - b_1^c} (\exp(a_j t) - \exp(b_1^c t)) \right. \\ \left. - \frac{1}{b_j - a_1^c} (\exp(b_j t) - \exp(a_1^c t)) \right] \end{aligned} \quad (8.3.5)$$

Figure 8.3 (a) shows the cable normalized mid-span in-plane displacement $v_m(t)$, under free vibrations, for a given value A_{Δ} . Figure 8.3 (b) shows the normalized mid-span out-of-plane displacement $w_m(t)$, under the same conditions. The uncontrolled solution is calculated by means of Equation (8.3.3), while the controlled one is calculated by means of Equation (8.3.4) and (8.3.6).

The MD controller introduces, as expected, an additional damping in the first in-plane and in the first out-of-plane cable modes. Such a damping is proportional to the control gains g_{d1}^y and g_{d1}^z . At the same time, the control action represents a disturbance in the higher modes. This aspect is pointed out in Figure 8.3 (c), which represents the PSD of the quarter-span displacement v_q . Indeed, the uncontrolled solution mainly possesses the frequencies of the first in-plane mode (3.93 Hz) and of the third one (6.73 Hz). In the controlled case the

first in-plane mode is damped out, but the motion of the second in-plane mode arises (4.37 Hz). This aspect might even become more relevant when nonlinearities take place, due to coupling phenomena. In order to introduce an additional damping in the first four in-plane and four out-of-plane modes, the control law must be therefore enriched by additional terms. The MPD controller is adopted for this purpose and its effectiveness is analyzed below, in the framework of large displacements.

8.3.2 Nonlinear free/forced vibrations

The nonlinear FE model described in Appendix C is here adopted and numerical simulations are performed in order to analyze the effectiveness of the MPD controller in the case of cable C^l . The free in-plane and out-of-plane vibrations are considered, at first, at different modal amplitudes. Four distinct cases are analyzed, with the in-plane and out-of-plane initial conditions assigned to the first two modes, as reassumed in Table 8.1. Small non-zero initial conditions are also assigned to higher order modes which may be activated by nonlinear couplings.

The most significant results of the free vibration analysis are represented in Figure 8.4. The main modes that take part to the motion are detected through the PSD of the quarter-span movements v_q and w_q . At small vibration amplitudes the cable behavior is approximately linear. This means, for instance, that only the modes with non-zero initial conditions are involved in the motion. The considered cases are such that: cases A and B are approximately in the linear field, while cases C and D involve larger displacements, thus enhancing the nonlinear phenomena. Out of plane bifurcation is not observed in case A and out-of-plane displacements in cases B and C are prevalent with respect to in-plane ones.

Case	A	B	C	D
q_1^{y0} / l	$0.7 \cdot 10^{-3}$	0.0	$0.4 \cdot 10^{-3}$	$1.6 \cdot 10^{-3}$
q_1^{z0} / l	$0.2 \cdot 10^{-3}$	$1.2 \cdot 10^{-3}$	$2.3 \cdot 10^{-3}$	$0.2 \cdot 10^{-3}$

Table 8.1. Analysis cases for nonlinear free oscillations

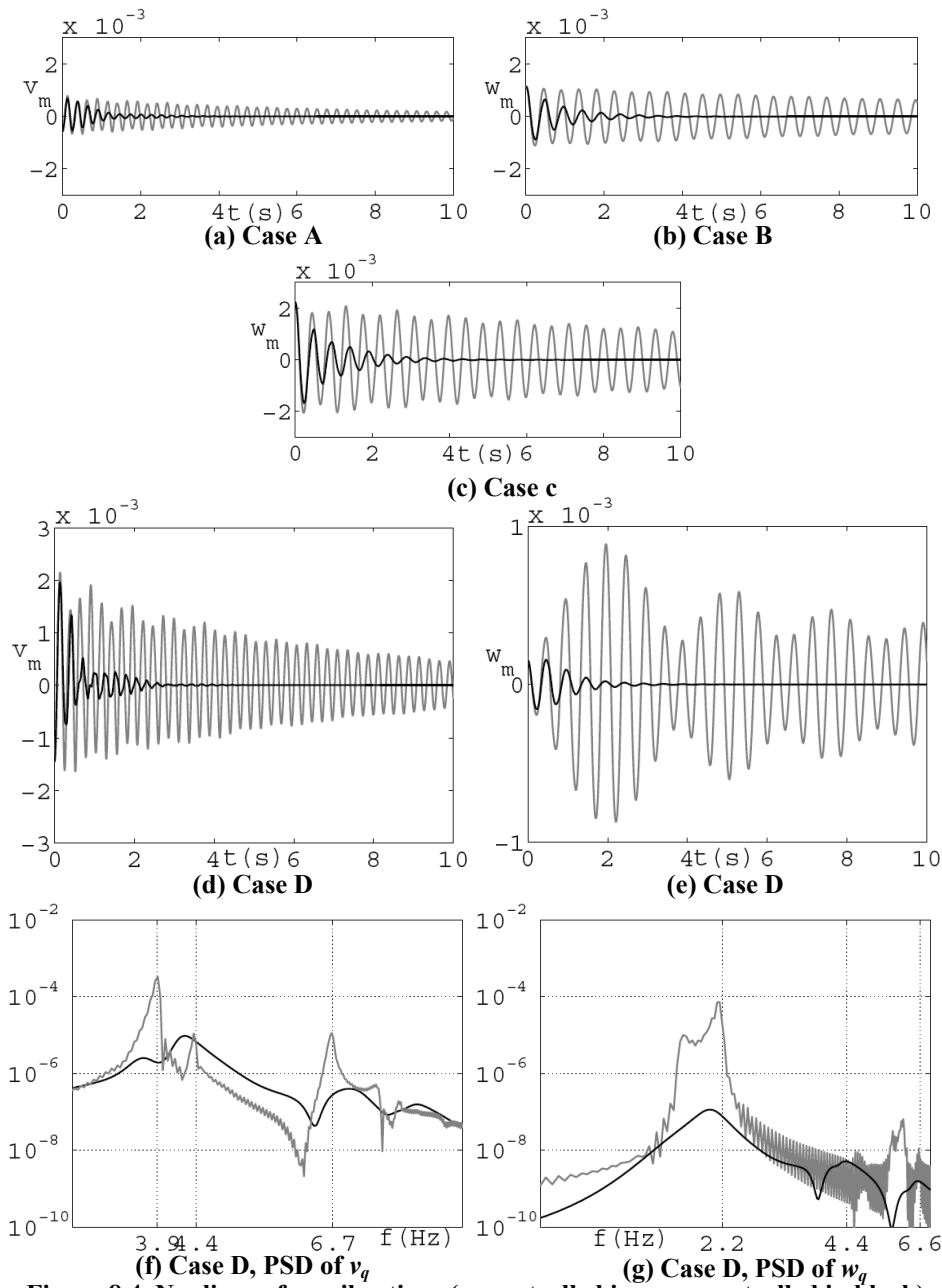
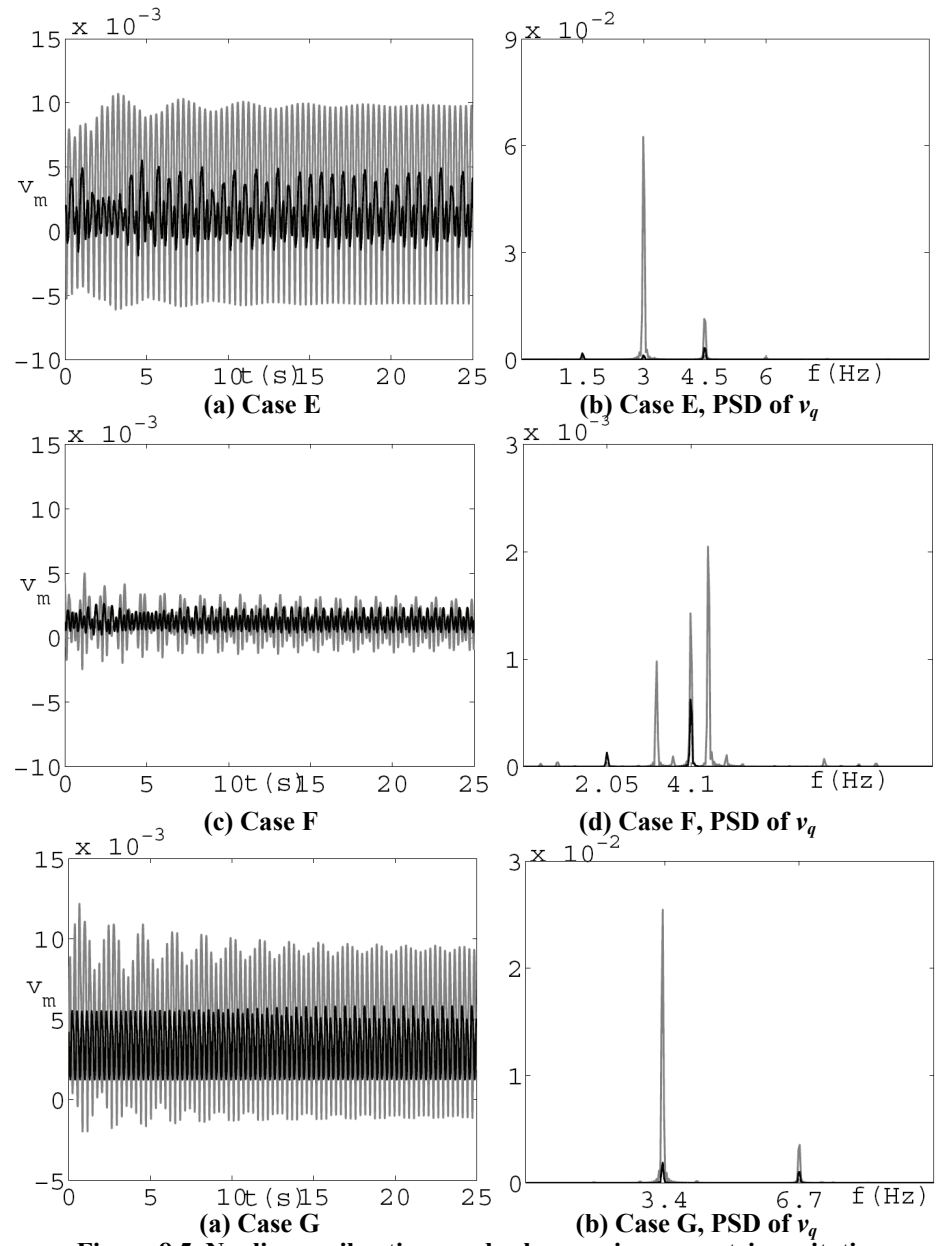


Figure 8.4. Nonlinear free vibrations (uncontrolled in grey, controlled in black)



**Figure 8.5. Nonlinear vibrations under harmonic parametric excitation
(uncontrolled in grey, controlled in black)**

Figure 8.4 shows that a considerable additional damping is introduced in both in-plane and out-of-plane modes by the MPD controller. Moreover the control effectiveness seems to be independent from the amplitudes of vibration. Case D is of particular interest and the results concerning such a case are analyzed in Figure 8.4 with higher detail. Figure 8.4 (f) shows that the second and the third in-plane modes (having frequencies of 4.37 Hz and 6.68 Hz, respectively) also participate to the motion. Moreover a significant spatial oscillation occurs in the same case, as observable in Figure 8.4 (e). Figure 8.4 (g) shows that such a motion is mainly concerning the first out of plane mode (2.18 Hz). This is probably due to the bifurcation of the first symmetric in-plane mode into a bi-modal spatial oscillation. Finally, Figures 8.4 (f) and (g) show that the first three peaks of the PSD of v_q and w_q are smoothed in the controlled case. It must be mentioned that, in the presented results, five nodal observations and the use of eight modes in the controller prevent control spillover from occurring. Less terms, on the contrary, are seen to determine control spillover at large vibration amplitudes.

Three cases of harmonically forced oscillations are also considered, as reassumed in Table 8.2. The external excitation is represented by the horizontal harmonic motion of one support $\Delta x_0(t)$ (parametric excitation), having normalized amplitude $\tilde{\Delta x}_0 = \Delta x_0 \cdot EA/IH$ and circular frequency ω . The value ω_1^y , in Table 8.2, indicates the natural circular frequency of the first in-plane symmetric mode ($\omega_1^y = 24.7$ Hz). The amplitude of the imposed horizontal displacement is chosen in such a way that the cable dynamics, under forced oscillations, is dominated by nonlinear phenomena. The excitation frequencies are such that: case E is between the superharmonic ($\omega/\omega_1^y = 0.5$) and the primary resonances with the first in-plane mode; case F is close to the primary resonance and case H is in resonance with the third in-plane mode. Near zero initial conditions are assigned to the system in the three cases.

The results show that stable motions take place, after the initial transitory, in both uncontrolled and controlled cases. In particular, the control action is seen able to highly reduce the vibration amplitudes in all the considered cases. Large in-plane uncontrolled vibrations are observed in case E, due to the vicinity of

the primary resonance (see Figure 8.5 (a)). The PSD of v_q in case E, shows that the uncontrolled motion mainly possesses the forcing frequency ($f=3$ Hz) plus a super-harmonic component $f3/2$ and a sub-harmonic one $f/2$. In the controlled case the forcing peak and the super-harmonic one are drastically reduced, while the small sub-harmonic peak remains almost unchanged. In case F the cable motion is characterized by small vibration amplitudes. The uncontrolled motion, in such a case, is composed by the forcing frequency ($f=4.1$ Hz) and the two harmonics corresponding to the first two in-plane modes. A small sub-harmonic component $f/2$ is also detected. In this case, therefore, the uncontrolled response is quasi-periodic, since it contains incommensurate frequencies (i.e. their ratios are irrational numbers). The controlled response, on the contrary, is periodic and contains the forcing frequency plus the subharmonic component $f/2$.

Case	E	F	G
$\tilde{\Delta}x_0$	0.55	0.55	0.55
ω / ω_1^y	0.76	1.04	1.70

Table 8.2. Analysis cases for parametric harmonic excitation

In order to give a deeper insight into the problem, a Galerkin model with 4 in-plane and 4 out-of-plane degrees of freedom is also adopted, as it practically catches the whole dynamics of the system (Ubertini, 2008). Cable C^2 is considered as the case study. The frequency response curves of the first in-plane and out-of-plane modes, obtained by means of an arclength continuation implemented in a dedicated software (AUTO 2000 by Doedel, E.J., et al.), are reported in Figure 8.6. A harmonic input of normalized amplitude $p=0.003$ and frequency ratio ω / ω_1^y enters the equation of the first in-plane or out-of-plane mode. Higher order modes are not retained at this preliminary stage. The results confirm the capability of the proposed approach to reduce the vibrations of the first two modes, in the highly nonlinear regime. In particular, the control action introduces a significant additional damping in the system, leading to a strong reduction of either the hardening peaks at primary resonance and the

superharmonic peaks. It must be mentioned, however, that the control action may locally increase the response with respect to the uncontrolled solution, such as, for instance, in the region around $\omega / \omega_1^y = 0.7$.

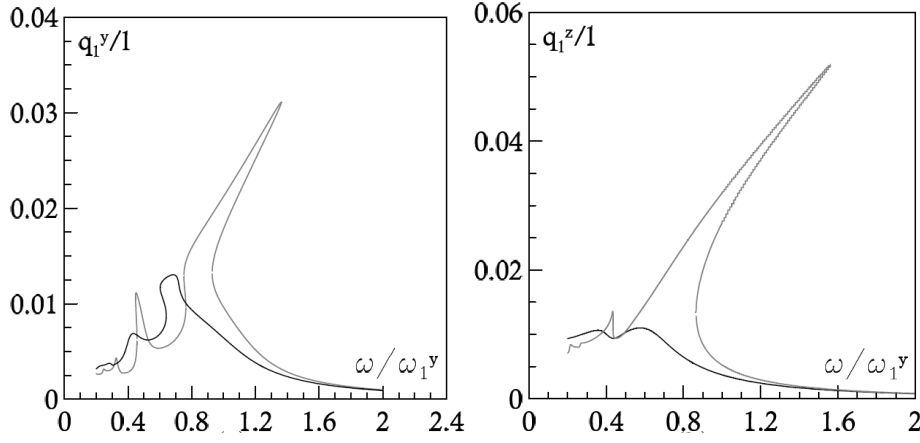


**Figure 8.6. Frequency response curves of cable C₂ with amplitude $p=0.003$
(uncontrolled response in grey, controlled response in black)**

The solutions at primary resonance ($\omega / \omega_1^y = 1.0$) obtained for a larger amplitude $p=0.005$ by means of the 8-dimensional Galerkin cable model, are reported in Figures 8.7 and 8.8. In the case of forced in-plane vibrations (Figure 8.7) a bifurcated spatial motion takes place in the uncontrolled case. The control action confirms its capability to stabilize the cable response in its plane. However, Figure 8.7 (c) shows that the second in-plane mode takes part to the motion in the controlled response, which is not the case in the uncontrolled one. This confirms that higher order modes may participate to the motion in the controlled case. Figure 8.7 (d) shows that the subharmonic frequency $f/2$ arises in the controlled in-plane harmonic response as a consequence of a period doubling bifurcation, $f=4.584$ Hz being the forcing frequency. The solution at primary resonance under out-of-plane harmonic loading is analyzed in Figure 8.8. The results confirm that the control action is able to mitigate the spatial response of the cable. It must be observed that subharmonic frequencies do not arise in the out-of-plane response, which possesses the only forcing frequency.

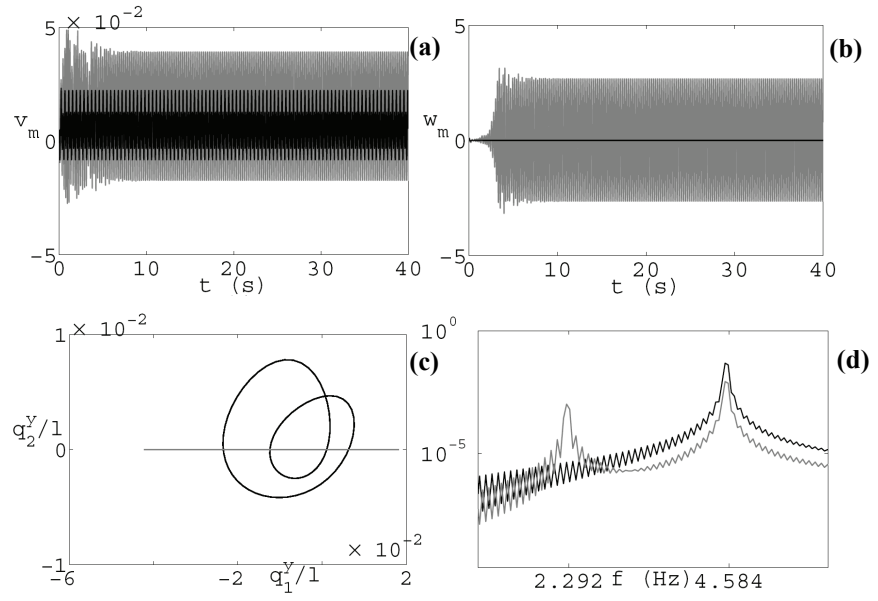


Figure 8.7. Harmonic vibrations under in-plane loading ($\omega/\omega_I=1.0$, $p=0.005$)

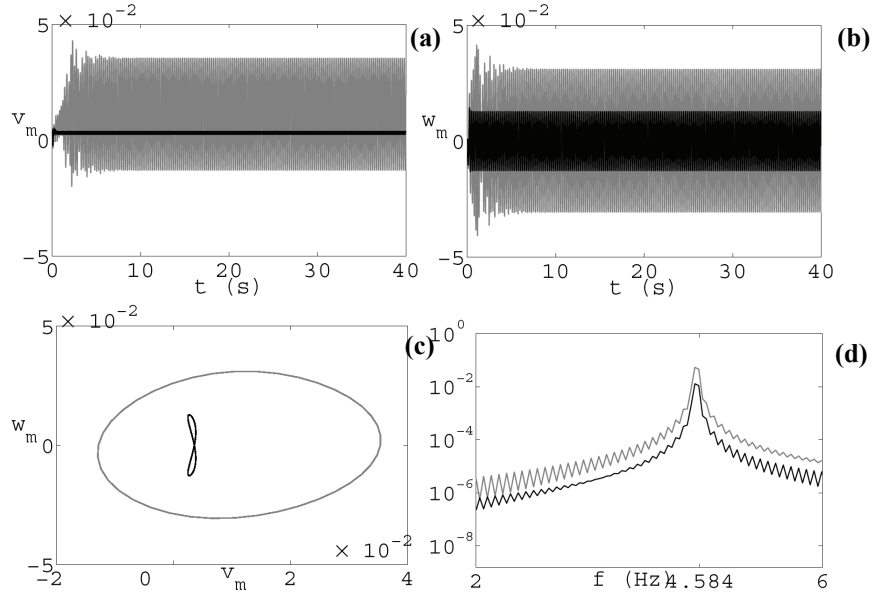


Figure 8.8. Harmonic vibrations under out-of-plane loading ($\omega/\omega_I=1.0$, $p=0.005$)

8.4 Adaptive solution for intelligent cable vibration mitigation

An open loop control strategy and a distributed passive strategy are proposed and combined together in a hybrid control solution. The control effectiveness is analyzed through a theoretical investigation and an experimental verification conducted on the physical cable model C^2 presented and identified in Appendix C.

8.4.1 Semi-active control policy via nonlinear energy transfer

In the proposed open loop actuation a transversal vertical control actuator, represented by a linear motor, is placed in the vicinity of one of the cable ends (at a distance x_c) and exerts the control force F_c (see Figure 8.9). The aim is to mitigate the cable response in the strongly nonlinear regime, i.e. when it is characterized by large limit cycles.

The external excitation is represented by a point load F_F applied at a distance x_f from one of the cable ends (see Figure 8.9). Asymmetry of the external load with respect to the cable mid-span ensures excitation of both symmetric and anti-symmetric modes.

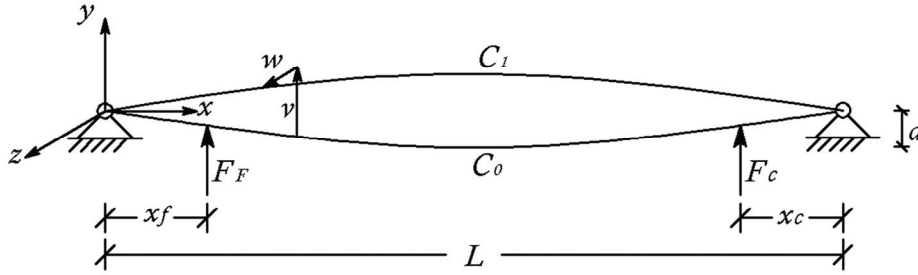


Figure 8.9. Control architecture

The main idea of the fully open loop control strategy here proposed is to exploit the nonlinear couplings between modes, appearing in the analytic Equations of motion, for control purposes. The aim is to make the vibration energy flow from low order modes to higher order ones. By operating in this

way, the motion is driven towards alternative dynamic regimes characterized by lower vibration amplitudes.

The following open loop control law, based on a sinusoidal transversal control force, is adopted:

$$F_c = \bar{F}_c \sin(2\pi \cdot f_c \cdot t + \phi_c) \quad (8.4.1)$$

where \bar{F}_c is a user-defined constant. Amplitude, frequency and phase of the control force, in Equation (8.4.1), must be chosen as discussed below. Clearly, the open loop controller cannot mitigate a linear response and thus the control actuator is activated only when the cable is undergoing large amplitude nonlinear vibrations. To this end, a convenient representative measure of the vibration amplitude must be chosen, depending on the modes that have to be controlled. As an example, the amplitude of the vertical movement of the point placed at the quarter span of the cable can be adopted as a measure of the vibration amplitude considering both the first and the second in-plane modes.

The capability of the control force to reduce the amplitudes of vibration of the system in the strongly nonlinear regime is discussed below by assuming a harmonic external excitation F_F . However, the presented results can be directly extended to the case of non-harmonic external loads.

The frequency of F_F is varied in the vicinity of the primary resonance with the first and the second in-plane modes. By operating in this way, the first two in-plane modes are directly excited by the external load, although higher order modes are also activated. Spatial motions may ensue from dynamic equilibrium bifurcations.

The system identification reported in Appendix C has shown that the cable C^2 is not far away for the 1:1 internal resonance between the first and the second in-plane modes. Moreover, the classic 1:2 resonance between the first and the third in-plane modes arises. Thus, a strong dynamic exchange is expectable between these modes due to well-known linear and nonlinear mechanisms (Rega, 2004).

Suppose, for instance, that the cable is forced by an external load F_F having frequency f close to the primary resonance with the first in-plane mode. Then,

the motion of the first mode is dominating the response with a leading harmonic component of frequency f . In the nonlinear regime superharmonic components with frequencies $2f$, $3f$ etc. appear in the responses of higher order modes due to the nonlinear (quadratic and cubic) couplings with the first mode, which appear in the analytic Equations of motion (see Appendix C). This means that some of the energy associated with the motion of the first mode flows naturally to higher order modes.

The proposed control strategy is meant to enhance this behavior by pushing the vibration energy towards higher order modes in the form of superharmonic components. In order to understand how this mechanism reflects in a reduction of the overall cable displacements, let us consider the case in which the vibration energy is constant. In such a case, being the kinetic energy proportional to the square of the product between the frequency and the vibration amplitude, increasing the frequency of the response reflects on a reduction of the displacement amplitudes. It must be mentioned, however, that the energy of the system is not constant as energy is supplied by the control actuator. This circumstance limits the maximum effectiveness of the open loop controller and indicates that an optimum value of \bar{F}_c exists. Moreover, the dependence of the energy of the uncontrolled response on the amplitude of vibration, i.e. on the region of the dynamic excitation F_F , entails that the optimum value of \bar{F}_c is also depending on these parameters.

In the considered case, the nonlinear couplings between the third and the first in-plane modes are enhanced by the 2:1 internal resonance condition. Thus, it seems convenient to tune the control force in such a way to make the energy flow from the latter to the former. In order to do so, the third mode must be excited by the control force such that the harmonic component with frequency f_c dominates the response of this mode without significantly exciting any other mode through linear or nonlinear mechanisms. A possible solution is to choose f_c as a multiple of the natural frequency of the third mode f_3 . The vicinity of the 1:1 resonance between the first and the second in-plane modes also ensures

that reducing the vibration amplitude of the first mode reflects on a reduction of the vibration amplitude of the second mode as well.

In the considered case study, the frequency of the controller is chosen such that $f_c \equiv 2f_3$. In particular, the value $f_c=18$ Hz is assumed ($f_c / f_3 = 1.75$) since it is clear from any natural frequency of the system (see Appendix C) and it is neither a multiple of f_1 nor of f_2 . Independence on the phase of the control force is desired and thus the value $\Phi_c=0$ is assumed without loss of generality.

8.4.2 Cable vibration mitigation via added SMA wires

A second approach for mitigating the cable response is to increase the modal damping of the structural system by wrapping a SMA wire (Casciati et al., 2008) along the cable. By operating in this way, one achieves a mitigation solution which is distributed along the cable and, hence, it is not affected by the device localization. Previous tests (Casciati et al., 2008) were realized by wrapping the SMA pre-stressed wire once, twice, etc. around the steel cable until the configuration offering the best increment in the modal damping value was found. In this paper, after having found the best system configuration, the cable response under forced in-plane excitation is analyzed, by varying the pretension force H in the SMA wire.

8.5 Analytical prediction and numerical validation

Before describing the experimental results, an analytical prediction and a numerical verification of the effectiveness of the open loop control strategy are proposed. To this end, a Galerkin model with four in-plane degrees of freedom is considered having the characteristics of the identified cable. The nonlinear equations of motion of this model are given in Appendix C. The large dimensional finite element (FE) model of the system described in Appendix C is also adopted. A Rayleigh damping matrix scaled on the experimentally identified damping parameters of the cable is assumed in this model.

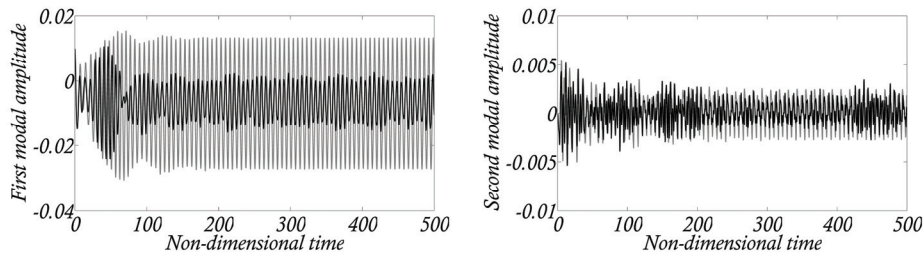


Figure 8.10. Analytic results: time histories of uncontrolled (grey lines) and open loop controlled (black lines) motions under harmonically forced excitation F_F in resonance with the first in-plane mode

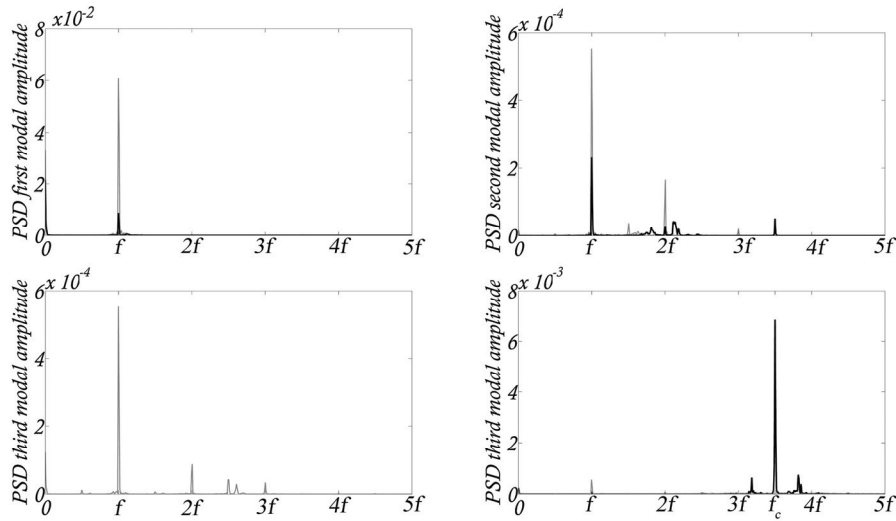


Figure 8.11. Analytic results: PSD functions of uncontrolled (grey lines) and open loop controlled (black lines) motions under harmonically forced excitation F_F in resonance with the first in-plane mode

The response to primary resonance excitation is studied at first using the analytic model. Particularly, the external load F_F is chosen to be harmonic in resonance with the first in-plane mode. The initial conditions and the amplitude of F_F are chosen in such a way that the cable attains the maximum response in the frequency response curve and that nonlinear phenomena are dominating the motion. Figure 8.10 shows the response of the first two in-plane modal

amplitudes q_1^v and q_2^v obtained by integrating the Equations of the Galerkin model in time by means of a fourth order time integrator. The uncontrolled solution is indicated by grey lines while the controlled solution is indicated by black lines. As customary in cable dynamics, the normalized time, in Figure 8.10, is obtained by multiplying the physical time by the circular frequency of the first in-plane mode.

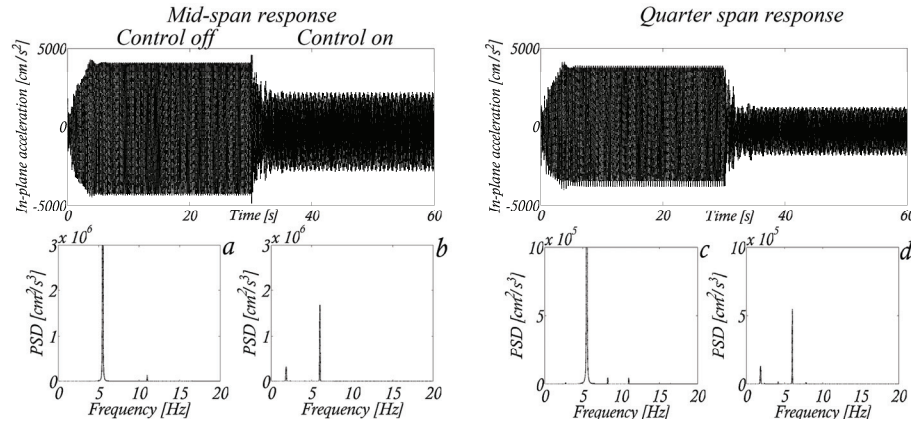


Figure 8.12. Numerical results: time histories of mid-span and quarter span displacements under harmonically forced excitation F_F in resonance with the first in-plane mode, before and after the application of the open loop control input (top); corresponding PSD of mid-span and quarter span displacements (bottom): uncontrolled interval (a), (c), open loop controlled interval (b), (d).

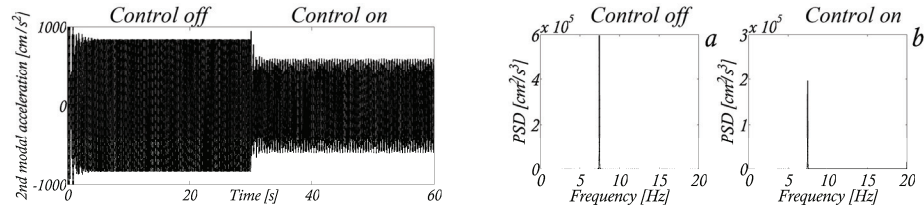


Figure 8.13. Numerical results: time history of second in-plane modal displacement under harmonically forced excitation F_F in resonance with the second in-plane mode (left); PSD of second in-plane modal displacement (right): uncontrolled interval (a); open loop controlled interval (b)

The results presented in Figure 8.10 emphasize that, as expected, the control force is able to strongly reduce the response of the first mode. A significant reduction of the amplitude of the second mode is also pointed out. The frequency analysis of the obtained results is shown in Figure 8.11 and confirms that the control force mainly excites the third mode with significant beneficial effects on both the first and the second modes. The presence of superharmonic components in the PSD of the second and the third modes is also emphasized, thus indicating the relevance of nonlinear phenomena in the cable response.

Similar results are obtained by means of the FE analysis. Both resonant cases with the first and the second in-plane modes are considered in this case. The FE analysis reproduces 30 s of uncontrolled forced motion, and successive 30 s of controlled forced motion. The equations of motion of the FE model are integrated by means of a numerical procedure based on the Newmark method. To ensure dynamic equilibrium at the end of the time step, the modified Newton–Raphson method is adopted.

The primary resonant case with the first in-plane mode is considered in Figure 8.12. The presented results emphasize the control effectiveness and evidence, in the controlled response, the presence of the harmonic component with the frequency of the control force (18 Hz). The capability of the controller to reduce the response of the second in-plane modal amplitude is shown in Figure 8.13. Particularly, the forced resonant case with the second in-plane mode is considered in such a case and the effectiveness of the controller in reducing the vibrations of this mode is pointed out. The peak corresponding to the control force is, in this case, not detected by the PSD analysis since, as analytically expected, the controller mainly excites the third in-plane mode.

8.6 Experimental results

A campaign of experimental tests has been carried out to evaluate the effectiveness of the proposed control solutions either separately and combined together. To this end, the forced oscillations of the cable under harmonic in-plane excitation F_F have been considered. For every test, the recorded signals have a sampling frequency of 250 Hz.

The experimental tests have been conducted in three stages:

- stage 1: cable without the wrapped SMA wire;
- stage 2: cable with the wrapped SMA wire;
- stage 3: hybrid solution.

8.6.1 Cable without the wrapped SMA wire

The case of the cable without the wrapped SMA wire is preliminary considered. In order to analyze the forced response of the system close to the primary resonance with the first in-plane mode the frequency f_f of the harmonic forcing load F_F is tuned, at first, to the value of 5.5 Hz. At this given frequency the open loop controlled response is compared to the uncontrolled one. The recorded time history of the in-plane mid-span acceleration component is shown in Figure 8.14. The presented results evidence the immediate effect which can be obtained just after turning on the open loop controller (the controller is turned on at time=30s). Figure 8.14 also shows the PSD of the acceleration record, which reveals that the control action is capable to reduce the main harmonic component of the response as well as to practically eliminate superharmonic and subharmonic components. The open loop controller is thus seen able to mitigate the nonlinear harmonically forced vibrations of the cable at the primary resonance with the first in-plane mode.

In order to investigate the effectiveness of the open loop controller in different regions of external excitation, the frequency response curves (*frcs*) to in-plane excitation are also considered. The *frcs* represent the amplitudes of the steady uncontrolled and controlled responses, normalized to the maximum values, as functions of the frequency of the external load F_F . The results are presented in Figure 8.14 by considering both in-plane and out-of-plane accelerations. In the uncontrolled cases two curves are presented which are obtained through forward and backward sweepings of the frequency. The presented results evidence that the uncontrolled response is significantly hardening close to the primary resonance. This circumstance emphasizes that the uncontrolled motion is dominated by nonlinear phenomena. The open loop controller is seen able to strongly reduce the response of the system for a wide

range of frequency values. Moreover, the control action cancels the hardening branch and the controlled response exhibits a vertical peak at the primary resonance. This last circumstance confirms that, as expected, the effect of the open loop controller is to inhibit nonlinear phenomena and to drive the system towards a linear behavior. The maximum control effectiveness is obtained, as expected, at the primary resonance with the first in-plane mode.

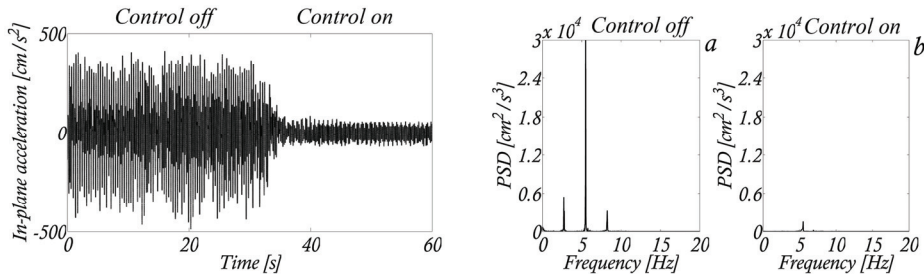


Figure 8.14. Cable without the SMA wire: experimental time history of in-plane mid-span acceleration record under forced in-plane excitation ($f_f=5.5$ Hz) before and after the application of the open loop control input (left); PSD of in-plane acceleration (right): uncontrolled interval (a); open loop controlled interval (b)

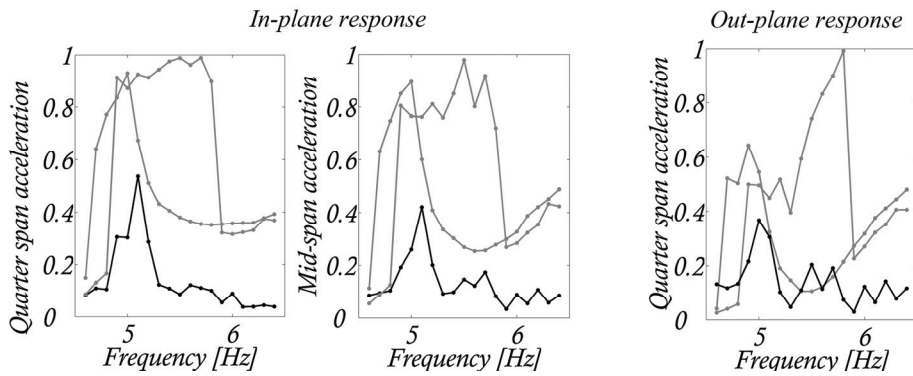


Figure 8.15. Cable without the SMA wire: experimental normalized frcs under in-plane excitation for uncontrolled (grey lines) and open loop controlled (black lines) cases

8.6.2 Cable equipped with the wrapped SMA wire

In the second stage of experimental tests particular attention is paid to the union of the SMA wire with the steel cable. The SMA wire (in austenite phase) of diameter 1 mm is anchored to the same vertical point of the steel cable, and it is fixed at one end by a device that allows to assign a pre-tension force H to the wire but not to the cable.

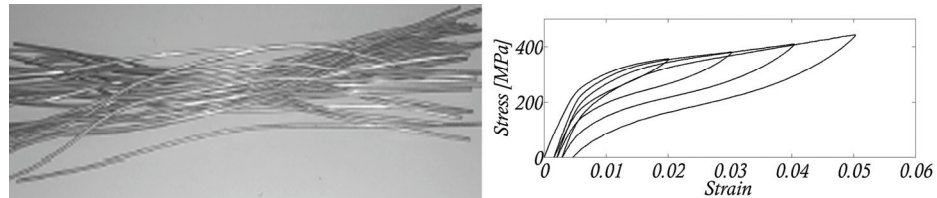


Figure 8.16. Stress-strain diagrams (right) for Cu-based SMA wire of 1 mm diameter (left)

First of all, the behavior of the system while varying the pre-tension in the SMA wire must be examined in order to find the optimal configuration. To this end, the harmonically forced case in resonance with the first in-plane mode is considered. Initially, H is calculated in order to produce a 1% strain into the wire. Then, the pre-tension force H is varied such that the strain in the SMA wire assumes values between the 1% and the 2%. It is worth noting that the 1-2 % interval of strain belongs to the so-called “plateau” of the stress-strain diagram represented in Figure 8.16 for the considered shape memory alloy. This entails that hysteresis is added by the SMA wire but not stiffness.

During the experimental test, the mid-span and the quarter span vertical displacements as well as the pretension force H have been measured by the laser displacement sensors and by the load cell, respectively. The results are presented in Figure 8.17 and emphasize that, as a 2% of strain in the SMA wire is reached, the amplitude of the response attains a minimum. This circumstance entails that the 2% of strain in the SMA wire corresponds to the configuration offering the best increment of the modal damping of the cable. The corresponding pretension in the SMA wire is thus retained in the following experimental tests. In order to stress the hysteretic control mechanism, Figure

8.17 also shows the cycles of the pretension force H plotted versus the mid-span and quarter span displacements of the cable.

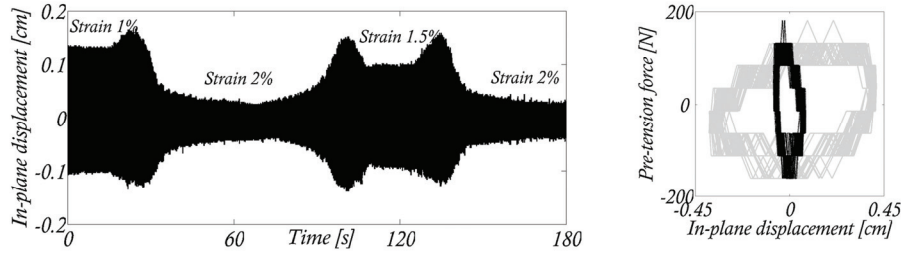


Figure 8.17. Cable with wrapped SMA wire: experimental recorded time history of mid-span displacement under forced in-plane excitation ($f_f=5.5$ Hz) while varying the pre-tension load in the SMA wire (left); SMA pre-tension force vs. displacement diagram (right) for a SMA wire pre-tension corresponding to a 2% strain: the in-plane displacement denotes the vertical quarter span (grey line) or mid-span (black line) cable displacement

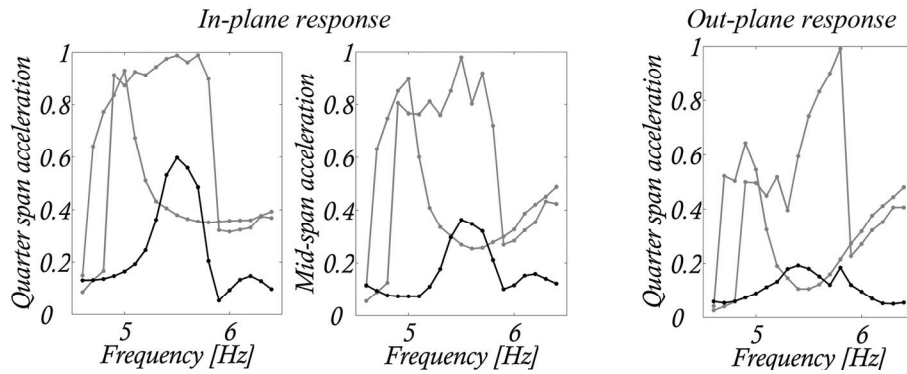


Figure 8.18 Experimental normalized *frfs* under in-plane excitation for uncontrolled (grey lines) and passively controlled utilizing wrapped SMA wire (black lines) cases

The capability of the SMA wire to reduce the harmonically forced response of the cable at different values of the frequency of the external load is pointed out in Figure 8.18 where the *frfs* of the system are presented. The results emphasize that the passive strategy guarantees a control performance which is comparable to the one of the open loop controller. The presented results also

show that, as expected, the SMA wire does not introduce a significant increment of stiffness in the cable. Indeed the frequency shift between the first in-plane modal frequency of the cable and the frequency value at which, in Figure 8.18, the in-plane response of the cable-SMA wire system is maximum is relatively small.

8.6.3 Hybrid solution

The results presented above have shown that the SMA wire introduces a significant amount of damping into the system and that the open loop controller is able to mitigate the large amplitude nonlinear vibrations of the cable. However, the open loop controller cannot mitigate the response in the linear regime and becomes effective only when nonlinearities play a primary role. The hybrid solution can overcome this drawback. Indeed, in most cases, the added damping is sufficient to mitigate the cable motion. Nonetheless, in the most demanding cases, the motion may still reach the nonlinear regime. In such cases, the open loop controller may inhibit nonlinear phenomena and mitigate the cable response.

The effectiveness of the hybrid solution is investigated at different frequency values of the external load. To this end, the $frcs$ of the cable-SMA wire system, with and without the open loop controller, are shown in Figure 8.19. The results outline that, as expected, the hybrid solution mitigates the peak response of the passive case. On the contrary the hybrid solution becomes disadvantageous when the cable response is already strongly mitigated by the passive solution. This was however expected since, as discussed above, the open loop controller is only effective in the nonlinear regime and it should be turned on only when the amplitudes of vibration are large. Similar results are evidenced in Figure 8.20 by comparing the hybrid strategy to the open loop controlled solution without the wrapped SMA wire. Particularly, the hybrid strategy is seen able to increase the effectiveness of the open loop controller in mitigating the vibrations of the cable close to the primary resonance with the first in-plane mode.

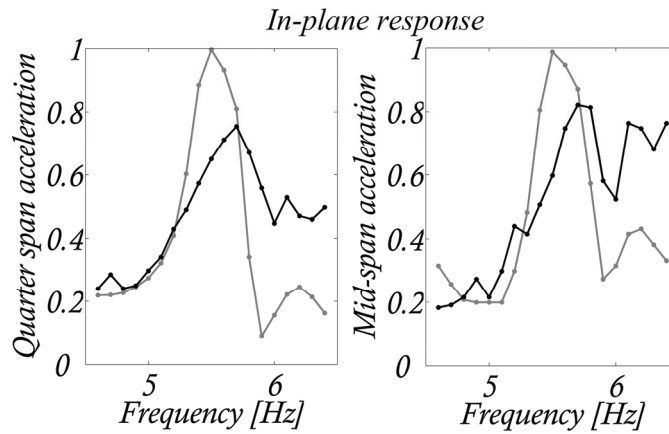


Figure 8.19 Experimental normalized *frcs* under in-plane excitation for passively controlled utilizing wrapped SMA wire (grey lines) and hybrid controlled (black lines) cases

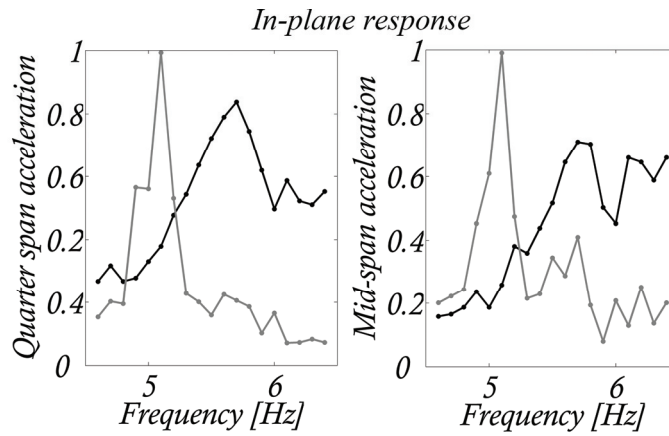


Figure 8.20 Experimental normalized *frcs* under in-plane excitation for open loop controlled without SMA wire (grey lines) and hybrid controlled (black lines) cases

8.7 Concluding remarks

An active state controller and a hybrid control strategy for cable vibration mitigation are conceived.

The effectiveness of the active solution is theoretically investigated. Analytical explicit solutions are derived under free vibrations, in both

uncontrolled and controlled cases. Higher order terms are then introduced in the control law, based on a linear quadratic regulator. A large dimensional geometric nonlinear FE model is coded to analyze the effectiveness of the control strategy and the stability of high order modes. The control action is seen able to reduce the cable vibrations in all the considered cases.

The hybrid control solution is obtained by combining an open loop actuation and a distributed passive solution utilizing wrapped SMA wires. The control actuator is fully open loop and thus it does not need nonlinear state estimation and meets the fundamental requirement of a large control robustness. The control force is designed to enhance the energy exchanges between modes arising in the strongly nonlinear field and to drive the motion towards more safe dynamic regions characterized by lower amplitudes of vibration. An analytical-numerical investigation is preliminary carried out to confirm the capability of the open loop actuator to reduce the harmonically forced nonlinear vibrations of the first two in-plane modes. Experimental results are then presented showing the effectiveness of the control action for a wide range of frequency values of the external load.

The passive solution is not affected by localization and provides a remarkable increment of the cable damping ratios. Experimental results indicate that a 2% of strain in the SMA wire guarantees the maximum passive control effectiveness. By retaining this optimal pre-tension, the effectiveness of the passive solution and of the hybrid solutions are investigated for different frequency values of the external excitation. The results evidence that the passive solution already guarantees a significant mitigation of the harmonically forced nonlinear vibrations of the cable. Moreover, it is confirmed that the hybrid strategy takes advantage of the added damping provided by the SMA wire and, in the meanwhile, it provides a further mitigation of the cable response in all those cases in which the external excitation is particularly severe and demanding leading to large amplitude nonlinear vibrations.

Chapter 9

NONLINEAR STATE OBSERVATION FOR CABLE DYNAMICS

Abstract

The relevant problem of state reconstruction for nonlinear cable dynamics is theoretically solved by introducing a suitable nonlinear state observer. The feasibility of the adopted observer is investigated and its application to active control is finally discussed.

9.1 Introduction

A very critical point when designing state controllers (Breccolotti et al., 2007) for cable vibration mitigation is the estimation of the cable state variables to be employed in the feedback control law. Usually, in the technical literature, this problem is addressed either by considering heuristic estimates of the state variables based on linear combinations of the nodal measurements, or by adopting linear representations of the mechanical system and then employing standard observation techniques proper of linear systems. A more rigorous approach should account for the system nonlinearities in the framework of nonlinear control theory (Isidori, 1985). To this end, in order to minimize the

number of measurements, a state observer has to be designed. However, the presence of quadratic and cubic terms in the equations of motion may likely cause observation error instability (Faravelli and Ubertini, 2007; Ubertini, 2007; Faravelli and Ubertini, 2008).

Because of its practical importance, such as in the case of an insufficient number of sensors, many recent works were devoted, in the literature, to the design of state observers for different kind of nonlinear systems. Without aiming at giving an exhaustive literature review on this large topic, some relevant references are given in (Isidori, 1985; Dalla Mora et al., 2000; Faravelli and Ubertini, 2008).

In this Chapter one presents a theoretical discussion and some numerical results relating to the application a nonlinear state observer for cable dynamics. More details on this approach can be found in (Faravelli and Ubertini, 2008). The observer is based on the property that the system is observable for zero input (drift-observability) and follows the work reported in reference (Dalla Mora et al., 2000). The simulations are meant to investigate the observation error stability, under different conditions. The non-collocated feedback strategy presented in Chapter 8 is the final application of the state observer.

9.2 Governing relations

The necessary background for modeling the nonlinear dynamics of cables, i.e. the nonlinear equations of motion of the continuous system, the Galerkin discrete approach and the FE representation of the problem, is summarized in Appendix C. Only a few details on state observation for nonlinear dynamical systems are therefore given here.

In order to discuss its applicability to cable dynamics, the main theoretical result presented in reference (Dalla Mora et al., 2000) is briefly recalled. Let a nonlinear dynamical system be given in first order form, as:

$$\begin{aligned}\dot{x} &= f(x(\tau)) + g(x(\tau))u(\tau) \\ y(\tau) &= h(x(\tau))\end{aligned}\tag{9.2.1}$$

where $x(\tau) \in X \subseteq \mathfrak{R}^n$ is the state vector of length n , $f(x(\tau))$ is a $C^\infty(X)$ vector field, $g(x(\tau))$ is a $n \times (n+1)$ matrix whose columns are $C^\infty(X)$ vector fields and $u(\tau) \in U \subseteq \mathfrak{R}^{n+1}$ is the input vector. In the second expression of equations (9.2.1), the vector $y \subseteq \mathfrak{R}^a$ is also introduced, which collects, via the $C^\infty(X)$ function $h(x(\tau))$, the measured outputs. The case in which y has dimension $a=2$ is considered in this Chapter, without loss of generality.

Assuming that the reader is familiar with the concept of Lie derivative of a function $\tilde{\lambda}(x)$ along a vector field $f(x)$, the Lie derivative of order c will be indicated, below, by $L_f^c(\tilde{\lambda}(x))$. It is also worth introducing the following definitions of state observation theory, which are also reported in reference (Dalla Mora et al., 2000):

DEFINITION 9.1 The *observation relative degree* r_j of the j -th output of system (9.2.1) in a set $\Omega \subseteq \mathfrak{R}^n$ is an integer such that:

$$\begin{aligned} \forall x \in \Omega : L_g L_f^c h_j(x) &= 0, \quad c = 0, 1, \dots, r_j - 2 \\ \exists x \in \Omega : L_g L_f^{r_j-1} h_j(x) &\neq 0 \end{aligned} \quad (9.2.2)$$

The multi-index $r=(r_1, \dots, r_a)$, being a the number of measured variables, is thus defined and represents the vector of observation relative degree.

DEFINITION 9.2 Let $r=(r_1, \dots, r_a)^T$ be a multi-index such that $\sum_{i=1}^a r_i = n$ and consider the following vector functions:

$$\mathcal{H}_{sj}(x) = \begin{bmatrix} h_j(x) & L_f h_j(x) & \dots & L_f^{s_j-1} h_j(x) \end{bmatrix}, \quad j = 1, \dots, a \quad (9.2.3)$$

The following map is then defined:

$$\mathcal{H}_s(x) = \begin{bmatrix} \mathcal{H}_{s1}(x) & \mathcal{H}_{s2}(x) & \dots & \mathcal{H}_{sa}(x) \end{bmatrix} \quad (9.2.4)$$

The map $\mathcal{H}_s(x)$ is called an *observability map* in a set $\Omega \subseteq \mathfrak{R}^n$ if it is a diffeomorphism in an open set $\overline{\Omega}$ such that $\Omega \subseteq \overline{\Omega}$. By looking at equation (9.2.4) one can note that the map $\mathcal{H}_s(x)$ is given by successive differentiation of the output y for $u(\tau) \equiv 0$:

$$\mathcal{H}_s(x) = (y_1, \dot{y}_1, \dots, y_1^{(s_1-1)}, \dots, y_a, \dot{y}_a, \dots, y_a^{(s_a-1)}) \quad (9.2.5)$$

DEFINITION 9.3 Let $\Omega \subseteq \mathfrak{R}^n$ be a compact set and δ be a real positive number, the set Ω_δ is defined as: $x \in \mathfrak{R}^n : \|x - y\| < \delta, \forall y \in \Omega$.

DEFINITION 9.4 A system that admits an observability map $\mathcal{H}_s(x)$ in a set $\Omega \subseteq \mathfrak{R}^n$ for some multi-index s is said to be *drift-observable* in Ω . If the system is drift-observable in Ω and the maps \mathcal{H}_s and \mathcal{H}_s^{-1} are uniformly Lipschitz in Ω and $\mathcal{H}_s(\Omega)$, respectively, then the system is said to be *uniformly Lipschitz drift-observable* in Ω .

The result here recalled is based on the change of coordinates $\xi = \mathcal{H}_s(x)$, which transforms the system (9.2.1) into the following form:

$$\begin{aligned} \dot{\xi} &= \underline{A}\xi + \underline{B}L(\mathcal{H}_s^{-1}(\xi)) + \underline{F}\underline{H}(\mathcal{H}_s^{-1}(\xi)) \\ y(\tau) &= \underline{C}\xi(\tau) \end{aligned} \quad (9.2.6)$$

where $L(\mathcal{H}_s^{-1}(\xi)) = [L_f^n h_1(x), L_f^n h_2(x)]$, $\underline{A} \in \mathfrak{R}^{s_1+s_2 \times s_1+s_2} = \text{blockdiag}[A_1, A_2]$, $\underline{B} \in \mathfrak{R}^{s_1+s_2 \times 1} = \text{blockdiag}[B_1, B_2]$ and $\underline{C} \in \mathfrak{R}^{1 \times s_1+s_2} = \text{blockdiag}[C_1, C_2]$, where $A_i \in \mathfrak{R}^{s_i \times s_i}$, $B_i \in \mathfrak{R}^{s_i}$ and $C_i \in \mathfrak{R}^{s_i}$ are Brunovsky matrices (Faravelli and Ubertini, 2008). The matrix function $\underline{H}(\mathcal{H}_s^{-1}(\xi))$, in Equation (9.2.6), is defined as:

$$\underline{H}(\mathcal{H}_s^{-1}(\xi)) = \begin{bmatrix} L_g L_f^{r_1-1} h_1(x) & L_g L_f^{r_2-1} h_2(x) \\ \vdots & \vdots \\ L_g L_f^{s_1-1} h_1(x) & L_g L_f^{s_2-1} h_2(x) \end{bmatrix} \quad (9.2.7)$$

while \underline{F} is the following matrix:

$$\underline{F} = \begin{bmatrix} 0_{(r_1-1) \times s_1 - r_1 + 1} & 0_{(r_1-1) \times s_2 - r_2 + 1} \\ I_{s_1 - r_1 + 1} & 0_{s_1 - r_1 + 1 \times s_2 - r_2 + 1} \\ 0_{(r_2-1) \times s_1 - r_1 + 1} & 0_{(r_2-1) \times s_2 - r_2 + 1} \\ 0_{s_2 - r_2 + 1 \times s_1 - r_1 + 1} & I_{s_2 - r_2 + 1} \end{bmatrix} \quad (9.2.8)$$

If one makes the hypothesis that the system (9.2.1) is observable for zero input (drift-observability) in an open set $\Omega \subseteq \mathfrak{R}^n$, the observability map $\mathcal{H}_s(x)$ is a diffeomorphism from Ω to $\mathcal{H}_s(\Omega)$. Its Jacobian $Q(x)$ is thus well defined and its calculation is straightforward. In the framework of nonlinear control theory, a state observer for system (9.2.1) can thus be written as (Dalla Mora et al., 2000):

$$\dot{\hat{x}} = f(\hat{x}(\tau)) + g(\hat{x}(\tau))u(\tau) + Q^{-1}(\hat{x}(\tau))K(y(\tau) - h(\hat{x}(\tau))) \quad (9.2.9)$$

where the over-hat indicates an estimate based on the observed variables, and K is a $n \times a$ gain matrix. The asymptotic properties of the observation error norm $\|x(\tau) - \hat{x}(\tau)\|$ can be studied by transforming the system (9.2.1) in the form reported in Equation (9.2.6), by means of the change of coordinates $\xi = \mathcal{H}_s(x)$.

In order to give the stability properties of the observer (9.2.9), let us assume that the following hypotheses hold true:

1) Bounded-input-bounded-state (BIBS) stability: for any bounded input $u(\tau)$ such that $\|u(\tau)\| \leq u_M \forall \tau > 0$, $x(\tau_0) \in \overline{\Omega} \Rightarrow x(\tau) \in \Omega, \forall \tau > \tau_0$, where $\overline{\Omega}$ and Ω are two compact sets such that $\overline{\Omega} \subseteq \Omega$.

2) a real positive δ exists such that the system is uniformly Lipschitz drift-observable in Ω_δ , with Lipschitz constants $\gamma_{\mathcal{H}_s(\Omega_\delta)}$ and $\gamma_{\mathcal{H}_s^{-1}(\mathcal{H}_s(\Omega_\delta))}$;

3) the matrix functions $L(\mathcal{H}_s^{-1}(\xi))$ and $\underline{H}(\mathcal{H}_s^{-1}(\xi))$, which appear in equation (9.2.6), are uniformly Lipschitz in $\mathcal{H}_s(\Omega_\delta)$ with Lipschitz constants γ_L and γ_H .

Then for a given positive α a $n \times 2$ matrix K , a constant μ and an input bound u_M exist such that:

$$\|x(\tau) - \hat{x}(\tau)\| \leq \mu \exp(-\alpha\tau) \cdot \|x(0) - \hat{x}(0)\| \quad (9.2.10)$$

provided that the initial observation error is such that:

$$\|x(0) - \hat{x}(0)\| \leq \frac{\delta}{\mu} \quad (9.2.11)$$

where $\exp(\cdot)$ denotes the exponential function and it results:

$$\mu = \sqrt{\frac{\lambda_{\max}(P)}{\lambda_{\min}(P)}} \gamma_{\mathcal{H}_s(\Omega_\delta)} \gamma_{\mathcal{H}_s^{-1}(\mathcal{H}_s(\Omega_\delta))} \quad (9.2.12)$$

where $\lambda_{\max}(P)$ and $\lambda_{\min}(P)$ are the maximum and minimum eigenvalues of a $n \times n$ matrix P , which is better specified in the following. Without entering in the details of the proof reported in reference (Dalla Mora et al., 2000), it is worth mentioning that the exponential decay of the observation error is related to the existence of a pair (K, P) that solves a H_∞ Riccati-like inequality, being P an unknown $n \times n$ matrix. This issue can be addressed by choosing the gain matrix with the form $K = \text{blockdiag}[K_1, K_2]$, where $K_i(\lambda_i) = [k_{i1}, k_{i2}, \dots, k_{isi}]^T$ is the vector gain that assigns eigenvalues $\lambda_i = [\lambda_{i1}, \lambda_{i2}, \dots, \lambda_{isi}]^T$ to the i -th block $A_i - K_i C_i$, A_i and C_i being the Brunowsky matrices. If the eigenvalues of each block are distinct, this is diagonalized by a *Vandermonde* matrix $V(\lambda_i)$. Here the eigenvalues of each block $A_i - K_i C_i$ are chosen in the form $\lambda_i(\sigma, \rho) = -\sigma[\rho, \rho^2, \dots, \rho^{si}]^T$, σ and ρ being two positive real numbers.

9.3 State observation for cable dynamics

9.3.1 Nonlinear state observer design

In order to apply the nonlinear observer (9.2.9) to cable dynamics, the equations of the Galerkin model (see Appendix C) must be rewritten in the first order form (9.2.1). This can be achieved by defining the state vector $x(\tau) \in X \subseteq \mathfrak{R}^n$, which has length $n = 2 \cdot (k + m)$, and the input vector $u(\tau) \in U \subseteq \mathfrak{R}^{n+1}$ as:

$$\begin{aligned}
x(\tau) &= (q_1(\tau), \dots, q_k(\tau), p_1(\tau), \dots, p_m(\tau), \\
&\quad \dot{q}_1(\tau), \dots, \dot{q}_k(\tau), \dot{p}_1(\tau), \dots, \dot{p}_m(\tau))^T \\
u(\tau) &= (\pi_1^y, 0, \dots, 0, \varphi_{1cv}, \dots, \varphi_{kcv}, \varphi_{1cw}, \dots, \varphi_{mcw})^T
\end{aligned} \tag{9.3.1}$$

where the components of vector u are the first in-plane symmetric modal load π_1^y and the modal components φ_{icv} and φ_{icw} of the control forces F_{cv} and F_{cw} (see Chapter 8). The vector field $f(x)$ and the matrix function $g(x)$, that appear in equation (9.2.1), in the case of cables reduce to:

$$\begin{aligned}
f_i &= x_{i+n/2} \quad \forall i = 1, \dots, n/2 \\
f_{i+n/2} &= -\sum_{j=1}^k a_{0ij} x_j - \Xi_i^v x_{i+n/2} - \\
&\quad \left(a_{1i} + \sum_{j=1}^k a_{2ij} x_j \right) \bar{e}(x) \quad \forall i = 1, \dots, k
\end{aligned} \tag{9.3.2a}$$

$$\begin{aligned}
f_{i+n/2} &= -\omega_{(i-k)w} x_i - \Xi_{(i-k)}^w x_{i+n/2} - \\
&\quad a_{3(i-k)} x_i \bar{e}(x) \quad \forall i = k+1, \dots, k+m \\
g(x(\tau)) &= \begin{bmatrix} 0_{n/2 \times 1} & 0_{n/2 \times n/2} & 0_{n/2 \times n/2} \\ (1, 0, 0, 0)^T & 0_{n/2 \times n/2} & I_{n/2 \times n/2} \end{bmatrix}
\end{aligned} \tag{9.3.2b}$$

The crucial point for the derivation of the observer (9.2.9) is to find the observability map $\mathcal{H}_s(x)$ and its Jacobian $Q(x)$. In order to do so, one must specialize the function $h(x)$ which defines the vector of the observed variables y . In the successive developments one considers the case in which y is composed by the in-plane and out-of-plane displacements v_θ and w_θ at a monitored point along the cable. Thus, the vector of the measured variables can be written as $y = \bar{C}x$ where \bar{C} is a $2 \times n$ matrix (Faravelli and Ubertaini, 2008). Looking at equations (9.3.2), one can recognize that the vector of observation relative degree is $r=(2,2)^T$. Without loss of generality, the observability map $\mathcal{H}_s(x)$ is here computed by defining the multi-index s as $s=(2k, 2m)^T$. It is worth noting

that the relevant result recalled in Section 9.2 does not require reconstructability for any input u but only observability for zero input (drift-observability). Therefore, it applies also to the case in which $s > r$ componentwise which, indeed, is the case of Galerkin cable models with $k, m > 1$. Thus, without loss of generality, one here assumes $k = m = 2$ and calculates the necessary Lie derivatives for the derivation of $\mathcal{H}_s(x)$ as:

$$\begin{aligned}
L_f h_1 &= \phi_1^0 x_5 + \phi_2^0 x_6 \\
L_f^2 h_1 &= -\phi_1^0 [a_{011} x_1 + \Xi_1^v x_5 + (a_{11} + a_{211} x_1) e(x)] - \\
&\quad \phi_2^0 [a_{022} x_2 + \Xi_2^v x_6 + a_{222} x_2 e(x)] \\
L_f^3 h_1 &= -[\phi_1^0 a_{011} + \phi_1^0 a_{211} e(x) + \\
&\quad (\phi_1^0 a_{11} + \phi_1^0 a_{211} x_1 + \phi_2^0 a_{222} x_2) e_{,1}(x)] x_5 - [\phi_2^0 a_{022} + \phi_2^0 a_{222} e(x) + \\
&\quad (\phi_2^0 a_{222} x_2 + \phi_1^0 (a_{11} + a_{211} x_1)) e_{,2}(x)] x_6 - [\phi_1^0 (a_{11} + a_{211} x_1) + \\
&\quad \phi_2^0 a_{222} x_2] (e_{,3} x_7 + e_{,4} x_8) + \Xi_1^v \phi_1^0 [a_{011} x_1 + \Xi_1^v x_5 \\
&\quad + (a_{11} + a_{211} x_1) e(x)] + \Xi_2^v \phi_2^0 [a_{022} x_2 + \Xi_2^v x_6 + a_{222} x_2 e(x)]
\end{aligned} \tag{9.3.3a}$$

$$\begin{aligned}
L_f h_2 &= \psi_1^0 x_7 + \psi_2^0 x_8 \\
L_f^2 h_2 &= -\psi_1^0 [\omega_{1w} x_3 + \Xi_1^w x_7 + a_{31} x_3 e(x)] - \\
&\quad \psi_2^0 [\omega_{2w} x_4 + \Xi_2^w x_8 + a_{32} x_4 e(x)] \\
L_f^3 h_2 &= -[\psi_1^0 a_{31} x_3 + \psi_2^0 a_{32} x_4] (e_{,1} x_5 + e_{,2} x_6) - \\
&\quad [\psi_1^0 \omega_{1w} + (\psi_1^0 a_{31} x_3 + \psi_2^0 a_{32} x_4) e_{,3}(x) + \psi_1^0 a_{31} e(x)] x_7 - \\
&\quad [\psi_2^0 \omega_{2w} + (\psi_1^0 a_{31} x_3 + \psi_2^0 a_{32} x_4) e_{,4}(x) + \psi_2^0 a_{32} e(x)] x_8 + \\
&\quad \Xi_1^w \psi_1^0 [\omega_{1w} x_3 + \Xi_1^w x_7 + a_{31} x_3 e(x)] + \\
&\quad \Xi_2^w \psi_2^0 [\omega_{2w} x_4 + \Xi_2^w x_8 + a_{32} x_4 e(x)]
\end{aligned} \tag{9.3.3b}$$

where the subscript $,i$ denotes differentiation with respect to x_i . The derivation of the single terms of matrix $Q(x)$ is straightforward and their expression is reported in (Faravelli and Ubertini, 2008). Clearly, Q results in a state-

dependent $n \times n$ matrix whose inverse Q^{-1} must be evaluated numerically as a function of the state estimate \hat{x} , which is indeed essential to preserve the relevant asymptotic stability property recalled in Section 9.2. It is also worth noting that matrices Q and Q^{-1} do not depend on the input vector (i.e. are independent on the matrix function g). Thus, considering different external inputs acting on the system is straightforward and does not affect the reported expressions for matrix Q .

Of course, the calculation of Q^{-1} , in technical applications, would lead to time delays that should be taken into account also in the numerical integration of the equations of motion. However, this would lead to a system of differential delay equations (DDEs) which would introduce a greater complexity into the problem. Analyzing such a point in detail goes beyond the aims of the present work, where the numeric calculation of Q^{-1} is performed at any integration step, accounting for the real time value of the state estimate \hat{x} . Looking at the above considerations, the central point for the analytic construction of a nonlinear state observer of the form (9.2.9) for cable dynamics is solved.

9.3.2 Observability conditions

Before going into the numerical results which explore the applicability of the state observer (9.2.9) to cable dynamics, a brief discussion on the observability of the system is worth doing. Specifically, the sufficient conditions for the observability of the cable model linearized in the neighborhood of $x \equiv 0$ (simply referred as *linear system*) can be stated, in order to properly choose the number and the location of the observed variables. Unfortunately, as explained below, these conditions result only necessary in the nonlinear regime.

The linear system is BIBS stable if and only if all the poles of the transfer functions are placed on the left of the imaginary axis. This condition is certainly verified in the uncontrolled case while, in the controlled one, a stabilizing feedback is required (i.e. the stability condition is imposed on the closed-loop transfer functions). Demonstrating that a non-collocated feedback is also stabilizing in the nonlinear regime is not as easy as in the linear case. However, one could design the feedback strategy in the linear system and assume that the

BIBS stability is also valid in the nonlinear case. Numerical results may then be adopted to confirm the adequateness of this hypothesis.

Assumption 2, regarding the system uniformly Lipschitz drift-observability in Ω_δ , is rather strong but indeed essential for the proof of the theorem. To show this property in a rigorous way, one should prove that $\mathcal{H}_s(x)$ is a Lipschitz diffeomorphism from Ω_δ to $\mathcal{H}_s(\Omega_\delta)$, such that the form reported in equation (9.2.6) is well defined. Nevertheless, this would require to find the inverse of the map $\mathcal{H}_s(x)$, which is an extremely difficult if not an impossible task. However, this is rather easy in the linear system. Indeed, by imposing the non-singularity of the observability matrix, one obtains that the linear system is observable in all \mathfrak{R}^n , as expected by linear control theory. Thus $\delta \rightarrow \infty$ and the observer is stable for any value of the initial error. Unfortunately, the observability condition of the linear system is only a necessary condition for the local invertibility of $\mathcal{H}_s(x)$ in the neighborhood of $x \equiv 0$. This turns out immediately by noting that the observability matrix of the linear system coincides with $Q(0)$ (i.e. with the Jacobian of $\mathcal{H}_s(x)$ calculated at $x \equiv 0$). As it is well-known, the local non-singularity of the Jacobian matrix is only a necessary condition for the local invertibility of the map $\mathcal{H}_s(x)$. Therefore no proof exists that $\mathcal{H}_s(x)$ is a Lipschitz diffeomorphism (which, indeed, would entail invertibility in all $\mathcal{H}_s(\Omega_\delta)$) and that assumption 2 holds true. Nevertheless, a possible strategy is to impose the sufficient condition on the linear system and to assume that assumption 2 is satisfied also in the nonlinear case. Numerical results are necessary to confirm, to some extent, the adequateness of such an assumption.

The matrix functions $\underline{H}(\xi)$ and $L(\xi)$, which appear in equation (9.2.6), are given by polynomials and therefore are locally Lipschitz in \mathfrak{R}^n and uniformly Lipschitz in any compact set of \mathfrak{R}^n . Thus assumption 3 is strictly satisfied and, according to the theory, the exponential decay of the observation error is ensured for suitable Ω and δ , provided that the initial error is sufficiently small.

As outlined above, the measured outputs $y_i = h_i(x)$ can be selected by satisfying the condition that the Jacobian $Q(x)$ is nonsingular at the origin $x \equiv 0$. For the linear Hamiltonian system ($\Xi_i^v = 0, \forall i = 1, \dots, k$ and $\Xi_i^w = 0, \forall i = 1, \dots, m$), the observability matrix can easily be derived as $Q(0) = [Q_\Phi; Q_\Psi]$, where:

$$Q_\Phi = \begin{bmatrix} \Phi & 0_{n/2 \times 1} \\ 0_{n/2 \times 1} & \Phi \\ \Phi \underline{\omega} & 0_{n/2 \times 1} \\ 0_{n/2 \times 1} & \Phi \underline{\omega} \\ \vdots & \vdots \\ \Phi \underline{\omega}^{k-1} & 0_{n/2 \times 1} \\ 0_{n/2 \times 1} & \Phi \underline{\omega}^{k-1} \end{bmatrix}, \quad Q_\Psi = \begin{bmatrix} \Psi & 0_{n/2 \times 1} \\ 0_{n/2 \times 1} & \Psi \\ \Psi \underline{\omega} & 0_{n/2 \times 1} \\ 0_{n/2 \times 1} & \Psi \underline{\omega} \\ \vdots & \vdots \\ \Psi \underline{\omega}^{m-1} & 0_{n/2 \times 1} \\ 0_{n/2 \times 1} & \Psi \underline{\omega}^{m-1} \end{bmatrix} \quad (9.3.4)$$

where:

$$\underline{\omega} = \begin{bmatrix} \omega_{1v} & 0 & \dots & 0 \\ 0 & \omega_{2v} / \omega_{1v} & & 0 \\ \vdots & & \ddots & \vdots \\ 0 & \dots & 0 & \omega_{mv} / \omega_{1v} \end{bmatrix} \quad (9.3.5)$$

$$\Phi = [\phi_1^0 \quad \phi_2^0 \quad \dots \quad \phi_k^0 \quad 0_{1 \times n/2}]$$

$$\Psi = [0_{1 \times n/2} \quad \psi_1^0 \quad \psi_2^0 \quad \dots \quad \psi_m^0]$$

In Equation (9.3.5), ϕ_i^0 and ψ_i^0 represent the i -th in-plane and out-of-plane eigenfunctions of the cable calculated at the monitored point. As already mentioned, equation (9.3.4) evaluated for $k=m=2$ coincides with the expression of matrix $Q(x)$, evaluated for $x \equiv 0$. The determinant of matrix $Q(0)$ can be calculated through the Gaussian elimination. After some computations, the following formulas can be given:

$$|\det(Q(0))| = \phi_1^{0^2} \psi_1^{0^2}, \quad k = m = 1 \quad (9.3.6a)$$

$$|\det(Q(0))| = \phi_1^{0^2} \phi_2^{0^2} \psi_1^{0^2} (\omega_{1v} - \omega_{2v}), \quad k = 2, m = 1$$

$$\begin{aligned}
|\det(Q(0))| &= \phi_1^{0^2} \psi_1^{0^2} \psi_2^{0^2} (\omega_{1w} - \omega_{2w}), \quad k=1, m=2 \\
|\det(Q(0))| &= \prod_{i=1}^k \phi_i^{0^2} \prod_{i \neq j=1}^k (\omega_{iv} - \omega_{jv}) \\
\prod_{i=1}^m \psi_i^{0^2} \prod_{i \neq j=1}^m (\omega_{iw} - \omega_{jw}), \quad k, m > 2
\end{aligned} \tag{9.3.6b}$$

From equations (9.3.6), one obtains the following observability conditions:

$$\begin{aligned}
\phi_i^0, \psi_j^0 &\neq 0, \quad \forall i=1, \dots, k \quad \forall j=1, \dots, m \\
i \neq j &\Rightarrow \omega_{iv} \neq \omega_{jv}, \quad \forall i, j=1, \dots, k \\
i \neq j &\Rightarrow \omega_{iw} \neq \omega_{jw}, \quad \forall i, j=1, \dots, m
\end{aligned} \tag{9.3.7}$$

As already observed, the conditions stated by equations (9.3.7) are sufficient for the linear system, but only necessary in the nonlinear case. The first expression of equations (9.3.7) requires the trivial condition that the nodal measurements are not located in modal nodes. The second one requires that the in-plane natural frequencies are all distinct. Such a condition entails that, if the cable is 1:1 internally resonant, one in-plane measurement is not sufficient for the observability of the system. It is worth noting, however, that one in-plane measurement is sufficient when different internal resonant conditions occur, such as the 2:1 case encountered in the identification of the physical model reported in Appendix C. Nevertheless, if the cable is 1:1 internally resonant, two in-plane measurements are at least required. The same condition holds for the out-of-plane natural frequencies as well, as stated in the third expression of equations (9.3.7). However, this condition is always satisfied for cables since the out-of-plane natural frequencies are always distinct as expected by Irvine's theory (Irvine and Caughey, 1974).

9.4 Numerical evaluation of the observer performances

With the aim of exploring numerically the applicability of the observer (9.2.9) to the nonlinear dynamics of cables, the uncontrolled vibrations of the a

sample cable model C^2 representing the physical model identified in Appendix C, are considered. The system is subjected to a harmonic modal in-plane excitation of the form $\pi_1^y = \pi_M \sin(\omega / \omega_1 \tau)$.

9.4.1 Planar motion

At a first stage of investigation, the superharmonic ($\omega / \omega_1 = 0.5$) and primary ($\omega / \omega_1 = 1.0$) forced resonant cases are analyzed with a planar model having 2 degrees-of-freedom (dofs) by adopting the input bound $\pi_M=0.0003$. By assigning to the system the initial conditions summarized in Table 9.1, convergence is achieved when the norm of the initial observation error is close to $0.4 \cdot 10^{-3}$ or smaller. The results are presented in Figures 9.1 and 9.2 where solid lines denote the state variables of the mechanical system (modal amplitudes), while dashed lines denote the estimated ones.

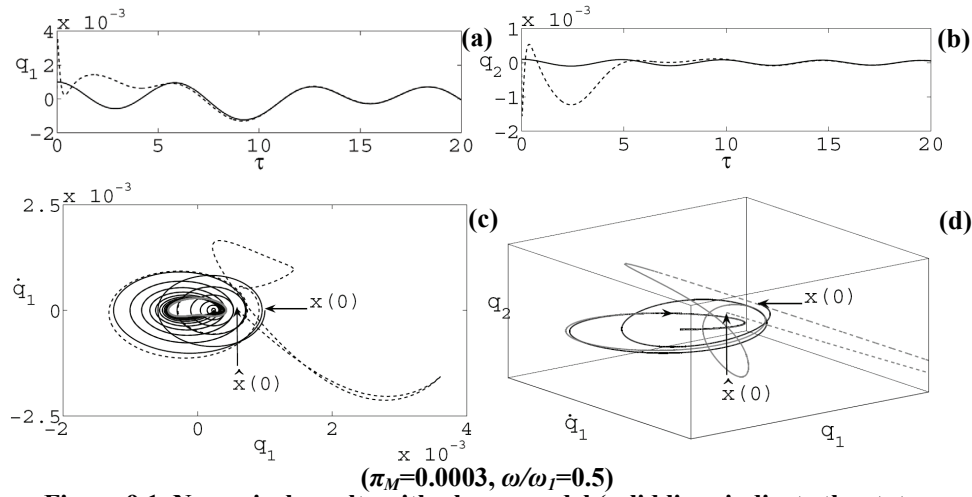


Figure 9.1. Numerical results with planar model (solid lines indicate the state variables of the mechanical system, dashed lines indicate the estimated ones). The solid grey line in (c) indicates the steady limit cycle

Figure 9.1 refers to the superharmonic resonant case ($\omega / \omega_1 = 0.5$), while Figure 9.2 refers to the primary resonant case ($\omega / \omega_1 = 1.0$). In particular,

Figures 9.1 (a) and (b) show the convergence of the estimated state variables to those of the mechanical system in the very initial part of the motion. Figure 9.1 (c) shows a phase portrait of the motion. As it is visible from such a figure, after the initial transitory, the motion becomes steady on a harmonic limit cycle represented by a grey solid line. Clearly, the state variables of the mechanical system and the estimated ones share the same harmonic attractor for $\tau \rightarrow \infty$. A detailed view of the initial transitory in the phase space, is also reported in Figure 9.1 (d), from which one can better evaluate the initial evolution of the observation error.

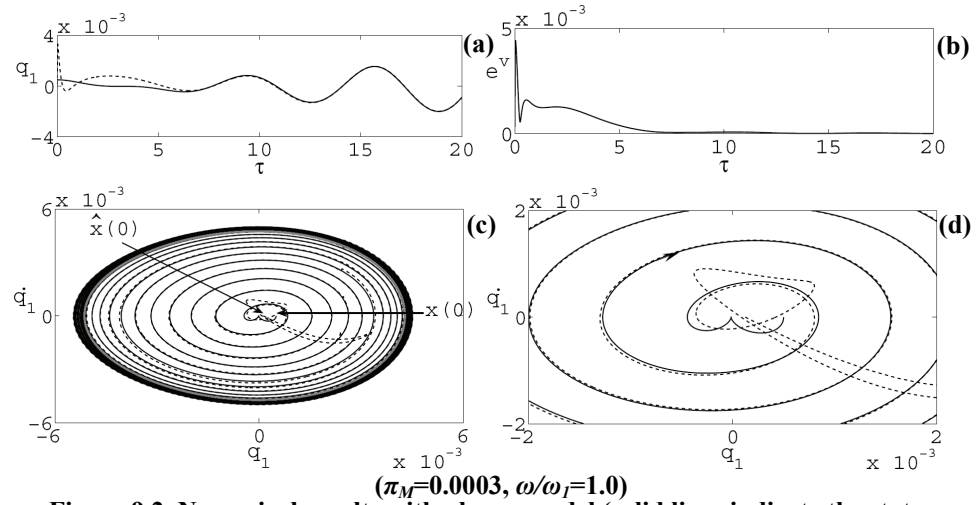


Figure 9.2. Numerical results with planar model (solid lines indicate the state variables of the mechanical system, dashed lines indicate the estimated ones). The solid grey line in (c) indicates the steady limit cycle

ω / ω_1	$q_1(0)$	$q_2(0)$	$\hat{q}_1(0)$	$\hat{q}_2(0)$	$\ x(0) - \hat{x}(0)\ $
0.5	$1.00 \cdot 10^{-3}$	$0.10 \cdot 10^{-3}$	$0.60 \cdot 10^{-3}$	$0.06 \cdot 10^{-3}$	$0.40 \cdot 10^{-3}$
1.0	$0.5 \cdot 10^{-3}$	$0.10 \cdot 10^{-3}$	$0.12 \cdot 10^{-3}$	$0.02 \cdot 10^{-3}$	$0.39 \cdot 10^{-3}$

Table 9.1. Analysis cases for in-plane harmonic loading with planar model
($\pi_M=0.0003, \sigma=0.04, \rho=14$)

Convergence is found to be a little more critic at the primary resonance. In this case, analyzed in Figure 9.2, it is necessary to slightly reduce the initial

conditions (but essentially not the error norm), in order to achieve convergence of the observation error $e^v = \|x(\tau) - \hat{x}(\tau)\|$, where the superscript v indicates that one is referring to the planar case. This seems to confirm that, as expected from the theory, convergence of the observation error is governed by the initial conditions and by the amplitudes of vibration. Particularly, given the initial conditions of the mechanical system, observation error stability is achieved only if the norm $e_0 = \|x(0) - \hat{x}(0)\|$ is sufficiently small. This point is analyzed below, in some detail, by considering the more general tridimensional case.

9.4.2 Spatial motion

Small non-zero initial conditions are always present in technical applications, due to the likely effects of ambient vibrations. Nevertheless, they are hardly measurable and normally one has no indications about which initial conditions should be assigned to the state observer. In order to skip this arbitrarily, it is of interest to analyze the case in which the observer starts with nil initial conditions ($\hat{x}(0) \equiv 0$) while a small perturbation is assigned to the mechanical system. Particularly, it is significant to investigate which is the upper bound of $\|x(0)\|$ in order to achieve observation error stability in the highly nonlinear regime.

As preliminary results, two cases of forced primary resonances with increasing input bounds are analyzed with the spatial model, as reassumed in Table 9.2. The first case is similar to the second one presented in Section 9.6.1, in the sense that one assumes $\pi_M = 0.0003$ and roughly the same initial error norm. The results of the analysis are represented in Figure 9.3. From the presented results one can observe that the participation of out-of-plane modes (and in particular of the first one having amplitude p_1) does not produce error convergence difficulties with respect to the corresponding planar case. However, this could be related to the fact that out-of-plane modes are damped out after the initial transitory and do not take part to the steady motion. In order to better investigate this aspect and to analyze the behavior of the observation error in the strongly nonlinear regime, a larger input bound π_M is assumed in

the second case. Particularly, the value $\pi_M=0.003$ is found to be sufficiently large such that nonlinear phenomena are strongly enhanced. As an example, the frequency response curve of the first in-plane mode, subjected to an in-plane harmonic load with amplitude $\pi_M=0.003$, is reported in Figure 9.4. The results are obtained by means of a continuation technique implemented in the software AUTO (Doedel et al., 2000). From the presented figure, one can recognize that, under the considered amplitude of excitation, the system undergoes large vibrations, characterized by the classic hardening primary resonant peak and by a relatively large superharmonic resonant peak.

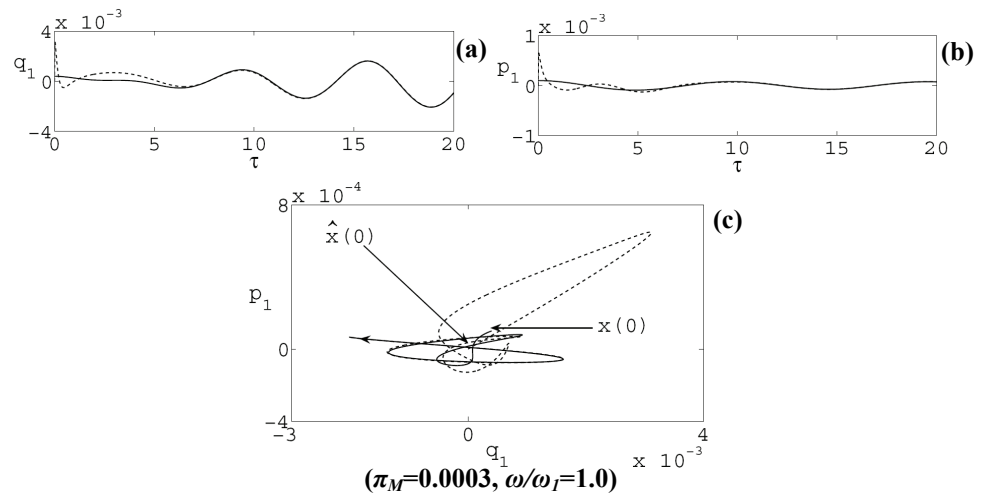


Figure 9.3. Numerical results with spatial model (solid lines indicate the state variables of the mechanical system, dashed lines indicate the estimated ones)

Assuming $\pi_M=0.003$ and $\omega/\omega_1=1.0$ (second case in Table 9.2) leads to the results presented in Figures 9.5 (b)-(d). In such a case a steady motion involving also the first out-of-plane mode ensues from a dynamic equilibrium bifurcation. The enhanced nonlinearity of the problem requires, in this case, to reduce the norm of the initial observation error by roughly 60% with respect to the corresponding case with $\pi_M=0.0003$. This confirms that, as expected from the theory, as the input bound increases the upper bound of the initial error norm decreases. However, as it can be recognized from Figures 9.5 (b) and (c), a

rapid convergence of the estimated state variables to those of the mechanical system is achieved also in this more demanding case. Moreover, as depicted in Figure 9.5 (d), both estimated state variables and those of the mechanical system converge to the same steady attractor as $\tau \rightarrow \infty$.

Before exploring systematically the influence of $\|x(0)\|$ on the stability of the observation error, the third case reported in Table 9.2 is worth considering. The results of such a case are represented in Figure 9.6 and show a particular behavior of the observation error. Namely, after a rapid convergence occurring, as expected, in the very initial part of the motion a sudden instability of the observation error is evidenced, which is recovered after a while. A similar behavior is not expected theoretically but is likely related to numerical errors. These last couple with observation errors and lead sometimes to numerical convergence failures. This may happen though a high order ODE integrator is adopted such as the Runge Kutta method of order 4 here considered.

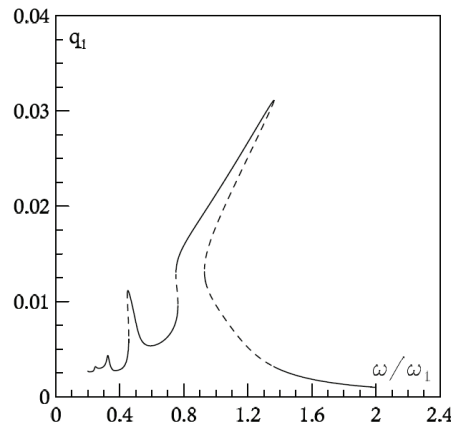


Figure 9.4. Frequency response curve of the first in-plane mode ($\pi_M=0.003$); solid lines denote stable harmonic solutions, dashed lines denote unstable harmonic solutions

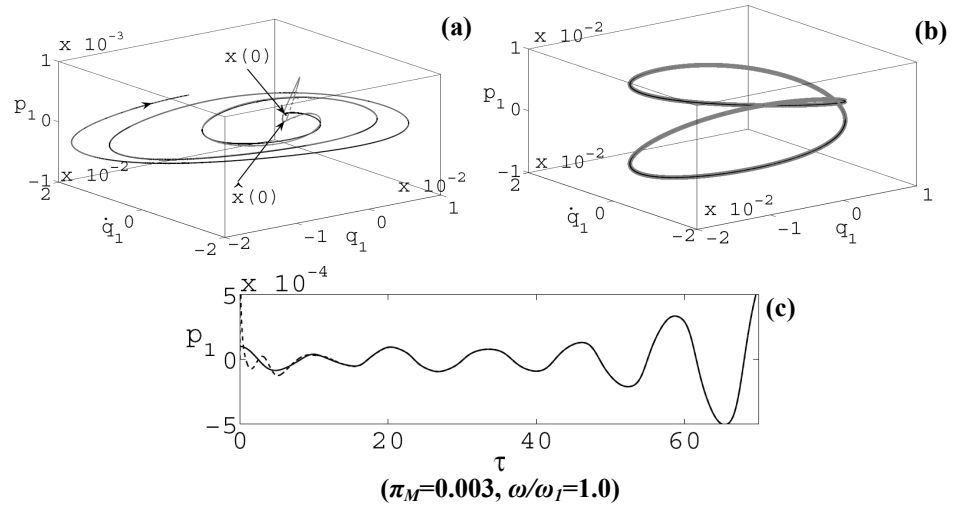


Figure 9.5. Numerical results with spatial model. The solid black line in (a) indicates the state of the mechanical system, the dashed grey line indicates the estimated state. The grey line and the black line in (b) denote the steady limit cycles of the mechanical system and of the estimated state, respectively. The solid line in (c) indicates the state of the mechanical system, the dashed line indicates the estimated state

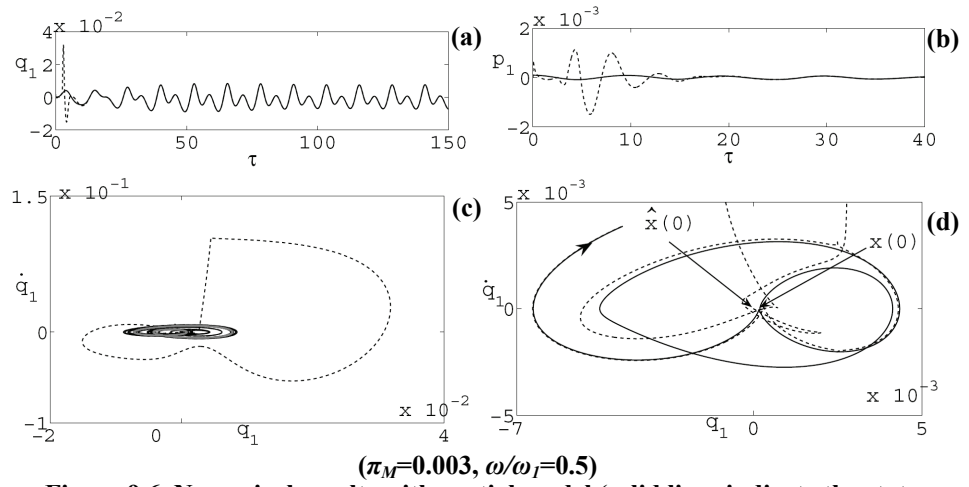


Figure 9.6. Numerical results with spatial model (solid lines indicate the state variables of the mechanical system, dashed lines indicate the estimated ones)

ω / ω_1	π_M	$q_1(0)$	$q_2(0)$	$p_1(0)$	$p_2(0)$	$\ x(0) - \hat{x}(0)\ $
1.0	0.0003	$0.40 \cdot 10^{-3}$	$0.05 \cdot 10^{-3}$	$0.01 \cdot 10^{-3}$	$0.05 \cdot 10^{-3}$	$0.42 \cdot 10^{-3}$
1.0	0.0030	$0.10 \cdot 10^{-3}$	$0.05 \cdot 10^{-3}$	$0.10 \cdot 10^{-3}$	$0.05 \cdot 10^{-3}$	$0.16 \cdot 10^{-3}$
0.5	0.0030	$0.20 \cdot 10^{-3}$	$0.05 \cdot 10^{-3}$	$0.10 \cdot 10^{-3}$	$0.05 \cdot 10^{-3}$	$0.23 \cdot 10^{-3}$

Table 9.2. Analysis cases for in-plane harmonic loading with spatial model: nil initial conditions are assigned to the observer

In order to better investigate the behavior of the observation error, numerical simulations are conducted by varying both the initial observation error norm $\|x(0)\|$ (assuming $\|x(0)\| \equiv 0$) and the frequency ratio of the harmonic modal load. The initial observation error norm is enlarged by increasing the initial conditions assigned to the first in-plane mode, which is the most relevant one since it is directly forced by the modal load. Small initial conditions of $1 \cdot 10^{-5}$ are also assigned to the other modes (q_2 , p_1 and p_2) to allow possible bifurcations to occur. The results are presented in Figures 9.7 (a) and (b), where the map of the observation error e_{rms} is reported. The heavy computational expense of the analysis makes, in this case, a variable order (between 1 and 5) Runge Kutta implicit time integrator preferable with respect to the 4-th order method. Indeed, the variable order scheme is more computationally efficient (the step size and the order are regulated on the basis of the numeric error behavior) but essentially as accurate as the 4-th order method. Thus, one adopts the variable order integrator for obtaining the results presented in Figure 9.7. In this figure the initial observation error norm $\|x(0)\|$ is indicated by e_0 and the error e_{rms} is calculated as the root mean square (rms) of the norm $\|x(\tau) - \hat{x}(\tau)\|$ in the interval $[\tau_{max}/2, \tau_{max}]$, τ_{max} being the total duration of the motion. In the present case one assumes $\tau_{max} = 100$, which is a sufficiently long duration to evaluate the long-term observation error behavior. By operating in the above described way, possible instabilities caused by the coupling of integration and observation errors are also accounted for. Particularly, when numerical instability is encountered (the integrator is unable to meet the integration tolerances before τ_{max}) one conventionally assigns a value e_{max} to the

observation error e_{rms} , e_{max} being the maximum value obtained in the simulations and denoting observation error instability. Thus, white regions ($e_{rms}=e_{max}$) in Figure 9.7 (a), denote instability of the observation error, while black regions denote convergence ($\|x(\tau) - \hat{x}(\tau)\| \rightarrow 0$). Figure 9.7 (b), reports the regions of numerical instabilities. Specifically, white regions denote numerical instability, while black regions denote numerical convergence. In all those cases in which the variable order method encounters convergence difficulties, the 4-th order method is also adopted. Nevertheless, it is worth mentioning that, mostly, the same convergence difficulties are encountered by both methods. Below the above described contour plots, one also reports the maximum amplitudes of the modal displacements q_1 and p_1 (which are not depending on $\|x(0)\|$), evaluated in the interval $[\tau_{max}/2, \tau_{max}]$. Regarding these two last curves, it must be observed that they are not frequency response curves of the system since they are not evaluated in the steady motion. This is the reason why, in the said curves, the hardening branch reported in Figure 9.4 around the primary resonance does not appear. Nevertheless, the behavior of the observation error is not affected by the steady amplitudes of vibration, but it is mainly governed by the transient phase. Thus, the amplitudes q_1 and p_1 , reported below the convergence maps in Figure 9.7, give a good indication of the potential effect of the vibration amplitudes on the observation error stability.

From Figures 9.7 (a) and (b) one can observe that, as expected, there is an upper bound of $\|x(0)\|$ above which convergence of the observation error and numeric stability become critic. However, several white regions are also visible below the above said threshold. Particularly, some of them are distributed in the interval $0.7 < \omega/\omega_1 < 1.0$, which is probably related to the large values that q_1 assumes in this region. Nevertheless, most of the said regions of instability (either numeric or related to the observer) appear at large frequencies (in the interval $1.3 < \omega/\omega_1 < 1.6$), where the vibration amplitudes are relatively small. This indicates the high sensitivity of the system to the frequency content of the input. Such a circumstance is probably related to the fact that, locally, $\mathcal{H}_s(x)$ is not invertible (and thus it is not an observability map for the system). This

entails that the form reported in equation (9.2.6) is locally not well defined and matrix $Q(x)$ becomes singular or nearly singular, leading to either numeric or observation error instabilities. This point is obviously hardly predictable and represents the main shortcoming of the proposed approach in technical applications.

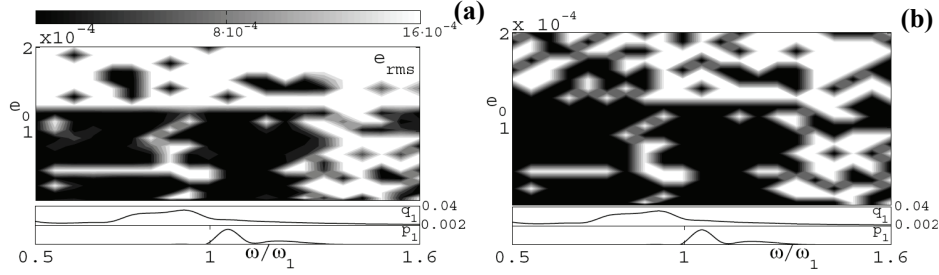


Figure 9.7. Map of the root mean square e_{rms} of the error norm evaluated in the interval $[\tau_{max}/2, \tau_{max}]$ as a function of ω/ω_1 and of the initial error norm e_0 : (a); numeric convergence map (white regions denote numeric instability): (b)

9.5 Application of the observer to active control

The natural applicability of state observation is represented by non-collocated active and semi-active control policies. Within this framework, the estimated state variables are employed in the control law which is adopted to calculate the feedback actions that stabilize the cable motion. In order to investigate, to some extent, the applicability of the nonlinear observer to the structural control of cables, the feedback strategy described in Section 9.3 is here combined with the nonlinear observer. Nevertheless, the considered control strategy does not limit the generality of the proposed approach, which would apply to every kind of active or semi-active control, such as, for example, the well-known longitudinal strategy studied in references (Susumpow and Fujino, 1995; Gattulli et al., 1997; Pasca et al., 1998; Gattulli and Vestroni, 2000; Gattulli et al., 2008).

In order to demonstrate, to some extent, the applicability of the nonlinear state observer to the considered feedback control strategy, the primary forced

resonant case with input bound $\pi_M=0.003$ (second case in Table 9.2) is considered. The results of the analysis are represented in Figures 9.8 and 9.9. Particularly, Figures 9.8 (a) and (b) represent the time histories of the uncontrolled and control-with-observer cases, while Figures 9.8 (c) and (d) represent the evolution in time of the observation error norm $e = \|x(\tau) - \hat{x}(\tau)\|$. Figure 9.8 (d) represents a detailed view of e vs. τ in the initial part of the motion. In such a figure one evidences the peculiar behavior of e which, at the beginning of the motion increases above the initial value and then rapidly decreases. Regarding this last point, it must be also mentioned that both uncontrolled and controlled cases require the same upper bound of the initial error norm (roughly equal to $0.16 \cdot 10^{-3}$) in order to achieve observation error convergence. This seems to indicate that observation error stability is not affected by the presence of the control forces.

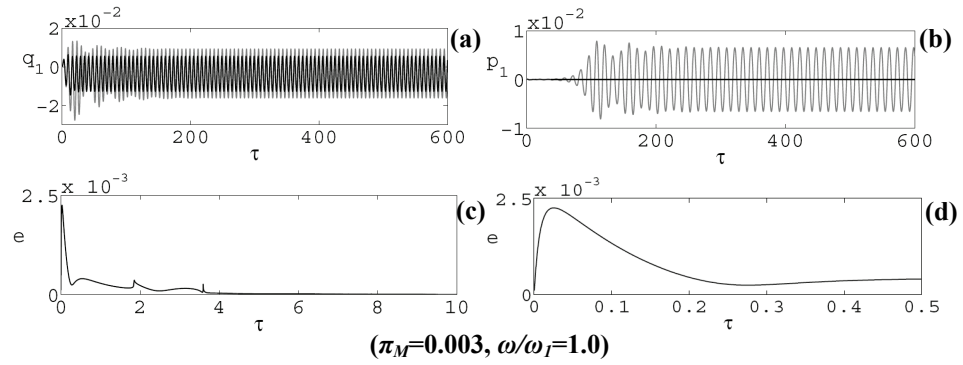


Figure 9.8. Controlled vibrations with spatial model (black lines indicate the control-with-observer case, grey lines indicate the uncontrolled case)

The uncontrolled and controlled (with observer) steady limit cycles are reported in Figure 9.9 (a). From the presented results one can observe that the steady controlled motion is stabilized in the vertical plane (the bifurcation leading to a spatial motion is not occurring). This confirms the capability of the proposed control law to mitigate the nonlinear cable vibration, with only two nodal measurements. The expected equivalence of the control-with-observer

solution with the ideal case in which all the state variables are known, is evidenced in Figure 9.9 (b).

The presented results emphasize that the observer guarantees optimal control by minimizing the nodal measurements. This, in fact, is a relevant point since, without employing state observation, the minimal number of nodal measurements may become unsustainable (equal or greater than the considered modal amplitudes). On the contrary, in the with-observer case, one may, in principle, estimate an infinite number of modal amplitudes with only two measurements. It must be noted, however, that no stabilizing feedback can be calculated in all those cases in which the observation error becomes unstable or the input is unknown (such as, for example, when wind and other external excitations couple). Nevertheless, a possible adaptive strategy to overcome these limitations is to switch in real time to a collocated strategy (no observer needed) until observation error stability is recovered. The most trivial collocated strategy that one could choose, is to make the device work as a passive one.

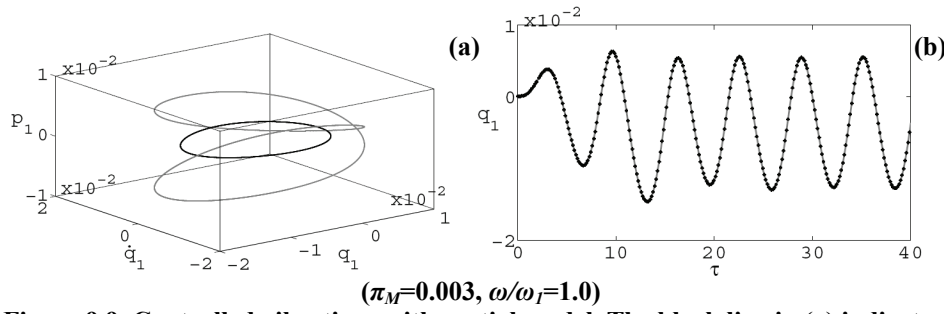


Figure 9.9. Controlled vibrations with spatial model. The black line in (a) indicates the steady limit cycle of the control-with-observer solution, the grey line indicates the one of the uncontrolled solution. The black dots in (b) indicate the control-with-observer solution while the grey line represents the theoretical case in which the entire state is known

9.6 Concluding remarks

A nonlinear state observer is designed analytically to be adopted in active state control policies for nonlinear cable dynamics.

A discussion on the observability of the system shows that two measured variables (one in-plane and one out-of-plane) are sufficient to construct an asymptotic state observer for the linear system if the cable is not 1:1 internally resonant. When the cable is at one crossover point, the minimum number of in-plane measurements is two. In the nonlinear regime, further conditions are required, which must be numerically verified. Nevertheless, the observation error stability is not guaranteed in every case for two fundamental reasons: the initial error and the input bound have to be sufficiently small; state estimation and time integration errors may couple thus leading to numerical instabilities.

The behavior of the observation error is investigated numerically utilizing a four dimensional Galerkin model. In order to avoid arbitrarily, nil initial conditions are assigned to the observer, whilst small initial perturbations are assigned to the mechanical system. The results show the feasibility of the observer for the purposes of the study. Namely, the minimal number of measurements allows the description of the entire state with exponential rate convergence of the observation error. This entails obvious benefits in the fields of active and semi-active feedback control. However, a significant sensitivity of the observer on the initial conditions and on the frequency content of the input is evidenced. In particular, as expected by the theory, convergence of the observation error becomes critic by enlarging the norm of the initial error above a certain threshold which obviously increases as the input bound decreases. Nevertheless, observation error instabilities also appear below the said threshold, even in dynamic regions in which the motion is characterized by relatively small amplitudes of vibration. This circumstance is mostly evidenced for large frequency values and it is either related to numeric errors in the calculation of the inverse of the state dependent observability matrix or, more suitably, on the local non-invertibility of the observability map. This point constitutes the main shortcoming of the proposed approach which, however, can be easily overcome in control applications by adopting suitable adaptive strategies.

CONCLUDING REMARKS

The thesis analyzes wind effects on cable-supported bridges, with emphasis given to the structural response, the aeroelastic stability and the main control priorities arising within this context.

The work is organized into three parts. The first part, including Chapters 0-2, summarizes the basic aspects of cable-supported bridges, devoting a special care to structural modeling (Chapter 1) and wind simulation (Chapter 2). The second part, including Chapters 3-6, focuses on the dynamic behavior of cable-supported bridges subjected to wind action. Particularly, Chapters 3 and 4 are devoted to buffeting response analysis, while Chapters 5 and 6 deal with the aeroelastic stability of cable-supported bridges. The third part of the thesis (Chapters 7-9) is entirely devoted to vibration control. Namely, two major risks in the field of wind-excited vibrations of bridges are identified in the onset of the flutter instability of the deck and in the excessive vibrations of long cables (especially in cable-stayed configurations) which may be originated either by dynamic instabilities or by ambient loads. Two suspension bridges are mainly considered as the case studies: the Tsing Ma Bridge and the New Carquinez Bridge. The main structural features of these bridges are presented in Appendix A.

An effort is made to balance brief literature reviews, original theoretical achievements, numerical investigations and experimental results. The main findings and original contributions of the work can be summarized as follows:

Part 1: Basic aspects of cable-supported bridges

Structural system:

- The capability of reduced dimensional numerical finite element models of long-span bridges to capture a large number of linear normal modes

identified from field measurements and to correctly reproduce the stiffening nonlinear behavior of the deck, is investigated with reference to the case study of the Tsing Ma Bridge, located in Hong Kong, China. Particularly, a sort of “minimal” macro-level model is achieved by properly simplifying a high dimensional numeric scheme corresponding to an accurate replication of the real structure. Reduced dimensional models are seen to guarantee a strong reduction of the computational effort along with an accurate agreement with the full order model for the purposes of the study.

Wind excitation:

- The digital simulation of the turbulent wind velocity field in high dimensional simulation domains requires a special attention to reduce the memory allocation and the computational effort. A numerical framework is proposed, at first, to handle digital wind simulations in a properly organized way. Afterwards, a comparative study between three relevant existing simulation techniques suggests the use of a simplified numerical procedure based on the proper orthogonal decomposition of the spectral matrix of the process. The comparative study accounts for computational efficiency and for the accuracy in preserving the frequency content and the coherence level of the target process.

Part 2: Fundamental aspects of the dynamics of cable-supported bridges

Buffeting response:

- Numerical simulations, conducted through a macro-level finite element model of the Tsing Ma Bridge, China, show that unsteady aerodynamic effects, adequately modeled by means of time domain representations of aeroelastic derivatives, may play a significant role in the buffeting response of bridges regardless the level of external excitation. The

analysis also reveals that these effects are not fully captured by quasi-steady representations of the aerodynamic loads. Indeed, the quasi-steady formulation results to be slightly conservative for the considered case study.

- A computational framework accounting for output only system identification, digital wind simulation based on in-site measurements and finite element model updating via optimization techniques is established and applied to the case study of the New Carquinez Bridge located in San Francisco, California. The proposed approach reveals to be an accurate tool for predicting the buffeting response of bridges if compared to field measurements. The model is thus ready to be used in online monitoring systems as well as a mean for safety evaluations or as a source of pseudo experimental data.

Aeroelastic stability:

- A simple treatment of the time domain representation of self-excited aeroelastic loads via the use of indicial functions allows to rewrite the flutter equations of bridge decks in the form of a fully analytical system of ordinary differential equations without integral terms. This permits the critic condition to be solved by simply evaluating the eigenvalues of a non-symmetric matrix operator. This approach is seen to be in perfect agreement with the more involved frequency domain approach requiring an iterative search of the Hopf bifurcation point. In the meanwhile, the time domain model allows to incorporate non-linearities and turbulence effects into the flutter problem, which are traditionally neglected by frequency domain methods.
- Time domain aeroelastic stability analysis of bridges using tridimensional finite element models of the structure is probably the most accurate and physically relevant approach to assess the level of safety against aeroelastic instabilities, fully accounting for structural

nonlinearities and multimodal participations. Two main applications of this approach are proposed with reference to the case study of the Tsing Ma Bridge.

- The type of system nonlinearities judge on the nature of the postcritic behavior of the bridge ensuing from a flutter bifurcation. Indeed, this last can be either of the benign supercritical nature (stable postcritic response) or of the more dangerous subcritical one (unstable postcritic response). Numerical simulations show that, in the case of an unstable postcritic behavior, turbulence effects may play a significant role on the system response. Indeed, fluctuating wind velocities modeled as stochastic Gaussian processes partially correlated along the bridge, are seen to destabilize the structural response slightly below the critic velocity and to shorten the route towards extremely large displacements leading to structural failures.
- Experimental data scattering in wind tunnel experiments must be incorporated in the aeroelastic stability analysis which thus assumes a probabilistic meaning. A direct Montecarlo simulation indicates that assuming a Gaussian variability in the input (aeroelastic derivatives) reflects on a strongly non-Gaussian outcome (critic velocity). Namely, the probability density function of the predicted critic velocity is seen to assume a dangerous right skew shape as the model uncertainty is increased. This entails that common levels of experimental uncertainties could lead to unsafe predictions of the critic flutter velocity.

Part 3: Advanced aspects of the dynamics of cable-supported bridges

Suppression of cable galloping and bridge flutter:

- Passive control solutions based on the use of tuned mass dampers are investigated with the aim of suppressing aeroelastic instabilities (cable galloping and bridge flutter). These passive solutions are seen to

guarantee satisfactory control performances despite their simplicity and economical convenience.

- With the aim of mitigating control sensitivity to mistuning effects, a multiple tuned mass damper is conceived for suppressing the occurrence of flutter instabilities in bridge decks. The effectiveness of such a control policy is analytically studied in the time domain by adopting the representation of self-excited loads via indicial functions approximated by exponential filters. The results seem promising towards the application of this strategy in a practical case.

Cable vibration mitigation:

- The problem of cable vibration mitigation is studied in the last two Chapters in some details, devoting a special care to the quite involved nonlinear phenomena. Indeed, long stay cables exhibit complex nonlinear behaviors even in very taut configurations, which must be attentively modeled in the analysis. After collecting the main literature findings on nonlinear cable dynamics, system identification of a physical cable is preliminary performed devoting a special care to detecting possible internal resonance conditions.
- Analytical tools and numerical simulations show that an active state controller, proper of linear systems, can introduce a large amount of damping and stabilize the response of the system even in the strongly nonlinear regime. However, in order to reduce the number of monitoring sensors, a suitable nonlinear state observer must be designed to track the state of the system during the motion.
- State estimation in nonlinear cable dynamics is addressed in details via analytical and numerical approaches. Analytical results show that one in-plane and one out-of-plane measurements are sufficient in order to capture the entire state of the system, provided that the cable is not 1:1

internally resonant. In the vicinity of one crossover point two in-plane measurements are at least required. It must be mentioned, however, that the observability conditions of the system, which are sufficient for the linear case, result only necessary in the nonlinear regime.

- An analytical nonlinear state observer for cable dynamics is designed on the basis of reduced order nonlinear cable models derived by means of the Galerkin approach. The observer appears to be feasible for semi-active or active control applications, as it is discussed through numerical simulations.
- An innovative hybrid control strategy for cable vibration mitigation is finally proposed and its effectiveness is analyzed through a theoretical investigation and an experimental validation. The control strategy combines a distributed passive solution, utilizing wrapped shape memory alloy wires, with a localized open loop actuation. The shape memory alloy wire is pre-tensioned up to an optimum value which maximizes the equivalent damping introduced into the system. The open loop actuation aims at mitigating the cable displacements by introducing energy into the system instead of taking energy out of it. To this end, a simple sinusoidal control law is designed to enhance the energy exchange between modes by exploiting nonlinear internal resonance conditions of the cable. This control policy is seen able to strongly reduce the response of the system in both linear and nonlinear regimes. Moreover, the proposed approach does not necessitate state reconstruction, thus meeting the fundamental requirement of a large control robustness.

Bibliography

- Ansys Inc. (2005). *ANSYS and CivilFEM 9.0 User Manual*, Madrid.
- Arafat H.N., Nayfeh A.H. (2002). "Nonlinear response of suspended cables to primary resonance excitation", *Journal of Sound and Vibration*, vol. 266, 325-354.
- Beard A.S., Young J.S. (1995). "Aspect of the design of the Tsing Ma bridge", *Proceedings of the International Conferences on Bridge into 21st Century*, Impressions Design and Print Ltd., Hong Kong, 93-100.
- Benedettini F., Rega G., Alaggio R. (1995). "Nonlinear oscillations of a four-degree of freedom model of a suspended cable under multiple internal resonance conditions", *Journal of Sound and Vibration*, vol. 182, 775-798.
- Betti R., Hong A.H., Lin C.C. (2008). "Identification of Dynamic Models of a Building Structure Using Multiple Earthquake Records", *Proceedings of the International Symposium on Structural Control and Health Monitoring*, Taichung, ROC, XV-1-23.
- Bisplinghoff R.L., Ahley H., Halfman R.L. (1955). *Aeroelasticity*, New York: Dover Publication Inc.
- Bontempi F., Malerba P.G. (1994). "Forzanti aerodinamiche nei modelli aeroelastici semplificati dei ponti sospesi e strallati" (in Italian), *Studi e Ricerche*, vol. 15, Scuola di Specializzazione "F.lli Pesenti.", Politecnico di Milano.
- Bontempi F., Malerba P.G. and Giudici M. (2000). "La formulazione matriciale dei problemi aeroelastici di ponti sospesi e strallati" (in Italian). *Studi e Ricerche Scuola di Specializzazione "F.lli Pesenti."*, Politecnico di Milano, vol. 21.
- Bontempi F., Gkoumas K., Arangio S. (2005). "System Engineering Framework for the knowledge based analysis of complex structural systems", *Proceedings of ICOSAR'05*, Rome.
- Borri C., Facchini L. (2000). "Artificial generation on non-Gaussian 3D wind pressure fields on structures or bluff body surfaces", in: *Proceedings of the 8th ASCE Specialty Conference on Probabilistic Mechanics and Structural Reliability*, Notre Dame, Indiana.

- Breccolotti M., Gusella V., Materazzi A.L. (2007). "Active displacement control of a wind-exposed mast", *Structural Control and Health Monitoring*, vol. 14, 556-575.
- Caetano E., Cunha A., Gattulli V., Lepidi M. (2008). "Cable-deck dynamic interactions at the International Gadiana Bridge: on-site measurements and finite element modelling", *Structural Control and Health Monitoring*, vol. 15, 237-264.
- Cai C.S., Wu W.J., Shi X.M. (2006). "Cable vibration reduction with a hung-on TMD system. Part I: Theoretical study", *Journal of Vibration and Control*, vol. 12, no. 7, 801-814.
- Cai C.S., Wu W.J., Shi X.M. (2006). "Cable vibration reduction with a hung-on TMD system. Part II: Parametric study", *Journal of Vibration and Control*, vol. 12, no. 8, 881-899.
- Caracoglia L., Jones N.P. (2003). "A methodology for the experimental extraction of indicial functions for streamlined and bluff deck sections". *Journal of Wind Engineering and Industrial Aerodynamics*, vol. 91, 609-36.
- Caracoglia L., Jones N.P. (2003). "Time domain vs. frequency domain characterization of aeroelastic forces for bridge deck sections". *Journal of Wind Engineering and Industrial Aerodynamics*, vol. 91, 371-402.
- Carassale L., Solari G. (2006). "Monte Carlo simulation of wind velocity fields on complex structures", *Journal of Wind Engineering and Industrial Aerodynamics*, vol. 94, 323-339.
- Casciati F., Ubertini F. (2006). "Control of cables nonlinear vibrations under turbulent wind action", *Proceedings of the fifth Computational Stochastic Mechanics Conference (CSM5)*, Rodos, Greece, June 21-23.
- Casciati F., Magonette G., Marazzi F. (2007). *Technology of Semiactive Devices and Applications in Vibration Mitigation*, Chichester: John Wiley & Sons.
- Casciati F., Faravelli L., Fuggini C. (2008). "Cable vibration mitigation by added SMA wires", *Acta Mechanica*, vol. 195, 141-155.
- Casciati F., Ubertini F. (2008). "Nonlinear vibration of shallow cables with semi-active tuned mass damper", *Nonlinear Dynamics*, vol. 53, 89-106.
- Cavagna L., Quaranta G., Ghiringhelli G.L., Mantegazza P. (2005). "Efficient application of CFD aeroelastic methods using commercial software", *Proceedings of the International Forum on Aeroelasticity and Structural Dynamics IFASD-2005*, Munich, Germany.
- Cavagna L., Quaranta G., Mantegazza P. (2005). "Aeroelasticità computazionale con modelli CFD" (in Italian), *Bollettino CILEA*, no. 98.

- Chen X., Kareem A., Matsumoto M. (2001). "Multimode coupled flutter and buffeting analysis of long span bridges", *Journal of Wind Engineering and Industrial Aerodynamics*, vol. 89, 649-664.
- Chen X., Kareem A. (2001). "Nonlinear response analysis of long-span suspension bridges under turbulent winds", *Journal of Wind Engineering and Industrial Aerodynamics*, vol. 89, 1335-1350.
- Chen X., Kareem A. (2002). "Advanced analysis of coupled buffeting response of bridges: a complex modal decomposition approach", *Probabilistic Engineering Mechanics*, vol. 17, 201-213.
- Chen X., Kareem A. (2003). "Efficacy of tuned mass dampers for bridge flutter control", *ASCE Journal of Structural Engineering*, vol. 129, no. 10, 1291-1300.
- Cluni F. (2004). "Studio del comportamento dinamico dei cavi strutturali: modelli numerici e prove sperimentali" (in Italian), *PhD Dissertation*, University of Perugia.
- Cluni F., Gusella V., Ubertini F. (2007). "A parametric investigation of wind-induced cable fatigue", *Engineering Structures*, vol. 29, no. 11, 3094-3105.
- Coller B.D., Chamara P.A. (2004). "Structural nonlinearities and the nature of the classic flutter instability", *Journal of Sound and Vibration*, vol. 277, 711-739.
- Conte J.P., He X., Moaveni B., Masri S.F., Caffrey J.P., Wahbeh M., Tasbihgoo F., Whang D.H., Elgamal A. (2008). "Dynamic testing of Alfred Zampa Memorial Bridge", *ASCE Journal of Structural Engineering*, vol. 134, 1006-1015.
- Costa C. (2007). "Aerodynamic admittance functions and buffeting forces for bridges via indicial functions", *Journal of Fluids and Structures*, vol. 23, 413-428.
- Costa C., Borri C. (2006). "Application of indicial functions in bridge deck aeroelasticity", *Journal of Wind Engineering and Industrial Aerodynamics*, vol. 94, 859-881.
- Dalla Mora M., Germani A., Manes C. (2000) "Design of state observers from a drift-observability property", *IEEE Transactions on Automatic Control*, vol. 45, 1536-1540.
- Deodatis G. (1996). "Simulation of ergodic multivariate stochastic processes", *Journal of Engineering Mechanics*, vol. 122, 778-787.
- Desai Y.M., Popplewell N., Shah, A.H. and Buragohain, D.N. (1988). "Geometric nonlinear analysis of cable supported structures". *Computer and Structures*, vol. 29, no. 6, 1001-1006.

- Desai Y.M., Popplewell N., Shah, A.H. (1995). "Finite element modeling of transmission line galloping". *Computer and Structures*, vol. 57, 407–420.
- Ding Q., Lee P.K.K. (2000). "Computer simulation of buffeting actions of suspension bridges under turbulent wind", *Computers & Structures*, vol. 76, 787-797.
- Ding Q., Lee P.K.K., Lo S.H. (2000). "Time domain buffeting analysis of suspension bridges subjected to turbulent wind with effective attack angle", *Journal of Sound and Vibration*, vol. 233, no. 2, 311-327.
- Di Paola M. (1998). "Digital simulation of wind field velocity", *Journal of Wind Engineering and Industrial Aerodynamics*, vol. 74-76, 91-109.
- Di Paola M., Gullo I. (2001). "Digital generation of multivariate wind field processes", *Probabilistic Engineering Mechanics*, vol. 16, 1-10.
- Doedel E.J., Paffenroth R.C., Champneys A.R., Fairgrieve T.F., Kuznetsov Y.A., Oldeman B.E. Sandstede B., Wang X. (2000). "AUTO2000: Continuation and bifurcation software for ordinary differential equations", software available online from: <http://indy.cs.concordia.ca/auto/>.
- Faravelli L., Ubertini F. (2007). "Estimation of cable states for active feedback control", *Proceedings of the MDP2007 Conference*, 3-6 June, Palermo, Italy.
- Faravelli L., Ubertini F. (2007). "Observability issues in the vibration of cables", *Proceedings of the ECCOMAS Thematic Conference on Computational Methods in Structural Dynamics and Earthquake Engineering (COMPDYN)*, 13-16 June, Crete, Greece.
- Faravelli L., Ubertini F. (2008). "Nonlinear state observation for cable dynamics", *Journal of Vibration and Control*, accepted for publication.
- Faravelli L., Ubertini F. (2008). "Experimental cable identification via dynamic testing", *Proceedings of the Fourth European Workshop on Structural Health Monitoring (4WSHM)*, 2-4 July, Krakow, Poland.
- Faravelli L., Ubertini F. (2008). "Experimental identification of cable damping parameters towards robust design against aeroelastic instability", *Proceedings of the First International Symposium on Life Cycle Engineering (IALCCE08)*, 11-14 June, Varenna, Italy.
- Faravelli L., Fuggini C., Ubertini F. (2008). "Adaptive solution for intelligent cable vibration mitigation", *Advances in Science and Technology*, vol. 56, 137-156.
- Gattulli V., Pasca M., Vestroni F. (1997). "Nonlinear oscillations of a nonresonant cable under in-plane excitation with a longitudinal control", *Nonlinear dynamics*, vol. 14, 139-156.

- Gattulli V., Vestroni F. (2000). "Nonlinear strategies for longitudinal control in the stabilization of an oscillating suspended cable", *Dynamics and Control*, vol. 10, no. 4, 359-374.
- Gattulli V., Lepidi M., Luongo A. (2003). "Controllo con una massa accordata dell'instabilità aeroelastica di un cavo sospeso" (in Italian), *Proceedings of the 16th Conference of the Italian Association of Theoretical and Applied Mechanics (AIMETA)*.
- Gattulli V., Martinelli L., Perotti F., Vestroni F. (2004). "Nonlinear oscillations of cables under harmonic loading using analytical and finite element models", *Computer Methods in Applied Mechanics and Engineering*, vol. 193, 69-85.
- Gattulli V. (2007). "Advanced control strategies in cable dynamics", *Civil Engineering Computations: Tools and Techniques*, 243-269.
- Gattulli V., Alaggio R., Potenza F. (2008). "Analytical prediction and experimental validation for longitudinal control of cable oscillations", *International Journal of Nonlinear Mechanics*, vol. 43, 36-52.
- Gentile C., Gallino N. (2008). "Ambient vibration testing and structural evaluation of an historic suspension footbridge", *Advanced Engineering Software*, vol. 39, 356-366.
- Gibson E.J. (1982). "Working with the Performance Approach in Building", *CIB State of the Art Report*, no. 64, CIB, Rotterdam.
- Gimsing N.J. (1983). *Cable Supported Bridges, concept and design*. New York: John Wiley & Sons.
- Gioffrè M., Gusella V., Grigoriu M. (2000). "Simulation of non-Gaussian field applied to wind pressure fluctuations", *Probabilistic Engineering Mechanics*, vol. 15, 339-345.
- Gioffrè M., Gusella V., Materazzi A.L., Venanzi I. (2004). "Removable guyed mast for mobile phone networks: wind load modeling and structural response", *Journal of Wind Engineering and Industrial Aerodynamics*, vol. 92, 463-475.
- Giuliano F. (2007). *Performance based design by structural control for suspension bridges*. PhD Dissertation, University of Pavia.
- Gu M., Chang C.C., Wu W., Xiang H.F. (1998). "Increase of critical flutter wind speed of long-span bridges using tuned mass dampers", *Journal of Wind Engineering and Industrial Aerodynamics*, vol. 74, 111-123.
- Guckenheimer J., Holmes P.J. (1983). *Nonlinear Oscillations, Dynamical Systems and Bifurcations of Vector Fields*, Berlin: Springer Verlag.

- Guo W.W., Xu Y.L., Xia H., Zhang W.S., Shum K.M. (2007). "Dynamic response of suspension bridge to typhoon and trains. II: Numerical results", *ASCE Journal of Structural Engineering*, vol. 133, 12-21.
- Gusella V., Materazzi A.L. (1998). "Non-Gaussian response of MDOF wind-exposed structures: analysis by bicomrelation function and bispectrum", *Meccanica*, vol. 33, 299-307.
- Gusella V., Materazzi A.L. (2000). "Non-Gaussian along-wind response analysis in time and frequency domains", *Engineering Structures*, vol. 22, 49-57.
- He X., Moaveni B., Conte J.P., Elgamal A., Masri S.F., Caffrey J.P., Wahbeh M., Tasbihgoo F. and Whang D.H. (2005). "System identification of New Carquinez Bridge Using Ambient Vibration Data", *Proceedings of the International Conference on Experimental Vibration Analysis for Civil Engineering Structures EVACES'05*, Bordeaux, France, 26-28 October.
- He X., Moaveni B., Conte J.P. and Elgamal A. (2006). "Comparative study of system identification techniques applied to New Carquinez Bridge", *Proceedings of IABMAS 2006 Conference*.
- Irvine H.M., Caughey T.K. (1974). "The linear theory of free vibrations of suspended cables", *Proceedings of the Royal Society of London*, vol. 341, 299-315.
- Isidori A. (1985). *Nonlinear Control Systems: An Introduction*, Berlin: Springer Verlag.
- Jacobsen J.B., Tanaka H. (2003). "Modelling uncertainties in prediction of aeroelastic bridge behavior", *Journal of Wind Engineering and Industrial Aerodynamics*, vol. 91, 1485-1498.
- Janberg N., "Structurae – international database and gallery of structures", available online at <http://en.structurae.de>.
- Jones R.T. (1940). "The unsteady lift of a wing of finite aspect ratio", *Technical Report 681, NACA Report*.
- Jones W.P. (1945). "Aerodynamic forces on wings in non-uniform motion", *Technical Report 2117, Aeronautical Research Council R. & M.*
- Kareem A., Kijewski T. (2002). "Time frequency analysis of wind effects on structures", *Journal of Wind Engineering and Industrial Aerodynamics*, vol. 90, 1435-1452.
- Kehoe M.W. (1995). "A historical overview of flight flutter testing", *NASA Technical Memorandum 4720*.
- Kwon S.D., Chang S.P. (2000). "Suppression of flutter and gust response of bridges using actively controlled edge surfaces", *Journal of Wind Engineering and Industrial Aerodynamics*, vol. 88, no. 2-3, 263-281.

- Kwon S.D., Park K.S. (2004). "Suppression of bridge flutter using tuned mass dampers based on robust performance design", *Journal of Wind Engineering and Industrial Aerodynamics*, vol. 92, no. 11, 919-934.
- Lau C.K., Wong K.Y. (1997). "Aerodynamic stability of Tsing Ma bridge", In: *Proceedings of the Fourth International Kerensky Conference on Structures in the New Millennium*, Hong Kong.
- Larsen J.W., Nielsen S.R.K. (2004). "Non-linear stochastic response of a shallow cable", *International Journal of Nonlinear Mechanics*, vol. 41, 327-344.
- Lazzari M. (2005). "Time domain modeling of aeroelastic bridge decks: a comparative study and an application", *International Journal for Numerical Methods in Engineering*, vol. 62, 1064-1104.
- Lazzari M., Vitaliani R.V., Saetta A. (2004). "Aeroelastic forces and dynamic response of long-span bridges", *International Journal for Numerical Methods in Engineering*, vol. 60, 1011-1048.
- Lee B.H.K., Gong L. and Wong Y.S. (1997). "Analysis and computation of nonlinear dynamic response of a two-degree-of-freedom system and its application in aeroelasticity", *Journal of Fluids and Structures*, vol. 11, 225-246.
- Lee B.H.K., Jiang L.Y. and Wong Y.S. (1999). "Flutter of an airfoil with a cubic restoring force", *Journal of Fluids and Structures*, vol. 13, 75-101.
- Lenci S. and Rega G. (2004). "A unified control framework of the non-regular dynamics of mechanical oscillators", *Journal of Sound and Vibration*, vol. 278, 1051-1080.
- Li Y., Kareem A. (1995). "Stochastic decomposition and application to probabilistic mechanics", *ASCE Journal of Engineering Mechanics*, vol. 121, n. 1, 162-174.
- Li Z.X., Chan T.H.T. (2006). "Fatigue criteria for integrity assessment of long-span steel bridge with health monitoring", *Theoretical and Applied Fracture Mechanics*, vol. 46, 114-127.
- Lin Y.Y., Cheng C.M., Lee C.H. (1999). "Multiple tuned mass dampers for controlling coupled buffeting and flutter of long-span bridges", *Wind & Structures*, vol. 2, no. 4.
- Lin Y.Y., Cheng C.M., Lee C.H. (2000). "A tuned mass damper for suppressing the coupled flexural and torsional buffeting response of long-span bridges", *Engineering Structures*, vol. 22, 1195-1204.
- Luongo A., Rega G., Vestroni F. (1984). "Parametric analysis of large amplitude free vibrations of a suspended cable", *International Journal of Solids and Structures*, vol. 20, 95-105.

- Luongo A., Piccardo G. (2005). "Linear instability mechanism for coupled translational galloping", *Journal of Sound and Vibration*, vol. 288, 1027-1047.
- Magalhães F., Caetano E., Cunha, Á. (2007). "Challenges in the Application of Stochastic Modal Identification Methods to a Cable-Stayed Bridge", *Journal of Bridge Engineering*, vol. 12, no. 6, 746-754.
- Maylibaev A. A., Kirillov O. N., Seyranian A. P. (2005). "Coupling of eigenvalues of complex matrices at diabolic and exceptional points", *Journal of Physics A: Mathematical and General*, vol. 38, no. 8, 1723-1740.
- Nayfeh A.H., Arafat H.N., Chin C.M., Lacarbonara W. (2002). "Multimode interactions in suspended cables", *Journal of Vibration and Control*, vol. 8, 337-387.
- Ni Y.Q., Zheng G., Ko J.M. (2004). "Nonlinear periodically forced vibration of stay cables", *Journal of Vibration and Acoustic*, vol. 126, no. 2, 245-252.
- Noh D., Jo N.H., Seo J.H. (2004). "Nonlinear observer design by dynamic observer error linearization", *IEEE Transaction on Automatic Control*, vol. 49, no. 10, 1746-1750.
- Omenzetter P., Wilde K., Fujino Y. (2000). "Suppression of wind-induced instabilities of a long span bridge by a passive deck-flaps control system. Part I: formulation", *Journal of Wind Engineering and Industrial Aerodynamics*, vol. 87, 61-79.
- Omenzetter P., Wilde K., Fujino Y. (2000). "Suppression of wind-induced instabilities of a long span bridge by a passive deck-flaps control system. Part II: Numerical simulations", *Journal of Wind Engineering and Industrial Aerodynamics*, vol. 87, 81-91.
- Pasca M., Vestroni F., Gattulli V. (1998). "Active longitudinal control of wind-induced oscillations of a suspended cable", *Meccanica*, vol. 33, 255-266.
- Petrini F., Giuliano F., Bontempi F. (2007). "Comparison of different time domain techniques for the evaluation of the response and the stability in long span suspension bridges", *Computers & Structures*, vol. 85, 1032-1048.
- Petrini F., Bontempi F. (2008). "Estimation of life-cycle fatigue damage for suspension bridge hangers", *Proceedings of the First International Symposium on Life Cycle Engineering (IALCCE08)*, 11-14 June, Varenna, Italy.
- Polytechnic University of Hong Kong. "Tsing Ma Bridge", available online at <http://www.cityu.edu.hk/CIVCAL/book/bridge.html>.
- Polytechnic University of Hong Kong. "Tsing Ma suspension bridge", available online at <http://www.cse.polyu.edu.hk/~ctbridge/case/tsingma.htm>.

- Pourzeynali S., Datta T.K. (2002). "Reliability analysis of suspension bridges against flutter", *Journal of Sound and Vibration*, vol. 254, no. 1, 143-162.
- Preidikman S., Mook D.T. (1997). "A new method for actively suppressing flutter of suspension bridges", *Journal of Wind Engineering and Industrial Aerodynamics*, vol. 69-71, 955-974.
- Raggett J.D. (1998). *Experimental Test Results Wind Study Third Carquinez Strait Bridge, Crockett to Vallejo, California*, West Wind Laboratory, Inc.
- Rega G. (2004). "Nonlinear vibrations of suspended cables – Part I: Modelling and analysis", *Applied Mechanics Reviews*, vol. 57, no. 6, 443-478.
- Rega G. (2004). "Nonlinear vibrations of suspended cables – Part II: Deterministic phenomena", *Applied Mechanics Reviews*, vol. 57, no. 6, 479-51.
- Rega G., Lenci S. (2008). "Dynamical integrity and control of nonlinear mechanical oscillators", *Journal of Vibration and Control*, vol.14, 159-179.
- Robertson I., Sherwin S.J., Bearman P.W. (2003). "Flutter instability prediction techniques for bridge deck sections", *International Journal for Numerical Methods in Fluids*, vol. 43, 1239-1256.
- Rossi R., Lazzari M., Vitaliani R. (2003). "Wind field simulation for structural engineering purposes", *International Journal of Numerical Methods in Engineering*, vol. 61, 738-763.
- Salvatori L., Spinelli P. (2006). "Effects of structural nonlinearity and along-span coherence on suspension bridge aerodynamics: some numerical simulation results", *Journal of Wind Engineering and Industrial Aerodynamics*, vol. 94, 415-430.
- Salvatori L., Borri C. (2007). "Frequency- and time-domain methods for the numerical modeling of full-bridge aeroelasticity", *Computers & Structures*, vol. 85, 675-687.
- Samaras E., Shinozuka M., Tsurui A. (1985). "ARMA representation of random processes", *Journal of Engineering Mechanics*, vol. 111, 449-461.
- Scanlan R.H., Béliveau J.G., Budlong K. (1974). "Indicial aerodynamics functions for bridge decks", *Journal of Engineering Mechanics*, vol. 100, 657-72.
- Scanlan R.H., Jones N.P. (1998). *Wind Response Study Carquinez Strait Suspended Span*, Report for West Wind Laboratory, Inc. and OPAC Consulting Engineers.
- Sepe V., D'Asdia P. (1998). "Aeroelastic instability of long-span suspended bridges: a multi-mode approach", *Journal of Wind Engineering and Industrial Aerodynamics*, vol. 74-76, 849-857.

- Sepe V., D'Asdia P. (2003). "Influence of low-frequency wind speed fluctuations on the aeroelastic stability of suspension bridges", *Journal of Wind Engineering and Industrial Aerodynamics*, vol. 91, 1285-1297.
- Shinozuka M., Deodatis G. (1997). "Simulation of stochastic processes and fields", *Probabilistic Engineering Mechanics*, vol. 12, no. 4, 203-207.
- Shinozuka M., Jan C.M. (1971). "Digital simulation of random processes and its applications", *Journal of Sound and Vibration*, vol. 25, n.1, 111-128.
- Schuëller G.I. (ed.) (1997). "A state-of-the-art report on computational stochastic mechanics", *Probabilistic Engineering Mechanics*, vol. 12, n. 4, 197-321.
- Simiu E., Scanlan R.H. (1996). *Wind Effects on Structures*, third ed., New York: John Wiley and Sons.
- Solari G., Carassale L. (2000). "Modal transformation tools in structural dynamics and wind engineering", *Wind and Structures*, vol. 3, no. 4, 221-241.
- Solari G., Piccardo G. (2001). "Probabilistic 3-D turbulence modeling for gust buffeting of structures", *Probabilistic Engineering Mechanics*, vol. 16, 73-86.
- Susumpow T., Fujino Y. (1995). "Active control of multimodal cable vibrations by axial support motion", *Earthquake Engineering and Industrial Aerodynamics*, vol. 5, 283-292.
- Thorbek L.T., Hansen S.O. (1998). "Coupled buffeting response of suspension bridges", *Journal of Wind Engineering and Industrial Aerodynamics*, vol. 74-76, 839-847.
- Ubertini F., Domaneschi M. (2006). "Analytic and numeric approach to controlled cables", *Proceedings of the 16th Italian Conference on Computational Mechanics (GIMC 2006)*, ISBN 88-371-1621-7, 26-28 June, Bologna, Italy.
- Ubertini F. (2007). "Computational issues in nonlinear cables observation", *Proceedings of the 18th Conference of the Italian Association of Theoretical and Applied Mechanics (AIMETA)*, 11-14 September, Brescia, Italy.
- Ubertini F., Fuggini C. (2007). "Confronto di due tecniche per l'identificazione e il monitoraggio di cavi strutturali mediante prove sperimentali" (in Italian), *Proceedings of the Italian Conference on Non-Destructive Tests (AIPND)*, Milan, Italy.
- Ubertini F. (2008). "Active feedback control for cable vibrations", *Smart Structures & Systems*, vol. 4, no. 4, 407-428.

- Ubertini F., Bontempi F. (2008). "Instabilità aeroelastica di impalcati da ponte: un caso di studio" (in Italian), *Proceedings of the 10th Conference of the Italian Association of Wind Engineering (INVENTO08)*, Cefalù, Italy.
- Ubertini F., Bontempi F. (2008). "Wind-induced fatigue assessment in the main cables and hangers of suspension bridges", *Proceedings of the Fourth International Conference on Bridge Maintenance, Safety and Management (IABMAS 2008)*, 13-17 July, Seoul, Korea.
- Ubertini F., Giuliano F. (submitted). "A comparative study on efficiency and accuracy of Gaussian wind simulation methods", *Journal of Wind Engineering and Industrial Aerodynamics*, submitted for publication.
- Venanzi I., Materazzi A.L. (2007). "Multi-objective optimization of wind-excited structures", *Engineering Structures*, vol. 29, no. 6, 983-990.
- Wong K.Y. (2004). "Instrumentation and health monitoring of cable-supported bridges", *Structural Control and Health Monitoring*, vol. 11, no. 2, 91-124.
- Xu Y.L., Ko J.M. (1997). "Vibration studies of Tsing Ma suspension bridge", *ASCE Journal of Bridge Engineering*, vol. 2, no. 4, 149-156.
- Xu Y.L., Guo W.W., Chen J., Shum K.M., Xia H. (2007). "Dynamic response of suspension bridge to typhoon and trains. I: field measurement results", *ASCE Journal of Structural Engineering*, vol. 133, 3-11.
- Xu Y.L., Chen J. (2004). "Characterizing nonstationary wind speed using empirical mode decomposition", *ASCE Journal of Structural Engineering*, vol. 130, no. 6, 912-920.
- Xu Y.L., Sun D.K., Ko J.M., Lin J.H. (2000). "Fully coupled buffeting analysis of Tsing Ma suspension bridge", *Journal of Wind Engineering and Industrial Aerodynamics*, vol. 85, 97-117.
- Zhu L.D., Xu Y.L., Xiang H.F. (2002). "Tsing Ma bridge deck under skew winds – Part I: aerodynamic coefficients", *Journal of Wind Engineering and Industrial Aerodynamics*, vol. 90, 781-805.
- Zhu L.D., Xu Y.L., Xiang H.F. (2002). "Tsing Ma bridge deck under skew winds – Part II: flutter derivatives", *Journal of Wind Engineering and Industrial Aerodynamics*, vol. 90, 807-837.

APPENDIX A

DESCRIPTION OF THE CASE STUDY BRIDGES

Abstract

The structural complexity of long-span cable-supported bridges requires multilevel and systemic approaches for design, construction, monitoring, maintenance and rehabilitation purposes. After briefly discussing the basic notions for complex structures, the main structural features of the two case study bridges analyzed in this thesis are presented. The two case studies are: the Tsing Ma Bridge, located in Hong Kong, China, and the New Carquinez Bridge, located in San Francisco, California.

A.1 Basic notions for complex structures

Cable-supported bridges are complex structural systems whose dominating character depends on the interrelationships between the parts. This complexity has pushed the engineers to develop new “organized” approaches and ways of thinking to handle design, construction, monitoring and maintenance of these structures.

Primarily, the traditional prescriptive design approach, in which the structure must satisfy some design targets, has revealed to be unfeasible for the design of

complex structural systems. To this end, the general framework of the *performance based design*, relying on the definition of “what a structure is expected to do” instead of “how it should be constructed” (Gibson, 1982), was recently applied to the case of a long-span suspension bridge (Giuliano, 2007). Within this context, different performances exhibit interconnections with each other and are influenced by several factors thus making the definition of a unified index of quality particularly useful. To this end the concept of system *dependability* was introduced (Bontempi, Gkoumas and Arangio, 2005) which can be interpreted as the availability of performances (attributes) and its influencing factors (threats).

Within the performance based design of complex structural systems, traditional approaches based on input-output relations should be integrated by the tools of System Engineering and Knowledge-Managements Sciences. This allows to handle the design variables and all the involved uncertainties in a properly organized way which can be generally referred to as *Systemic Approach* (Giuliano, 2007). This approach relies on a methodological simplification of the problem leading to a series of *decompositions* in which the capabilities of the system are explored. Following such an approach the complexity of the system is organized into a so-called *multilevel complexity* which can be simplified through a formal operation of *hierarchical layering*.

A.2 Structural decomposition of cable-supported bridges

Global performances of cable-supported bridges are usually affected by local behaviors. Thus, a multilevel layering is required to decompose the structure in a proper number of *substructures* which should satisfy performance requirements both at the global and at the local scales. This representation makes use of a distinction of different levels of the system from the global (*macro-level*) to the local (*micro-level*) scales.

For the purposes of the study, i.e. for analyzing global and global/local responses of cable-supported bridges, the structural decomposition represented

in Figure A.1 is adopted. It is implicit that the structural components which are included in the different layers depend upon the problem under investigation. As an example, being interested in the dynamic behavior of cable-supported bridges, the scale of the problem corresponds to the scale of the whole structure. Thus, for instance, a tower saddle can be considered as a micro-level component, though a saddle itself could be decomposed into plates, welded joints, connections and so forth.

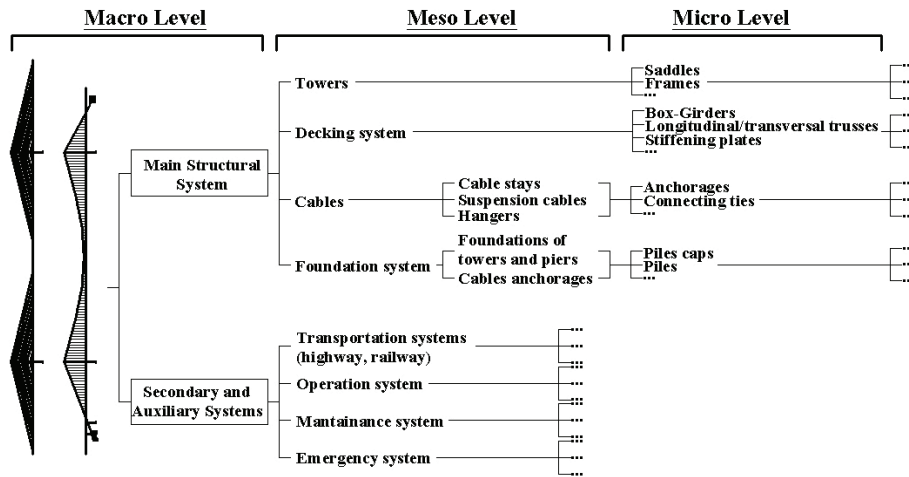


Figure A.1. Structural decomposition of cable-supported bridges

The hierarchical organization of the structural system depicted in Figure A.1 directly reflects on the need of developing multi layered mathematical models. Namely, global models are adopted to describe the global response at the macroscopic scale using a reasonable number of degrees of freedom. More refined models can then be used to assess local behaviors at the meso and micro scales, such as, for instance, the vibrations of bridge stays. It is worth noting that structural decomposition can be an effective tool for developing substructure models at the meso scale. Nevertheless, substructuring is not always allowed since global/local interactions, such as those between the deck and the stays of a cable stayed bridge, are usually neglected by substructure

models though they may play a significant role in the behavior of local elements at the meso scale.

A.3 The Tsing Ma Bridge

The Tsing Ma Bridge, located in Hong Kong, China, is a suspension bridge that crosses the Ma Wan Channel and links the Tsi Yi Isle to the Ma Wan Bay (see Figure A.3). Due to its inherent complexity, all the concepts presented in the previous sections can be directly applied to the case of this structure.



Figure A.3. The Tsing Ma Bridge

The technical and scientific relevance of the Tsing Ma Bridge is motivated by numerous reasons. Among those, the Tsing Ma is the world's longest span suspension bridge carrying both road and railway traffic and the world's largest deck carrying rail traffic. Besides, the bridge is located in a strong typhoon region that exposes the structure to extremely severe conditions, such as the York Typhoon occurred in 1999. For this reason, a wind and structural health monitoring system (WASHMS) has been installed on the bridge since the year of its completion (Wong, 2004). The WASHMS system has also given the chance of accessing a richness of field measurement results, regarding both the structural response (strains, displacements and accelerations) and the wind field (wind velocities). These results provide a distinctive opportunity to examine the dynamics of the Tsing Ma Bridge and to investigate the reliability of the numerical models for predicting its behavior.

The main span of the Tsing Ma Bridge is 1377 m in length and the overall length of the bridge is 2160 m (see Figure A.4 (a)). The two main cables have a diameter of 1.1 m and are 36 m apart. The towers have a total height of 206 m, measured from the base level to the tower saddle. The bridge deck is suspended by steel hangers in the Ma Wan side and in the main span and supported by three piers on the Tsing Yi side. In this side hangers are therefore missing and the two main cables behave as free stays (Ni et al., 2004).

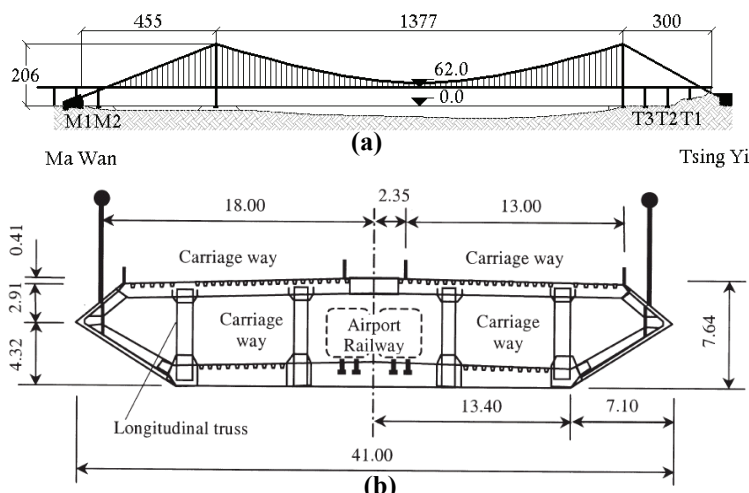


Figure A.4. Main geometry of the Tsing Ma Bridge (a); decking system (Li and Chan, 2006) (b)

Each of the two main cables is composed by 91 strands of parallel galvanized steel wires in the main span and by 97 strands in the side spans. The number of wires per strand is 360 or 368, resulting in a cross sectional area of 0.759 m² in the main span and of 0.801 m² in the side spans. The cables are formed by means of the traditional aerial spinning technique. Each hanger is made of four wire ropes of 76 mm diameter, that pass over the clamps on the main cables and are then attached to the chords by steel sockets. The longitudinal distance between each suspender unit is 18 m.

The bridge deck is a two-level hybrid steel structure, consisting of two longitudinal trusses and Vierendeel cross frames (see Figure A.4 (b)). Stiffening

steel plates complete the deck section that carries a dual three-lane highway on the upper level and two railway tracks and two carriageways on the lower level.

Each tower of the bridge is composed of two reinforced concrete legs and four deep pre-stressed concrete beams. Two hollow shafts are symmetrically arranged inside each leg, from the level of the top beam to a point located approximately 15 m above the base level. The towers are built on massive reinforced concrete slabs found on competent rock. All the supporting piers in the side spans are reinforced concrete structures founded on reinforced concrete pad footings, laying on competent rock.

A.4 The New Carquinez Bridge

The New Carquinez Bridge (NCB), also named the Alfred Zampa Memorial Bridge, is a suspension bridge completely built in 2003, which links Vallejo with Crockett in California over the Carquinez Strait (see Figure A.5). It consists of a main span of 728 m and two side spans of 147 m (southern) and 181 m (northern), respectively.



Figure A.5. The New Carquinez Bridge (from (Conte et al., 2008))

The New Carquinez Bridge is the longest suspension bridge that has been built in the United States since the 1960s and it is the first suspension bridge in the world with concrete towers in a high seismic zone (Conte et al., 2008). The design of the New Carquinez Bridge is characterized by the orthotropic aerodynamic steel deck, the reinforced concrete towers and the large-diameter drilled shaft foundations. The closed steel box girder of the deck is light, durable, and has low-maintenance expenses. The shape of the deck section was optimized through wind tunnel experiments in order to provide aerodynamic stability and low drag. The deck is continuous through the towers, with expansion joints located at the ends of the side spans.

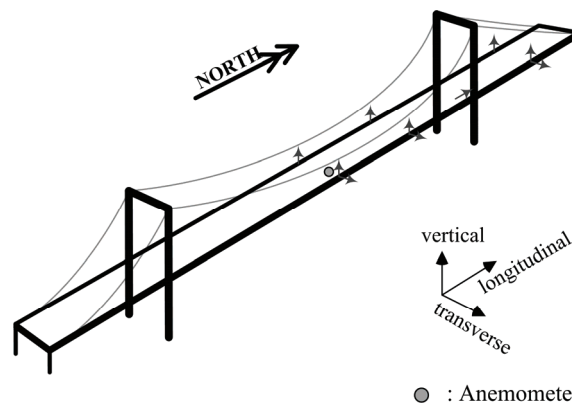


Figure A.6. Location of sensors installed on the New Carquinez Bridge (from (Ubertini et al., submitted))

As a part of the California Strong Motion Instrumentation Program, 76 accelerometers were placed over the New Carquinez Bridge including towers, piers, abutments, anchorages, piles and deck. The records of a set of ten accelerometers located on the northern half of the deck have been used in Chapter 4 to collect structural responses of the bridge and to examine its dynamical behavior under operating conditions. Figure A.6 displays the locations of such ten accelerometers (six in vertical, three in transverse, and one in longitudinal directions) with the addition of one anemometer at the mid-span.

The reinforced concrete towers are certainly the main architectural and aesthetic assets of the bridge. Their height reaches approximately 125 m above the water level. Reinforced frames are allocated at the corners of the cellular shafts in order to improve seismic ductility. According to the adopted seismic standards, the towers were designed to remain elastic during earthquakes of average intensity, with some exceptions at their lower sections (Conte et al., 2008). The towers are founded on pile caps supported by drilled shaft foundations which were subjected to the same seismic standard adopted for the towers. Particularly, each tower is supported by 12 shafts, with a maximum length of about 90 m. On the south span, a transition pier supports the end of the steel deck girder, houses tie downs of the cables, and supports the end of the south viaduct. This pier is structurally and architecturally similar to the main towers, with cellular reinforced concrete shafts and pile foundations. The cable anchorage at the south span is a massive concrete anchor block combined with piles. On the contrary, the north cable anchorage transfers the tension of the cables to the ground by direct bearing on the underlying rock.

APPENDIX B

STATIC AND MODAL ANALYSIS USING REDUCED DIMENSIONAL MODELS OF SUSPENSION BRIDGES

Abstract

The large dimensional TMC model of the Tsing Ma Bridge has been presented in Chapter 1 and validated on the basis of static and modal results. Two simplified models (TMR and TMS models) have also been presented in Chapter 1 and their capability to give similar results to the TMC model has been discussed. The results of the static and modal analysis conducted by using TMR and TMS models are here reported.

B.1 Static and modal results using the Tsing Ma Reduced (TMR) model

The deformed configuration of the bridge under dead loads, calculated via nonlinear static analysis using the TMR model, is presented in Figure B.1. Table B.1 presents a comparison between the vertical reactions calculated using the TMR model and those obtained by using the TMC model. Table B.2 presents the comparison between the natural frequencies of the bridge

calculated using the TMR model and those obtained experimentally by Xu and Ko (1997). The corresponding mode shapes are shown in Figures B.2 and B.3.

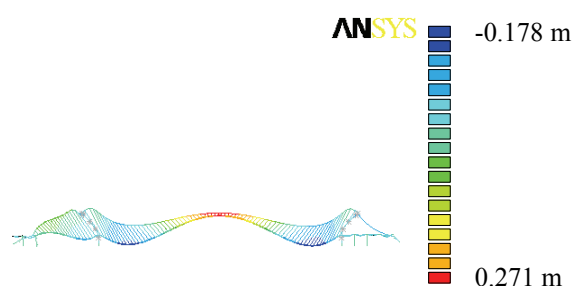


Figure B.1. Computed (TMR) vertical displacements under dead loads

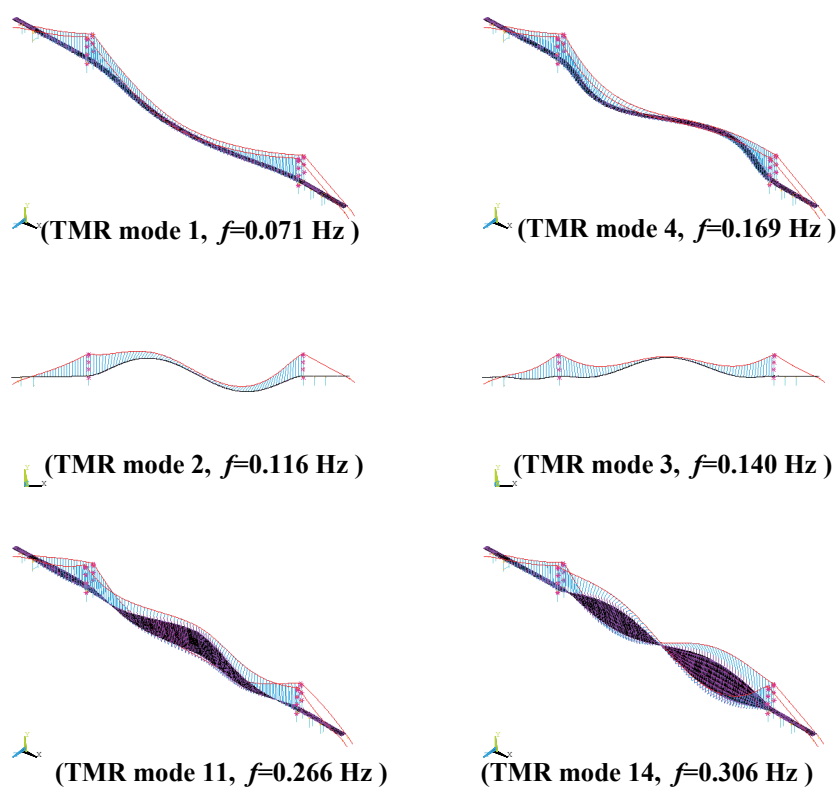


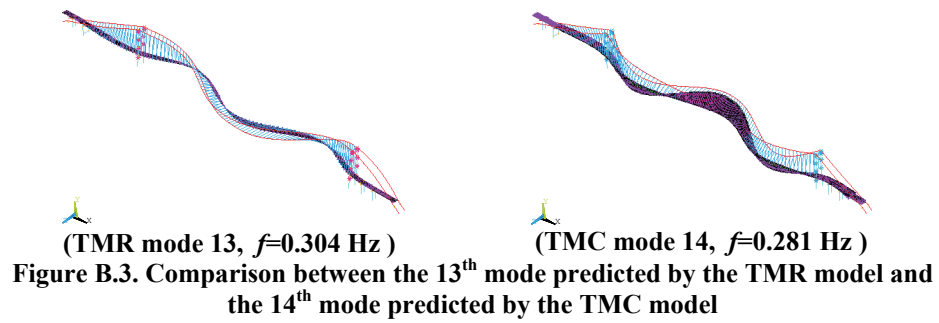
Figure B.2. First 2 transverse, vertical and torsional mode shapes predicted by the TMR model

Model	Vertical Reaction (kN)	Cable Horizontal Tension (kN)
TMC	2245300	388863
TMR	2288600	388169
Δ (%)	1.9	0.2

Table B.1 Comparison between static results obtained with the TMC and the TMR models

Vertical Modes			
Bridge Mode	TMR	Xu & Ko, 1997	Δ (%)
2	0.116	0.113	2.6
3	0.140	0.130	7.1
5	0.188	0.184	2.1
9	0.241	0.241	0.0
12	0.299	0.284	5.0
15	0.321	0.327	1.8
Transverse Modes			
Bridge Mode	TMR	Xu & Ko, 1997	Δ (%)
1	0.071	0.069	2.8
4	0.169	0.164	2.6
6	0.210	0.214	1.9
7	0.228	0.226	0.9
8	0.232	0.236	1.7
10	0.241	0.240	0.4
16	0.341	0.336	1.5
17	0.351	0.352	0.3
19	0.387	0.381	1.5
Torsional Modes			
Bridge Mode	TMR	Xu & Ko, 1997	Δ (%)
11	0.266	0.267	0.4
14	0.306	0.320	4.4
MEAN DIFFERENCE Δ_{mean} (%)			2.2

Table B.2 Computed (TMR) vs. measured natural frequencies



B.2 Static and modal results using the Tsing Ma Spine (TMS) model

The deformed configuration of the bridge under dead loads, calculated via nonlinear static analysis using the TMS model, is presented in Figure B.4. Table B.3 presents a comparison between the vertical reactions calculated using the TMS model and those obtained by using the TMC model. Table B.4 presents the comparison between the natural frequencies of the bridge calculated using the TMS model and those obtained experimentally by Xu and Ko (1997). The corresponding mode shapes are shown in Figures B.5 and B.6.

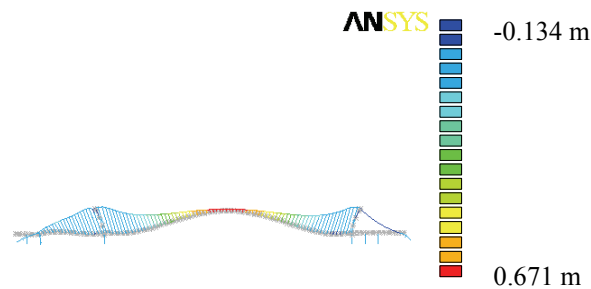


Figure B.4. Computed (TMS) vertical displacements under dead loads with pre-tensioned cables

Model	Vertical Reaction (kN)	Cable Horizontal Tension (kN)
TMC	2242200	388870
TMS	2238700	377666
Δ (%)	0.16	2.9

Table B.3 Static results obtained using TMC and TMS models

Vertical Modes			
Bridge Mode	TMS	Xu & Ko, 1997	Δ (%)
2	0.118	0.113	4.2
3	0.141	0.130	7.8
5	0.191	0.184	3.7
10	0.247	0.241	2.4
13	0.303	0.284	6.3
15	0.332	0.327	1.5
Transverse Modes			
Bridge Mode	TMS	Xu & Ko, 1997	Δ (%)
1	0.069	0.069	0.0
4	0.162	0.164	1.2
6	0.207	0.214	3.3
7	0.224	0.226	0.9
8	0.228	0.236	3.4
9	0.236	0.240	1.7
16	0.337	0.336	0.3
17	0.346	0.352	1.7
20	0.380	0.381	0.3
Torsional Modes			
Bridge Mode	TMS	Xu & Ko, 1997	Δ (%)
11	0.264	0.267	1.1
14	0.306	0.320	4.4
MEAN DIFFERENCE Δ_{mean} (%)			2.6

Table B.4 Computed (TMS) vs. measured natural frequencies

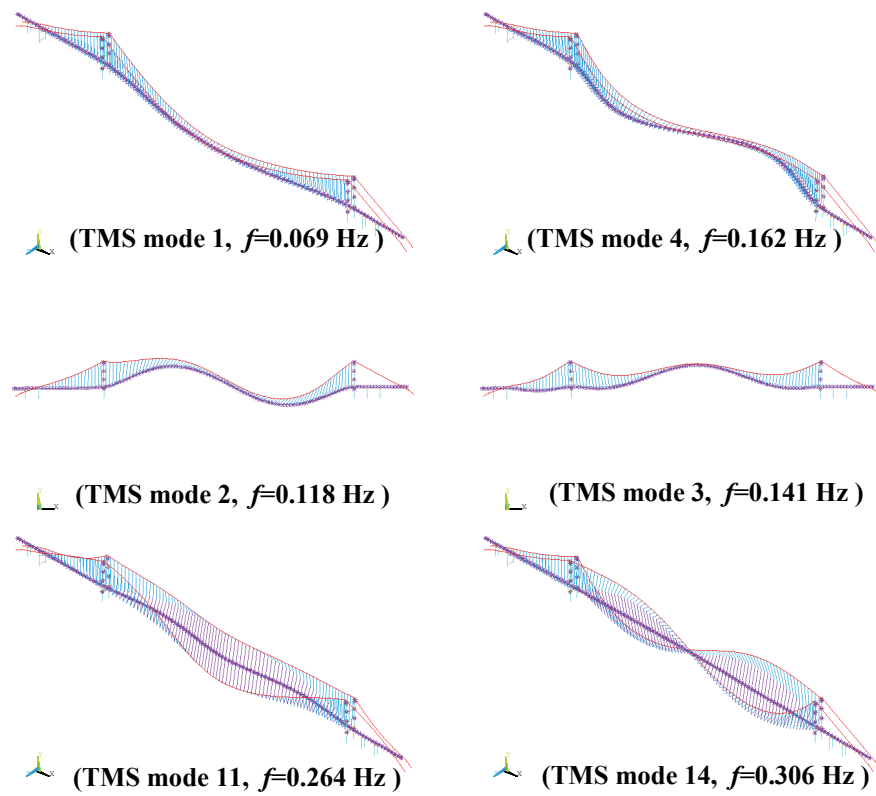


Figure B.5. First 2 transverse, vertical and torsional mode shapes predicted by the TMS model

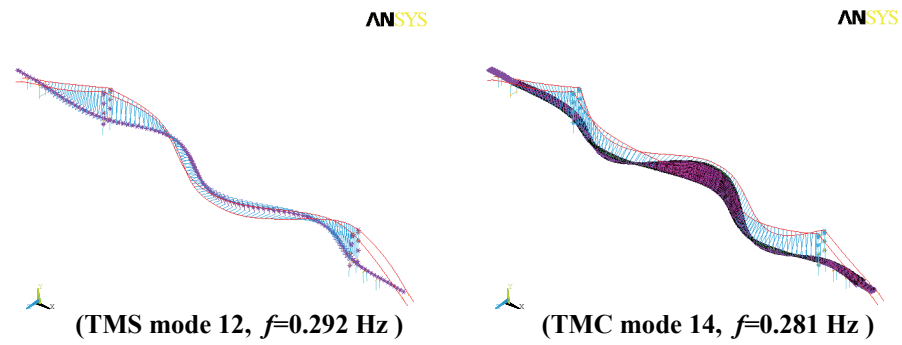


Figure B.6. Comparison between the 12th mode predicted by the TMR model and the 14th mode predicted by the TMC model

APPENDIX C

MODELING AND IDENTIFICATION STRATEGIES FOR CABLE DYNAMICS

Abstract

A brief insight to cable dynamics is given with a particular care to the experimental identification phase. To this end, after introducing the problem with the necessary theoretical background, a linear modal representation of a physical suspended cable is identified via dynamic testing by devoting a special care to detecting possible internal resonance conditions.

C.1 Introduction

The behavior of an arbitrarily sagged cable (such as bridge stays, transmission power lines, mooring cables and so on) can be modeled as a prestressed mono-dimensional linearly elastic continuum with no flexural, torsional or shear stiffness, as early outlined by Luongo et al. (1984). Different elastic cable theories were developed referring to either small-sag or large-sag cables. In the former case, particularly suitable for the analysis of cable stays, the analytical continuum formulation is simplified by the parabolic assumption, as outlined by Benedettini et al. (1995), while in the latter case discrete formulations and numerical methods are mostly used. Nearly all of the cable

discrete models available in the literature were formulated through a space discretization based on the Galerkin approach. This issue is addressed by expanding the displacement functions in the space of the linear eigenfunctions, early obtained in the paper by Irvine and Caughey (1974). By retaining a finite number of degrees of freedom (DOFs, i.e. modal amplitudes), the cable vibration is thus described by a system of nonlinear ordinary differential equations (ODEs). A fairly systematic analysis of the influence of the number of modes retained in the discrete model on the accuracy of the predicted nonlinear response was carried out by Arafat and Nayfeh (2002).

Among the numerical approaches, many papers focused on the finite element method (FEM) applied to cable modeling in the framework of large displacements (e.g., Cluni et al. 2007).

The nonlinear dynamics of cables was widely investigated in the literature and the most important aspects on this topic were summarized in two recent review articles by Rega (2004). The former was mainly focused on cable dynamics modeling, while the latter dealt with deterministic nonlinear phenomena that arise in the cable motion. Among those, some are worth citing, such as the well known bifurcation of the first in-plane mode into a bi-modal spatial oscillation (Larsen and Nielsen, 2004) and the complex behavior of multiple internally resonant cables (Nayfeh et al., 2002).

C.2 Modeling the nonlinear dynamics of cables

C.2.1 Continuous equations of motion

Let us consider the motion of an inclined elastic cable hanging in the vertical plane Oxy (see figure C.1). The cable chord coincides with the Ox axis and defines the angle θ with the horizontal direction. The Oz axis is parallel to the out-of-plane direction. The cable is assumed to behave as an ideal string with no bending, shear or torsion rigidities. Its static configuration C_0 is described by the function $y(s)$, s being the curvilinear abscissa defined along the cable. The

displacements u , v , and w in the coordinate directions define the general dynamic varied configuration C_t .

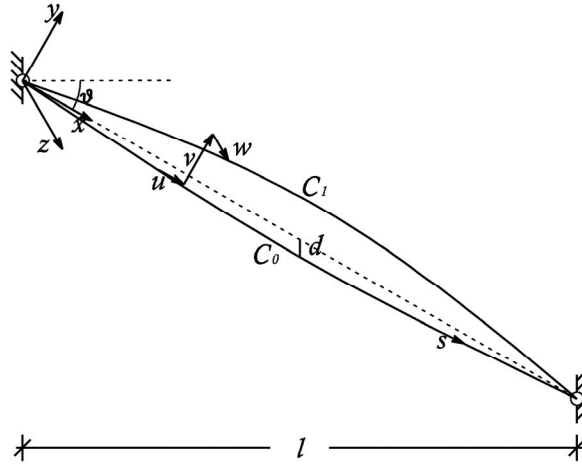


Figure C.2. Initial and dynamic varied cable configuration

Under the assumption of small sag d to span l ratio, the infinitesimal curvilinear abscissa element ds can be approximated by dx and the static configuration C_0 is described by the parabola:

$$y(x) = \frac{4d}{\cos(\vartheta)} \left[\left(\frac{x \cos(\vartheta)}{l} \right)^2 - \frac{x \cos(\vartheta)}{l} \right] \quad (\text{C.2.1})$$

The equations of motion of the continuous system, under distributed time varying loads $p_x(x, t)$, $p_y(x, t)$ and $p_z(x, t)$, are described by three well-known partial differential equations (PDEs) of the form (Benedettini et al., 1995):

$$\begin{aligned} m\ddot{u} + c_u \dot{u} - EAe' &= p_x(x, t) \\ m\ddot{v} + c_v \dot{v} - \left[\frac{H}{\cos(\vartheta)} v' + EA(y' + v')e \right]' &= p_y(x, t) \\ m\ddot{w} + c_w \dot{w} - \left[\frac{H}{\cos(\vartheta)} w' + EA w'e \right]' &= p_z(x, t) \end{aligned} \quad (\text{C.2.2})$$

where E is the Young modulus, A is the cross section, H is the horizontal reaction at the boundary, m , c_u , c_v , c_w are the mass and damping coefficients per unit length and e is the second-order truncation of the cable elongation:

$$e(x, t) = u' + y'v' + \frac{1}{2}(v'^2 + w'^2) \quad (\text{C.2.3})$$

Equation (C.2.3) represents the Lagrangian strain measure of the cable modeled as a mono-dimensional linearly elastic continuous with no flexural, torsional or shear rigidities. In equations (C.2.2) and (C.2.3) a dot and a prime indicate respectively derivatives with respect to time t and to the abscissa x . By assuming that the gradient of u in equation (C.2.3) is negligible with respect to the gradients of the transversal components ($u' \ll v', w'$), that $y' \ll 1$ and that $H / EA \ll 1$, the horizontal component $u(x, t)$ of the dynamic displacement can be eliminated through a standard condensation procedure. This leads to the definition of a uniform strain $\bar{e}(t)$ as:

$$\bar{e}(t) = \frac{\cos(\vartheta)}{l} \int_0^{l/\cos(\vartheta)} \left(y'v' + \frac{1}{2}(v'^2 + w'^2) \right) dx \quad (\text{C.2.4})$$

Equation (C.2.4) corresponds to the assumption that the additional dynamic cable tension $h(t)$ is spatially uniform, namely $h(t) = EA\bar{e}(t)$. Equations (C.2.2) are thus reduced to a system of two integral-differential equations of motion, involving the vertical and the out-of-plane displacements $v(x, t)$ and $w(x, t)$:

$$\begin{aligned} m\ddot{v} + c_v\dot{v} - \left[\frac{H}{\cos(\vartheta)} v' + EA(y' + v')\bar{e} \right]' &= p_y(x, t) \\ m\ddot{w} + c_w\dot{w} - \left[\frac{H}{\cos(\vartheta)} w' + EA w'\bar{e} \right]' &= p_z(x, t) \end{aligned} \quad (\text{C.2.5})$$

The problem is completed by homogeneous boundary conditions.

C.2.2 Reduced nonlinear analytical models

Reduced nonlinear models can be derived from equations (C.2.4) and (C.2.5) through the standard Galerkin procedure. This is achieved by expanding the

cable displacement functions v and w in the space of the in-plane and out-of-plane modal shapes. To obtain non-dimensional equations, the normalized time $\tau = t \cdot \omega_1$ and abscissa $\tilde{x} = x \cos(\vartheta)/l$ are introduced, where ω_1 is the natural circular frequency of the first in-plane mode, calculated by Irvine's theory (Irvine and Caughey, 1974). The modal coordinates $q_i^v(\tau)$ and $q_i^w(\tau)$, are thus defined as:

$$\begin{aligned} \frac{v(\chi, \tau) \cos(\vartheta)}{l} &= \sum_{i=1}^{\infty} \varphi_i(\chi) q_i^v(\tau) \\ \frac{w(\chi, \tau) \cos(\vartheta)}{l} &= \sum_{k=1}^{\infty} \psi_k(\chi) q_k^w(\tau) \end{aligned} \quad (\text{C.2.6})$$

where $\varphi_i(\chi)$ and $\psi_k(\chi)$ are the i -th and k -th in-plane and out-of-plane linear cable eigenfunctions. In practical applications the summations reported in equations (C.2.6) are truncated to $i, k = n/2$, being n a small (even) number (usually 2 or 4). A system of n nonlinear ODEs is then written by substituting equations (C.2.6) into equations (C.2.4) and (C.2.5):

$$\begin{aligned} \ddot{q}_i^v + \xi_i^v \dot{q}_i^v + \sum_{j=1}^{n/2} a_{0ij} q_j^v + \left(a_{1i} + \sum_{j=1}^{n/2} a_{2j} q_j^v \right) \bar{e} &= p_i^v \\ \ddot{q}_i^w + \xi_i^w \dot{q}_i^w + \omega_{iw}^2 q_i^w + a_{3i} q_i^w \bar{e} &= p_i^w \end{aligned} \quad (\text{C.2.7})$$

where the in-plane cable circular frequencies can be obtained as $\omega_{iv}^2 = (a_{0ij} + a_{1i} b_{1i})$, while ω_{iw} are the out-of-plane circular frequencies. The constant elongation term \bar{e} , in equation (C.2.7), is given by:

$$\bar{e}(t) = \sum_{j=1}^{n/2} b_{1j} q_j^v + \sum_{i=1, j=1}^{n/2} b_{2ij} q_i^v q_j^v + \sum_{k=1}^{n/2} b_{3k} q_k^{w^2} \quad (\text{C.2.8})$$

The expressions of the coefficients a_{0ij} , a_{1i} , a_{2j} , a_{3i} , b_{1j} , b_{2ij} , b_{3k} and of the normalized modal loads p_{iv} and p_{iw} can be found in (Gattulli et al., 2004). In the linear part of Equations (C.2.7) off-diagonal terms $a_{0ij} + a_{1i} b_{1j}$ vanish due to the orthogonality of the eigenfunctions. Nevertheless modal coupling arise in the nonlinear part, due to quadratic and cubic nonlinearities. In particular an

out-of-plane motion is always coupled with an in-plane one, due to second order effects. Moreover the elongation term $\bar{\epsilon}$ enters only parametrically the out-of-plane and the antisymmetric in-plane modes, which therefore generates only second order tension increments.

C.2.3 FE models

Reduced Galerkin models apply to shallow cables for which the condensation hypothesis can be made. A way to circumvent such a limitation is represented by the FEM method which apply to arbitrarily sagged cables. Different finite elements were employed in the literature to reproduce the dynamics of suspended cables. Three nodes isoparametric elements, which account for the curvature of the cable, were utilized in references (Desai et al. 1988; Desai et al., 1995; Gattulli et al., 2004) while tridimensional geometric nonlinear trusses were utilized, for instance, by Cluni et al. (2007). Beam elements (with various shape functions and integration points) can also be employed in order to account for the effective bending, shear and torsion rigidities of the cables. Indeed those rigidities, traditionally neglected in the literature on cable dynamics, may become significant in special cases such as bending near the terminations.

Once the adopted finite element has been chosen, the vector of n degrees of freedom \mathbf{U} is defined and the equations of motion, in the framework of large displacements and arbitrary (small or large) strains, are written following the classic *Updated Lagrangian* approach:

$$\mathbf{M}\ddot{\mathbf{U}}(t) + \mathbf{C}\dot{\mathbf{U}}(t) + \mathbf{Q}(\mathbf{U}(t), \dot{\mathbf{U}}(t)) = \mathbf{F}(t) \quad (\text{C.2.9})$$

where \mathbf{M} is the mass matrix, \mathbf{C} is the damping matrix, $\mathbf{Q}(\mathbf{U}(t), \dot{\mathbf{U}}(t))$ is the vector of generalized restoring forces and $\mathbf{F}(t)$ is the vector of nodal loads. Within the framework of large displacements, vector \mathbf{Q} is expressed by the following equation:

$$\mathbf{Q}(\mathbf{U}(t), \dot{\mathbf{U}}(t)) = [\mathbf{K}_E + \mathbf{K}_T(\mathbf{U}(t))]\mathbf{U}(t) \quad (\text{C.2.10})$$

where \mathbf{K}_E and $\mathbf{K}_T(\mathbf{U}(t))$ are the elastic and geometric tangent stiffness matrices respectively.

The time integration of Equation (C.2.9) can be carried out through the Hilber-Hughes algorithm. With such an approach the scalar parameter α is introduced for controlling the numerical damping of higher modes without reducing the algorithm accuracy. The equations of motion at time $t+\Delta t$, are thus written with temporal averaging (through the scalar parameter α) of the stiffness, damping and force terms:

$$\mathbf{M}\ddot{\mathbf{U}}(t+\Delta t) + (1+\alpha)(\mathbf{C}\dot{\mathbf{U}}(t+\Delta t) + \mathbf{Q}(t+\Delta t) - \mathbf{F}(t+\Delta t)) - \alpha(\mathbf{C}\dot{\mathbf{U}}(t) + \mathbf{Q}(t) - \mathbf{F}(t)) = 0 \quad (\text{C.2.11})$$

Since Equation (C.2.11) is non-linear, due to the presence of the geometric term $\mathbf{K}_T(\mathbf{U}(t+\Delta t))$, its numerical solution requires an iterative procedure. This issue can be addressed by adopting the Newton-Raphson scheme, with a linear initial estimate of the vector of restoring forces $\mathbf{Q}(t+\Delta t)$ as a function of the displacement increments $\Delta\mathbf{U}(t+\Delta t)$:

$$\mathbf{Q}(t+\Delta t) = \mathbf{Q}(t) + [\mathbf{K}_E + \mathbf{K}_T(\mathbf{U}(t))]\Delta\mathbf{U}(t+\Delta t) \quad (\text{C.2.12})$$

Equation (C.2.12) is substituted into equation (C.2.11) and the iterative equation is obtained through the generalized trapezoidal finite difference scheme. The vector of displacement increments $\Delta\mathbf{U}(t+\Delta t)$ is thus calculated iteratively until the error σ^k at the k -th iteration satisfies:

$$\sigma^k = \sqrt{\left| \frac{\delta\mathbf{U}^k \delta\mathbf{U}^{kT}}{\mathbf{U}^k \mathbf{U}^{kT}} \right|} < \tilde{\sigma} \quad (\text{C.2.13})$$

where $\Delta\mathbf{U}(t+\Delta t) = \sum_{i=1}^k \delta\mathbf{U}^i$ and $\tilde{\sigma}$ is a suitably small given tolerance. The above described method is second order accurate (Cluni, 2004).

A comparison between analytical Galerkin models and numerical FE models was conducted by Gattulli et al. (2004). This comparison showed the feasibility of the FEM procedures to catch most of the coupling and bifurcation phenomena occurring in the cable response. Moreover, it was emphasized that

an analytic Galerkin model (GAL model) with 4 DOFs (two in-plane and two out-of-plane modal amplitudes) is usually sufficient to describe the non-linear dynamics of the system with a high accuracy.

C.3 Cables as parts of complex structures

Since cables are usually parts of complex structures, such as cable-stayed and suspension bridges, their interaction with the whole structural system cannot a-priori be disregarded. Nevertheless, at a first stage of approximation, cable-structure interaction can be neglected when the fundamental modes of the cables are uncoupled from the vibration of other structural components (i.e. the modes involving the vibration of cables are local modes). The main consequence of this assumption is that the cable motion can be studied using substructure models such as those presented in Section C.2. As an example, this point is discussed with reference to the main cables of the Tsing Ma Bridge on the Tsing Yi lateral span. Indeed, as described in Appendix A, suspenders are missing in this side of the bridge and the cables behave as free stays. The geometric characteristics of the considered cables are summarized in Table C.1.

d/L	Θ (°)	A (m ²)	L (m)	λ^2/π^2
0.005	27.83	0.8007	293.2	0.058

Table C.1. Characteristics of the main cables on the Tsing Yi lateral span

Cable feature	IRVINE'S TH.	COMPUTED	Δ (%)
H (kN)	389910	388863	0.3
Cable Mode	IRVINE'S TH.	COMPUTED	Δ (%)
1 st Out Plane	0.397 Hz	0.407 Hz	2.5
1 st In Plane	0.407 Hz	0.411 Hz	1.0
2 nd Out Plane	0.795 Hz	0.813 Hz	2.2
2 nd In Plane	0.795 Hz	0.815 Hz	2.4
3 rd Out Plane	1.192 Hz	1.218 Hz	2.1
3 rd In Plane	1.192 Hz	1.220 Hz	2.3

Table C.2. Computed vs. analytical horizontal reaction H and natural frequencies of the main cables on the Tsing Yi lateral span of the Tsing Ma Bridge

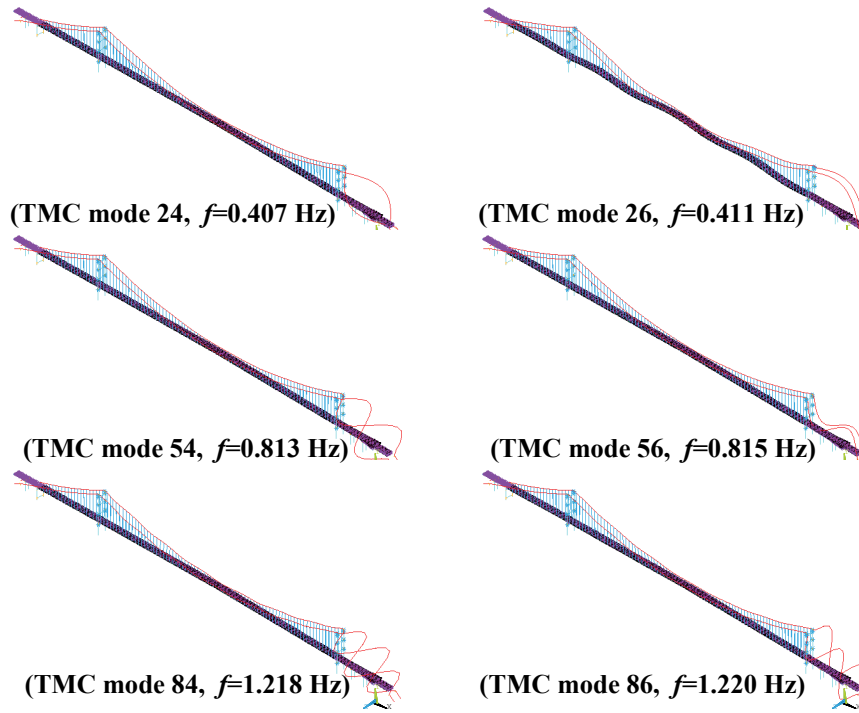


Figure C.2. First 6 computed (TMC model) mode shapes of the Tsing Yi free cables

Figure C.2 shows 6 local modes involving the cables and obtained from the modal analysis of the whole bridge conducted using the TMC model described in Chapter 1. The shapes of these modes correspond to those of the first six cable modes expected from Irvine's Theory (Irvine and Caughey, 1972). A good agreement is also found between the natural frequencies of these modes and the values predicted by Irvine's Theory, as reported in Table C.2. Indeed, the residual small percentage differences, close to 2%, can be attributed to the presence of flexural rigidity that is incorporated in the TMC model but is disregarded by Irvine's Theory.

Global bridge modes involving cable motions are also detected. This is the case of modes 22 and 25 which are shown in Figure C.3. However, these modes are high order modes of the deck and their effects can be neglected in many

practical cases. Thus, since the main modes of the cables are local modes or at least are not interacting with any fundamental low order mode of the deck, cables-structure interaction can be neglected in the presented case with a good approximation.

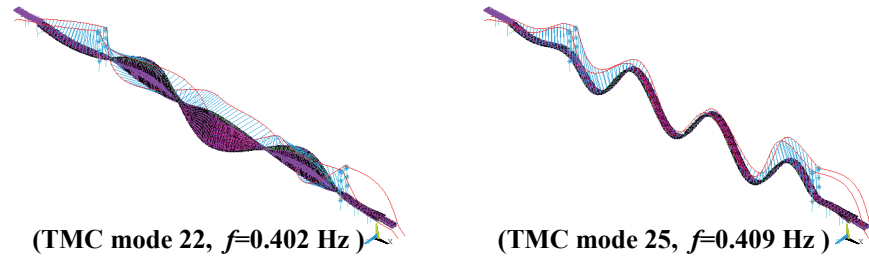


Figure C.3. 22nd and 25th bridge modes (TMC model), evidencing coupling between deck and cables vibrations

C.4 Experimental identification of a physical cable via dynamic testing

The identification of the natural frequencies and damping ratios of a physical cable is presented. The singular value decomposition (SVD) of the spectral matrix of the measurements is adopted to identify the natural frequencies of the system since this technique allows to detect possible internally 1:1 resonant modes. Wavelet analysis is adopted to identify the modal damping ratios.

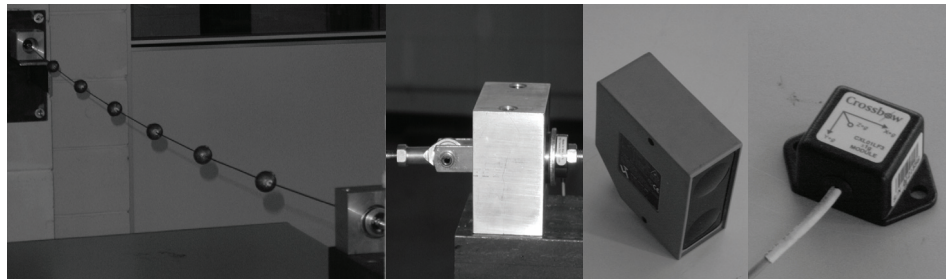


Figure C.4. From the left: physical cable, detailed view of the anchor with mounted load cell, laser displacement sensor, crossbow triaxial accelerometer

The observability conditions of the system were reported in (Faravelli and Ubertini, in press) and in Chapter 9, thus showing that one in-plane and one out-of-plane observations are sufficient to identify the natural frequencies of the system provided that the cable is not 1:1 in-plane internally resonant. At the so-called crossover points (1:1 in-plane internal resonance conditions) two in-plane observations are at least required. For this reason, two well-posed in-plane measurements have been adopted in the experimental tests, as described in Section C.4.1.

C.4.1 Experimental setup

An experimental suspended cable model is here considered (see Figure C.4) with span length $L=2.36$ m. The cable is supported at its ends by two identical devices, each one having a spherical joint, of the Tescubal type, fixed to rigid supports placed at the same height. The anchorages are realized by inserting the end threaded parts of the cable in the spherical joints. Two laser sensors, type Wenglor, allow to measure the vertical movements v_θ in the in-plane direction and w_θ in the out-of-plane one, of a point placed in the middle of the cable span L . Two tri-axial accelerometers, Crossbow LF type, are fixed to the cable approximately to the three quarters of the span and to the one fifth of the span, respectively. The accelerometers record the acceleration time history signals both in the vertical in-plane and in the transversal out-of-plane directions of the two application points. The possibility of detecting 1:1 internally resonant modes is thus ensured by the observability conditions.

The cable, made by a stainless steel wire of diameter 2 mm, has an elastic modulus E roughly equal to 85000 MPa. The cable mounts six equally-spaced spherical masses. One of the two anchorages is “dead”, while the other end allows to vary the tension in the cable by a screw, connected to the cable through a bearing ball. The unit mass of the cable is 0.02 kg/m, which corresponds to a weight of 0.46 N. Each of the spherical masses adds a weight of 1.42 N. The total static weight for the length unit is $q = 3.805$ N/m. The initial configuration chosen for the cable has a sag $f=2.0$ cm, which corresponds to a taut rope with a static shooting to the supports $H=133.8$ N.

C.4.2 System identification

The modal identification of the cable (spectral components and damping ratios) has been carried out in free/forced oscillations and small displacements. As it was reported in reference (Faravelli and Ubertini, 2008), the analysis of the acceleration measurements guaranteed a higher accuracy with respect to the analysis of displacement measurements. Thus, for the seek of brevity, one here only reports the results obtained by using accelerometer records.

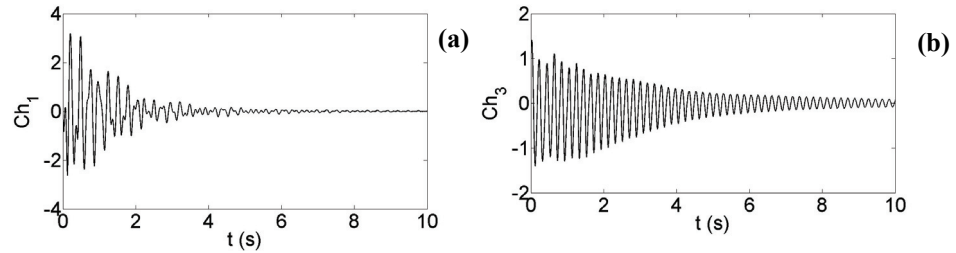


Figure C.5. Time history signals of in-plane acceleration (Ch1) and out-of-plane acceleration (Ch3) in free vibration tests: (a) and (b)

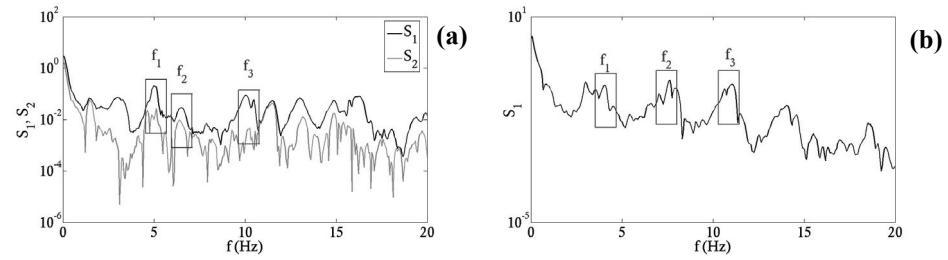


Figure C.6. Singular values of spectral matrix of the acceleration records. In-plane test: (a); out-of-plane test: (b)

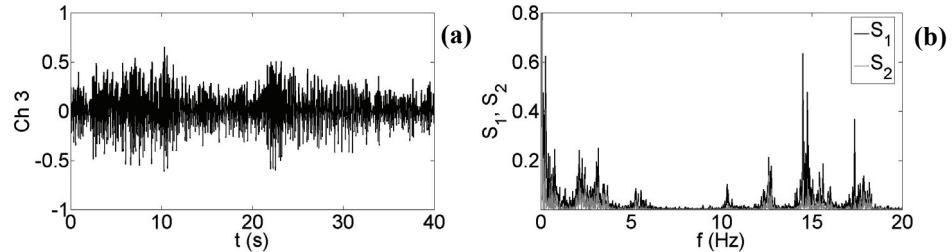


Figure C.7. Time history signal of in-plane acceleration (Ch3) under forced white noise excitation: (a); singular values of the spectral matrix of the acceleration records: (b)

Two tests have been carried out. The former test consists in free in-plane/out-of-plane oscillations. In this case, particular care was devoted to exert the external impulse so as to excite also the anti-symmetric modes. The external impulse was provided by a linear motor. The latter test consists in forced in-plane oscillations exerted by a linear motor which applies a white noise excitation to the cable. In this case a particular care was posed to apply the dynamic force to the cable without contact in such a way not to modify the structural system. This has been achieved by mounting a ring on the edge of the linear motor which was sufficiently larger than the cable diameter. The cable passed through the ring which was moved by the linear motor and excited the cable by simply impacting on it.

Each acquisition has a duration varying from 10 to 30 s and the sampling frequency, for all the measured data, is 250 Hz. For every test, the following sets of voltage data were recorded: six accelerations (Channels (Ch) 1 to 6) in the coordinate directions and two displacements (in-plane vertical and out-of-plane, Channels 7 and 8) at the cable mid-span.

The time history signals (voltage signals) of Ch 1 and Ch 3 are represented in Figure C.5. In order to identify the natural frequencies of the system, the frequency dependent singular values of the spectral matrix of the acceleration records have been calculated. By repeating the tests three times, the peaks of the singular values corresponding to the natural frequencies of the cable have been identified. When modes are well-separated the first singular value S_1 is much larger than the remaining ones. However, if in correspondence of one peaks two singular values reach approximately the same value, two 1:1 internally resonant modes are detected.

Figure C.6 (a) represents the two singular values S_1 and S_2 of the 2×2 spectral matrix composed by the PSD functions of the two in-plane acceleration records. As emphasized by the presented results, S_1 is much larger than S_2 in correspondence of the first three in-plane frequencies f_1 , f_2 and f_3 . Therefore, each peak corresponds to a single vibration mode and no 1:1 in-plane resonant modes are detected within the considered frequency interval. The same approach has been applied also to the results of the in-plane forced vibration

tests which are represented in Figure C.7 and gave similar results. The first singular value of the spectral matrix of the out-of-plane acceleration measurements under free vibrations is represented in Figure C.6 (b). In this case, comparing S_1 to S_2 is not necessary since, according to Irvine's theory, out-of-plane modes are always well-separated.

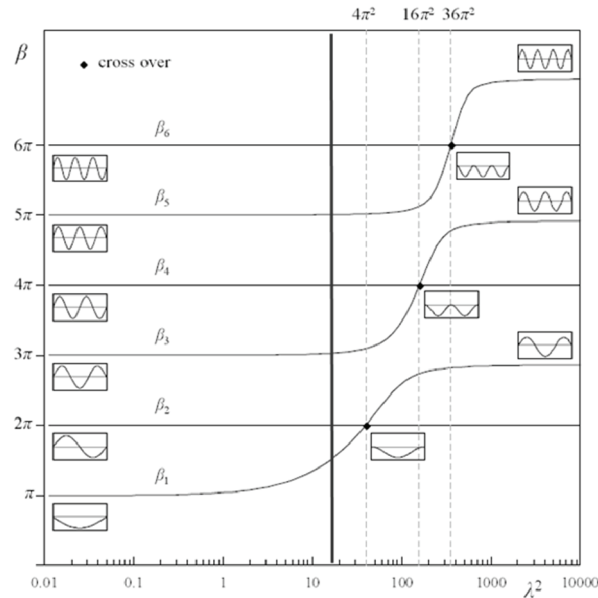


Figure C.8. Approximate location of the physical model in the Irvine's spectrum

In-plane frequencies (Hz)	Out-of-plane frequencies (Hz)
$f_1=5.25$	$f_1=4.03$
$f_2=7.30$	$f_2=7.63$
$f_3=10.31$	$f_3=11.05$

Table C.3 Identified natural frequencies of the physical cable

The results of the system identification are reported in Table C.3, while Figure C.8 represents the approximate location of the physical model in the Irvine's spectrum (Gattulli, 2007). It is worth mentioning that the cable is not far away from the 1:1 internal resonance between the first and the second in-

plane modes ($f_2/f_1=1.39$) and very close to the 2:1 internal resonance between the third and the first in-plane modes ($f_3/f_1=1.96$). As commented in Chapter 8, this circumstances have strong influences on the nonlinear dynamic behavior of the system and can be exploited in order to design a suitable control strategy for vibration mitigation purposes.

C.4.3 Damping identification via Wavelet analysis

Since 1:1 internally resonant in-plane modes are not detected, the modal damping parameters have been measured via wavelet analysis of the accelerations under free vibration tests. Details on this approach can be found in (Faravelli and Ubertini, 2008).

Figure C.9 represents the logarithm of the modulus of the wavelet transform along the ridges corresponding to the first in-plane (W_2) and out-of-plane (W_1) modes. Usually W_i are referred to as *wavelet skeletons*. As reported in reference (Faravelli and Ubertini, 2008) the modal damping ratios are proportional to the slopes of the wavelet skeletons.

After performing three experimental tests, under free spatial vibrations, the damping ratios ζ_i of the first three in-plane and out-of-plane modes have been identified. Particularly, for each test, one identified three values of the modal damping ratios, corresponding to three distinct intervals in which the wavelet skeletons were subdivided. The damping ratio ζ_i of the i -th mode was calculated as the mean value of the results obtained in the different intervals. The obtained results are summarized in Table C.4.

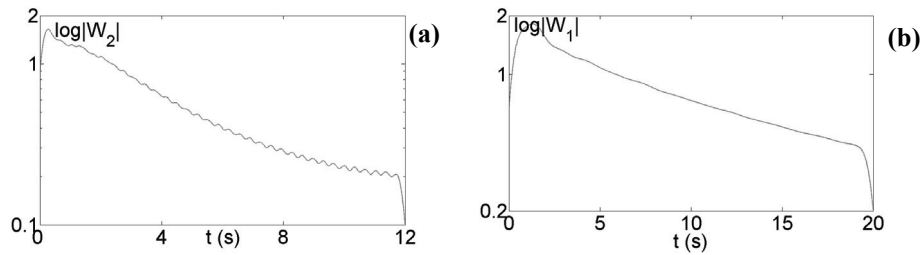


Figure C.9. Time-variation of wavelet modulus along the ridges corresponding to the first in-plane and out-of-plane modes: (a) and (b) respectively

In-plane modes	Out-of-plane modes
$\xi_1=0.0198$	$\xi_1=0.0156$
$\xi_2=0.0152$	$\xi_2=0.0196$
$\xi_3=0.0110$	$\xi_3=0.0098$

Table C.4 Identified modal damping ratios via wavelet analysis

C.5 Damping effects on nonlinear cable response

It is of interest to analyze how damping uncertainties reflect on the nonlinear response of cables. To this end, the frequency response curves of the first in-plane and out-of-plane modes of the physical cable identified in Section C.3 have been calculated by means of a continuation technique implemented in a dedicated software (AUTO2000) (see Figure C.10). A nonlinear Galerkin model with two degrees of freedom has been adopted in the simulation, assuming that the response of the considered modes is weakly influenced by the neglected higher order modes.

The results presented in Figure C.10 (a) refer to a harmonic in-plane excitation of normalized amplitude p and frequency ratio Ω with respect to the first in-plane cable frequency. The amplitude q_2 of the harmonic response is represented as a function of Ω . Three different values of the damping ratios are assumed, by reducing the maximum experimentally measured value $\xi_2=0.026$ by 25% and 50%. As it can be observed from such a figure, a softening-hardening behavior of the system is observed around the primary resonance ($\Omega=1$). Super-harmonic resonant peaks are also observed at $\Omega=1/2$, $\Omega=1/4$, etc. Those circumstances indicate that the cable behavior is essentially nonlinear, even at low vibration amplitudes. The figure also shows that reducing the damping ratio reflects on a drastic cut-off of the cable hardening harmonic branch around the main resonance. Consequently, the frequency range in which the cable may undergo the largest displacements is also cut-off. Analogous results are presented in Figure C.10 (b), with reference to the out-of-plane harmonic vibrations.

A Galerkin model with 4 in-plane and 4 out-of-plane degrees of freedom has also been considered. Figure C.11 shows the phase plane projections of the steady harmonic limit cycles obtained, under in-plane harmonic excitation, for

$\Omega=1.1$. As one can observe from such a figure, depending on the initial conditions, the system, at the considered amplitude of excitation, may undergo a bifurcated spatial motion involving the out-of-plane mode q_1 . Nevertheless, if one slightly increases the damping of the system, the limit cycle is destroyed and the out-of-plane bifurcation does not appear. In contrast, a reduction of the damping of the system reflects on a larger participation of the out-of-plane mode.

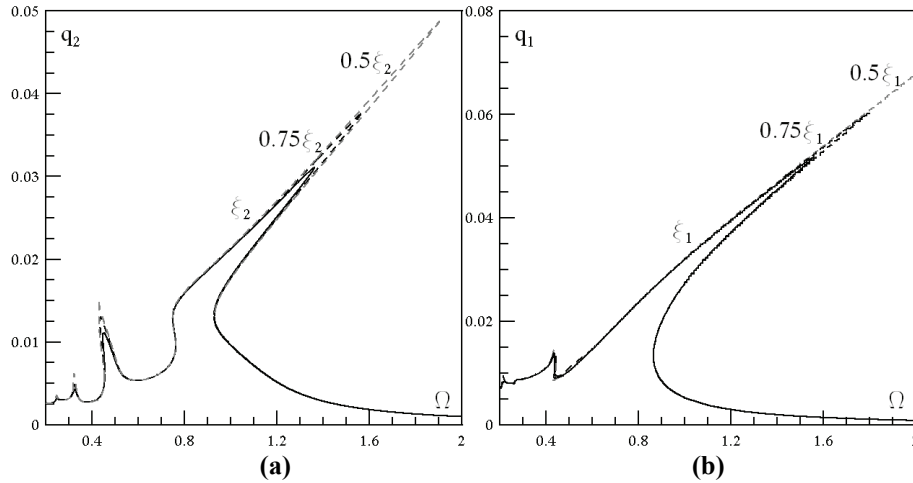


Figure C.10. Frequency response curves of the first in-plane (q_2) and out of plane (q_1) modes assuming different modal damping ratios ($p=0.003$)

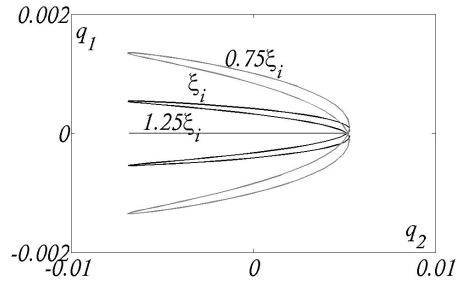


Figure C.11. Phase plane projections of relevant harmonic limit cycles for different damping ratios ($\Omega=1.1$, $p=0.002$)

C.6 Concluding remarks

After recalling the necessary background for modeling the nonlinear dynamics of cables, the modal identification of a physical cable via an output only technique has been conducted in the laboratory environment. As discussed in Chapter 9, the observability conditions of the system are satisfied by installing two in-plane and one out-of-plane sensors. The results emphasize that the cable is placed on the left of the first crossover point and it is close to the 2:1 internal resonance between the third and the first in-plane modes. Modal damping ratios have been identified via wavelet analysis.